



# THÈSE

PRÉSENTÉE A

**L'UNIVERSITÉ BORDEAUX 1**

ÉCOLE DOCTORALE DES SCIENCES PHYSIQUES ET DE L'INGÉNIEUR

Par Aitor, ETXEBERRIA

POUR OBTENIR LE GRADE DE

DOCTEUR

SPÉCIALITÉ : Électronique

## **Microgrid Hybrid Energy Storage Integration and Control using a Three-Level NPC Converter**

Intégration et commande d'un système de stockage hybride dans un  
microréseau utilisant un convertisseur NPC à trois niveaux

Directeur de recherche : Jean-Michel VINASSA

Soutenue le 7 décembre 2012

Devant la commission d'examen formée de :

M. BACHA, Seddik  
M. MARTINEZ, Luis  
M. TAPIA, Gerardo  
M. VINASSA, Jean-Michel  
M. CAMBLONG, Haritza  
M. VECHIU, Ionel

Professeur, Université Joseph Fourier  
Professeur, Universitat Rovira i Virgili  
Maître de conférences, EHU/UPV  
Professeur, Université Bordeaux 1  
Maître de conférences, EHU/UPV  
Maître de conférences, ESTIA

Rapporteur  
Rapporteur  
Examineur  
Directeur de thèse  
Co-directeur de thèse  
Co-directeur de thèse



Izan zirelako, gara; garelako, izango dira  
*Joxemiel Barandiaran*





# Acknowledgments

First of all I would like to show my gratitude to the director and co-directors of my thesis, Jean-Michel Vinassa, Ionel Vechiu and Haritza Camblong for their help during these long three years. I have to specially thank Ionel Vechiu for his guidance and for all the time he spent discussing with me several technical issues.

I gratefully acknowledge the financial support of the *Conseil Régional d'Aquitaine*. I am also grateful to the director of ESTIA Jean-Roch Guiresse for giving me the opportunity to work in ESTIA and to be part of it.

I show my gratitude to Seddik Bacha, professor at *Université Joseph Fourier Grenoble*, and Luis Martinez Salamero, professor at *Universitat Rovira i Virgili*, for having reviewed this dissertation, as well as to Gerardo Tapia, associate professor of *Euskal Herriko Unibertsitatea*, for being part of the jury.

Je voudrais aussi remercier à tous les membres du groupe EneR-GEA, Octavian Curea, Amélie Hacala, Stéphane Kreckelbergh et Sylvain Baudoin pour leur soutien et surtout de m'avoir aidé à améliorer mon français. Merci aussi à tous les doctorants et stagiaires que j'ai connu pendant les trois ans de thèse.

Ez nuke eskertzen zati hau senideei gure hizkuntza zahar honen bidez hitzik eskaini gabe amaitu nahi. Mila esker familia osoari, emandako laguntzagatik eta batez ere lana ahazten laguntzeagatik. Zuek gabe ezin izango nukeen sekula tesi hau bukatu. Nire neskala-gunak, jakina, atal berezi bat merezi du batez ere nire egun txar guztiak bikain kudeatzeko erakutsi duen gaitasunagatik. Nik adina baba atera ditu berak eltzetik.

Eskerrik asko guztioi!



# Abstract

The increasing penetration of Distributed Generation systems based on Renewable Energy Sources is introducing new challenges in the current centralised electric grid. The microgrid is one of the alternatives that is being analysed in order to increase the penetration level of renewable energy sources in electrical grids and improve the power quality.

The microgrid stability is highly sensitive to power variations coming from the energy sources or loads. In this context, an energy storage system is essential and it must satisfy two criteria: to have a high storage capacity to adapt the generation to the demand and to be able to supply fast power variations to overcome the power quality problems that may arise.

The main objective of this thesis has been to design a power conversion system and the associated control algorithm for a storage system management in order to satisfy the defined requirements, as well as to experimentally validate the proposed solution.

After an analysis of different storage system technologies, it can be concluded that there is not any storage system capable of offering the energy and power requirements at the same time. Consequently, the association of a SuperCapacitor bank and a Vanadium Redox Battery is used to satisfy the mentioned requirements.

This thesis has been focused on the power and energy flow management of the proposed Hybrid Energy Storage System through an innovative power conversion system and its control method. A Three-Level Neutral Point Clamped converter has been used to control at the same time the two storage systems, due to the reduced power losses and harmonic distortion compared to other existing topologies. A control algorithm that uses the operational limits of the converter in its entire operation range has been designed in order to allow selecting the best operation point according to the specified criteria.

The operation of the power conversion system and the proposed control method have been first validated in simulations and then experimentally using the microgrid installed in *ESTIA*.



# Résumé

L'intégration croissante de la Génération Distribuée basée sur des sources d'énergies renouvelables présente de nouveaux défis pour le réseau électrique centralisé actuel. Le micro-réseau est une des alternatives envisagées afin d'augmenter le taux de pénétration d'énergie renouvelable et d'améliorer la qualité de l'énergie. La stabilité d'un micro-réseau est fortement sensible aux variations de puissance venant des sources d'énergie ou des charges.

Dans ce contexte, un système de stockage d'énergie joue un rôle essentiel et doit satisfaire deux conditions : disposer d'une capacité de stockage importante pour adapter la production à la demande et être capable de fournir rapidement une puissance instantanée suffisante pour pallier les problèmes de qualité d'énergie.

L'objectif principal de cette thèse est de concevoir et valider expérimentalement un système de conversion de puissance et l'algorithme de contrôle associé pour la gestion du stockage dans un micro-réseau afin de satisfaire les deux conditions.

Suite à l'analyse de différentes technologies de stockage, on peut conclure qu'il n'y a pas de système de stockage capable de satisfaire les conditions d'énergie et de puissance en même temps. Par conséquent, l'association d'un supercondensateur et d'une batterie Redox au Vanadium dans un Système de Stockage Hybride est utilisée pour satisfaire les conditions mentionnées.

Le travail de recherche est axé sur la gestion du flux d'énergie et de puissance du Système de Stockage Hybride proposé à l'aide d'un système de conversion de puissance innovant et son algorithme de commande. Un convertisseur multi-niveaux 3LNPC a été choisi pour commander en même temps les deux systèmes de stockage, en raison de faibles pertes de puissance et de distorsions harmoniques réduites en comparaison avec d'autres topologies existantes. Un algorithme de commande capable d'exploiter les limites de fonctionnement du convertisseur sur toute sa plage de fonctionnement a été conçu afin de satisfaire de manière optimale les critères spécifiés.

Le fonctionnement du système de conversion et la stratégie de commande proposée ont été validés d'abord en simulation et ensuite expérimentalement en utilisant le micro-réseau installé à l'ESTIA.



# **Intégration et commande d'un système de stockage hybride dans un microréseau utilisant un convertisseur NPC à trois niveaux**

L'infrastructure vieillissante et le manque de fiabilité du réseau électrique traditionnel en cas d'événements imprévus, la crise énergétique due aux combustibles fossiles et la nécessité de réduire les émissions de gaz à effet de serre conduisent à augmenter l'utilisation des énergies renouvelables et la Génération Distribuée (GD). Le niveau de pénétration toujours plus élevée des énergies renouvelables implique de nouveaux défis pour le réseau électrique centralisé actuel.

Le microréseau est une des alternatives envisagées afin de proposer une solution viable pour les problèmes que pose l'intégration des sources d'énergies renouvelables. Ce type de réseau peut généralement être défini comme un réseau électrique faible constitué par différentes sources d'énergie distribuées (principalement des sources d'énergie renouvelables), des charges et des systèmes de stockage. Une des caractéristiques principales d'un microréseau est sa capacité de fonctionner interconnecté avec un réseau principal ou en îlotage.

Dans un microréseau, le niveau de puissance générée est variable et les oscillations de puissance qui en résultent ont un réel impact sur le réseau et sur les charges qu'il alimente. En sens inverse, un réseau faible peut connaître lui aussi des variations induites par le comportement de ses charges et des autres sources, et ces variations peuvent influencer ou détériorer les systèmes qui y sont connectés. Dans ce type de réseau, un système de stockage joue un rôle essentiel et doit disposer d'une capacité de stockage importante pour adapter la production à la demande, mais aussi être capable de fournir rapidement une

puissance instantanée suffisante pour pallier les problèmes de qualité d'énergie.

L'objectif principal de cette thèse est de concevoir et de valider expérimentalement un système de conversion de puissance et l'algorithme de contrôle associé pour la gestion du stockage dans un microréseau afin de satisfaire les deux conditions.

L'analyse de différentes technologies de stockage a permis de conclure qu'il n'y a pas de système de stockage capable de satisfaire les conditions d'énergie et de puissance en même temps. Par conséquent, dans cette thèse un module de SuperCondensateurs (SC) et une Batterie Redox au Vanadium (VRB) ont été associés en un Système de Stockage Hybride (SSH) utilisé pour satisfaire les conditions mentionnées.

La batterie Redox au Vanadium est un système de stockage particulièrement intéressant pour les applications stationnaires. L'un des grands avantages de ce type de batterie est de pouvoir facilement augmenter sa capacité et sa puissance, même une fois installée. En effet, pour augmenter sa capacité, il suffit d'augmenter la taille des réservoirs à électrolyte.

La durée de vie de l'électrolyte est aussi un aspect intéressant. Les deux électrolytes mis en contact dans les cellules sont tous les deux à base de vanadium. Il n'y a pas de contamination croisée, phénomène qui diminue les rendements de la pile avec le temps, et la batterie peut être complètement déchargée sans impact sur sa durée de vie.

D'autre part, des SC ont été sélectionnés pour faire face aux variations rapides de puissance. Ce système de stockage dispose d'un taux d'autodécharge très réduit, est facile à installer et ne pose pas de problèmes de sécurité ou de maintenance par rapport à d'autres types de stockage qui peuvent être utilisés pour les mêmes objectifs.

Dans un premier temps, ces deux systèmes de stockage ont été modélisés en prenant en compte les contraintes et la dynamique du microréseau étudié. Ces modèles de simulation ont été ensuite validés expérimentalement.

Une fois les modèles des systèmes de stockage validés, une revue de la littérature a été réalisée afin d'identifier les topologies les plus adaptées pour



## Résumé étendu

contrôler le flux de puissance d'un Système de Stockage Hybride et son intégration dans l'environnement microréseau. L'objectif est de diviser la puissance entre le SC et le VRB en fonction de sa fréquence. Les variations à haute fréquence doivent être absorbées par le SC et les variations à basse fréquence par le VRB.

Trois topologies ont été identifiées et comparées en simulation en conditions similaires pour souligner les avantages et désavantages de chacun dans un contexte SSH et microréseau. Les topologies analysées sont illustrées dans la Figure 1.

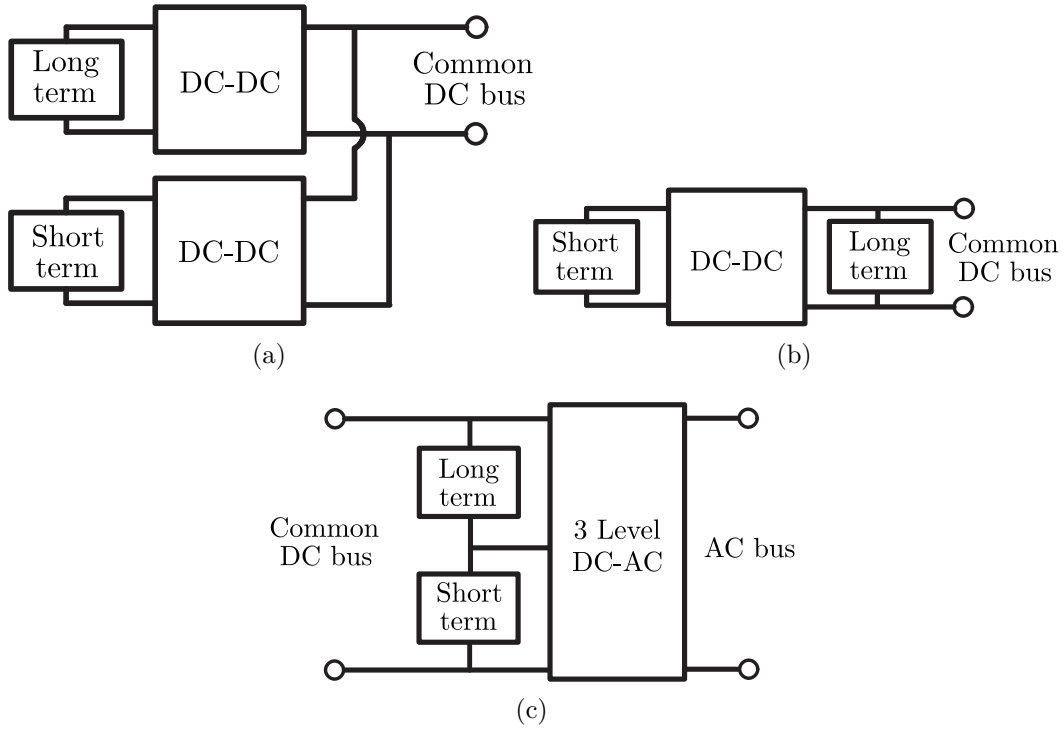


Figure 1: Configurations des topologies (a) parallèle, (b) flottante et (c) convertisseur à trois-niveaux (*Three-Level Neutral Point Clamped Converter, 3LNPC*).

Pour comparer les topologies sélectionnées, deux scénarios ont été analysés en utilisant le logiciel *Matlab/Simulink* et la boîte à outils *SimPowerSystems*. Dans le premier scénario le microréseau fonctionne connecté au réseau principal et un courant variable généré par les sources renouvelables est injecté dans le bus à courant continu (CC). Le deuxième scénario traite la déconnexion du

réseau principal. Les résultats ont montré que la topologie 3LNPC permet d'avoir une dynamique similaire aux autres topologies mais avec des pertes de puissance et distorsions harmoniques réduites. Par conséquent, la topologie 3LNPC a été sélectionnée pour contrôler le flux de puissance entre le SSH et le microréseau.

Une fois que le convertisseur de puissance a été choisi, son fonctionnement a été analysé afin de déterminer le système de commande pour la régulation du flux de puissance dans le SSH. Une comparaison entre les différentes stratégies de modulation a été également réalisée d'un point de vue de la division de puissance dans le SSH. Suite à cette analyse, la stratégie de modulation Third Harmonic Injection Pulse Width a été choisie pour réguler la puissance échangée au niveau du SSH en injectant la séquence homopolaire dans les signaux de modulation.

En utilisant cette technique de modulation, le fonctionnement du convertisseur 3LNPC a été analysé afin de déterminer ses limites concernant le maximum et le minimum de courant qui peuvent être extraits du SSH. Les variables qui affectent ces limites de courant sont l'index de modulation, le déphasage entre les courants alternatifs, les rapports cycliques et la relation entre les tensions des deux systèmes de stockage. En exploitant la valeur maximale et minimale de la séquence homopolaire, il est possible de déterminer le courant maximal et minimal qui peut être extrait du SSH. Les limites de fonctionnement du convertisseur 3LNPC sont ensuite exploitées pour concevoir la stratégie de commande permettant de réguler le courant dans la batterie redox et indirectement le courant dans le module de SC.

Le fonctionnement de la topologie choisie et de l'algorithme de commande associé ont été validés expérimentalement dans le laboratoire d'Estia-Recherche. Un module commercial de SC *Maxwell BM0D0083*, une batterie redox au vanadium faite sur mesure et un prototype de convertisseur 3LNPC ont été intégrés dans le microréseau existant à l'*ESTIA* pour évaluer expérimentalement les solutions proposées dans cette thèse. L'algorithme de commande est implémenté dans un système Hardware-in-the-loop d'*Opal-RT*.

L'ensemble du système utilisé pour la validation expérimentale est illustré dans la Figure 2.

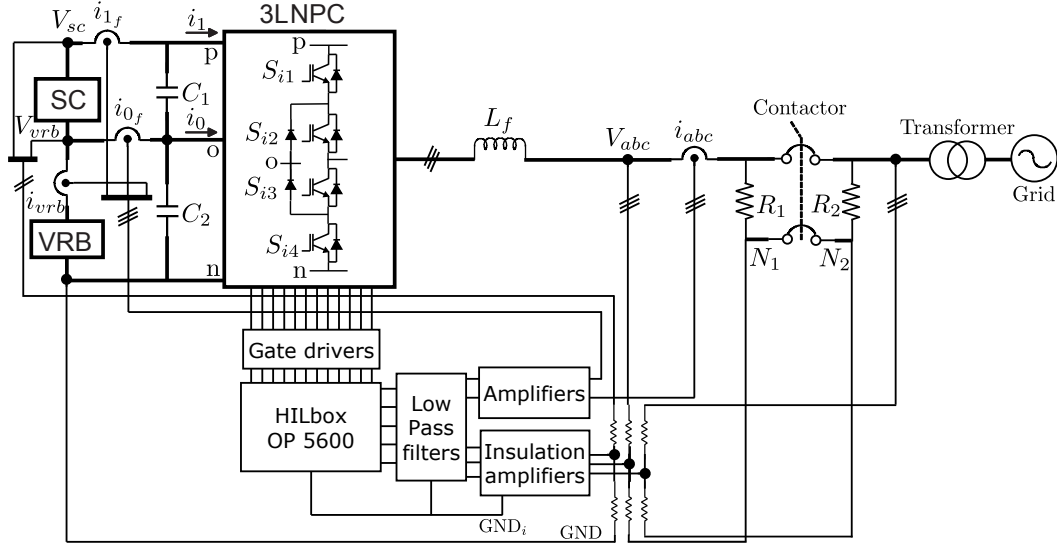


Figure 2: Diagramme bloc du système expérimental.

Les deux scénarios définis pour analyser le fonctionnement du système étudié en simulation ont été reproduits expérimentalement.

Tout d'abord, le SSH et le convertisseur 3LNPC ont été analysés pour un fonctionnement isolé du réseau principal. Dans un premier temps, une augmentation soudaine de la puissance a été provoquée sur le bus à courant alternatif (CA). Dans un deuxième temps, une puissance variable a été injectée dans le bus à CC. Les résultats de ce deuxième test sont montrés dans la Figure 3.

La Figure 3a montre la puissance injectée dans le bus à CC et la Figure 3b les puissances dans chaque système de stockage. La séparation du flux de puissance entre les deux systèmes de stockage permet de valider l'algorithme de commande proposé. Les variations rapides de puissance sont absorbées par le SC et les variations lentes par la batterie redox.

Un deuxième scénario a permis d'étudier la déconnexion du microréseau du réseau principal. Quand le microréseau est déconnecté du réseau principal, le SSH doit fournir un pic de puissance pour répondre aux besoins des charges et maintenir la tension au niveau de référence.

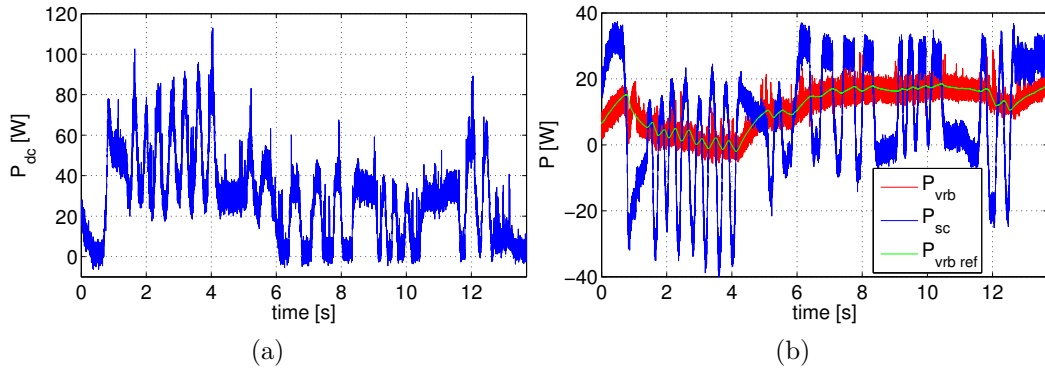


Figure 3: Évolution de la puissance: (a) dans le bus à CC,  $P_{dc}$  et (b) dans la batterie redox et le SC.

Les résultats obtenus ont été comparés avec les résultats de simulation et sont illustrés dans la Figure 4.

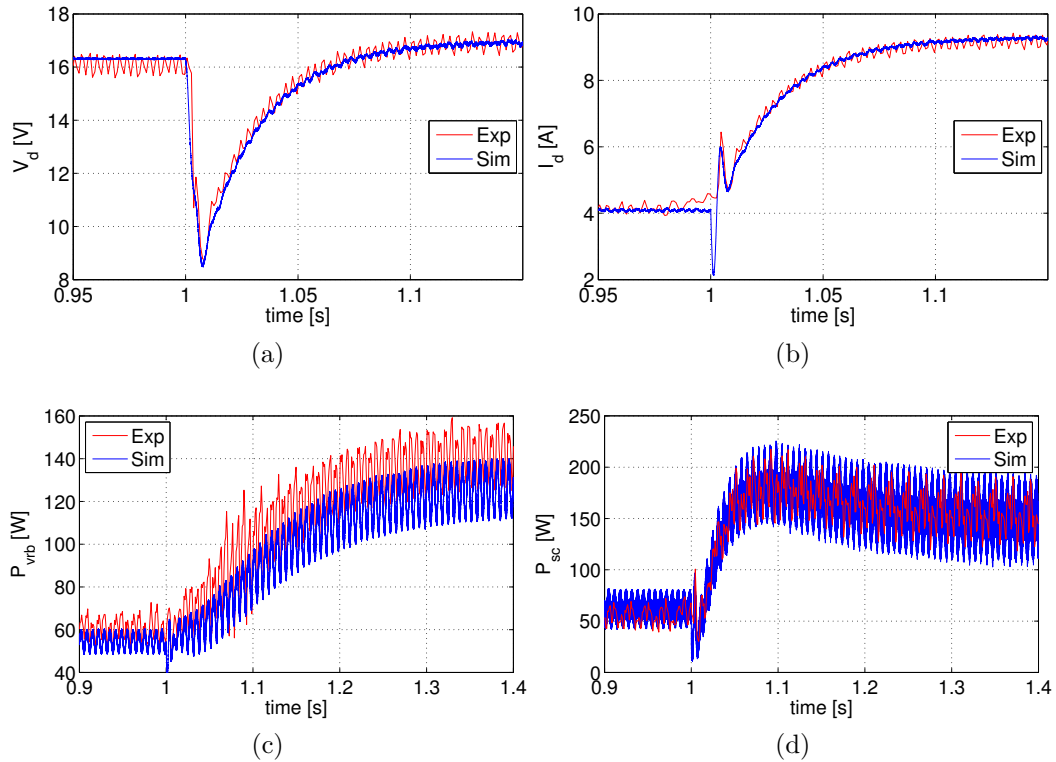


Figure 4: Évolution de : (a) la composante  $V_d$  de la tension alternative, (b) la composante  $I_d$  du courant alternatif, (c) la puissance dans la batterie redox  $P_{vrb}$  et (d) la puissance  $P_{sc}$  pendant la déconnexion du microréseau.

Comme la Figure 4a et la Figure 4b le montrent, le système est capable de maintenir la tension au niveau de la valeur de référence et d'ajuster le courant en fonction de la variation de la charge après la déconnexion. En même temps, la puissance est divisée entre le VRB et le SC (Figure 4c et Figure 4d), de sorte que le pic de puissance soit complètement fourni par le SC. Ce test a aussi démontré que la transition d'un fonctionnement en îlotage à un fonctionnement connecté au réseau, d'un point de vue commande, est faite sans transitoires brusques.

Les résultats expérimentaux ont validé les résultats de simulation et ont démontré que les solutions proposées dans cette thèse satisfont les objectifs fixés. La bonne corrélation entre les résultats de simulation et les résultats expérimentaux valide aussi les modèles de simulation et permet d'envisager l'analyse de différents autres scénarios.



# Table of Contents

<b>Acknowledgments</b>	<b>i</b>
<b>Abstract</b>	<b>iii</b>
<b>Résumé</b>	<b>v</b>
<b>Résumé étendu</b>	<b>vii</b>
<b>Table of Contents</b>	<b>xv</b>
<b>List of Figures</b>	<b>xix</b>
<b>List of Tables</b>	<b>xxv</b>
<b>Nomenclature</b>	<b>xxvii</b>
<b>1 Introduction</b>	<b>1</b>
1.1 Distributed Generation . . . . .	2
1.1.1 Introduction . . . . .	2
1.1.2 Definition of DG . . . . .	6
1.1.3 DG technologies . . . . .	6
1.1.4 Benefits and drawbacks of using DG . . . . .	8
1.1.5 Microgrid . . . . .	11
1.2 Objectives of the thesis . . . . .	14
1.3 Structure of the document . . . . .	15
Chapter References . . . . .	16
<b>2 Energy Storage Systems</b>	<b>21</b>
2.1 Benefits of storing energy . . . . .	22
2.1.1 Generation and transmission systems . . . . .	22
2.1.2 Operation of power systems . . . . .	22

## Table of Contents

---

2.1.3	RES integration . . . . .	25
2.2	Types of energy storage technologies . . . . .	25
2.2.1	Electrochemical storage systems . . . . .	27
2.2.2	Electrical storage systems . . . . .	35
2.2.3	Mechanical storage systems . . . . .	37
2.3	Comparison of storage technologies . . . . .	38
2.4	Modelling of the HESS . . . . .	44
2.4.1	Modelling of SC . . . . .	45
2.4.2	Modelling of VRB . . . . .	52
2.4.3	Chapter Conclusions . . . . .	62
	Chapter References . . . . .	62
<b>3</b>	<b>Power electronics topologies and the associated control for interfacing the HESS with a microgrid</b>	<b>71</b>
3.1	Literature survey . . . . .	72
3.2	Comparison among topologies . . . . .	80
3.2.1	Parallel DC-DC converters topology . . . . .	84
3.2.2	Floating topology . . . . .	96
3.2.3	3LNPC topology . . . . .	97
3.3	Simulation Results . . . . .	100
3.3.1	First case study . . . . .	103
3.3.2	Second case study . . . . .	107
3.4	Results discussion . . . . .	113
3.5	Chapter conclusions . . . . .	114
	Chapter References . . . . .	115
<b>4</b>	<b>3LNPC converter for HESS control</b>	<b>123</b>
4.1	Main characteristics of a 3LNPC converter . . . . .	124
4.2	Switching level analysis . . . . .	126
4.2.1	Neutral point voltage unbalance effect . . . . .	132
4.2.2	Switching model . . . . .	136
4.3	Modulation strategies . . . . .	137



## Table of Contents

---

4.3.1	Space Vector Modulation . . . . .	138
4.3.2	Carrier-based PWM . . . . .	138
4.3.3	Relationship between SVM and carrier-based PWM . .	141
4.4	Operational limits of 3LNPC . . . . .	152
4.4.1	Balanced DC side voltages . . . . .	154
4.4.2	Unbalanced DC side voltages . . . . .	159
4.5	DC bus voltage selection . . . . .	165
4.6	Chapter conclusions . . . . .	166
	Chapter References . . . . .	167
<b>5</b>	<b>3LNPC controller design and experimental results</b>	<b>169</b>
5.1	Control of a 3LNPC converter . . . . .	169
5.1.1	AC variables control system design . . . . .	171
5.1.2	VRB current controller design . . . . .	174
5.2	Experimental results . . . . .	179
5.2.1	Description of the platform . . . . .	179
5.2.2	3LNPC converter . . . . .	184
5.2.3	Isolated case study . . . . .	186
5.2.4	Grid-connected case study . . . . .	193
5.3	Chapter conclusions . . . . .	197
	Chapter References . . . . .	198
<b>6</b>	<b>Conclusions and Future Lines</b>	<b>199</b>
6.1	Conclusions . . . . .	199
6.2	Future lines . . . . .	201
6.3	Publications . . . . .	202
	<b>Appendix A Power losses</b>	<b>205</b>
A.1	Conduction losses . . . . .	205
A.2	Switching losses . . . . .	206
A.3	Power losses calculation . . . . .	207

<b>Appendix B Clarke and Park transforms</b>	<b>209</b>
B.1 Clarke transform . . . . .	209
B.2 Park transform . . . . .	210
B.3 Application to the converter case . . . . .	211
B.3.1 Isolated operation mode . . . . .	211
B.3.2 Grid-connected operation mode . . . . .	212
<b>Appendix C Digitalisation of continuous algorithms</b>	<b>215</b>
C.1 PI controllers and low-pass filters . . . . .	215
C.2 Synchronisation algorithm . . . . .	217
References . . . . .	219

# List of Figures

1.1	Centralised electric grid topology (source: SDM). . . . .	3
1.2	Topology of a decentralised electric grid (source: CRE). . . . .	5
1.3	Basic MG architecture. . . . .	12
2.1	Structure of a Li-ion battery (source: <i>digital-camera-battery.net</i> )	28
2.2	Structure of a Lead-acid battery (source: <i>Power Sonic</i> ). . . . .	29
2.3	Structure of a NiCd cell (source: <i>Encyclopædia Britannica</i> ). . . . .	30
2.4	Structure of a NaS cell (source: <i>California Energy Commission</i> ). . . . .	31
2.5	Structure of a Vanadium Redox Battery [13]. . . . .	32
2.6	Series connection of VRB cells [24]. . . . .	33
2.7	Simplified operation of a PSB [25] . . . . .	34
2.8	Simplified operation of a ZnBr flow battery (source: <i>Energy Storage Association</i> ) . . . . .	35
2.9	Schematic representation of a SC cell (source: <i>ultracapacitors.org</i> ). . . . .	36
2.10	Components of a superconducting magnetic energy storage device [26]. . . . .	37
2.11	Schematic representation of a flywheel [7]. . . . .	38
2.12	ESS classification according to their power rating and discharge time (source: <i>Energy Storage Association</i> ). . . . .	42
2.13	Basic structure of a SC cell [51]. . . . .	45
2.14	Dynamic model of a SC based on constant series connected resistor and capacitor. . . . .	48
2.15	Voltage dependent dynamic model. . . . .	48
2.16	SC unit used in the experimental tests. . . . .	50
2.17	Details about the voltage variation measurement used to calculate the ESR. . . . .	51
2.18	Relation between capacitance and voltage of the used SC unit. . . . .	51

2.19 Comparison between experimental and simulation results of constant current (a) charging at 61A, (b) discharging at 61A, (c) charging at 122A (d) discharging at 122A. . . . .	52
2.20 VRB reactions during charge and discharge [13]. . . . .	53
2.21 Relation between SOC and OCV of a VRB cell. . . . .	54
2.22 VRB cell charge-discharge cycle at constant current divided in three stages [70]. . . . .	56
2.23 Dynamic model of the VRB presented in [71]. . . . .	57
2.24 VRB unit used in the experimental tests. . . . .	57
2.25 (a)Connection and (b)disconnection of the R to/from the VRB.	59
2.26 Comparison between experimental and simulation behaviour of the self-discharge. . . . .	59
2.27 Simulation model of the VRB. . . . .	60
2.28 Comparison among experimental and simulated charge and discharge cycles of the VRB. . . . .	61
3.1 Schematic representation of the passive topology. . . . .	75
3.2 Schematic representation of the series topology. . . . .	76
3.3 Schematic representation of the parallel topology. . . . .	76
3.4 Schematic representation of the floating topology. . . . .	76
3.5 Schematic representation of the 3LNPC topology. . . . .	79
3.6 Simulation system used to compare the selected power electron- ics topologies. . . . .	81
3.7 Parallel DC-DC converters topology. . . . .	85
3.8 Two-loop control of the DC-DC of the SC storage system. . .	85
3.9 Control structure of the DC-DC of the VRB. . . . .	88
3.10 Structure of the two-level inverter in the isolated case. . . . .	89
3.11 Structure of the two-level inverter in the grid-connected case. .	91
3.12 Two-level inverter control structure . . . . .	93
3.13 Structure of the FLL. . . . .	95
3.14 Structure of the DSOGI-QSG. . . . .	95
3.15 General schematic of the DSOGI-FLL algorithm. . . . .	95

## List of Figures

---

3.16	Floating topology. . . . .	97
3.17	Control algorithm of the floating topology. . . . .	97
3.18	3LNPC converter topology. . . . .	98
3.19	Control algorithm of the 3LNPC converter. . . . .	101
3.20	Power injected by RES and the power of the HESS in the parallel topology. . . . .	104
3.21	DC bus voltage in the parallel topology. . . . .	104
3.22	Power injected by RES and the power of the HESS in the floating topology. . . . .	105
3.23	DC bus voltage in the floating topology. . . . .	105
3.24	Power injected by RES and the power of the HESS in the 3LNPC topology. . . . .	106
3.25	DC bus voltage in the 3LNPC topology. . . . .	106
3.26	Power of the HESS in the parallel topology. . . . .	108
3.27	DC bus voltage in the parallel topology. . . . .	108
3.28	Load voltage in the parallel topology. . . . .	109
3.29	Power of the inverter in the parallel topology. . . . .	109
3.30	Power of the HESS in the floating topology. . . . .	110
3.31	Load voltage in the floating topology. . . . .	110
3.32	DC bus voltage in the floating topology. . . . .	110
3.33	Power of the inverter in the floating topology. . . . .	111
3.34	Power of the HESS in the 3LNPC topology. . . . .	111
3.35	Load voltage in the 3LNPC topology. . . . .	112
3.36	DC bus voltage in the 3LNPC topology. . . . .	112
3.37	Power of the inverter in the 3LNPC topology . . . . .	113
4.1	Structure of a 3LNPC converter. . . . .	124
4.2	Space vector diagram of a 3LNPC in the balanced neutral point voltage case. . . . .	128
4.3	Configurations of the different vector types. . . . .	131
4.4	Effect of neutral point unbalances on the space vector diagram. . . . .	133
4.5	(a)Variations in the DC voltage sources, (b) $V_{abc}$ voltages. . . . .	134

4.6	Comparison between the modification of the carrier signals and of the modulating signal. . . . .	135
4.7	$a$ phase duty cycles. . . . .	143
4.8	Differences among the three types of duty cycles. . . . .	143
4.9	(a) Load current evolution and (b) section and triangle evolution. . . . .	144
4.10	Evolution of (a) $i_0$ and (b) $i_{c1}$ during the first case study. . . . .	144
4.11	Use of vectors in section 1. . . . .	145
4.12	Use of vectors in section 2. . . . .	147
4.13	$a$ phase duty cycles when only upper vectors are used. . . . .	148
4.14	Evolution of (a) $i_0$ and (b) $i_{c1}$ during the second case study. . . . .	149
4.15	Use of vectors in section 1. . . . .	150
4.16	Use of vectors in section 2. . . . .	151
4.17	Relation between capacitor currents, modulation index and $v-i$ phase difference. . . . .	155
4.18	Relation between capacitor currents, modulation index and the zero-sequence. . . . .	157
4.19	Experimental test of the effect of a zero-sequence injection. . . . .	158
4.20	Maximum current division in the balanced DC voltages case when a maximum offset is injected. . . . .	160
4.21	DC currents when a maximum zero-sequence is injected. . . . .	161
4.22	DC currents when a minimum zero-sequence is injected. . . . .	162
4.23	Maximum current division in the unbalanced DC voltages case. . . . .	162
4.24	Division between $i_{c1}$ results when the phase shift is $\frac{\pi}{4}$ and $0 \text{ rad}$ and a maximum offset is injected. . . . .	164
4.25	Constant value used to represent the effect of the phase shift. . . . .	164
5.1	Control structure of the isolated case. . . . .	172
5.2	Control structure of the grid-connected case. . . . .	173
5.3	Control structure of the current of the VRB. . . . .	175
5.4	Schematical representation of the operation of the state manager. . . . .	176
5.5	Complete control algorithm of the 3LNPC converter. . . . .	180
5.6	Scheme of the experimental microgrid. . . . .	181

## List of Figures

---

5.7	Front panel view of the OP5600 HILbox. . . . .	184
5.8	Picture of the 3LNPC unit used in the experimental tests. . .	185
5.9	Photograph of the experimental platform. . . . .	186
5.10	Block diagram of the experimental tests in the isolated case study.	187
5.11	Evolution of (a) $V_d$ , (b) $I_d$ , (c) $P$ and (d) $Q$ variables during the sudden power increase test. . . . .	189
5.12	Evolution of (a) $P_{vrb}$ , (b) $P_{sc}$ and (c) $P_{dc}$ variables during the sudden power increase test. . . . .	190
5.13	Evolution of (a) offset, (b) $m$ and (c) phase difference variables during the sudden power increase test. . . . .	191
5.14	Evolution of (a) $P_{dc}$ and (b) $P_{vrb_{ref}}$ , $P_{vrb}$ , $P_{sc}$ variables during the variable DC power injection test. . . . .	192
5.15	Evolution of the offset during the variable DC power injection test. . . . .	192
5.16	Evolution of the AC side variables during the variable DC power injection test. . . . .	193
5.17	Block diagram of the experimental tests in the grid-connected case study. . . . .	194
5.18	Evolution of (a) $V_d$ , (b) $I_d$ , (c) $P$ and (d) $Q$ variables during the disconnection from the main grid. . . . .	195
5.19	Evolution of (a) $P_{vrb}$ , (b) $P_{sc}$ and (c) $P_{dc}$ variables during the disconnection from the main grid. . . . .	196
5.20	Evolution of (a) offset, (b) $m$ and (c) phase difference variables during the disconnection from the main grid. . . . .	197
A.1	Block diagram of the switching losses calculation. . . . .	207
B.1	$abc$ , $\alpha\beta 0$ and $dq0$ reference systems. . . . .	210
C.1	Structure of the DSOGI-QSG. . . . .	217
C.2	Discrete implementation of SOGI-QSG algorithm. . . . .	218





# List of Tables

2.1	Summarise of the characteristics of the analysed ESS technologies.	39
2.2	Summarise of the characteristics of the analysed ESS technologies.	40
2.3	Parameters of the SC unit. . . . .	50
2.4	Constants of the Nernst's equation. . . . .	54
2.5	Parameters of the VRB unit used in the experimental tests. .	58
3.1	Simulation parameters . . . . .	102
3.2	Power losses of the first case study . . . . .	103
3.3	Power losses of the second case study . . . . .	107
4.1	The 27 different switching vectors that can be generated by a 3LNPC converter. . . . .	127
4.2	Phase-neutral voltages and their $\alpha\beta$ transforms. . . . .	129
4.3	Relation between AC and DC currents in each switching vector.	132
4.4	Effect of switching vectors in the DC side currents. . . . .	146
4.5	Relation between modulation index and the DC bus voltage. .	166
5.1	Selection of the current reference of the VRB. . . . .	178
5.2	Parameters of the 3LNPC converter. . . . .	185
C.1	Parameters of the controllers used in the experimental tests. .	216
C.2	Parameters of the DSOGI-FLL algorithm. . . . .	218



# Nomenclature

3LNPC Three Level Neutral Point Clamped

AC Alternating Current

CHP Combined Heat and Power

DC Direct Current

DG Distributed Generation

DOD Depth Of Discharge

DSOGI-FLL Dual Second Order Generalized Integrator-Frequency-Locked  
Loop

EIS Electrochemical Impedance Spectroscopy

ESR Equivalent Series Resistance

ESS Energy Storage System

FC Fuel Cells

HESS Hybrid Energy Storage System

ICE Internal Combustion Engines

IEA International Energy Agency

IGBT Insulated Gate Bipolar Transistor

Li-ion Lithium-ion

LV Low Voltage

MG MicroGrid

MT Micro-Turbines

MV Medium Voltage

NaS Sodium Sulphur

NiCd Nickel Cadmium

OCV Open Circuit Voltage

PCC Point of Common Coupling

PI Proportional-Integral

PLL Phase-Locked Loop

PQR Power Quality and Reliability

PSB PolySulphide-Bromide

PV Photo-Voltaic

RES Renewable Energy Sources

SC SuperCapacitor

SMES Superconducting Magnetic Energy Storage

SOC State-Of-Charge

SPWM Sinusoidal Pulse Width Modulation

SVM Space Vector Modulation

T&D Transmission and Distribution

THD Total Harmonic Distortion

THIPWM Third Harmonic Injection Pulse Width Modulation

UPS Uninterruptible Power Supply

VRB Vanadium Redox Battery

## Nomenclature

---

WT Wind Turbines

ZnBr Zinc Bromine



# CHAPTER 1

## Introduction

---

### Contents

---

<b>1.1 Distributed Generation . . . . .</b>	<b>2</b>
1.1.1 Introduction . . . . .	2
1.1.2 Definition of DG . . . . .	6
1.1.3 DG technologies . . . . .	6
1.1.4 Benefits and drawbacks of using DG . . . . .	8
1.1.5 Microgrid . . . . .	11
<b>1.2 Objectives of the thesis . . . . .</b>	<b>14</b>
<b>1.3 Structure of the document . . . . .</b>	<b>15</b>
<b>Chapter References . . . . .</b>	<b>16</b>

---

The present thesis work has been prepared in the laboratory *ESTIA-Recherche* of the *Ecole Supérieure des Technologies Industrielles Avancées (ESTIA)* engineering school, namely within *EneR-GEA* research group. The main research interests of this group are related to the power electronics and automation applied to the Renewable Energy Sources (RES) and MicroGrids (MG).

The research work has been carried out in collaboration with two other institutions. The *IMS* laboratory from *Université Bordeaux 1* and *Euskal Herriko Unibertsitatea-Universidad del País Vasco (EHU-UPV)*, and it has been supported by the *Conseil Régional d'Aquitaine*.

The objective of this first chapter is to present the problematic of the thesis as well as to explain which are the main objectives of this research work and to present the structure of the document. The chapter begins with an introduction to the Distributed Generation (DG) concept and then continues

analysing the microgrid as a solution to obtain a high penetration of DG, especially of RES, without compromising the reliability, stability and power quality of the grid.

In the end of the chapter the objectives of the thesis are explained and the structure of the document is detailed.

## 1.1 Distributed Generation

### 1.1.1 Introduction

The electric grid had been one of the most important advances of the Twentieth century, an invention that has completely changed the social life and customs.

The first practical applications of an electric grid (in the decade 1880-1890) were based on Direct Current (DC). The supply voltage and the distance between the generator and the consumer were limited by the high losses that appear in a DC grid due to the impossibility of rising the voltage to values that would allow a transmission with low losses. Balancing demand and supply was partially done using local storage, i.e. batteries, which could be directly connected to the DC grid. Later, the emergence of Alternating Current (AC) electric grids permitted to transport electricity over longer distances, and economies of scale in electricity generation lead to an increase in the power output of the generation units. Massive electricity systems were constructed, consisting of huge transmission and distribution grids and large generation plants. The demand-supply balance was done through the big generation plants, which also offered security of supply [1].

This traditional centralised approach of the electric grid spread all around the world during the last century [2]. The traditional electric grid is formed by three main elements: big power plants which generate electricity using different energy sources (coal, natural gas, biomass, nuclear, wind, solar, etc.), transmission lines that are used to transport electricity from power plants to demand sites and transformers that increase/decrease the voltage in order that distribution networks carry power for final delivery [3] (Figure 1.1). Demands,



## 1.1. Distributed Generation

---

as well as distribution networks, are passive. Consequently, they only consume electricity and do not inject power nor take part in grid support applications. Thus, the power flow is unidirectional, from the centralised big generation plants to a large number of dispersed end-users [4, 5].

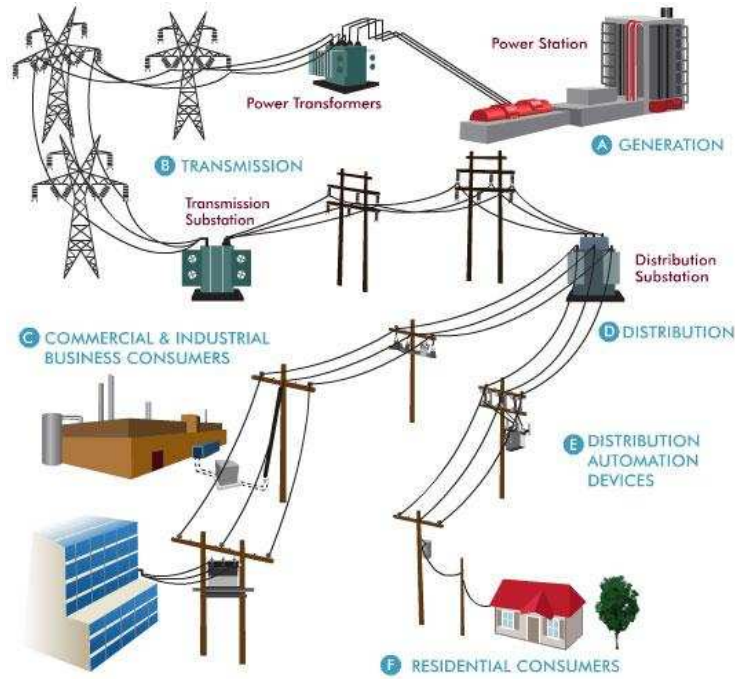


Figure 1.1: Centralised electric grid topology (source: SDM).

However, the traditional grid has become old and unreliable in unpredicted events [6]. One of the existing problems is the saturation of distribution and transmission lines in some points of the grid. In other cases the lines must be changed as they have been damaged by time. Furthermore, the energetic crisis created by the limited existence of fossil fuels is creating the necessity of increasing the use of generation systems that are not based in this energy source. Moreover, many countries have taken policies at different levels in order to reduce the emission of greenhouse gases. These policies include a minimal use of RES [7]. Furthermore, the past few years and especially Post-Fukushima, for the first time in history many countries with a nuclear past considered the level of future demand for electricity being unclear. The Fukushima crisis only exacerbates the major changes that the energy sector is

facing due to a combination of environmental, resource, and demand factors. Under such circumstances, the advantages of renewable and distributed energy generation offer an attractive alternative for power supply. This, in parallel to the increasing social awareness about the climate change, has increased the importance of the RES as an alternative to the fossil fuel based energy sources.

On the other hand, the power market liberalisation has permitted customers not only to consume electricity, but also to generate and sell it. As a consequence, the number of small generation systems that are connected at the distribution line level is continuously increasing [8]. This generation systems are called DG due to their physical distributed nature. The increasing penetration of DG sources is changing the perspective of the grid from centralised to decentralised [7] (Figure 1.2). In this kind of grid the power is generated by many small generation systems in physical locations that are far away each one from the other.

The International Energy Agency (IEA) listed 5 reasons in 2002 that contribute to the increasing penetration of DG [9]:

1. Developments in DG technologies
2. Constraints on the construction of new transmission lines
3. Increased customer demand for highly reliable electricity

One of the advantages of DG systems is that they can be located near the loads. According to [10], this could result in cost savings in transmission and distribution losses.

Reliability of an electric grid usually refers to voltage drops to near zero, also called outages. Having a reliable electricity supply is a highly important issue especially in industry. The liberalisation of electricity market could decrease the reliability as a high reliability level implies high investment and maintenance costs for the network and generation infrastructure. Some DG technologies can help to avoid those power interruptions, for example fuel cells [1].

## 1.1. Distributed Generation

### 4. The electricity market liberalisation

In a liberalised electricity market customers will look for the electricity service best suited for them. A DG system offers a high flexibility to a electricity supplier because of their small sizes and the short construction lead times compared to most types of larger central power plants [4].

### 5. Concerns about climate change

Many countries have taken policies at different levels in order to reduce the emission of greenhouse gases. These policies include an obligation to generate a minimal part of the energy using RES [7].

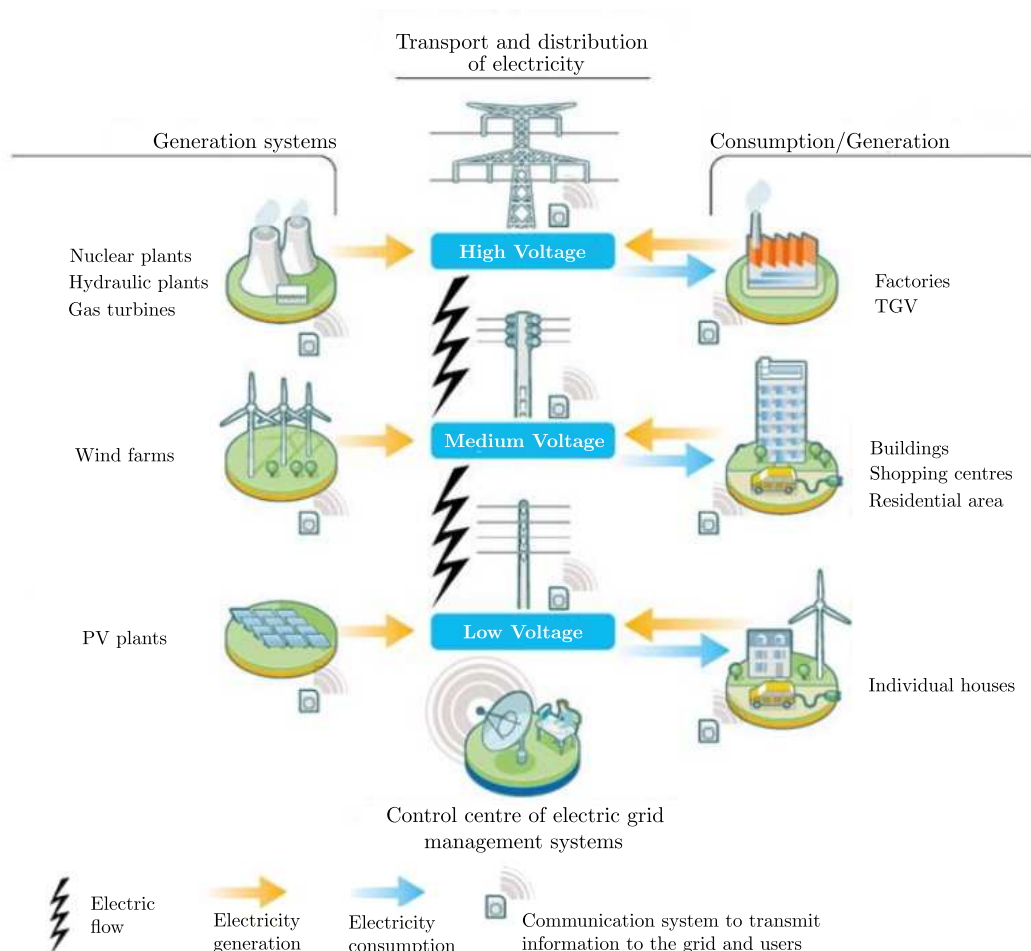


Figure 1.2: Topology of a decentralised electric grid (source: CRE).

### **1.1.2 Definition of DG**

Nowadays DG cannot be considered as a new approach, but even if it is being some years since many researchers are working in this field, there is not yet any consensus about the definition of what a DG is. Actually, many authors, organisation and even countries fix their own definition for this concept [1, 5, 10–17]. Different papers define several maximum power generation capacities for a DG. Moreover, other authors assume that a DG is connected to the distribution grid or at the customer side of the meter.

However, this latter feature includes in some cases generation systems connected to the transmission lines, which is not accepted as DG by other authors.

Nevertheless, there are some common features in the different definitions, which can be used to determine which generation system is accepted to be DG by all definitions. All papers assume that a small scale generation unit that provides at least active power, which is connected to the distribution grid and closely to the load is considered as DG.

In the following subsection different types of DG are summarised.

### **1.1.3 DG technologies**

#### **1.1.3.1 Internal Combustion Engines (ICE)**

ICE are the most common and mature DG technology [9]. An internal combustion engine converts the energy contained in a fuel, typically natural gas or diesel, into mechanical power to move a generator, which converts the mechanical power into electrical. The typical power rating of an ICE varies from some *kW* to several *MW* [14]. Their main advantages are their low capital and start-up costs. On the other hand, maintenance cost, high emissions and noise are their main drawbacks. The efficiency can be up to 43% [9].

## 1.1. Distributed Generation

---

### 1.1.3.2 Gas turbines

A gas turbine is particularly useful when higher temperature steam is required than that which can be produced by an ICE. The maintenance cost is slightly lower than for reciprocating engines with an electrical conversion efficiency of up to 40% [9, 14]. The size of a gas turbine varies between 30 kW and 300 MW [18].

### 1.1.3.3 Micro-Turbines (MT)

A micro-turbine is a low capacity combustion turbine that can work using natural gas, propane and fuel oil [12]. Typical size of an individual unit of MT ranges from 30-200 kW but can be combined readily into systems of multiple units [9]. Unlike the traditional combustion turbines, MT run at less temperature (which assures lower  $NO_x$  emissions) and pressure and faster speed (in the range 50000-120000 rpm). Their advantages comparing to ICE are the mentioned low air pollution rate and reduced noise levels and vibrations. On the other hand, the capital cost, on a per installed kW basis, can be several times higher than of an ICE and the lifetime is several times shorter [2]. Their efficiency is typically in the range 25-30% [9].

### 1.1.3.4 Fuel Cells (FC)

FC are electrochemical devices that convert chemical energy of a fuel directly into usable energy (heat and electricity). FC technology is based on an electrochemical process in which hydrogen and oxygen (oxidant) are combined to produce electricity without combustion. The operating stages and products of this electrochemical process are direct current electric power, water, heat, and some low emitted gases (like  $NO_x$  and  $CO_2$ ) with respect to traditional generators and hence is considered an environmentally safe electric power generation [12]. As the chemical energy of the fuel is directly converted into electricity and heat without any intermediate step, a fuel cell offers higher efficiencies (around 40-60% [19]) than any thermomechanical system [14].

### 1.1.3.5 Wind Turbines (WT)

WT generate electrical power using aerodynamic power. A WT consists of three main elements: a rotor system (which includes the blades), the nacelle (including main shaft, gearbox and generator among other elements) and the tower and foundation [20]. Wind moves the blades of the WT which turn the generator attached to the internal shaft, generating electric power. As a clean energy source, it has advantages like the reduction of fossil fuel consumption and the consequent reduction in green-house gas emissions. On the other hand, as the wind is stochastic, the power generated by WT can create several problems in the grid if the generated power is not injected in a controlled way.

### 1.1.3.6 Photo-Voltaic (PV) panels

PV generation is based on the direct conversion of the sunlight into electricity [11]. A PV cell absorbs solar energy from the sunlight, where the light photons force cell electrons to flow, and converts it to DC electricity [12].

Use of PV panels is especially interesting to avoid the construction of new distribution lines in off-grid places or for remote telecommunications systems [9]. As WT, their output power is variable and stochastic and must be smoothed using storage systems or other solutions.

### 1.1.4 Benefits and drawbacks of using DG<sup>1</sup>

The traditional electric grid is configured to work in unidirectional power flow, where the power flows from high voltage transmission grids to lower voltage distribution grids. The distribution grid is passive and it is not designed to respond as an active network, it is supposed to be stable as long as the transmission grid is stable [10, 11]. However, as the distribution grid is not designed to support a high penetration of DG, the injected power can create several issues that must be taken into account in order to maintain a power supply with high power quality, reliability and stability.

---

<sup>1</sup>This section takes into account only the technical advantages and issues, economical or regulatory aspects are neglected.

### 1.1. Distributed Generation

---

The power flow inversion, i.e. a power flow from the low voltage side to the high voltage side, that a DG might generate is one of the drawbacks of this type of generation systems. This power flow inversion requires variations in the security systems of both voltage sides, higher and lower [21].

Another effect of connecting a DG to the distribution grid is the voltage rise in the network. Depending on the distribution grid characteristics this might be beneficial or an inconvenience: if the grid where the DG is installed suffers from low voltage problems, especially in rural grids, the DG can improve the voltage profile if it is controlled to satisfy that objective. On the other hand, if the distribution network works under normal conditions, the introduction of, for example, a RES based DG can introduce undesired voltage increases if the input power is too high and the system is weakly loaded [5, 21].

Taking into account that the RES are not fully controllable power sources, a high penetration level of them can create reliability and stability problems in the network. The stochastic and variable nature of the resources used with the RES are their biggest drawbacks. Indeed, the energy generated by RES is difficult to predict and variable, which could create stability and reliability problems in the traditional electric grid if the penetration of RES is big enough comparing the introduced power to the short circuit power of the grid [22]. Consequently, generally speaking, it cannot be said that the integration of DG improves the reliability and stability of the grid. A DG will improve reliability and stability only if it is correctly coordinated with the rest of the network [5].

Another issue created by the introduction of DG is their effect on the power quality of the grid. This effect cannot be considered positive or negative for all different cases. Usually the addition of a controlled generation system improves power quality as it can be used to meet the different requirements.

However, in the case of RES the effect is not the same. Two characteristics of power quality are typically considered to be important, transient voltage variations and harmonic distortion of the network voltage [11, 23]. Fast active or reactive power fluctuations of a DG can create voltage variations (typically voltage dips), which are especially noticeable in case of RES. On the other

hand, some types of DG are connected to the distribution grid through power conversion systems due to different reasons. Those power converters may introduce harmonics in the distribution grid decreasing its power quality [2].

The traditional grid is based on big synchronous generators that provide the possibility of facing fast power variations using the inertia-effect of the rotating mass. Nevertheless, in the case of DG most of them are interconnected with the grid using power conversion systems, which do not have the mentioned inertia effect. Consequently, DG have problems to respond to the initial surge of power [24] and load tracking problems arise [25]. DG are generally considered as inertia-less systems [26]. However, the use of power conversion systems also allows a DG system to participate not only in active power control but also in reactive power control [27].

Concerning the advantages of DG, one of the most important is the reduction of fossil fuel consumption and the consequent reduction in green-house gas emissions obtained due to the RES [28].

The proximity between the DG and the loads introduces several advantages as well. The reduction of the physical distance between the load and the generation system helps to reduce the power losses [12]. At the same time, as the power is locally generated, the construction of new Transmission and Distribution (T&D) lines can be postponed and local resources can be better exploited [5]. Another advantage of local power generation is the possibility of improving the efficiency of different DG through Combined Heat and Power (CHP) plants. An energy generation system that generates electricity and heat can be installed near the heat load as the electricity transportation is easier than the heat one. This way, the waste heat generated by the DG can be used for other purposes increasing the overall efficiency of the generation system [29]. This will, at the same time, reduce the energy consumption that was previously used to generate the heat.



## 1.1. Distributed Generation

---

### 1.1.5 Microgrid

The point of view of an electric grid where big centralised energy generators provide power through transmission and distribution grids in an unidirectional way has started to change due to the reasons explained in Section 1.1.1. The continuously higher penetration of DG in the distribution grid is replacing a part of the power supplied by the centralised power generators, which creates several challenges mentioned in the previous subsection that must be carefully addressed in order to keep the proper operation of the electric grid.

To ensure all those challenges, a solution capable of guaranteeing a controlled injection of the power generated by DG must be defined. The MG is being analysed as a solution to these issues [30].

Today, there is no standard definition to describe what a MG is. Even though many different definitions of the MG can be found in the literature, almost all authors agree in certain characteristics. A MG is generally defined as a weak electric grid based on localised grouping of electricity DG (<100kW [31]), loads [32] and storage systems [33] that normally operates connected to the Low Voltage (LV) or Medium Voltage (MV) distribution network in a unique point [6] called Point of Common Coupling (PCC). One of the essential characteristics of the MG is its ability to operate connected or disconnected from the main grid as physical and economic conditions dictate [31]. From the grid's point of view a MG can be regarded as a controlled entity that can be operated as a single aggregated load or even as a small power source or ancillary service supporting the network [34]. From the customer's point of view, a MG provides enhanced Power Quality and Reliability (PQR) energy supply [35].

The basic architecture of a MG was defined by the *Consortium for Electric Reliability Technology Solutions* and it is shown in Figure 1.3.

In this architecture the electrical system is supposed to be radial and it has several feeders as well as loads. The microsources are interconnected with the system through power converters, which allow to control their power flow. In Figure 1.3 there are three feeders (A, B and C), two of them (A

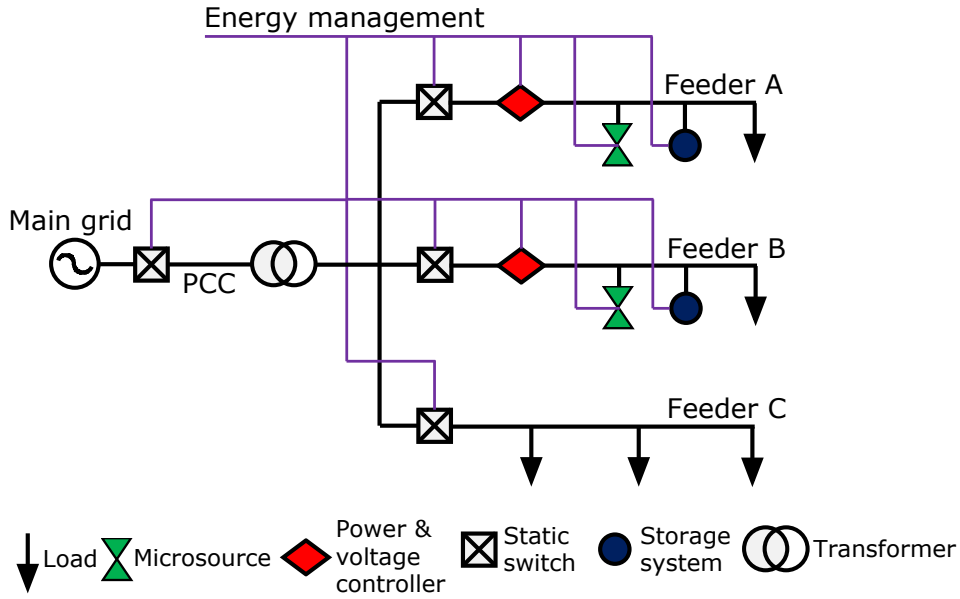


Figure 1.3: Basic MG architecture.

and B) are supplying power to sensitive loads and the last feeder only to non-sensitive loads. A sensitive load must always receive power, while a non-sensitive load can be interrupted if there is a power quality problem in the MG. Consequently, each feeder that has sensitive loads has also at least one microsource. The feeders A and B can also be disconnected from the rest of the MG if a disturbance requires so. The MG is connected to the main grid in the PCC. If a disturbance occur in the main grid, the MG can be disconnected from it using the static switch and it can continue working in islanding mode.

If the microsources of the sensitive feeders generate more power than the power needed by the sensitive loads, the power difference will be used to either feed the non-sensitive loads, charge the different storage devices of the MG or to supply ancillary services to the grid selling the surplus energy to the utility [33].

The most important characteristic of a MG is its ability to operate in islanding mode. This way, if a problem is detected in the main grid, the MG will be disconnected and it will continue working autonomously. Depending on its configuration, a MG would be able also to disconnect only some feeders in order to continue feeding the most important loads [36].

## 1.1. Distributed Generation

---

The interconnection with the main grid, i.e. the algorithm used to define the operation mode (grid-connected or islanding) in each operation point as well as the synchronisation to allow the reconnection to the grid represents also a contest [37].

The control of a MG is another issue that must be addressed. Control refers to all the algorithms and equipment used to ensure the desired behaviour of the different DG sources, loads and storage. In a MG the use of storage systems is essential, among other reasons, to be able to maintain power balance when power fluctuations generated by load or generation systems occur. In the bulk grid these power variations are typically faced using the inertia effect of the big synchronous generators, but in the MG the power generation systems are considered to be inertia-less. Storage plays a vital role in order to ensure energy balance and also allowing to maintain high power quality [37]. This is especially true for the voltage and frequency control. The MG must be able to satisfy the different standards facing mainly voltage sags, flickers and harmonics.

Thus, the use of an Energy Storage System (ESS) is a key element in a microgrid context, especially if there is a high penetration of renewable sources. An energy storage system helps to smooth the power variations introduced by RES and at the same time they can store the excess of energy when the generation is higher than the demand and provide the previously stored energy when the generation is lower than the demand. Consequently, an ESS can be controlled in order to maintain the power balance, the energy balance and also to improve the power quality of the MG [38].

The first issue when selecting an ESS is to define which from the different available technologies will be used. On the other hand, even if a storage system can provide many benefits, they have to be properly controlled in order to fulfil the fixed specifications. The power flow of the storage systems is controlled through power converters. However, there are many types of converters and several topologies can be created using different converters. Numerous aspects must be taken into account in order to select the proper topology for

each application: power losses, obtained Total Harmonic Distortion (THD), flexibility of the system, etc. The research work presented in this thesis analyses all these issues and proposes an integrated solution for the storage system of a MG.

### 1.2 Objectives of the thesis

The main objective of this thesis has been to propose a storage system and its associated power electronics interface and control in order to keep the energy balance, the power balance and also to improve the power quality of a MG. Taking into account the lack of experimental results that can be checked with a short survey of the literature, one of the most important parts of the thesis was the experimental validation of the proposed solution using for that objective the experimental MG installed in ESTIA.

In order to satisfy the defined main objective, the following intermediate objectives were fixed to properly divide the work to be carried out:

- Analyse the existing storage technologies and identify the best adapted solution for the MG application. Characterise the chosen solutions.
- Analyse the existing power electronics interface (between the storage system and MG) used for controlling the power flow of a storage system of a MG. Compare the existing solutions and propose an integrated solution to satisfy the main objectives defined previously.
- Design and validate the control method for the selected topology in order to manage both power and energy in the MG.
- Modelling and simulation of the investigated system taking into account the variability of the power coming from the DG and the power absorbed by the loads.
- Implement and test experimentally the proposed integrated solution.

## 1.3 Structure of the document

The memory is divided in five different chapters and three appendixes. This section is oriented to give details about the composition of each chapter.

Chapter 2 makes a review of the different existing storage technologies that can be useful from the MG application point of view, taking into account which the specifications of that storage system are. First of all the advantages of using an ESS in a MG context are analysed. Then, a short description of the different interesting storage technologies is carried out, giving in the end a classification that summarises all the relevant information. The mentioned table helps to better understand the advantages and drawbacks of each technology. This comparison is used to select a Hybrid Energy Storage System (HESS) formed by two storage technologies as the best compromise to satisfy the objectives that were fixed. The specific details of the selected storage technologies, i.e. SuperCapacitor (SC) and Vanadium Redox Battery (VRB), are analysed. The chapter finishes with the modelling of the selected storage devices, which have been experimentally validated.

Chapter 3 analyses the different topologies of power converters that were presented in different research works in order to integrate the HESS in the MG. First of all a state-of-the-art analysis is made to identify which the most important topologies are. Three topologies are selected, parallel topology, floating topology and Three Level Neutral Point Clamped (3LNPC). Once the topologies are determined, a similar control structure is defined for all of them in order to analyse the behaviour of each one in similar conditions. Two different case studies are defined to carry out the comparison. From the conclusions of the comparison 3LNPC converter topology is selected as the best compromise between the compared characteristics.

Chapter 4 focuses on the 3LNPC topology. A comparison between the most used modulation strategies is carried out from the DC current division point of view. A Sinusoidal Pulse Width Modulation (SPWM) is selected for the 3LNPC converter control due to its easy implementation. Then, a complete

analysis of the 3LNPC converter is carried out to determine its operational limits in its entire operation range. From this analysis, the maximum and minimum DC currents that can be obtained in all the operation points are determined, which are used in Chapter 5 to design the controller of the power flow of the HESS.

Chapter 5 explains the final control algorithm that has been selected to control the 3LNPC converter and the power flow of the HESS. The details of the experimental platform are provided and the proposed topology and its control algorithm are experimentally tested in two case studies, isolated and grid-connected case studies. These experimental results show that the designed system satisfies the specifications determined in Chapter 1 and validate the simulation results.

Chapter 6 summarises the main conclusions obtained in this work. The future research lines are also given in this chapter, as well as the list of publications that were done during this thesis.

Finally, there are three appendixes, which give details about the power losses calculation method in Appendix A, the reference system transformations in Appendix B and the digitalisation process of the different designed continuous algorithms in Appendix C.

## Chapter References

- [1] G. Pepermans, J. Driesen, D. Haeseldonckx, R. Belmans, and W. D'haeseleer. Distributed generation: definition, benefits and issues. *Energy policy*, 33(6):787–798, 2005.
- [2] H. B Puttgen, P. R MacGregor, and F. C Lambert. Distributed generation: Semantic hype or the dawn of a new era? *IEEE Power and Energy Magazine*, 1(1):22– 29, February 2003.
- [3] S.M. Kaplan. Electric power transmission: background and policy issues. *US Congressional Research Service*, April 2009.

## Chapter References

---

- [4] J. Morren. Grid support by power electronic converters of distributed generation units, November 2006.
- [5] A. A. Bayod-Rújula. Future development of the electricity systems with distributed generation. *Energy*, 34(3):377–383, March 2009.
- [6] J. Driesen and F. Katiraei. Design for distributed energy resources. *IEEE Power and Energy Magazine*, 6(3):30–40, May 2008.
- [7] A. Ipakchi and F. Albuyeh. Grid of the future. *IEEE Power and Energy Magazine*, 7(2):52–62, April 2009.
- [8] A. Hajizadeh and M. A. Golkar. Control of hybrid fuel cell/energy storage distributed generation system against voltage sag. *Int. J. Electrical Power & Energy Systems*, 32(5):488–497, June 2010.
- [9] IEA. Distributed generation in liberalised electricity markets. *OECD*, 2002.
- [10] P. Dondi, D. Bayoumi, C. Haederli, D. Julian, and M. Suter. Network integration of distributed power generation. *J. of Power Sources*, 106(1-2):1–9, 2002.
- [11] N. Jenkins, R. Allan, P. Crossley, D. Kirschen, and G. Strbac. *Embedded Generation*. 31. The Institution of Engineering and Technology, June 2000.
- [12] W. El-Khattam and MMA Salama. Distributed generation technologies, definitions and benefits. *Electric Power Systems Research*, 71(2):119–128, 2004.
- [13] T. Ackermann, G. Andersson, and L. Söder. Distributed generation: a definition. *Electric Power Systems Research*, 57(3):195–204, 2001.
- [14] A. Poullikkas. Implementation of distributed generation technologies in isolated power systems. *Renewable and Sustainable Energy Reviews*, 11(1):30–56, 2007.

- [15] R. Cossent, T. Gómez, and P. Frías. Towards a future with large penetration of distributed generation: Is the current regulation of electricity distribution ready? regulatory recommendations under a european perspective. *Energy Policy*, 37(3):1145–1155, 2009.
- [16] K. Alanne and A. Saari. Distributed energy generation and sustainable development. *Renewable and Sustainable Energy Reviews*, 10(6):539–558, 2006.
- [17] A. Goikoetxea. *Integration of Distributed Generation Using Energy Storage Systems*. Ph.D. dissertation, Mondragon Unibertsitatea, February 2011.
- [18] T. Lund. *Analysis of distribution systems with a high penetration of distributed generation*. Ph.D. dissertation, Technical University of Denmark, 2007.
- [19] A. Kirubakaran, S. Jain, and R. K. Nema. A review on fuel cell technologies and power electronic interface. *Renewable and Sustainable Energy Reviews*, 13(9):2430–2440, 2009.
- [20] P. Jain. *Wind Energy Engineering*. McGraw-Hill Professional, September 2010.
- [21] K. Purchala, R. Belmans, L. Exarchakos, and A. D. Hawkes. Distributed generation and the grid integration issues. Technical report, European Sustainable Electricity, 2006.
- [22] J. Soens, J. Driesen, and R. Belmans. Interaction between electrical grid phenomena and the wind turbine’s behaviour. In *Proc. ISMA*, 2004.
- [23] JA Lopes, N. Hatziargyriou, J. Mutale, P. Djapic, and N. Jenkins. Integrating distributed generation into electric power systems: A review of drivers, challenges and opportunities. *Electric Power Systems Research*, 77(9):1189–1203, 2007.



## Chapter References

---

- [24] O. M. Toledo, D. Oliveira Filho, and A. S. A. Cardoso Diniz. Distributed photovoltaic generation and energy storage systems: A review. *Renewable and Sustainable Energy Reviews*, 14(1):506–511, 2010.
- [25] Integration of distributed energy Resources-The CERTS MicroGrid concept. Technical Report P500-03-089F, CERTS Program Office, October 2003.
- [26] R. Majumder, A. Ghosh, G. Ledwich, and F. Zare. Power management and power flow control with Back-to-Back converters in a utility connected microgrid. *IEEE Trans. Power Systems*, 25(2):821–834, May 2010.
- [27] M. Dai. *Control of power converters for distributed generation applications*. Ph.D. dissertation, Ohio State University, 2005.
- [28] K. Angelopoulos. *Integration of Distributed Generation in Low Voltage Networks: Power Quality and Economics*. Master dissertation, University of Strathclyde in Glasgow, 2004.
- [29] R. H Lasseter. Microgrids and distributed generation. *J. of Energy Engineering*, 133(3), September 2007.
- [30] N. Hatziargyriou, H. Asano, R. Iravani, and C. Marnay. Microgrids. *IEEE Power and Energy Magazine*, 5(4):78–94, August 2007.
- [31] R. H Lasseter. MicroGrids. In *IEEE PES Winter Meeting, 2002*, volume 1, pages 305–308, 2002.
- [32] H. Jiayi, J. Chuanwen, and X. Rong. A review on distributed energy resources and MicroGrid. *Renewable and Sustainable Energy Reviews*, 12(9):2472–2483, 2008.
- [33] R. Zamora and A. K. Srivastava. Controls for microgrids with storage: Review, challenges, and research needs. *Renewable and Sustainable Energy Reviews*, 14(7):2009–2018, September 2010.

- [34] A.G. Tsikalakis and N.D. Hatziargyriou. Centralized control for optimizing microgrids operation. *IEEE Trans. Energy Conversion*, 23(1):241–248, March 2008.
- [35] F. D. Kanellos, A. I Tsouchnikas, and N. D. Hatziargyriou. Micro-grid simulation during grid-connected and islanded modes of operation. In *Proc. Int. Conf. Power Systems Transients (IPST'05)*, 2005.
- [36] A. Llaria, O. Curea, J. Jiménez, and H. Camblong. Survey on microgrids: Unplanned islanding and related inverter control techniques. *Renewable Energy*, 36(8):2052–2061, August 2011.
- [37] S. Abu-Sharkh, R. Li, T. Markvart, N. Ross, P. Wilson, R. Yao, K. Steemers, J. Kohler, and R. Arnold. Microgrids: Distributed on-site generation. Technical report, Tyndall research centre, University of Southampton, 2005.
- [38] A. Etxeberria, I. Vechiu, H. Camblong, and J.M. Vinassa. Hybrid energy storage systems for renewable energy sources integration in microgrids: A review. In *Proc. IEEE IPEC*, pages 532–537, October 2010.

## CHAPTER 2

# Energy Storage Systems

---

### Contents

---

<b>2.1</b>	<b>Benefits of storing energy</b>	<b>22</b>
2.1.1	Generation and transmission systems	22
2.1.2	Operation of power systems	22
2.1.3	RES integration	25
<b>2.2</b>	<b>Types of energy storage technologies</b>	<b>25</b>
2.2.1	Electrochemical storage systems	27
2.2.2	Electrical storage systems	35
2.2.3	Mechanical storage systems	37
<b>2.3</b>	<b>Comparison of storage technologies</b>	<b>38</b>
<b>2.4</b>	<b>Modelling of the HESS</b>	<b>44</b>
2.4.1	Modelling of SC	45
2.4.2	Modelling of VRB	52
2.4.3	Chapter Conclusions	62
	<b>Chapter References</b>	<b>62</b>

---

This chapter analyses the state-of-the-art of different storage technologies from the microgrid application's point of view. First of all, the main advantages introduced by an ESS are analysed. The main objective of this chapter is to propose a review of the most important storage technologies that can be used in the MG context in order to select a storage system that satisfies the specified requirements. From the survey results, a HESS formed by a SC and a VRB is selected as the best solution for the MG application. Finally, the modelling of the selected storage devices is carried out. The presented dynamic models have been experimentally validated.

## **2.1 Benefits of storing energy**

In Chapter 1 the necessity of an ESS in order to facilitate a high penetration of DG in the main grid was stressed. However, an energy storage system could introduce many other benefits, which are analysed in this section. Only technical benefits are taken into account, economic advantages are neglected.

Technical advantages introduced by an ESS can be classified in three main groups: advantages on generation and transmission of power, on operation of the power system and on RES integration.

### **2.1.1 Generation and transmission systems**

The power consumption in any electric grid varies according to time. The worst consumption case from the point of view of generation and transmission systems is the peak demand case needed in order to generate/transmit maximum power. Generation and transmission systems are sized to be able to supply the power in peak demand cases. However, due to the continuously increasing electric power consumption, the capacity of those systems must be updated according to this increase. The use of an ESS can postpone and/or reduce the necessity of new generation units and the rise of capacity of transmission lines. As the storage system is located downstream from the overloaded T&D node, it can be charged during off peak periods and then discharged during peak demands reducing the transmitted power. From the point of view of the generation/transmission system there is no power increase as it is directly supplied by the storage system. Consequently, the upgrade of transmission and distribution grids as well as of electric supply capacity of the generators can be deferred and/or reduced [1].

### **2.1.2 Operation of power systems**

A properly designed and operated power system should meet the following fundamental requirements [2]:

1. The system must be able to meet the continually changing load demand

## 2.1. Benefits of storing energy

---

for active and reactive power.

2. The system should supply energy at minimum cost and with minimum ecological impact.
3. The power supply must meet certain minimum standards with regard to the following factors:
  - (a) constancy of frequency
  - (b) constancy of voltage
  - (c) level of reliability

An ESS can be used in order to satisfy the mentioned requirements. The benefits introduced by an ESS in the operation of a network can be classified in two main groups: ancillary services and power quality and reliability.

### 2.1.2.1 Ancillary services

Ancillary services are those services necessary to support the delivery of electricity from seller to purchaser while maintaining the integrity and reliability of the interconnected transmission system. The ancillary services that an ESS can provide are listed below [3]:

- **Reactive power supply and voltage control:** The injection or absorption of reactive power to maintain the transmission system voltages within the required ranges.
- **Area regulation:** Minute-by-minute generation/load balance within a control area, mainly to keep the frequency of the grid.
- **Spinning reserve:** On-line generation capacity that is synchronised to the grid but unloaded and that can respond immediately to compensate for generation or transmission outages.
- **Supplemental reserve:** Generation capacity that may be off-line or curtailable load that can respond within 10 minutes to compensate for generation or transmission outages.

- **Load following:** Adjusting the generated power according to the fluctuating demand of electricity throughout the day.
- **Energy imbalance:** Correcting for mismatches between actual and scheduled transactions on an hourly basis.
- **Backup supply:** Generation available within an hour, for backing up reserves or for commercial transactions.
- **Real power loss replacement:** Generation that compensates for losses in the T&D system.
- **Black start:** Ability to energise part of a grid without outside assistance after a blackout has occurred.
- **Network stability:** Real-time response to system disturbances to maintain system stability or security.

### 2.1.2.2 Power quality and reliability

Reliability and power quality are two important factors from the customer's point of view, especially if critical loads are to be fed. For the end-use customer highly reliable electric energy with the highest possible power quality has to be supplied. Storage systems play a vital role to provide these requirements [4, 5].

Reliability is related to the complete loss of voltage of a grid. It can be defined as the degree to which the performance of the elements in a bulk system results in electricity being delivered to customers within accepted standards and in the amount desired [6]. Storage systems can be used to provide ride through capability when outages of extended duration occur. They can be used to substitute the power supply for a certain period of time or for middle-time power supply, to maintain power until another on-site generation system is started [1, 7].

On the other hand, storage systems can also be used to face different issues that affect power quality. Usually two power quality problems are considered

## 2.2. Types of energy storage technologies

---

to be important: transient voltage events (typically voltage dips) and harmonic distortion [8]. Other power quality problems include frequency variations and low power factor [1]. Storage systems controlled with power converters can be used to mitigate harmonics as well as to avoid frequency variations and transient voltage variations improving the power quality of the grid [9–11].

### 2.1.3 RES integration

The output variations of the RES that are most used in the MG context, i.e. WT and PV panels, are classified as short-duration and slow duration or diurnal. The effect of clouds in case of PV and wind gusts in case of WT can create fast power variations and consequently power generation systems that can react at the same speed should be used to keep the operation of the network under standard conditions. As the classical generators are not able to face those variations, the use of storage systems is necessary.

An energy storage device offers the possibility of storing the surplus energy generated by RES when the generation is higher than the demand and then giving the stored energy back to the grid when the generation is lower than the demand [12]. This way, the energy generated by RES is better harnessed and at the same time the power injected in the grid is smoothed, reducing the negative impact of RES. The use of a storage system in parallel to a RES allows to keep the output power of the system at constant level [1].

## 2.2 Types of energy storage technologies

Once the different benefits that an ESS can introduce in a microgrid have been reviewed, it is necessary to analyse which are the storage technologies that are available for the selected application, in order to compare them and define the best adapted storage system.

The comparison has been carried out in the basis of the requirements of a MG application. A storage system that is used in this application should need a high power capacity and a fast response time to keep the power balance.

It also requires a high energy capacity to keep energy balance as well as to improve RES energy integration. High efficiency and long lifetime are also specifications that the selected ESS must fulfil. The characteristics that will be used to carry out the comparison are listed below:

- **Energy rating:** maximum energy quantity that a storage device can store, measured in  $MWh$ .
- **Power rating:** maximum power that an energy storage technology can supply/absorb, measured in  $MW$ .
- **Specific energy:** energy storage capacity per mass unit, measured in  $Wh/kg$ .
- **Specific power:** maximum power capacity per mass unit, measured in  $W/kg$ .
- **Life time and cycle life:** both characteristics define the durability of a storage system. The life time is measured in years. On the other hand, the cycle life is measured in charge-discharge cycles. As the durability depends on the Depth Of Discharge (DOD), the cycle life is usually given according to the DOD level. The higher the DOD, the smaller the durability.
- **Self-discharge:** defines the energy lost by a storage system during non-use time. This parameter is measured by the relation between the energy lost during a certain period of time (hour, day or month) and the energy capacity of the storage device.
- **Response time:** time needed by the storage device to pass from no-discharge state to the state where it supplies the rated output power.
- **Round-trip efficiency:** the ratio between the energy received and relieved by the storage system.



## 2.2. Types of energy storage technologies

---

- **Operational constraints:** operational limits that the storage technologies may have, for example a certain temperature range, pressure, DOD limit, etc.

There are several ways of classifying the different storage technologies. In this work they have been classified according to the way of storing energy. The different storage technologies are classified in three groups: mechanical, electrochemical and electrical storage systems. In the following two subsections the different storage technologies that can be used in the microgrid context are shortly described. The pumped hydro and compressed air energy storage technologies have not been taken into account due to the geographical restrictions of their installations.

### 2.2.1 Electrochemical storage systems

Batteries are storage devices that store the energy in chemical form. They are able to charge or discharge through electrochemical reactions converting chemical energy into electrical and vice-versa. They are formed by cells that are connected in series and/or in parallel in order to obtain the desired characteristics. Each cell is formed by two electrodes, which are connected to an external source/load, and an electrolyte, which allows the exchange of ions between the two electrodes in order to allow the chemical reaction to occur [13]. The following subsections analyse the most important battery technologies.

#### 2.2.1.1 Lithium-ion (Li-ion)

The cathode in this kind of battery is a lithiated metal oxide and the anode is made of graphitic carbon with a layering structure. The electrolyte is made up of lithium salts dissolved in organic carbonates, as it is shown in the simplified structure of Figure 2.1. When the battery is charged, the lithium atoms in the cathode become ions and migrate through the electrolyte toward the carbon anode where they combine with external electrons and are deposited between the carbon layers as lithium atoms. This process is reversed during the discharge process [7].

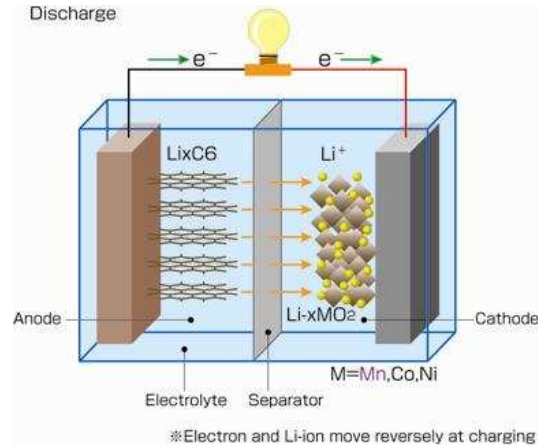


Figure 2.1: Structure of a Li-ion battery (source: *digital-camera-battery.net*)

The main advantages of Li-ion batteries compared to other types of batteries are their high specific energy (200  $\text{Wh/kg}$  [14]), very high efficiency (around 95% [15]) and relatively long cycle life (3000 cycles at 80% DOD [16]). The main disadvantage of this type of battery is its cost and the limited lithium resources as well as the need of protection circuits to keep voltage and current within safety limits [14]. Another important drawback of this type of battery is that its life expectancy is affected by the operating temperature and the DOD, in such a way that a high temperature and discharge rate will severely shorten its cycle life [17].

Li-ion batteries are mainly used in small applications, especially in portable ones like laptop computers or mobile phones. The use of Li-ion batteries in large-scale applications is still limited due to its high cost per  $\text{kWh}$  [7] and DOD dependant life expectancy [18].

### 2.2.1.2 Lead-acid

Lead-acid batteries are the oldest and well-known types of batteries. A Lead-acid cell is made of two electrodes: one electrode is of lead metal and the other of lead oxide, and both are placed in a sulphuric acid electrolyte. The simplified structure of a Lead-acid battery is shown in Figure 2.2.

The main advantages of Lead-acid batteries are their relatively low investment cost, low self-discharge (around 2% of rated capacity per month

## 2.2. Types of energy storage technologies

---

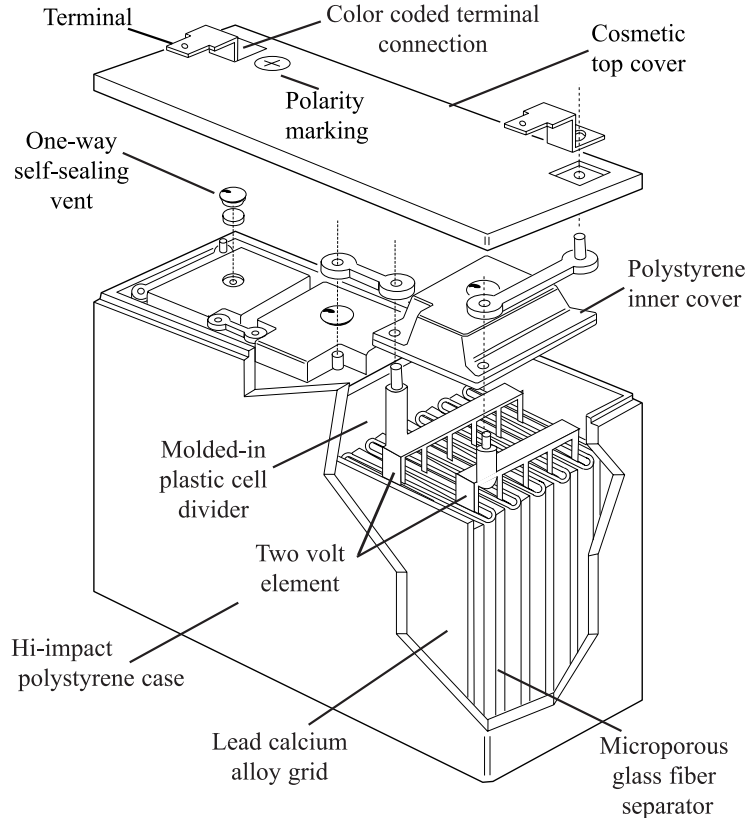


Figure 2.2: Structure of a Lead-acid battery (source: *Power Sonic*).

[17]), high reliability and high efficiency (72-90%) [7]. On the other hand, the disadvantages are the low specific energy (30-50 Wh/kg), the limited cycle life (500-1000 cycles) [7], the environmentally unfriendly content, frequent maintenance to replace water lost in operation and the recommended low DOD not to reduce the lifespan [15, 19]. Lead-acid batteries also have a poor low temperature performance and therefore require a thermal management system [7].

Typical applications of Lead-acid batteries include automotive starting, lighting, and ignition and battery powered Uninterruptible Power Supply (UPS), cost-sensitive applications where the low specific energy and limited cycle life are not an issue [14]. It is also a popular storage choice for power quality and some spinning reserve applications [7].

### 2.2.1.3 Nickel Cadmium (NiCd)

A NiCd battery is formed by a positive electrode of nickel oxyhydroxide, a negative electrode of metallic cadmium and an alkaline electrolyte, usually potassium hydroxide [16]. The structure of a NiCd cell is shown in Figure 2.3.

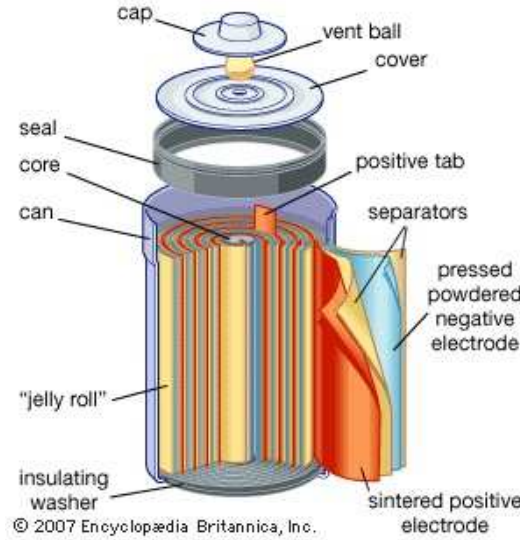


Figure 2.3: Structure of a NiCd cell (source: *Encyclopædia Britannica*).

A NiCd battery has a specific energy of (50-75  $Wh/kg$ ), an efficiency of 60-73% [17], a relatively low cycle life (2000-2500 cycles), a robust reliability, very low maintenance requirements [7], relatively high rates of self-discharge (10% of rated capacity per month [17]) and *memory* effect, where the batteries will only take full charge after a series of full discharges [16]. NiCd batteries withstand extreme working conditions like overcharging, high temperature and high pressure [20].

One of the biggest disadvantages of NiCd is its high cost due to expensive manufacturing process. NiCd is a robust and proven alternative to Lead-acid batteries, with higher specific energy, a longer cycle life and low maintenance requirements [21]. However, the elevated cost limits its industrial UPS applications such as in large energy storage for renewable energy systems [17]. The toxicity of cadmium and the related recycling issues are also a limiting factor for the use of this type of batteries [21].

## 2.2. Types of energy storage technologies

---

NiCd batteries are used in emergency lighting, telecommunications, and generator starting applications [7].

### 2.2.1.4 Sodium Sulphur (NaS)

A NaS battery is a high temperature battery formed by a molten sulphur at the positive electrode and a molten sodium at the negative electrode, separated by a solid beta alumina ceramic electrolyte. The electrolyte allows only the positive sodium ions to go through it and combine with the sulphur to form sodium polysulphides. The structure of a NaS cell is shown in Figure 2.4. During discharge, positive sodium ions flow through the electrolyte and electrons flow in the external circuit of the battery. The battery is kept at  $290\text{--}380^\circ\text{C}$  to allow this process which requires constant heat input to maintain the molten states of the electrolytes [19, 22].

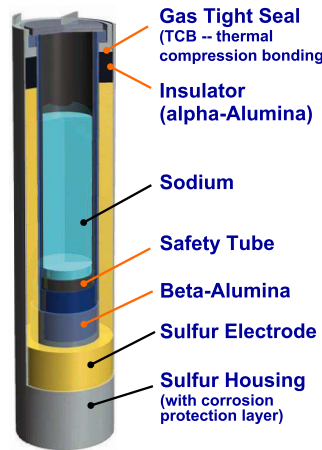


Figure 2.4: Structure of a NaS cell (source: *California Energy Commission*).

NaS batteries are made from inexpensive and non-toxic materials and their efficiency is in the range 89-92%. However, the high operating temperatures and the highly corrosive nature of sodium make them suitable only for large-scale stationary applications [17]. Their cycle life is around 2500 cycles and their typical specific energy is  $150\text{--}230\text{ Wh/kg}$ . Apart from the need to externally heat the battery, another issue of NaS batteries is the initial cost [7].

Due to their pulse power capability over six times their continuous rating

(for 30 s), NaS batteries are used in combined power quality and peak shaving applications [7]. NaS are also used in UPS applications [14].

### 2.2.1.5 Flow Batteries

Flow batteries are special types of batteries where electrolytes are stored in external tanks and moved through the stack using pumps, obtaining this way decoupled energy capacity and power rating [14]. This is the main advantage of flow batteries over conventional ones. The second main difference between flow batteries and conventional batteries is that in flow batteries the reaction occurs between two electrolytes, rather than between an electrolyte and an electrode. Consequently, there is no loss in electroactive substances when the battery is repeatedly deeply cycled [13].

A flow battery is formed by a stack (where the electrochemical reaction occurs), the external tanks (where both electrolytes are stored) and the circulation circuit through where pumps move the electrolyte from the tanks to the stack and back to the tanks, as shown in Figure 2.5.

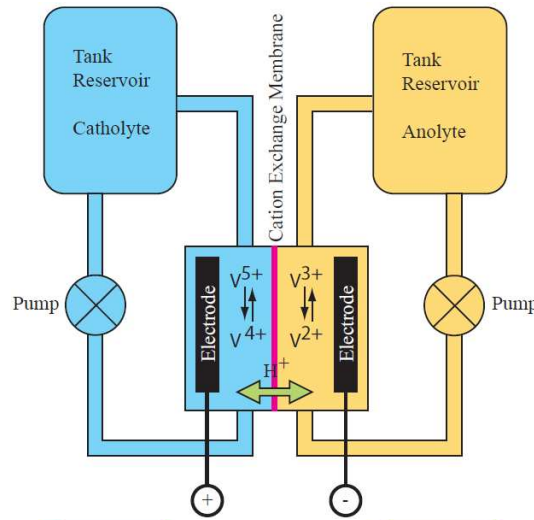


Figure 2.5: Structure of a Vanadium Redox Battery [13].

There are three main types of flow batteries, which are differentiated according to the chemistry of electrolytes: VRB, PolySulphide-Bromide (PSB) and Zinc Bromine (ZnBr).

## 2.2. Types of energy storage technologies

---

**VRB** This type of flow battery stores energy by employing vanadium redox couples ( $V^{2+}/V^{3+}$  in the negative and  $V^{4+}/V^{5+}$  in the positive half-cells). These are stored in mild sulphuric acid solutions (electrolytes). During the charge/discharge cycles,  $H^+$  ions are exchanged between the two electrolyte tanks through the hydrogen-ion permeable polymer membrane (Figure 2.6). The efficiency of VRB can be as high as 85% and their cycle life is expected to be higher than 16000 cycles. The electrolytes have an indefinite life and it can be transferred charged to be reused in other applications [16]. Furthermore, as vanadium is present in both electrolytes, the electrolyte cross-contamination is eliminated [23]. The main disadvantages of VRB are the relatively low specific energy and specific power.

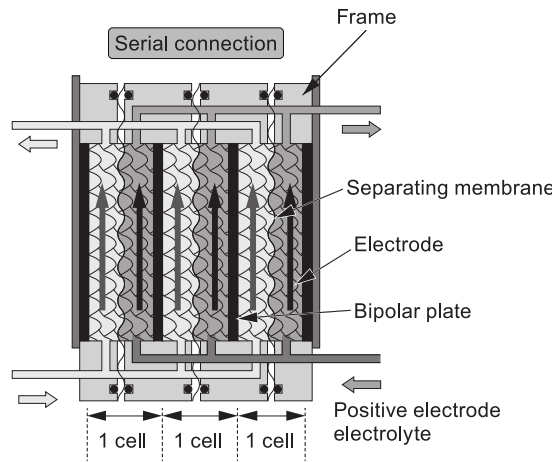


Figure 2.6: Series connection of VRB cells [24].

VRB is usually used in stationary applications like power quality, UPS, peak shaving and integration of RES.

**PSB** PSB provides a reversible electrochemical reaction between two salt solution electrolytes, sodium bromide and sodium polysulfide. PSB electrolytes are brought close together in the battery cells where they are separated by a polymer membrane that only allows positive sodium ions to go through it [7]. Figure 2.7 shows the simplified operation of the PSB flow battery.

The net efficiency of this battery is about 75% and the cycle life is estimated

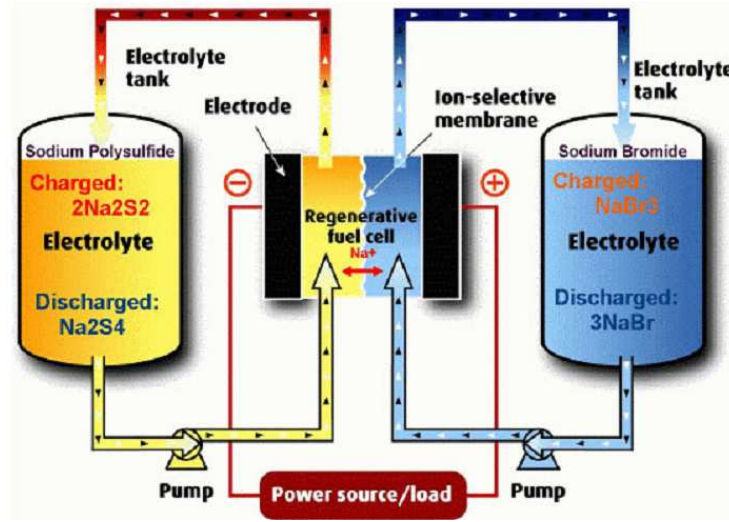


Figure 2.7: Simplified operation of a PSB [25]

at 2000 cycles. PSB flow batteries can be used for all energy storage requirements including load levelling, peak shaving, and integration of renewable resources. During the chemical reaction small quantities of bromine, hydrogen, and sodium sulphate crystals are produced and consequently maintenance is required to remove the sodium-sulphate by-products [26].

**ZnBr** The design and electrochemistry of ZnBr flow batteries is not the same as the one of VRB and PSB. A ZnBr electrolyte flows through two half-cells divided by a microporous membrane, with a  $Zn^-$  electrode and a  $Br^+$  electrode. These electrodes work as substrates for the reactions and their performance capacity can be degraded if the battery is not completely and regularly discharged. During charge, zinc is electroplated on the anode and bromine is evolved at the cathode. An agent in the electrolyte is used to reduce the reactivity of the elemental bromine by forming a polybromide complex, thus minimising the self-discharge of the battery. The complexed bromine is then removed from the stacks via the flowing electrolyte and is stored in the external reservoir. During the discharge, the complexed bromine is returned to the battery stacks and reduced to bromide on the cathodes, while zinc is oxidized to zinc ions on the anodes.



## 2.2. Types of energy storage technologies

A ZnBr battery has a lifetime of up to 2000 cycles, an efficiency of 75% and it has the highest specific energy among the flow batteries (75-85 Wh/kg). Applications of ZnBr include facility-scale UPS and load management, support for microturbines, solar generators, substations and T&D grids [16]. Figure 2.8 shows the operation of a ZnBr flow battery schematically.

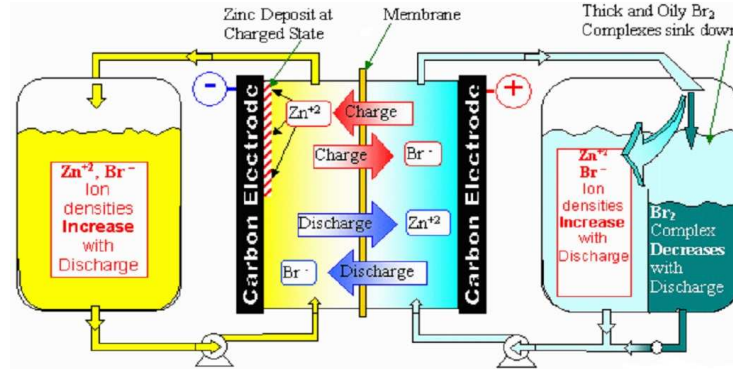


Figure 2.8: Simplified operation of a ZnBr flow battery (source: *Energy Storage Association*)

### 2.2.2 Electrical storage systems

#### 2.2.2.1 SC

In this storage technology there is not any transformation of energy as it is stored electrically, by means of an electric field between two electrodes. Figure 2.9 shows an illustration that represents the structure of a SC cell.

SC have a very high capacitance (up to several thousand farads) and consequently they are capable of supplying high power. However, their specific energy is very low. The response time of SC is very fast, with a life expectancy of millions of cycles and an efficiency of about 95%. The main disadvantage is their self-discharge rate, which has an approximated value of 5% per day [13, 25]. As the voltage of a SC cell is very low, several cells have to be connected in series to obtain a higher voltage value.

Due to their high lifespan, efficiency and specific power, the supercapacitors are being used in several applications as high peak power sources for a few milliseconds-several minutes, especially in power quality applications such as

ride through, and also for other applications like blade-pitch control in WT and energy recovery in mass transit systems [7, 27].

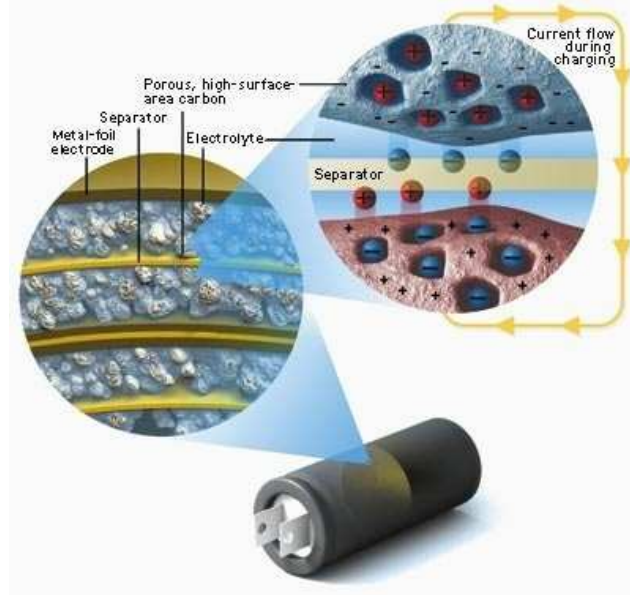


Figure 2.9: Schematic representation of a SC cell (source: *ultracapacitors.org*).

### 2.2.2.2 Superconducting Magnetic Energy Storage (SMES)

A SMES stores energy in the magnetic field of a large superconducting material coil, which at very low temperature (around  $-270^{\circ}\text{C}$ ) offers almost no resistance to the current. The superconducting coil is immersed in liquid, which has to be maintained at low temperature. This refrigeration system requires approximately  $1.5\text{ kW}$  continuously per  $\text{MWh}$  of storage capacity [14]. Figure 2.10 shows the main components of a SMES storage system.

The round trip efficiency of a SMES is typically 95%. The SMES can be totally discharged without affecting its life time. The SMES is used for short duration storage processes because of its rapid response. Its typical power rating is between  $1\text{ MW}$  and  $10\text{ MW}$  for a storage time of seconds, but new researches are working with SMES of  $10\text{-}100\text{ MW}$  for a storage of minutes [7, 13, 22, 25].

Due to their high power capacity, fast response and high self-discharge rate,

## 2.2. Types of energy storage technologies

---

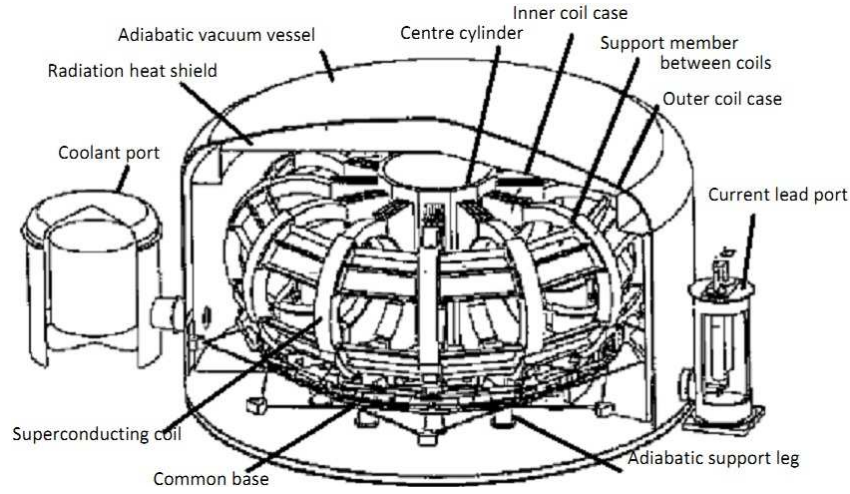


Figure 2.10: Components of a superconducting magnetic energy storage device [26].

the SMES are mainly used in power quality and UPS applications, but also for spinning reserve [26, 28].

### 2.2.3 Mechanical storage systems

#### 2.2.3.1 Flywheels

The flywheels store the energy mechanically by means of a rotating cylinder, using a vacuum environment to reduce the windage losses. During the charge process an electric machine accelerates the cylinder, and in the discharge process the electric machine works as a generator. The amount of stored energy depends on the rotational speed and the mass of the cylinder, and its power rating is related to the electrical machine. Figure 2.11 shows the schematic representation of the structure of a flywheel.

Nowadays, most of the research efforts are oriented to high speed flywheels (more than 20000 *rpm*). The lifetime of the flywheels is very high (tens of thousands of cycles or more than 20 years), as well as their efficiency, which is typically around 90-95%. The typical ratings of the commercial flywheels are a rated power of 100-250 *kW* with a stored energy of 3.3-25 *kWh* and a storage time of several seconds. Flywheels cannot be used for long-time storage because of their high self-discharge (100% in a day) [7, 13, 22].

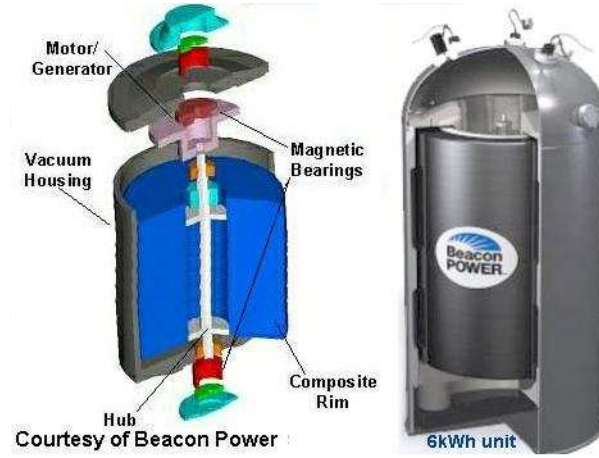


Figure 2.11: Schematic representation of a flywheel [7].

The most common application of flywheels, as of SC and SMES, is power quality, such as ride through. Flywheels are also used for reactive power support, spinning reserve, voltage support and wind power smoothing [7, 28, 29].

## 2.3 Comparison of storage technologies

Once the main storage technologies have been shortly introduced, their main characteristics will be analysed and compared in order to determine which are the storage technologies that are better adapted for the microgrid application.

In order to facilitate the comparison, Table 2.1 and Table 2.2 were created, where the aforementioned characteristics are summarised. In those tables *neg.* means negligible and *n/a* not available.

From the point of view of the power quality, the most important characteristics of an ESS are the life expectancy, efficiency, time response and power rating. A high life expectancy is necessary to support the large amount of charge-discharge cycles that the ESS will have in the MG application. A high efficiency would minimise the energy lost in each of those cycles. A high power rating is required to be able to absorb/supply a high input and output power. Finally, the ESS should also have a fast response to face fast power variations. On the other hand, from the energy point of view, the selected storage system needs a high storage capacity and very low self-discharge which will allow to

### 2.3. Comparison of storage technologies

Technology	Energy rating [MWh]	Power rating [MW]	Specific energy [Wh/kg]	Specific power [W/kg]	Efficiency [%]
Lead-acid	0.58[19] 0.001-40[18]	0.3[19] 0-20[7]	10-20[16] 20-35[14] 30[17] 30-50[19] 35-50[7]	25[14] 180[17] 75-300[7]	72-78[19] 75-80[13, 15] 85-90[17] 85[16, 26]
NiCd	6.75[18, 19]	0-40[7, 28, 29] 27[19] 40[21] 45[18] 50[26]	30-37[16] 40-60[14] 45-80[19, 21] 50[17] 50-75[7]	130-300[7] 140-180[14]	60-65[29] 60-70[26] 60-83[17] 60-90[14] 72[18] 72-78[19]
NaS	64[19] 0.4-244.8[18]	0.05-8[7] 9.6[19] 20[13]	53-116[16] 100[19] 120[14] 150-240[7]	120[14] 150-230[7]	70[14] 75[13] 75-85[15] 89[13] 89-92[17]
Li-ion	0.0015-50[18]	0-0.1[7] 0.15-50[18]	75-200[7] 80-150[17] 90-190[19] 110-160[21] 130[13] 150[16]	150-315[7] 360[14] 500-2000[17]	70-85[14] 78-88[18] 95[15, 16]
VRB	1.2-60[18] 1.5[19] 0.5-20[15]	0.03-3[7] 0.05-100[15] 1.5[19] 3[26]	10-30[7] 25[14] 25-35[18] 30-50[19]	80-150[14] 166[18]	70-85[26] 78[23] 80[14] 85[19]
PSB	0.005-120[18] 120[19]	0.1-15[18] 1-15[7] 15[19]	n/a	n/a	55-75[16] 60-75[16] 75[19]
ZnBr	0.1-4[18] 4[19] 4-10[15]	0.05-2[7] 0.1-2[18] 1[19] 4-5[15]	30-50[7] 60-85[18] 70[19]	45[18]	65-85[18] 70[14] 75[16, 19]
SC	0.01[18]	0-0.3[7] 0.05-0.25[18]	2.5-15[7] 5[17] 5-15[25]	500-5000[7] 800-2000[25] 10000[17] 23600[18]	85-98[17] 95[22]
SMES	0.00083-0.015[18]	0.1-10[7] 1-10[22] 2.5[13]	0.5-5[7] 10-75[18]	500-2000[7]	80-95[18] 90[13] 90-95[18]
Flywheel	0.0052-5[18]	0.1-20[18] 0.25[7]	5-100[18] 10-30[7] 100[17]	400-1500[7] 11900[18]	85[15] 90[17] 93-95[29]

Table 2.1: Summarise of the characteristics of the analysed ESS technologies.

store energy for periods of time of hours-days, allowing the MG to operate autonomously.

The specific power and specific energy are two of the most important characteristics to determine the validity of a storage system for the MG application. The different values of these two characteristics can be observed

## Chapter 2. Energy Storage Systems

Technology	Cycle life [cycles]	Life time [years]	Self-discharge [%]	Response time
Lead-acid	200-1800[13] 200-2000[14] 1000-2000 (70 %)[19] 500-1000[7] 1500 (deep)[17]	5-8[15] 5-10[26] 5-15[7, 17]	2[17] 2-5[19] (month)	fast ( <i>ms</i> )[29] <1/4 cycle[26, 28]
NiCd	500-2000[14] 1500-3000 (deep)[17] 2000[16] 2000-2500[7] 3000 (100%)[19] 3500[26]	10-20[29] 13-16[18] 20[21]	5-20[19] 10[16, 17] (month)	fast ( <i>ms</i> )[29] <1/4 cycle[28]
NaS	2000[14] 2250[16] 2500 (100%)[7, 19]	10-15[7, 15] 15[13]	neg.[16, 19, 21]	fast ( <i>ms</i> )[29] <1/4 cycle[28]
Li-ion	500-2000[14] 1000-10000[7] 1500[17] 2500(80%)[13] 3000(80%)[19]	5-15[7] 14-16[18]	1[19] 2[19] 5[17] (month)	fast ( <i>ms</i> )[29] <1/4 cycle[28]
VRB	10000 (75%)[16, 19] 12000[7] 13000[23] 16000[14]	5-10[7] 8-10[16] 10[26] 15-20[18]	neg.[14, 19, 26] very low[18]	n/a
PSB	2000[26]	10-15[7] 15[18]	neg.[19] small[7]	n/a
ZnBr	2000 (100%)[7, 16] 2500[23]	5-10[7] 8-10[18]	neg.[19]	n/a
SC	100k[7] 500k (100%)[17] 1M[18]	8-10[25] 12[17] 20[7]	5[25] 5-20[18] 20-40[7] (day)	very fast (<3 <i>ms</i> )[29] <1/4 cycle[26, 28]
SMES	10k-100k[18] 100k[7]	20[7]	10-15[7] (day)	very fast (<3 <i>ms</i> )[29] <1/4 cycle[26, 28]
Flywheel	10k-100k[25] 20k[7] 30k[13] 100k-10M (100%)[17]	15[7] 20[16, 17, 22]	100[7] (day)	very fast (<4 <i>ms</i> )[29] <1 cycle[26, 28]

Table 2.2: Summarise of the characteristics of the analysed ESS technologies.

in Table 2.1. From there, it can be concluded that there is not any storage technology with a high specific power and at the same time a high specific energy.

The different types of batteries (Lead-acid, NiCd, Li-ion, NaS and the flow batteries) have a relatively high specific energy but a low specific power. On the other hand, the storage technologies of high specific power (SC, Flywheels and SMES) have low specific energy comparing with the batteries. Consequently, if only one storage technology is used, it must be oversized in power or in energy in order to satisfy all the requirements. A battery should be oversized

### 2.3. Comparison of storage technologies

---

from the point of view of the power rating, which will lead to a physically big and economically costly storage system. On the other hand, the storage technologies of high specific power need to be oversized from the energy capacity point of view to satisfy the storage capability requirement [30], leading to a high cost ESS as well.

Furthermore, even if a storage system is able to satisfy both energy and power rating requirements, it should also satisfy the response time specification.

The electrochemical reaction of the flow batteries have a very fast response time, which has been measured to be less than a *ms* [13]. Flow batteries use pumps to move the electrolyte through the stack and consequently the possibility of having a certain reaction rate depends on the flow rate of the electrolyte. At the same time, the flow rate depends on the power supplied to the pumps. Keeping the pumps at maximum power in any case would generate a high amount of losses. Consequently, the flow rate must be adapted for the current absorbed/supplied by the flow battery in order to work always in the optimum point minimising the pumps losses. This way, if the current of the battery is low, the flow rate should be low too. Thus, the reaction time of a flow battery is not defined by the reaction speed, but it is defined by the response time of the pumps and the hydraulic system. Therefore, if a flow battery is operated optimally from the power losses point of view, the response time is slowed down in such a way that it is necessary to use in parallel another system capable of facing fast power variations.

The other types of batteries, i.e. NaS, NiCd, Li-ion and Lead-acid, have fast response times. However, their use to face fast power variations would decrease their cycle life as they would produce overheating of the batteries. Furthermore, a high DOD level has the same negative effect on the durability of the batteries. Consequently, in order to avoid charge-discharge cycles generated by fast power variations and increase the system efficiency, cycle life and also to reduce the power rating, many works suggest the use of a high specific power storage device in parallel with batteries. The use of a complementary storage technologies is especially extended in the field of electric vehicles due



to the importance of volume and weight of the storage system. However, many literature works use a hybrid storage system in grid support applications, mainly for improving RES power integration, using different types of storage technologies: SC and Lead-acid [31], battery and SC [30, 32–38], VRB and SC [39–41], flywheel, VRB and Lead-acid [42] and SMES and battery [43] are some of the examples that can be found in the literature.

This association between two different storage technologies is called HESS [44] and it is usually formed by a short-term storage device and a long-term storage device. An ESS is classified as long-term if it is used to store energy during long periods of time (minutes-hours range) and as short-term if it is used to store energy during short periods (milliseconds-minutes range) and absorb/supply high power [45]. Figure 2.12 shows the classification of different storage technologies according to their power rating and discharge time. This latter characteristic is used to divide the storage technologies between long and short-term groups.

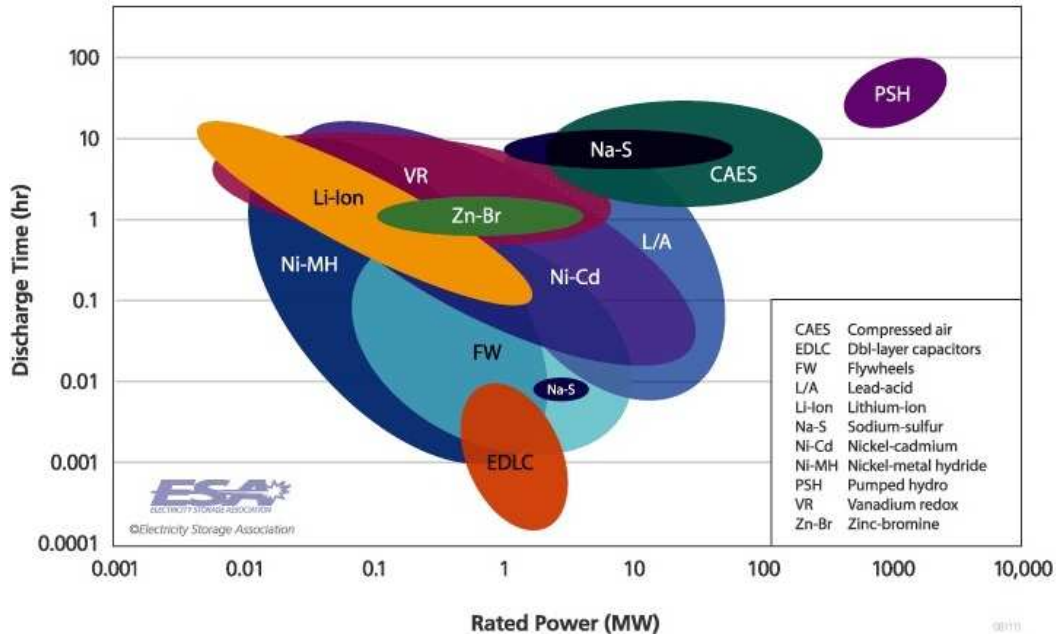


Figure 2.12: ESS classification according to their power rating and discharge time (source: *Energy Storage Association*).

The addition of a short-term storage system alleviates the operating condi-



### 2.3. Comparison of storage technologies

---

tions of the main storage system, prolonging its cycle life and simultaneously allowing to satisfy the power requirements. In addition, the use of a short-term storage system in parallel to a long-term storage one reduces the size and the power losses of the latter storage system [39]. The behaviour of a system when it has a unique ESS (VRB) and when it has a HESS formed by a VRB and a SC is compared in [39]. The results show that for the same wind power profile the maximum power for the VRB in the HESS is less than the half of that in the unique ESS. The VRB depth of discharge is 5-8% less in the HESS and the power losses referred to the storage are also reduced in 15%. In [46] similar results are obtained. The size of a reversible fuel cell and a battery are reduced in 75% and 64% respectively when they are associated creating a HESS, than when they were used as unique ESS.

The selection of the storage technology for the long-term and short-term storage devices is the last issue that must be addressed.

Li-ion batteries have a high efficiency and a relatively small self-discharge. However, their DOD rate highly dependant cycle life is a factor that limits their usability as long-term storage devices. The operation constraint related to the limited DOD rate is especially important in a MG application, as the storage will suffer many charge-discharge cycles with high DOD rates. Lead-acid batteries have the same DOD constraint and furthermore contain environmentally unfriendly materials. Their low life expectancy comparing to other types of batteries and the necessity of periodical water maintenance are other disadvantages for the use of this type of battery in a MG application. In the case of NiCd, their environmentally harmful materials are limiting factors for their use. The new directives that have been approved concerning recycling targets for this type of battery make their future uncertain [18]. NaS batteries are well adapted for high energy rating applications, they have a negligible self discharge and contain environmentally friendly materials. However, the necessity to externally heat the batteries to keep the operational temperature in the required range is their most important disadvantage. In the case of flow batteries, the possibility of easily increasing the storage capacity using

higher tanks and more electrolyte make them highly interesting from the MG application's point of view. Furthermore, their self-discharge is negligible and the efficiency is similar to the one of other types of batteries, which make them interesting for long-term storage applications [19]. In addition, they can be fully discharged with no life expectancy reduction [18]. One of the most important disadvantages of flow batteries is the necessity of pumps to move the electrolytes and the consequent loss of energy. Among the flow batteries, VRB has the highest efficiency and cycle life, and it is considered to be a promising storage technology for RES integration [40, 47–50].

Taking into account that the life expectancy of the batteries Lead-acid, NiCd, NaS and Li-ion is several times smaller than the cycle life of the flow batteries, that they have higher self-discharge rates as well as DOD rate limitations and other operational constraints, in this thesis a VRB flow battery has been selected as long-term storage device.

On the other hand, among the different high specific power and fast response time storage technologies, the SC has been selected. SMES technology has the disadvantage of having to maintain at a low temperature the superconducting coil and the use of a strong magnetic field, which can be harmful for human health. Comparing to flywheels, SC offers an easier installation, no security issues created by a rotating mass, no maintenance costs and much smaller self-discharge.

## 2.4 Modelling of the HESS

The accuracy and the complexity of the dynamic models of the selected storage technologies were defined according to the dynamics that are required to reach the objectives of this thesis. Special attention has been paid on power quality issues, like voltage dips and harmonics, and the power flow control of the HESS, especially the smoothing of energy generated by RES. As the control of the power of the storage devices is carried out using power conversion systems, the *SimPowerSystems* toolbox of *Matlab/Simulink* software has been used.

## 2.4. Modelling of the HESS

---

The simulation of this kind of systems requires a low computational period due to the elevated switching frequency (typically several  $kHz$ ) used by the power converters. Consequently, a simulation time of a few seconds has been used. The modelling process of the selected storage technologies has been carried out according to the specified simulation environment and addressed dynamics. The defined dynamic models have been experimentally validated.

### 2.4.1 Modelling of SC

#### 2.4.1.1 Principle of operation

A SC cell is formed by two electrodes immersed in electrolyte and a separator (Figure 2.13). Each of the electrodes is formed by a metallic current collector and a high surface active material. The porous nature of the electrode creates a high surface in comparison with the surface of classical electrodes, allowing to increase the storage capacity. The separator has a high ionic conductivity and high electronic resistance [51].

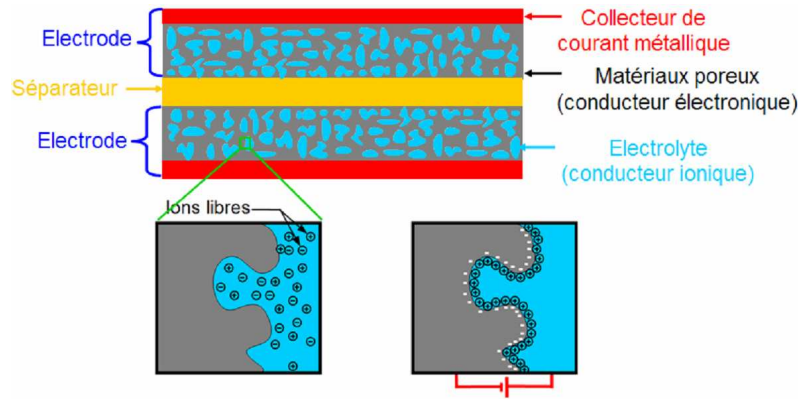


Figure 2.13: Basic structure of a SC cell [51].

Energy is stored in the SC cell as a charge separation in the double-layer (known as Helmholtz Layer) formed at the interface between the electrode material surface and the electrolyte in the micropores of the electrodes. When a DC voltage is applied, the electric double-layer is formed to store electric energy. The double-layer capacitance is proportional to the surface area of the electrode and inversely proportional to the thickness of the double-layer. This

thickness depends on the concentration of the electrolyte and on the size of the ions and it is in the order of some ångströms [52, 53].

The high conductivity of the used materials has as a consequence a very low internal series resistor, allowing to absorb/supply instantaneous high power values [51].

One of the drawbacks of a SC cell is its low voltage level. The electrolyte is the limiting factor for the voltage. An aqueous electrolyte obtains a voltage of 1 V and an organic electrolyte of 2.3-2.8 V. If a higher voltage is applied to a SC cell it will cause the decomposition of the electrolyte. Consequently, a protection system must be used to avoid overvoltages. As the voltage of a SC cell is small, several cells are typically connected in series to obtain a higher voltage and allow the use of the SC in different applications. This series connection makes the overvoltage protection more difficult as the voltage division among cells will not be equilibrated. Thus, a voltage balancing system will be necessary in those cases [54].

### 2.4.1.2 Dynamic modelling and experimental validation

The supercapacitors have been used in many different applications and thus several dynamic models can be found in the literature. A review of those dynamic models is carried out in this subsection in order to identify the model that best fits the defined criteria. A trade-off between accuracy and complexity of the model is carried out taking into account the specifications defined for the dynamic model of the SC.

The characterization of the SC can be carried out in the temporal domain or in the frequency domain [55]. The temporal analysis is based on identifying the parameters of the SC using temporal measurements of the voltage and the current. The frequency analysis is based on Electrochemical Impedance Spectroscopy (EIS), a method to measure the complex impedance of electrochemical cells. EIS is based on introducing an AC current/voltage with a certain DC offset, measuring the output voltage/current and calculating the difference in amplitude and phase between those variables. The frequency

## 2.4. Modelling of the HESS

---

domain models are formed by impedances that approximate the frequency response of a SC for a frequency range between  $mHz$  level to several  $kHz$ .

Frequency domain models require characterisation processes that are more complex than the tests needed to identify the parameters of the time domain models. In addition, taking into account that the dynamic model will be used in the software *Matlab/Simulink* and *SimPowerSystems* toolbox, frequency models of the SC need to be converted to the time domain [56]. Consequently, in this work a time domain model has been used to represent the dynamics of the SC, due to its simplicity, easier characterisation and implementation.

In the time domain models, electric equivalent circuits based on passive elements whose parameters can be adapted to represent the non-linear behaviour of the SC are used. The employed passive elements are typically resistors and capacitors, which are used to represent the Equivalent Series Resistance (ESR) and the capacitance of the SC.

In the literature several equivalent electric circuits can be found, varying from very simple ones to complex dynamic models. The equivalent electric circuits do not represent the real physical system but they are very useful in order to simplify the model: this will simplify both the characterization process and the simulations. One of the most important specifications for the dynamic model is that it must have the smallest possible number of parameters in order to simplify the characterization process, keeping at the same time the desired accuracy.

The simplest dynamic model found in the literature is shown in Figure 2.14. It is formed by a constant capacitor that represents the energy storage capacity of the SC, and the ESR, which represents the resistive losses in the dielectric, plate material, and electrolytic solution. The simplicity of this model makes possible to represent the SC in an easy way and to simplify also the simulations. However, the obtained results are not exact enough to represent adequately the behaviour of a SC: it is a linear model while the SC behaviour is non-linear and dependant on temperature, voltage and frequency. Anyway, this model has been used in different fields due to its simplicity, mainly in hybrid/electric

vehicles but also in RES power smoothing applications [36, 39, 57–63].

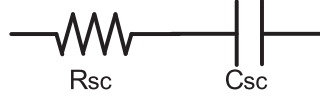


Figure 2.14: Dynamic model of a SC based on constant series connected resistor and capacitor.

Nevertheless, this model does not include the dependence of the capacitance of the SC on the voltage. As the SC will be continuously charged and discharged, from the point of view of the microgrid application it is necessary to take into account the variation of the storage capacity depending on the voltage level. Taking into account this dependency, it will be possible to obtain the proper voltage value at different State-Of-Charge (SOC) levels. In [64] the dependence of capacitance in voltage is included in the dynamic model, as well as a parallel resistor to represent the self-discharge of the SC (Figure 2.15).

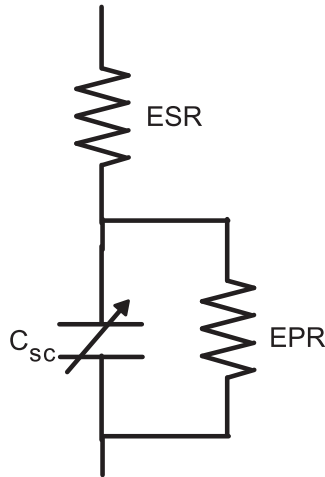


Figure 2.15: Voltage dependent dynamic model.

Other works ([65, 66]) propose a more complicated dynamic model formed by different RC branches, which represent different time constants. The SC is considered to be a capacitance distributed along the volume, with more or less accessible areas. The different branches represent this effect of the SC. Using more branches the accuracy of the model is increased, but the complexity of

## 2.4. Modelling of the HESS

---

the simulation, the number of parameters and in consequence the complexity of the obtaining of those parameters are also higher.

In [65] a dynamic model which has three RC branches is used: the first branch represents the immediate behaviour of the voltage of the SC, in the range of seconds. The second branch represent the behaviour of the voltage in the range of minutes and the third branch covers the time periods higher than 10 minutes. This model represents the SC adequately for time periods smaller than 30 minutes.

As a result of the trade-off between accuracy and complexity of the model, it was decided to use only the fast branch, as the simulation time will be of several seconds and the important part of the SC response from the point of view of this work is the fast one. The voltage evolution due to the charge redistribution that occurs on the SC after a current is applied is not considered to be important in this work. The voltage dependence of the capacitance is taken into account, though. From several research works [51, 65–68], it is clear that the ESR and the capacitance of a SC depend not only in voltage, but also in frequency and temperature. For simplicity reasons, the effect of frequency and temperature on both parameters has been neglected. The temperature has been assumed to be constant and equal to the ambient one. At the same time, the self-discharge is neglected as in the mentioned simulation time its effect will be almost null. The dynamic model used in this work is the one shown in Figure 2.15 but eliminating the parallel resistor used to represent the self-discharge.

The SC unit that has been used in the experimental tests is the *BMOD0083* commercial model of *Maxwell* manufacturer, which is shown in Figure 2.16.

The characteristics of the SC bank as well as the parameters of the dynamic model are shown in Table 2.3, where  $N$  represents the number of series connected SC cells.

The characterisation of the selected dynamic model has been carried out using constant current charge and discharge curves and some impedance measurements at low frequency ( $10\text{ mHz}$ ).



Figure 2.16: SC unit used in the experimental tests.

Parameter	Value
$N$	18
$V_{max}$	48.6 V
$I_{cont}$	61 A
$I_{max}$	1090 A
$P_{rated}$	3 kW
$C_0$	63.157 F
$K_v$	$0.77521 \frac{F}{V}$
$ESR$	7.4 mΩ

Table 2.3: Parameters of the SC unit.

The ESR resistance has been calculated measuring the almost instantaneous voltage variation that appears when the charging current is applied, and dividing this value by the charging current, as shown in eq. (2.1) and Figure 2.17.

$$ESR = \frac{\Delta V}{I_c} \quad (2.1)$$

On the other hand, the dependence of the capacitance on the voltage has been modelled measuring the low frequency impedance of the SC. In the low frequency range the SC behaves as a capacitor and consequently the imaginary part of the measured impedance can be considered completely capacitive. This way, and measuring the impedance at different voltage levels, the relation between capacitance and frequency has been obtained, which is shown in Figure 2.18.

The relation between the capacitance and the voltage is linearised as shown in eq. (2.2). The numerical values of the parameters of the eq. (2.2) are given



## 2.4. Modelling of the HESS

---

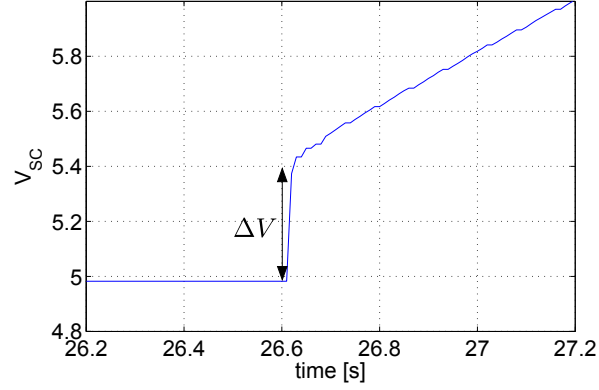


Figure 2.17: Details about the voltage variation measurement used to calculate the ESR.

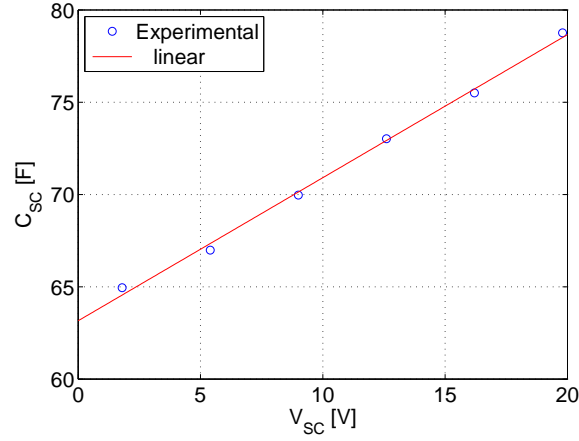


Figure 2.18: Relation between capacitance and voltage of the used SC unit.

in Table 2.3.

$$C_{SC} = C_0 + K_v V_{SC} \quad (2.2)$$

The validation of the dynamic model has been carried out comparing a constant current charge-discharge cycle at two different current levels, 61A as it is the continuous rated current and 122A. The results are shown in Figure 2.19.

From Figures 2.19a to 2.19d it can be seen that the relation between experimental results and the response of the dynamic model is acceptable for the four different charge and discharge cases.

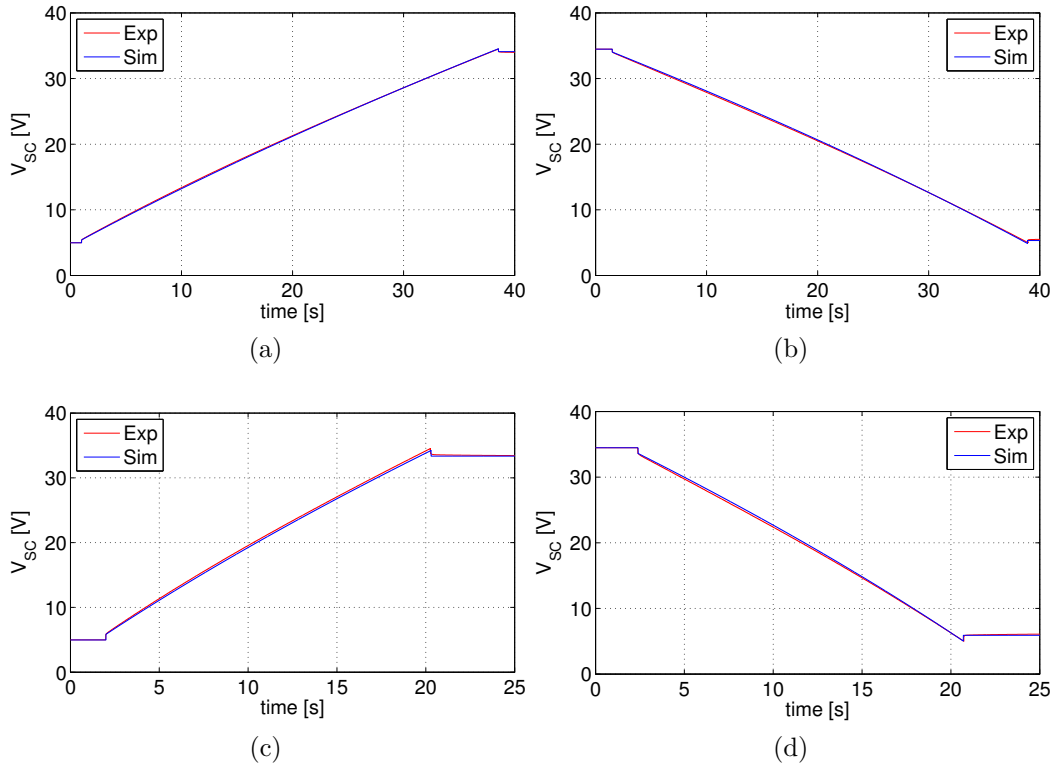


Figure 2.19: Comparison between experimental and simulation results of constant current (a) charging at 61A, (b) discharging at 61A, (c) charging at 122A (d) discharging at 122A.

## 2.4.2 Modelling of VRB

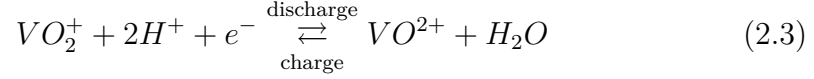
### 2.4.2.1 Principle of operation

Flow batteries are based on a redox or reduction-oxidation reaction. This reaction is based on the transfer of an electron from one species to another. The specie that losses the electron is oxidised and the specie that gains an electron is reduced.

In the specific case of a VRB battery, the oxidation and reduction occur in each side of the membrane in two simultaneous steps. Figure 2.20 shows the simplified diagram of the reactions that occur in the VRB. The vanadium ions  $V^{4+}$  and  $V^{5+}$  (oxidation states +4 and +5) shown in Figure 2.20 are in reality vanadium oxides  $VO^{2+}$  and  $VO_2^+$  respectively. In order to maintain

## 2.4. Modelling of the HESS

the charge balance and stoichiometry, water molecules  $H_2O$  and  $H^+$  protons must be introduced in the cathodic reaction. The reaction of the cathode is shown by eq. (2.3).



The water molecules and protons do not take part in the reaction of the anode, which is shown in eq. (2.4).

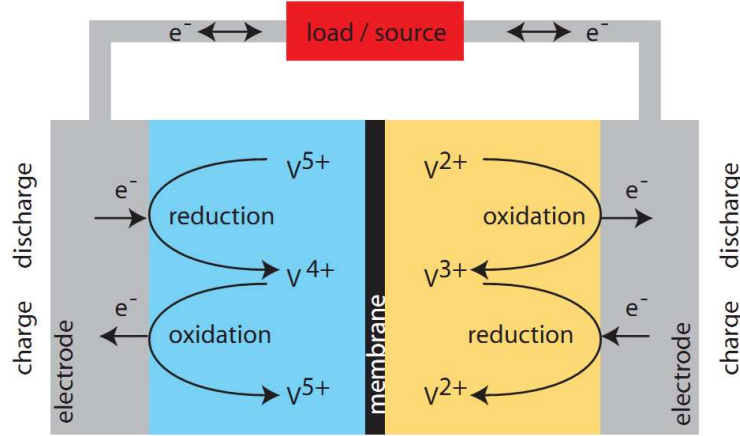


Figure 2.20: VRB reactions during charge and discharge [13].

Consequently, if the battery is completely charged, it will have just  $VO_2^+$  in the catholyte and  $V^{2+}$  in the anolyte. On the other hand if the battery is completely discharged, it will have just  $VO^{2+}$  in the catholyte and  $V^{3+}$  in the anolyte.

The equilibrium voltage of a redox reaction is defined by the Nernst's equation, which depends on the concentrations of the different vanadium oxides,  $H^+$  proton and the standard potential. This voltage represents the Open Circuit Voltage (OCV) of a VRB cell. Knowing that the SOC of a VRB depends on the different concentrations of the vanadium oxides, eq. (2.5) can be represented in function of SOC (as a fraction) using eq. (2.6) [69].

$$E = E^0 + \frac{RT}{nF} \ln \left( \left( \frac{c_{VO_2^+} c_{H^+}^2}{c_{VO^{2+}}} \right)_{catholyte} \left( \frac{c_{V^{2+}}}{c_{V^{3+}}} \right)_{anolyte} \right) \quad (2.5)$$

$$E = E^{0,*} + \frac{RT}{nF} \ln \left( \frac{SOC^2}{(1 - SOC)^2} \right) \quad (2.6)$$

Table 2.4 shows the values of the constants of the Nersnt's equation and Figure 2.21 shows the graphical representation of eq. (2.6).

Symbol	Parameter	Value
$R$	Gas constant	$8.314 \frac{J}{Kmol}$
$T$	Temperature	$298.15 K$
$F$	Faraday's constant	$96.487 \frac{C}{mol}$
$n$	Number of electrons	1
$E^{0,*}$	Cell potential at $SOC = 50\%$	$1.4 V[69]$

Table 2.4: Constants of the Nernst's equation.

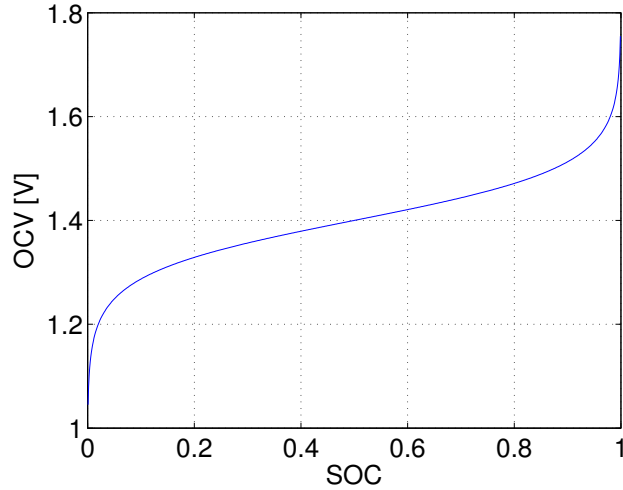


Figure 2.21: Relation between SOC and OCV of a VRB cell.

However, when a current starts to flow through a cell, eq. (2.6) is not valid any more to represent the voltage of the cell. This current will create voltage drops or overpotentials that will make the voltage of the VRB to differ from the one defined by the Nernst's equation.

## 2.4. Modelling of the HESS

---

There are four different overpotentials: activation, concentration, ohmic and ionic overpotentials. The activation overpotential is associated with energy required to initiate a charge transfer. The concentration overpotential occurs when the rate of the electrochemical reaction is sufficiently rapid that the reactant species do not reach the electrode surface or that the product species do not leave the electrode fast enough. The ohmic overpotential is created by the electrical resistance of the electrodes, bipolar plates, collector plates and wires. The resistance of the electrolyte and the membrane to the flow of an ionic current creates the ionic overpotential. The four different overpotentials share a common characteristic: they are all amplified by the current. During the discharge, these overpotentials reduce the available voltage and in consequence the power. Furthermore, they must be compensated during the charge, i.e. an additional voltage has to be applied to maintain the reaction rate [13].

The effect of the overpotentials in the constant current charge-discharge cycles was analysed in [70]. Each charge and discharge current is divided in three stages (A, B and C) as shown in Figure 2.22. In stage A, the changes in the concentrations of vanadium species in the anolyte and catholyte determine the voltage changes of the VRB cell. In stage B, concentration polarization led to dramatic voltage decreases at the end of charge/discharge. The ohmic overpotential dominates the voltage of the cell in stage C.

These overpotentials are created due to several physical phenomena and they depend in variables like the electrolytes composition, the cell geometry, the material and different operating conditions (temperature, flow rate and current). Due to the difficulties to identify each of the overpotentials, their effect is represented using just one parameter. If the temperature and the flow rate of the VRB are assumed constant, those overpotentials can be approximated by a unique equivalent resistance [13]. The use of this series resistance and the OCV defined by the Nernst's equation can be used to represent the voltage of the VRB battery.

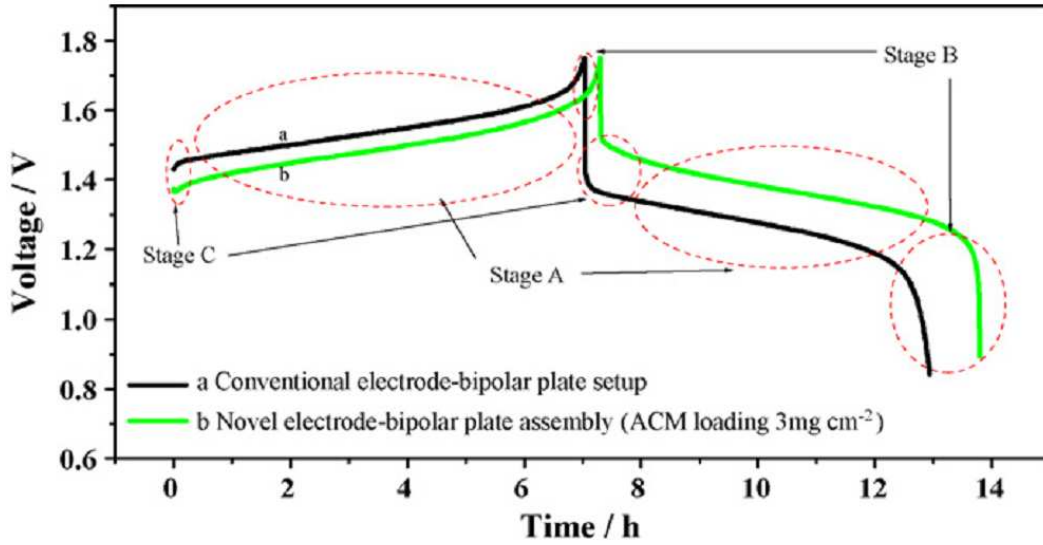


Figure 2.22: VRB cell charge-discharge cycle at constant current divided in three stages [70].

#### 2.4.2.2 VRB model and experimental validation

Once the basic operation of the VRB has been defined, the mathematical representation of those physical phenomena will be analysed, as well as the experimental validation of the selected model.

A short literature review will reveal that there are not many interesting VRB dynamic models from the point of view of this work. One of the dynamic models of a VRB flow battery that has been used in RES power smoothing applications was first presented, to the knowledge of the author, in [71]. The presented dynamic model is shown in Figure 2.23. This dynamic model has been used in different research works [39, 40, 48, 50, 72] where the VRB has been used for wind power smoothing.

The model shown in Figure 2.23 was developed for a specific VRB battery and the characterisation process defined to identify the parameters is not directly applicable for other systems. The identification process is based on the efficiency of the VRB when it is working in rated conditions. The different resistors are calculated using some relations whose validity for other systems cannot be ensured. Consequently, this model has not been used to represent

## 2.4. Modelling of the HESS

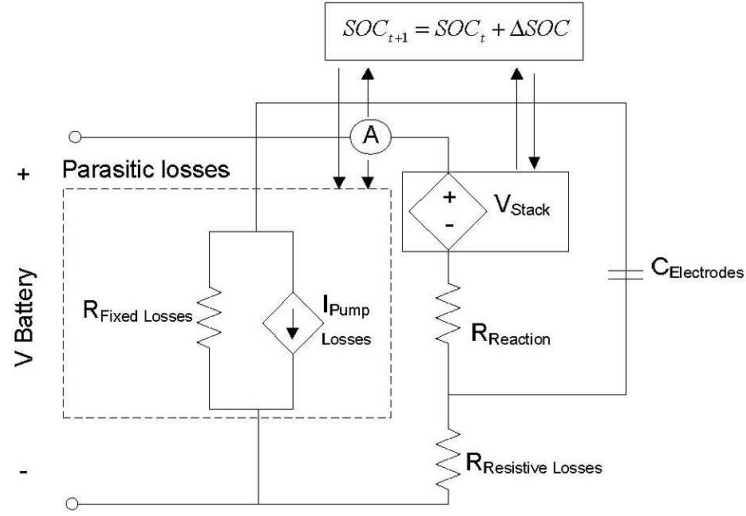


Figure 2.23: Dynamic model of the VRB presented in [71].

the dynamics of the VRB unit used in this thesis.

The VRB used for the experimental tests is a custom-made VRB constructed by *GEFC* manufacturer for *Estia-Recherche* laboratory, which is shown in Figure 2.24. The main characteristics of this experimental unit are shown in Table 2.5, where  $N$  represents the number of series connected VRB cells and  $Q$  indicates the constant flow rate level.



Figure 2.24: VRB unit used in the experimental tests.

Parameter	Value
$N$	20
$V_{rated}$	25 V
$I_{rated}$	50 A
$P_{rated}$	1.25 kW
$t_{rated}$	0.75 h
$P_{pump}$	15 W
$Q$	30-40 $\frac{l}{min}$

Table 2.5: Parameters of the VRB unit used in the experimental tests.

As it was previously explained, the flow rate has a direct effect on the time response of a VRB battery. The flow rate is typically adjusted to the current in each operation point in order to reduce the power losses of the pumps. Consequently, rather than the time of the electrochemical reaction, the reaction time of the pumps and the hydraulic circuit is the limiting factor for the time response characteristic of a flow battery. This time response needs to be modelled in order to represent the behaviour of the VRB in an accurate manner.

In the case of the VRB used in the experimental tests, the pumping system receives power directly from the grid and it is not possible to adjust the supplied power in order to control the flow rate. Consequently, a constant flow rate is used in all operation points.

The first test that was carried out in order to define a dynamic model for the VRB was the measurement of the time needed by the VRB to respond to a power step. Figure 2.25 shows the evolution of the current when a 2.8  $\Omega$  resistance is suddenly connected/disconnected to/from the VRB.

It can be concluded from Figure 2.25 that the response time of the VRB to fast power variations is below 1ms and consequently it will be assumed to be instantaneous for both charge and discharge. These results are logical as the flow rate is maintained at maximum value during the entire operation of the VRB, which ensures the fast response of the battery.

The self-discharge of the VRB due to the losses generated by the crossover



## 2.4. Modelling of the HESS

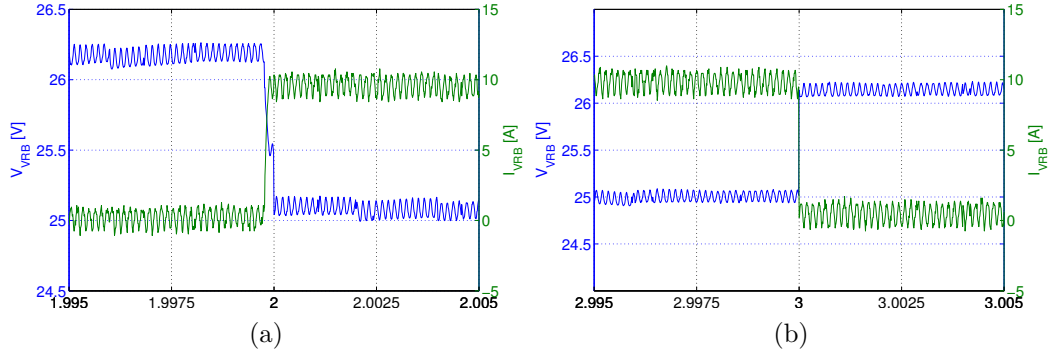


Figure 2.25: (a) Connection and (b) disconnection of the R to/from the VRB.

of vanadium ions across the cation exchange membrane [73] has been measured keeping the pumps working for a couple of hours and the battery in open circuit. The voltage decrease has been measured and then it has been simulated using the parallel resistor  $R_p$  shown in Figure 2.27, which has been estimated to be  $28.5\Omega$ . Figure 2.26 shows the comparison of the experimental and simulated voltage decrease.

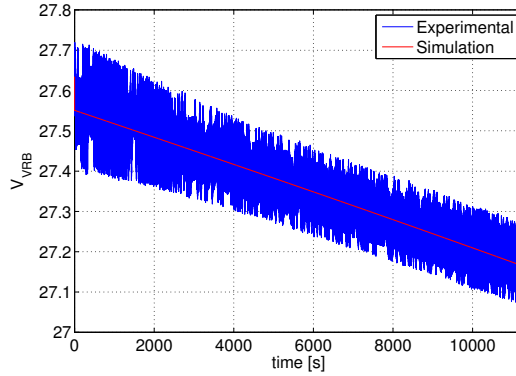


Figure 2.26: Comparison between experimental and simulation behaviour of the self-discharge.

The OCV of a VRB is defined by the Nernst's equation, whose expression is shown in eq. (2.6). The value of the SOC of the VRB is dynamically updated every computational cycle measuring the voltage and the current of the stack, as shown in eq. (2.7).

$$SOC(t) = \frac{\int I_{stack} V_{stack} dt}{E_{nom}} + SOC(0) \quad (2.7)$$

As it was explained in the previous subsection, once a current starts to flow through the battery, the voltage of the VRB differs from the OCV value due to the different overpotentials. According to [74], apart from the series connected resistor, an overpotential should also be used to properly represent the voltage difference created by the current of the VRB. However, [75] proved that this overpotential can be neglected, obtaining a simplified approximation of the overpotentials. Consequently, the different voltage drops have been represented using a constant series resistor, in order to simplify the model.

Therefore, the model of the VRB that has been used in this work is formed by a variable voltage source whose value is defined by the Nernst's equation, a series connected resistor that represents the different overpotentials and a parallel connected resistor that is used to represent the losses due to the crossover of vanadium ions across the cation exchange membrane. Figure 2.27 shows this model.

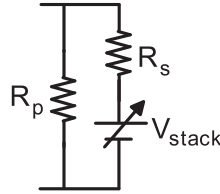


Figure 2.27: Simulation model of the VRB.

The value of the series connected resistor has been obtained comparing the experimental results and the simulation results of a constant current charge-discharge cycle. Two cycles have been carried out, at 30 A the first and at 25 A the second one. In the case of the experimental tests, each cycle has been carried out after a complete discharge of the VRB. Therefore, in the initial point of each charge cycle the SOC has been assumed to be almost 0%, as this value cannot be used. At the same time, the discharge of the VRB has been completed and consequently in the simulations the final value has

## 2.4. Modelling of the HESS

---

been assumed to be near 0% as well. Through the comparison between the experimental and simulation results it has been concluded that the value of the series resistor is different for the charge and discharge cycles. A value of  $75m\Omega$  has been obtained for the charging case and a value of  $78m\Omega$  for the discharge case. Figure 2.28 shows the comparison among experimental and simulation results.

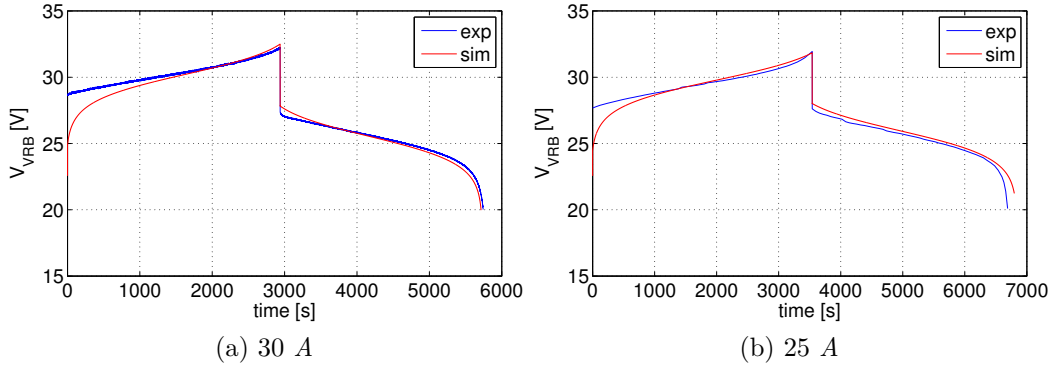


Figure 2.28: Comparison among experimental and simulated charge and discharge cycles of the VRB.

Figure 2.28a shows the comparison between simulation results and experimental tests during a 30 A constant current charge/discharge cycle and Figure 2.28b when a current of 25 A is applied. It can be seen that there are noticeable differences among the charge processes, and that the discharge process relation is better. However, the objective of this thesis has not been to go deep in the modelling of a VRB storage system and consequently the presented model has been used for the sake of simplicity.

According to the results obtained from the experimental tests, the storage capacity of the redox battery is 24.5 Ah. On the other hand, the efficiencies obtained at 30 A and 25 A are 81.8 % and 76.62 % respectively. These efficiency values do not take into account the losses introduced by the pumps.

### **2.4.3 Chapter Conclusions**

In this chapter the benefits of using storage system for grid support application were shortly reviewed. A state-of-the-art analysis of the currently available storage technologies was also presented summarising their most important characteristics and representing them using tables in order to facilitate the comparison. Once the most important characteristics of the main storage systems were analysed, a HESS formed by a SC bank and a VRB flow battery was selected as the best adapted storage system for the microgrid application. Then the modelling of the selected storage technologies was carried out. The presented dynamic modes were experimentally validated.

## **Chapter References**

- [1] J. Eyer and G. Corey. Energy storage for the electricity grid: Benefits and market potential assessment guide. Sandia Report SAND2010-0815, February 2010.
- [2] P. Kundur, N. J. Balu, and M. G. Lauby. *Power System Stability and Control*. McGraw-Hill, January 1994.
- [3] J. M. Eyer, J. J. Iannucci, and P. C. Garth. Energy storage benefits and market analysis handbook. Technical Report SAND2004-6177, Sandia National Laboratories, December 2004.
- [4] D. Sutanto. Energy storage system to improve power quality and system reliability. In *Student Conf. Research and Development SCOReD*, pages 8–11, 2002.
- [5] P.F. Ribeiro, B.K. Johnson, M.L. Crow, A. Arsoy, and Y. Liu. Energy storage systems for advanced power applications. *Proc. of the IEEE*, 89 (12):1744–1756, 2001.
- [6] J. Kueck, B. Kirby, P. Overholt, and M. Lawrence. Measurement practices for reliability and power Quality-A toolkit of reliability measurement

## Chapter References

---

- practices. Technical Report ORNL/TM-2004/91, Oak Ridge National Laboratory, June 2004.
- [7] H. Chen, T. N Cong, W. Yang, C. Tan, Y. Li, and Y. Ding. Progress in electrical energy storage system: A critical review. *Progress in Natural Science*, 19(3):291–312, March 2009.
- [8] M. H. J. Bollen. What is power quality? *Electric Power Systems Research*, 66(1):5–14, 2003.
- [9] G.D. Rodriguez. A utility perspective of the role of energy storage in the smart grid. In *Proc. IEEE PES General Meeting*, 2010.
- [10] D. Casadei, G. Grandi, and C. Rossi. Power quality and reliability supply improvement using a power conditioning system with energy storage capability. In *IEEE Int. Symposium Ind. Electron.*, volume 2, pages 1135–1140, May 2004.
- [11] J.A. Barrado, R. Grino, and H. Valderrama-Blavi. Power-Quality improvement of a Stand-Alone induction generator using a STATCOM with battery energy storage system. *IEEE Trans. Power Delivery*, 25(4):2734–2741, October 2010.
- [12] D. Conolly. *The Integration of Fluctuating Renewable Energy Storage*. Ph.D. dissertation, University of Limerick, December 2010.
- [13] C. Blanc. *Modeling of a Vanadium Redox Flow Battery Electricity Storage System*. Ph.D. dissertation, École Polytechnique Fédérale de Lausanne, 2009.
- [14] S. Vazquez, S.M. Lukic, E. Galvan, L.G. Franquelo, and J.M. Carrasco. Energy storage systems for transport and grid applications. *IEEE Trans. Ind. Electron.*, 57(12):3881–3895, December 2010.
- [15] J. Kaldellis, D. Zafirakis, and K. Kavadias. Techno-economic comparison of energy storage systems for island autonomous electrical networks.

- Renewable and Sustainable Energy Reviews*, 13(2):378–392, February 2009.
- [16] A. Gonzalez, B. Ó Gallachóir, E. McKeogh, and K. Lynch. Study of electricity storage technologies and their potential to address wind energy intermittency in ireland. Technical Report RE/HC/03/001, Sustainable Energy Ireland, May 2004.
- [17] I. Hadjipaschalis, A. Poullikkas, and V. Efthimiou. Overview of current and future energy storage technologies for electric power applications. *Renewable and Sustainable Energy Reviews*, 13(6-7):1513–1522, 2009.
- [18] F. Díaz-González, A. Sumper, O. Gomis-Bellmunt, and R. Villafafila-Robles. A review of energy storage technologies for wind power applications. *Renewable and Sustainable Energy Reviews*, 16(4):2154–2171, May 2012.
- [19] K. C. Divya and J. Østergaard. Battery energy storage technology for power systems-an overview. *Electric Power Systems Research*, 79(4):511–520, April 2009.
- [20] A. Goikoetxea. *Integration of Distributed Generation Using Energy Storage Systems*. Ph.D. dissertation, Mondragon Unibertsitatea, February 2011.
- [21] J. Baker. New technology and possible advances in energy storage. *Energy Policy*, 36(12):4368–4373, 2008.
- [22] P. J Hall and E. J Bain. Energy-storage technologies and electricity generation. *Energy Policy*, 36(12):4352–4355, December 2008.
- [23] K.-L. Huang, X.-G. Li, S.-Q. Liu, N. Tan, and Li-Q. Chen. Research progress of vanadium redox flow battery for energy storage in china. *Renewable Energy*, 33(2):186–192, February 2008.
- [24] T. Shigematsu. Redox flow battery for energy storage. *SEI Technical Review*, (73):5, 2011.

## Chapter References

---

- [25] H. Ibrahim, A. Ilinca, and J. Perron. Energy storage systems—Characteristics and comparisons. *Renewable and Sustainable Energy Reviews*, 12(5):1221–1250, June 2008.
- [26] D. Conolly. A review of energy storage technologies. Technical report, University of Limerick, October 2010.
- [27] B. Roberts. Capturing grid power. *IEEE Power and Energy Magazine*, 7(4):32–41, July 2009.
- [28] H. Beaudin, M. and Zareipour, A. Schellenberglobe, and W. Rosehart. Energy storage for mitigating the variability of renewable electricity sources: An updated review. *Energy for Sustainable Development*, 14(4):302–314, December 2010.
- [29] A. Evans, V. Strezov, and T. J. Evans. Assessment of utility energy storage options for increased renewable energy penetration. *Renewable and Sustainable Energy Reviews*, 16(6):4141–4147, August 2012.
- [30] H. Zhou, T. Bhattacharya, D. Tran, T. Siew, and A. Khambadkone. Composite energy storage system involving battery and ultracapacitor with dynamic energy management in microgrid applications. *IEEE Trans. Power Electron.*, 26(3):923–930, March 2011.
- [31] M.E. Glavin, P.K.W. Chan, S. Armstrong, and W.G. Hurley. A stand-alone photovoltaic supercapacitor battery hybrid energy storage system. In *Proc. 13th EPE-PEMCC Conf.*, pages 1688 –1695, September 2008.
- [32] Z. Guoju, T. Xisheng, and Q. Zhiping. Research on battery supercapacitor hybrid storage and its application in MicroGrid. In *Proc. APPEEC*, pages 1–4. March 2010.
- [33] S. D. G. Jayasinghe, D. M. Vilathgamuwa, and U. K. Madawala. Diode-Clamped Three-Level Inverter-Based Battery/Supercapacitor direct integration scheme for renewable energy systems. *IEEE Trans. Power Electron.*, 26(12):3720–3729, December 2011.

- [34] S. D. G. Jayasinghe, D. M. Vilathgamuwa, and U. K. Madawala. A direct integration scheme for battery-supercapacitor hybrid energy storage systems with the use of grid side inverter. In *Proc. 26th Annu. IEEE APEC*, pages 1388–1393. March 2011.
- [35] S. D. G. Jayasinghe, D. M. Vilathgamuwa, and U. K. Madawala. A new method of interfacing Battery/Supercapacitor energy storage systems for distributed energy sources. In *Proc. IPEC*, pages 1211–1216, 2010.
- [36] M.-E. Choi, S.-W. Kim, and S.-W. Seo. Energy management optimization in a Battery/Supercapacitor hybrid energy storage system. *IEEE Trans. Smart Grid*, 3(1):463–472, March 2012.
- [37] F. Liu, J. Liu, and L. Zhou. A novel control strategy for hybrid energy storage system to relieve battery stress. In *Proc. 2nd IEEE Int. Symposium PEDG*, pages 929 –934, June 2010.
- [38] H. Babazadeh, W. Gao, and X. Wang. Controller design for a hybrid energy storage system enabling longer battery life in wind turbine generators. In *Proc. NAPS*, pages 1 –7, August 2011.
- [39] W. Li and G. Joós. A power electronic interface for a battery supercapacitor hybrid energy storage system for wind applications. In *Proc. 39th Annu. IEEE PESC*, pages 1762–1768, 2008.
- [40] W. Li, G. Joós, and J. Belanger. Real-Time simulation of a wind turbine generator coupled with a battery supercapacitor energy storage system. *IEEE Trans. Ind. Electron.*, 57(4):1137–1145, April 2010.
- [41] C. Abbey, Wei Li, and G. Joós. An online control algorithm for application of a hybrid ESS to a Wind-Diesel system. *IEEE Trans. Ind. Electron.*, 57(12):3896–3904, 2010.
- [42] M. Georgescu, L. Barote, C. Marinescu, and L. Clotea. Smart electrical energy storage system for small power wind turbines. In *Proc. 12th Int. Conf. OPTIM*, pages 1192–1197, 2010.



## Chapter References

---

- [43] T. Ise, M. Kita, and A. Taguchi. A hybrid energy storage with a SMES and secondary battery. *IEEE Trans. Applied Superconductivity*, 15(2): 1915–1918, 2005.
- [44] A. Etxeberria, I. Vechiu, H. Camblong, and J.M. Vinassa. Hybrid energy storage systems for renewable energy sources integration in microgrids: A review. In *Proc. IEEE IPEC*, pages 532–537, October 2010.
- [45] S. Faias, P. Santos, J. Sousa, and R. Castro. An overview on short and long-term response energy storage devices for power systems applications. In *Proc. ICREPQ*, 2008.
- [46] J. D Maclay, J. Brouwer, and G. S Samuelson. Dynamic modeling of hybrid energy storage systems coupled to photovoltaic generation in residential applications. *J. Power Sources*, 163(2):916–925, 2007.
- [47] W. Wang, B. Ge, D. Bi, M. Qin, and W. Liu. Energy storage based LVRT and stabilizing power control for direct-drive wind power system. In *Proc. Int. Conf. POWERCON*, pages 1–6, 2010.
- [48] W. Wang, B. Ge, D. Bi, and D. Sun. Grid-connected wind farm power control using VRB-based energy storage system. In *Proc. IEEE ECCE*, pages 3772–3777, 2010.
- [49] A. Testa, S. De Caro, and T. Scimone. Analysis of a VRB energy storage system for a tidal turbine generator. In *13th European Conf. EPE*, pages 1–10, 2009.
- [50] L. Barote, C. Marinescu, and M. Georgescu. VRB modeling for storage in stand-alone wind energy systems. In *Proc. IEEE Power Tech Conf.*, pages 1–6, 2009.
- [51] W. Lajnef. *Modélisation des supercondensateurs et évaluation de leur vieillissement en cyclage actif à forts niveaux de courant pour des applications véhicules électriques et hybrides*. Ph.D. dissertation, Université Bordeaux 1, 2006.

- [52] R. Kötz and M. Carlen. Principles and applications of electrochemical capacitors. *Electrochimica Acta*, 45(15-16):2483–2498, 2000.
- [53] H. Gualous, D. Bouquain, A. Berthon, and J. M. Kauffmann. Experimental study of supercapacitor serial resistance and capacitance variations with temperature. *J. Power Sources*, 123(1):86–93, 2003.
- [54] R. Kötz, J. C Sauter, P. Ruch, P. Dietrich, F. N. B\Äijchi, P. A. Magne, and P. Varenne. Voltage balancing: long-term experience with the 250 v supercapacitor module of the hybrid fuel cell vehicle HY-LIGHT. *J. Power Sources*, 174(1):264–271, 2007.
- [55] N. Rizoug, P. Bartholomeus, and P. Le Moigne. Modeling and characterizing supercapacitors using an online method. *IEEE Trans. Ind. Electron.*, 57(12):3980–3990, 2010.
- [56] S. Buller, E. Karden, D. Kok, and R.W. De Doncker. Modeling the dynamic behavior of supercapacitors using impedance spectroscopy. *IEEE Trans. Ind. Appl.*, 38(6):1622–1626, November 2002.
- [57] S. Pay and Y. Baghzouz. Effectiveness of battery-supercapacitor combination in electric vehicles. In *Proc. IEEE Power Tech Conf.*, volume 3, 2003.
- [58] A. Etxeberria, I. Vechiu, H. Camblong, and J.-M. Vinassa. Comparison of three topologies and controls of a hybrid energy storage system for microgrids. *Energy Conversion and Management*, 54(1):113–121, February 2012.
- [59] E. Bilbao, H. Gaztanaga, L. Mir, I. Etxeberria-Otadui, and A. Milo. Design and development of a supercapacitor-based microgrid dynamic support system. In *Proc. 13th EPE*, pages 1–10. September 2009.
- [60] E. Ozatay, B. Zile, J. Anstrom, and S. Brennan. Power distribution control coordinating ultracapacitors and batteries for electric vehicles. In *Proc. American Control Conf.*, volume 5, pages 4716–4721, 2004.

## Chapter References

---

- [61] M. Ortuzar, J. Moreno, and J. Dixon. Ultracapacitor-Based auxiliary energy system for an electric vehicle: Implementation and evaluation. *IEEE Trans. Ind. Electron.*, 54(4):2147–2156, 2007.
- [62] M. Pagano and L. Piegari. Supercapacitor flywheel for high power electrochemical sources. In *Proc. 35th Annu. IEEE PESC*, volume 1, pages 718–723, 2004.
- [63] H. Maker. *Optimisation et gestion d’énergie pour un système hybride: association Pile à Combustible et Supercondensateurs*. Ph.D. dissertation, Université de Technologies Belfort Montbéliard, November 2008.
- [64] M. Hadartz and M. Julander. *Battery-Supercapacitor Energy Storage*. Master dissertation, Chalmers University of Technology, 2008.
- [65] L. Zubieta and R. Bonert. Characterization of double-layer capacitors for power electronics applications. *IEEE Trans. Ind. Appl.*, 36(1):199–205, 2000.
- [66] R. Faranda. A new parameters identification procedure for simplified double layer capacitor two-branch model. *Electric Power Systems Research*, 80(4):363–371, 2010.
- [67] F. Rafik, H. Gualous, R. Gallay, A. Crausaz, and A. Berthon. Frequency, thermal and voltage supercapacitor characterization and modeling. *J. Power Sources*, 165(2):928–934, March 2007.
- [68] H. El Brouji. *Prise en compte du vieillissement dans la modélisation des supercondensateurs*. Ph.D. dissertation, Université Bordeaux 1, December 2009.
- [69] T. Sukkar and M. Skyllas-Kazacos. Water transfer behaviour across cation exchange membranes in the vanadium redox battery. *J. Membrane Science*, 222(1-2):235–247, September 2003.

- [70] P. Qian, H. Zhang, J. Chen, Y. Wen, Qi. Luo, Z. Liu, D. You, and B. Yi. A novel electrode-bipolar plate assembly for vanadium redox flow battery applications. *J. Power Sources*, 175(1):613–620, January 2008.
- [71] J. Chahwan, C. Abbey, and G. Joós. VRB modelling for the study of output terminal voltages, internal losses and performance. In *Proc. IEEE Canada Electrical Power Conf.*, pages 387–392, 2007.
- [72] Z. Chen, M. Ding, and J. Su. Modeling and control for large capacity battery energy storage system. In *Proc. 4th Int. Con. Electric Utility Deregulation and Restructuring and Power Technologies*, pages 1429–1436. July 2011.
- [73] D. You, H. Zhang, C. Sun, and X. Ma. Simulation of the self-discharge process in vanadium redox flow battery. *J. Power Sources*, 196(3):1578–1585, February 2011.
- [74] M. Skyllas-Kazacos and C. Menictas. The vanadium redox battery for emergency back-up applications. In *Proc. 19th Int. Conf INTELEC*, pages 463–471. October 1997.
- [75] M. Schreiber, A.H. Whitehead, M. Harrer, and R. Moser. The vanadium redox battery - an energy reservoir for stand-alone ITS applications along motor and expressways. In *Proc. IEEE Intelligent Transportation Systems*, pages 391–395, September 2005.

# Power electronics topologies and the associated control for interfacing the HESS with a microgrid

---

## Contents

<b>3.1 Literature survey . . . . .</b>	<b>72</b>
<b>3.2 Comparison among topologies . . . . .</b>	<b>80</b>
3.2.1 Parallel DC-DC converters topology . . . . .	84
3.2.2 Floating topology . . . . .	96
3.2.3 3LNPC topology . . . . .	97
<b>3.3 Simulation Results . . . . .</b>	<b>100</b>
3.3.1 First case study . . . . .	103
3.3.2 Second case study . . . . .	107
<b>3.4 Results discussion . . . . .</b>	<b>113</b>
<b>3.5 Chapter conclusions . . . . .</b>	<b>114</b>
<b>Chapter References . . . . .</b>	<b>115</b>

---

This chapter is oriented to analyse the different adequate topologies that could be used for controlling the power flow of a HESS formed by a SC bank and a VRB flow battery in a MG context. First of all, a literature survey is carried out to identify the most important topologies that were selected in different research works. Three main topologies are identified and then they are compared in similar conditions to stress the advantages and disadvantages of each one. This comparison has been carried out by means of simulations.

From the results of the comparison, the 3LNPC topology is selected as a promising solution to control the power flow of a HESS with the objective of supporting the operation of a MG and of improving its power quality.

### 3.1 Literature survey

An ESS can introduce many benefits in a MG, as it was analysed in Chapter 2. However, this affirmation only holds if the power flow of the storage system is controlled in such a way that the defined specifications are satisfied. The control of the power flow of an ESS is carried out using power converters, which are used as interfaces between the storage systems and the microgrid.

The power converters are energy conversion systems that allow carrying out this conversion process in a controlled manner. Power converters are mainly formed on the one hand by power semiconductor components (as for example different types of transistors, thyristors and diodes), and on the other hand by passive components (capacitors and inductors). The most well known types of power converters are rectifiers, choppers or DC-DC converters and inverters. They can work in one, two or four voltage/current quadrants according to the configuration of the converter. The operation of the power converters is based on the conduction of the semiconductor devices, which can be controlled or not.

Power converters can be classified according to the energy type conversion that they perform: DC-DC, AC-DC or DC-AC. Taking into account that the selected storage devices have a DC voltage, only DC-DC or DC-AC power converters can be used in the application analysed in this thesis. Furthermore, the required power converter also needs to be able to allow bidirectional power flow, as a storage device can supply but also absorb energy. The selection of the power conversion system must take into account the particularity of each application and must be done according to the advantages and disadvantages of each alternative.

The most important drawback of a power converter is the power loss ratio

### 3.1. Literature survey

---

that it introduces. The power losses of a power converter can be classified in three main groups: switching losses, conduction losses and blocking losses. More details about the power losses of a semiconductor component can be found in Appendix A. Another disadvantage associated with power converters is the harmonics of output waveforms due to the commutation process that is performed to generate them, which has a negative impact on the THD. The cost can be also another limiting factor for the utilisation of a power converter. Each power conversion system offers better or worse characteristics, and consequently a trade-off between these advantages and disadvantages must be carried out to determine the best solution for each specific case.

Due to the necessity of using more than one storage technology in order to satisfy the requirements of the microgrid application, many different power conversion systems can be used creating different topologies for the application investigated in this work.

A literature review has been carried out to determine which are the topologies that have been proposed in several research works. The final objective of this survey has been to determine which is the topology that is best adapted to integrate the HESS proposed in this thesis in a microgrid. The literature review allows concluding that the use of a HESS in a MG application is not extended. Their use is much more extended in the electric vehicles field, due to the pulsed load profile and the problems that it creates in the life cycle of batteries. At the same time, the low specific energy of batteries can create mass and/or volume problems, as they should be oversized to satisfy the power requirements. Consequently, the use of a high specific power storage system in parallel to a battery is extended in electric vehicles in order to smooth the current and reduce the current peaks to prolong the life expectancy of the batteries and reduce their size and mass. Therefore, the literature review will take into account the works that have been published in the last years in the microgrid field, but also in the electric vehicles application.

Analysing the papers that use a hybrid storage system [1–30], the following classification of the topologies has been concluded:

### Chapter 3. Power electronics topologies and control for HESS

---

- Passive topology [1, 2]
- Active topology
  - Series topology [3]
  - Floating topology [4–15]
  - Parallel topology [16–27]
  - 3LNPC topology [28–30]

In [1, 2] the two ESSs (a battery and a SC bank) are connected directly in parallel, using a passive configuration (Figure 3.1). Although some of the benefits of a HESS are also obtained in such a simple topology, the storage system capabilities are not completely harnessed. The current is divided between the two devices depending on the internal impedances. Therefore, the power flow of the system cannot be controlled. On the other hand, the voltage is the same for the battery and the SC. Due to this, if a high fast current is required, the SC as well as the battery will react, and not just the SC as it would be preferable. The passive topology does not allow to harness all the advantages that a HESS can provide. The fact of having the same voltage in the long-term and the short-term storage devices also limits the selection of the array size of the SC bank, because they must have the same voltage. Furthermore, this voltage cannot be controlled and it varies according to the SOC of the battery and the SC. Using a power converter as interface for the SC permits to actively control its power flow, and consequently an energy management algorithm can be designed and applied. The SOC of the SC can be controlled and it can be charged or discharged until the selected value with no limitation introduced by the battery. The topologies that use a power converter to control the power flow of at least one storage device are classified as active topologies.

A comparison between the passive and active topologies is carried out in [5–7]. In [5], the two configurations are compared by means of simulations. The results show that using a power converter the peak current of the battery



### 3.1. Literature survey

---



Figure 3.1: Schematic representation of the passive topology.

is reduced in 40%, the DC bus voltage control is improved in 30% and the SC characteristics are better harnessed. In [6], simulation and experimental results show that the specific power of the active HESS is 3.2 times higher than the passive one and that the battery current is drastically decreased, obtaining a much more stable DC bus voltage. In [7] it is shown that using a power converter the same life time extension as in the direct connection of battery-SC can be achieved, but with the half quantity of SC cells.

Hence, the utilisation of more than one ESS requires a power converter to directly control the power flow of at least one storage device, which will allow to optimise the system. In the literature, several types of active topologies can be found, namely series, floating, parallel and 3LNPC topologies.

The series connection of both storage technologies is not usual, but some works, like [3], have analysed the feasibility of this type of topology. The series connection, which is schematically shown in Figure 3.2, allows a simplification in the architecture of the system and reduces the cost of the short-term storage device. This is because it does not need a high voltage in the DC bus and, therefore, just few SC cells can be used. However, the power distribution of the system is limited as it cannot be divided between the two ESS. The regenerated power is completely absorbed by the SC and the battery cannot be charged using it. The series connection reduces the flexibility and the power capacity of the system. As a consequence, it is not well suited for the MG application.

This way, most of the reviewed works use a parallel structure for the connection of the two storage technologies. According to the specifications of the application, the selected topology is different. In some cases, the direct control of both ESS is necessary because their SOC have to be controlled. In

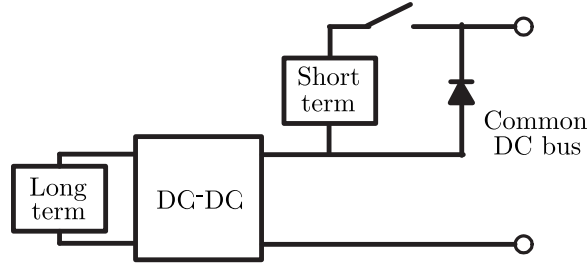


Figure 3.2: Schematic representation of the series topology.

those cases, it is necessary to use a DC-DC converter for each storage device, i.e. the parallel topology (Figure 3.3). In that configuration, the power flow of each ESS can be independently controlled. In other cases, the application is not so demanding and the long-term storage can be directly coupled with the DC bus, creating a floating topology (Figure 3.4).

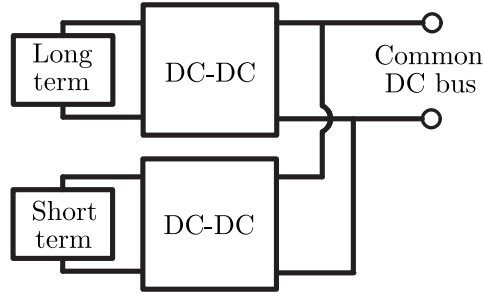


Figure 3.3: Schematic representation of the parallel topology.

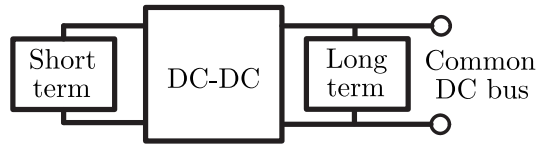


Figure 3.4: Schematic representation of the floating topology.

In the case of the floating topology, in almost all research works the short-term storage device is connected using a power conversion system to the DC bus. However, in [6, 7, 13, 14] the power conversion system is used to control the power flow of the long-term storage device, while the short-term storage system is directly connected to the DC bus. In the mentioned works a battery is used as long-term storage device and a SC bank as short-term storage

### 3.1. Literature survey

---

device. This topology is able to reduce the current demand for the battery and thus to prolong its life cycle. Its main drawback is that the SC has a low voltage and consequently it requires the connection of many SC cells in series to obtain a high DC bus voltage, as many as 120 in [13]. This will require a voltage balancing system, as an overvoltage can severely damage a SC cell. Furthermore, the operation of the HESS is limited to the voltage of the SC, as the inverter needs a certain DC bus voltage to be able to operate properly connected to the rest of the AC bus. Even if the SC is oversized from the energy storage capacity point of view, as its specific energy is low the voltage could have severe variations and the battery must be used to overcome this problem, as it can be clearly seen in the control strategies of [6, 14]. This limits the flexibility that the floating topology can offer to the application. In [6] during the on interval of the pulsed load current, the SC voltage and consequently the load voltage experiments a decrease of 27%, which can be a problem if the load is sensitive to the voltage level that it should have. In the case of the MG application, as an inverter is used like the interface between the common DC bus and the rest of the microgrid, the DC bus voltage must be inside a certain limit to ensure the proper operation of the system.

Consequently, the floating topology where the long-term storage device is directly linked to the DC bus and the short-term storage technology is controlled by the power converter (Figure 3.4) is better adapted from the point of view of the MG application. This is the topology used in [5, 10–12] (SC bank and Lead-acid battery), [9, 15] (SC bank and Li-ion battery), [4] (SC bank and VRB flow battery) and [8] (SMES and a battery). As in the previous floating topology, the voltage of the DC bus will vary according to the SOC of an ESS, which in this case is a long-term one. This voltage must be maintained inside a certain range if the application requires so, as for example in [4] where the inverter needs the DC bus voltage to be inside a range to operate properly. The advantage of connecting a high storage capacity ESS to the DC bus is that the voltage variations will be much smaller than when a short-term ESS is used. Comparing to the parallel topologies, where each

storage device is interfaced by a power converter, the floating topology has the advantage of having reduced power losses due to the elimination of one of the power converters. The negative side of this is that the operation of the system is limited as the SOC of the long-term storage system is limited to the fixed DC bus voltage range and the power flow of the floating ESS is not directly controllable.

In [8] it is shown that a unique power converter, used as interface for the short-term storage device (a SMES), together with an adequate energy management algorithm is able to maintain the SOC of both storage devices inside the given ranges. However, the voltage of the DC bus varies according to the SOC of the battery, which can be a problem for some applications. The direct connection of a long-term storage device to the common DC bus can have as a consequence the necessity of connecting many cells in series to obtain the desired voltage level. At the same time, it might be necessary to increase the energy storage capacity of the device connected to the DC bus in order to reduce the voltage variations, comparing to the capacity necessary in the parallel topology.

The papers [16–27] present a HESS where both storage devices have a DC-DC converter as interface, creating a parallel topology (Figure 3.3). The storage technologies that are used in the mentioned papers are a battery and a SC bank in [21–23, 26], flywheel, VRB and a Lead-acid battery in [25], a Lead-acid battery and a SC bank in [24] and a VRB flow battery and a SC in [18]. The fact of using a DC-DC converter with each storage device allows to control the power flow of each ESS independently. This way, the control algorithm of the HESS is less limited and has a higher flexibility. Comparing to the operation of the floating topology, in the parallel topology the DOD rate of the used storage technologies is not limited as the DC bus voltage does not depend on the SOC of one of the ESS. Consequently, the ESS can be discharged more deeply and their energy storage capacity is better harnessed.

Finally, another topology presented in the literature to control a HESS is the one which uses a 3LNPC converter [28–30]. Both storage devices are used

### 3.1. Literature survey

---

as the two input voltage sources of the converter, as it is shown in Figure 3.5. From a microgrid point of view, one of the most important advantages of this topology is its ability to control the power flow of a HESS through just one power converter. In the case of the other types of topologies that were analysed, the DC bus voltage is used to connect the HESS and then an inverter is used to interface the HESS to the rest of the microgrid. From the point of view of the DG applications, the fact of having an integral solution of the power conversion system of the HESS is especially interesting as the system will need to be installed in several locations. This novel topology takes advantage of the possibilities of a three-level converter to reduce the number of power converters, reduce the power losses and increase the THD comparing to the systems where a typical two-level inverter is used. As for the same DC bus voltage the voltage applied to each semiconductor device in a 3LNPC converter is the half of the voltage applied in a two-level inverter, the power losses obtained by a 3LNPC converter are smaller for the same switching frequency and operating conditions. At the same time, as the three-level converter uses three DC bus voltage levels, the output AC signals have a better THD [31].

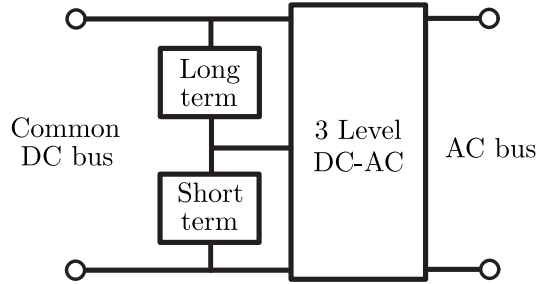


Figure 3.5: Schematic representation of the 3LNPC topology.

The different literature research works that have been analysed propose different topologies for applications that can be grouped in mobile applications (pulsed loads, hybrid electric vehicles, railways, etc.) and microgrid applications (WT and/or PV power smoothing, etc.).

In the case of mobile applications, the mass is a characteristic that must be taken into account as it will have a direct effect on the energy consumption

of the vehicle. The mass of the hybrid storage system must be minimised, and consequently most of the analysed papers that treat this subject propose to employ a floating topology in order to eliminate one power converter [5–12, 15]. At the same time, this simplification will reduce also the volume, which is also important in mobile systems. The number of research works of mobile applications that use a parallel topology is considerably smaller: [19, 20, 22, 27].

In stationary applications, as a general rule, the mass and volume cannot be considered as limiting factors. This way, most of the reviewed research works of this field use a parallel topology due to the higher flexibility of the control system and better utilisation of the energy capacity of each ESS [16–18, 21, 23, 25]. However, there are also works that use a floating topology for a microgrid application: [4, 13, 14].

Although several works propose different topologies and they justify their selection using different arguments analysed in the previous paragraphs, none of them makes a comparison between the different topologies to justify their choice. Consequently, in this work a comparison among the three most important topologies from the point of view of the MG application has been carried out by means of simulations.

## 3.2 Comparison among topologies

From the analysis carried out in Section 3.1, three topologies were selected as the most interesting ones to control a HESS in a microgrid context: the floating, parallel and 3LNPC topologies.

In this section the details of each topology, their control structure and the simulation context that has been used to carry out the comparison among them are presented. The mentioned simulation context, which is shown in Figure 3.6, represents some of the issues that appear in a microgrid application.

The investigated system is formed by six parts: energy generation, storage system and power converter interface, line emulators, resistive loads and finally

### 3.2. Comparison among topologies

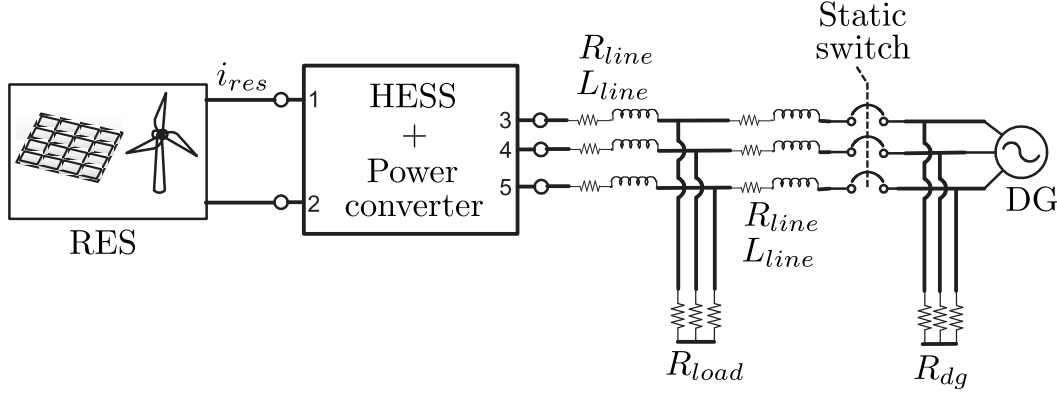


Figure 3.6: Simulation system used to compare the selected power electronics topologies.

a diesel generator. Firstly, the energy generated by different RES has been simulated as a variable DC current source [32, 33], which is directly injected in the DC bus of the HESS, in order to simplify the complexity of the simulation model. Secondly, the storage system and the selected power conversion system are represented by a block that carries out the interconnection between the DC bus and the AC bus of the simulated microgrid. Thirdly, different electric power transmission lines are used to take into account the effect of the grid-lines. Finally, a diesel generator is used as the element that fixes the main weak grid. In a microgrid, auxiliary generators are often used in parallel to the storage system to provide certain autonomy in order to allow the islanding operation. These auxiliary generators are used to provide energy when the generation of the RES and the capabilities of the storage system are not enough to satisfy the power requirements of the loads. The diesel generator is based, as it has been previously explained in Chapter 1, on a diesel motor and a synchronous generator. The hybrid storage system is connected or disconnected from the diesel generator using a static switch. Two resistive loads are connected in each side of the static switch.

Two different case studies have been defined to analyse and compare the behaviour of the selected topologies. On the one hand, the effect of the HESS on the smoothing of the energy injected by RES is analysed while the storage

system is interconnected with the diesel generator and both generation systems are used to satisfy the power requirements of the loads. On the other hand, the disconnection of the HESS from the diesel generator is analysed. In this second case study the HESS will have to transit from the grid-connected mode to the isolated mode. One of the disadvantages of the diesel generators is that their efficiency considerably decreases if they do not work at the rated power. Consequently, according to the operating conditions, this disconnection is a routine event that a HESS must be able to handle.

The comparison has been carried out taking into account several aspects, which are summarised below:

- **Power losses:** The power losses of any semiconductor component can be classified in three groups: conduction losses, switching losses and blocking losses. The conduction losses are also named as on-state losses and they refer to the power losses generated by the voltage drop of the semiconductor device and the current flowing through it. The blocking losses, on the other hand, refer to the off-state or leakage losses. As the leakage current is small, these losses are typically neglected. Finally, the switching losses refer to the energy that is lost during the turn-on and turn-off transitions. More details about the power losses of a power converter and how they have been calculated in this work can be found in [Appendix A](#).
- **THD:** It represents the harmonic distortion, which is measured by the relation between the harmonic components and the fundamental component as shown in eq. (3.1).

$$THD = \frac{\sqrt{\sum_{i=2}^{\infty} U_i^2}}{U_1} \quad (3.1)$$

- **Flexibility of the control system:** The flexibility of the control system is the last characteristic that is analysed. As the flexibility is an ambiguous concept, it is necessary to clearly specify what it is referring



### 3.2. Comparison among topologies

---

to in this comparison. The flexibility of the controller refers to the possibilities that the control system has to divide the power between the VRB and the SC taking into account the technical limitations of the different topologies due to their structure. For example, while in the parallel topology it is possible to directly control the DC bus voltage, in the floating or 3LNPC topologies it directly depends on the SOC of the ESS. Consequently, from the point of view of the control of the DC bus voltage the control system has a higher flexibility in the parallel topology than in the floating one. Special attention has been given to the flexibility of the control system to divide the power between the SC and the VRB. As it has been previously explained, the VRB will be used as a long-term storage device, to provide autonomy to the MG. The SC will be used to face high fast power variations.

Even if the characteristics of each of the analysed topologies are different, similar operating conditions have been defined in order to obtain comparable results. The selected simulation context uses the standard  $230 V_{RMS}$  value for the AC side voltage. The DC bus voltage selection has been carried out taking into account the limitations of the 3LNPC topology. As it is explained in detail in Chapter 4, the DC bus voltage has a direct effect in the possibility of dividing the power between the SC and the VRB. From this analysis, a DC bus voltage of  $900 V$  has been selected instead of the typical  $700 V$  one. Go to Section 4.5 to obtain more details about this.

Due to the necessity of measuring the power losses, the switching effect of the power converters cannot be avoided and average dynamic models cannot be used. Consequently, the computational step must be low enough to well represent the switching effect, which slows down the simulations. Due to this time limitation, the profile of RES power that has been used during simulations has been created based on a average current component and different variations that have been used to test the ability of each topology to divide the power between the SC and the VRB. The frequencies of these variations have been selected according to the mentioned time limitation. The obtained simulation

results will be completely representative of what would happen in a real system with the power variations coming from WT and PV panels, as the only difference would be the frequency of the variations. This profile can be found in the simulation results shown in Section 3.3.

Finally, classical control algorithms based on two-loop Proportional-Integral (PI) regulators were used to control the different power converters. The main objective of the control algorithm is the same in all topologies: to divide the power variations of the system into two parts depending on their frequency. The low frequency part is absorbed/supplied by the VRB and the high frequency part by the SC. Low pass filters were used to divide the power variations according to their frequency between the SC and the VRB.

The following three subsections show the details of each topology and their control structures.

### 3.2.1 Parallel DC-DC converters topology

This topology is based on the use of parallel bidirectional DC-DC converters to control the power flow of each storage device. The structure of this topology is shown in Figure 3.7.

The employed DC-DC converter is formed by two Insulated Gate Bipolar Transistor (IGBT), which allows to have bidirectional power flow. Each storage device can be independently controlled, and consequently individual control algorithms can be applied. Therefore, the control system of the parallel topology has the highest flexibility among the three analysed topologies. Both DC-DC converters are connected to the common DC bus and a capacitor  $C_{bus}$  is used in each DC-DC converter to smooth the DC bus voltage ripple. Then a typical two-level DC-AC bidirectional converter is used to generate the AC side  $230 V_{rms}/50Hz$  voltage. An inductance-based first-order low pass filter is used to filter the high frequency harmonics introduced by the converter switches.

### 3.2. Comparison among topologies

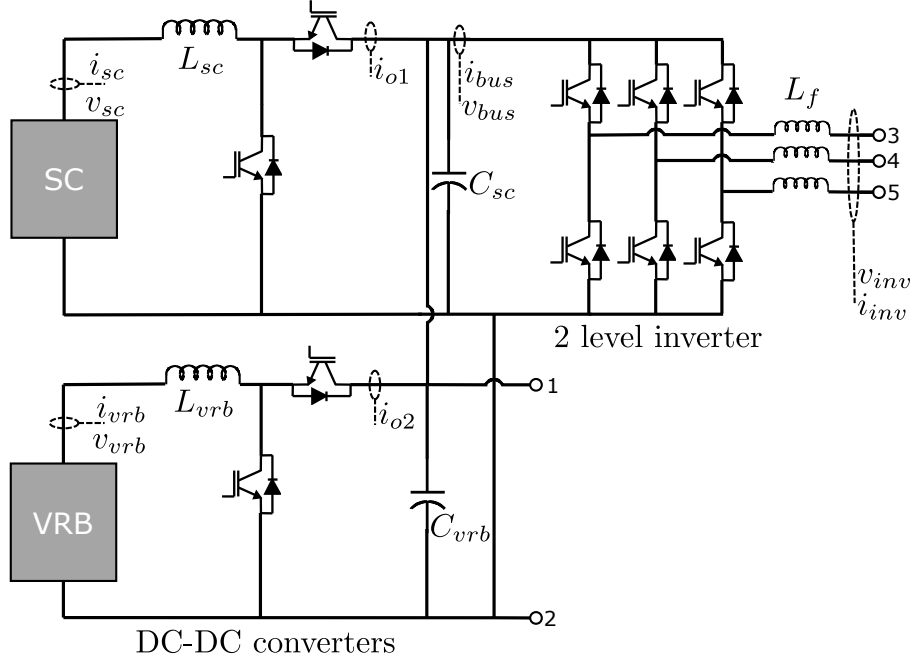


Figure 3.7: Parallel DC-DC converters topology.

#### 3.2.1.1 Control algorithm of DC-DC converters

Each DC-DC converter is controlled to fulfil a different objective. The main goal of the control system is to divide the power injected/absorbed by the HESS between the SC and the VRB according to its frequency. High frequency variations must be faced by the SC and low frequency variations by the VRB. As in the parallel topology the power flow of each storage device can be independently controlled this objective is easily satisfied.

The SC bank is used to keep the DC bus voltage at the fixed reference value. This is obtained using a two-loop PI-based control system, as it is shown in Figure 3.8. The inner loop is used to control the current of the SC and the outer loop to keep the DC bus voltage constant.

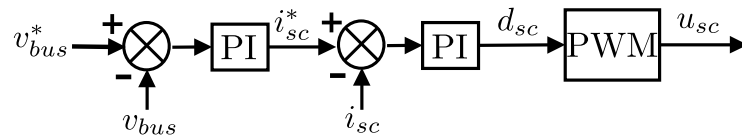


Figure 3.8: Two-loop control of the DC-DC of the SC storage system.

The two-loop based  $PI$  control of the DC-DC converters have been designed through the well-known averaging method. If the switching frequency is assumed to be much higher than the main dynamic of the system, then the high frequency modes of the converter can be avoided and it can be represented by the average model [34]. Applying the average modelling to the DC-DC converter shown in Figure 3.7 the averaged system shown in eq. (3.2) can be obtained.

$$\begin{aligned}\frac{dv_{bus}}{dt} &= -\frac{i_o}{C} + \frac{di_L}{C} \\ \frac{di_L}{dt} &= \frac{v_{ess}}{L} - \frac{dv_{bus}}{L}\end{aligned}\tag{3.2}$$

The eq. (3.2) are clearly non-linear (the input  $d$  is multiplying a state variable in both cases) and coupled. The analysed system has three inputs, the voltage of the storage system  $v_{ess}$ , the current of the DC bus side of the converter  $i_o$  and the duty cycle  $d$ . Two state variables are selected in order to define the state space representation of the DC-DC bidirectional converter, the current of the inductor  $i_L$  and the voltage of the DC bus capacitor  $v_{bus}$ . As eq. (3.2) is non-linear, they are linearised around an operation point in order to obtain a transfer function that relates the selected input and output that can be used afterwards to design the regulators. During the linearisation process, the three inputs have been kept and the state-space system shown in eq. (3.3) has been obtained. In the selected operation point a duty cycle of  $D = 0.5$ , an inductor current of  $I_L = 0\text{ A}$  and a DC bus voltage of  $900\text{ V}$  have been selected.

$$\begin{bmatrix} \frac{d\tilde{v}_{bus}}{dt} \\ \frac{d\tilde{i}_L}{dt} \end{bmatrix} = \begin{bmatrix} 0 & \frac{D}{C} \\ -\frac{D}{L} & 0 \end{bmatrix} \begin{bmatrix} \tilde{v}_{bus} \\ \tilde{i}_L \end{bmatrix} + \begin{bmatrix} -\frac{1}{C} & \frac{I_L}{C} & 0 \\ 0 & -\frac{V_{bus}}{L} & \frac{1}{L} \end{bmatrix} \begin{bmatrix} \tilde{i}_o \\ \tilde{d} \\ \tilde{v}_{ess} \end{bmatrix}\tag{3.3}$$

However, it is necessary to assume two of the inputs null in the linearised model in order to obtain a transfer function. In this case, the inputs  $v_{ess}$  and  $i_o$  are assumed to be null and only the duty cycle  $d$  has been used. Taking as

### 3.2. Comparison among topologies

---

output the variations of the current of the inductance  $\tilde{i}_L$ , the transfer function shown in eq. (3.4) can be obtained, which is used to design the PI controller of the inner current loop using the *rltool* function of *Matlab*. This inner loop PI controller has been designed to have a settling time of 2 ms and no overshoot.

$$\frac{\tilde{i}_L}{\tilde{u}} = \frac{-V_{bus}Cs - DI_L}{LCs^2 + D^2} \quad (3.4)$$

Then, knowing that the expression of a PI controller is the one shown in eq. (3.5) and substituting it in the linearised system, the transfer function between the DC bus voltage  $\tilde{v}_{bus}$  and  $\tilde{i}_L^{ref}$  can be obtained (refer to eq. (3.6)).

$$u_{PI} = (K_p + \frac{1}{T_i s})(\tilde{i}_L^{ref} - \tilde{i}_L) \quad (3.5)$$

$$\frac{\tilde{v}_{bus}}{\tilde{i}_L^{ref}} = \frac{I_L L K_p T_i s^2 - (DV_{bus} K_p T_i - I_L L)s - DV_{bus}}{CLT_i s^3 - CV_{bus} K_p T_i s^2 - (I_L D K_p T_i + CV_{bus} - D^2 T_i)s - I_L D} \quad (3.6)$$

This transfer function have been used to design the outer DC bus voltage controller, using the *rltool* function as in the previous case. The outer loop PI has been designed to have a settling time of 10 ms and no overshoot.

On the other hand, the control of the VRB has a unique loop to control the current of the battery. This control loop has been designed following the same steps as in the case of the DC-DC converter of the SC. The reference of the VRB current is generated by a low-pass filter system, which has a cut-off frequency of 10 rad/s. This reference signal is generated mainly by the low-frequency part of the power required by the load of the inverter: the power through the inverter is filtered and the low frequency part is used as a part of the reference signal. The other part is generated by a PI controller in order to maintain at 0 A the average current of the SC. The PWM is used to generate the switching signals. The control structure of the DC-DC of the VRB is shown in Figure 3.9.

#### 3.2.1.2 Control algorithm of the two-level inverter

The control of the two-level inverter used to interconnect the HESS with the rest of the microgrid has been carried out through the averaging method, as

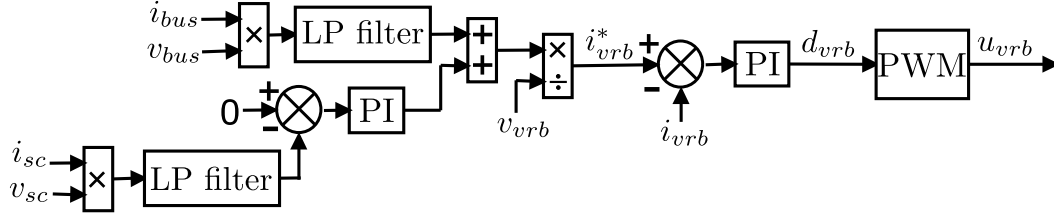


Figure 3.9: Control structure of the DC-DC of the VRB.

in the control design process of the DC-DC converters. The HESS can work connected or disconnected from the weak grid fixed by the diesel generator and consequently the control of the inverter must be adapted for each operation mode. When the HESS is operating in grid-disconnected mode, the inverter fixes the AC side voltage/frequency in order to feed the loads with the standard voltage characteristics. In the second case, when the HESS is connected to the diesel generator, this latter generation system fixes the three-phase voltage of the microgrid. Consequently, in the grid connected mode the active and reactive power injected by the inverter are the controlled variables.

The first step in the control design process is to define the dynamic model of the inverter. The two following subsections analyse the dynamic model and controller design processes for the isolated and grid-connected cases. The average modelling has been used to neglect the high frequency dynamics of the inverter and simplify the model in order to design the control.

**Isolated operation mode** Figure 3.10 shows the structure of the inverter when it is in isolated case, where a resistive load has been used as the only element fed by the inverter.

The equation of the load can be written as in eq. (3.7), where  $\vec{V}_{inv}^s = \begin{bmatrix} V_{a0} \\ V_{b0} \\ V_{c0} \end{bmatrix}$

and  $\vec{i}_{inv}^s = \begin{bmatrix} i_a \\ i_b \\ i_c \end{bmatrix}$ .

$$\vec{V}_{inv}^s = R_L \vec{i}_{inv}^s + L \frac{d\vec{i}_{inv}^s}{dt} + \vec{V}_{N0}^s \quad (3.7)$$

From the switching pattern of a two-level inverter and applying the averag-

### 3.2. Comparison among topologies

---

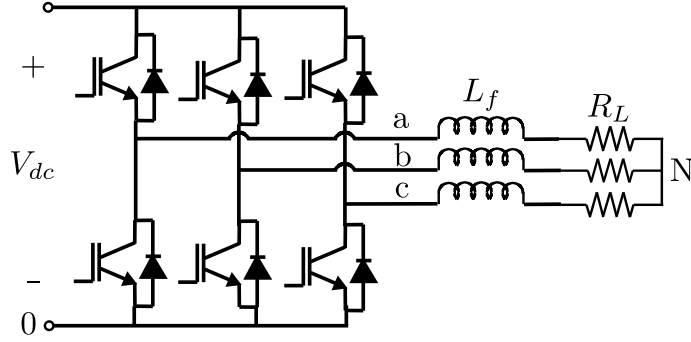


Figure 3.10: Structure of the two-level inverter in the isolated case.

ing method, the relation between the AC bus voltage, DC bus voltage and the switching orders is defined by eq. (3.8).

$$\vec{V}_{inv}^s = \vec{d}^{ts} V_{dc} \quad (3.8)$$

The output voltage of the inverter  $\vec{V}_{inv}^s$  is generated commutating the IGBT according to the switching signals generated by the PWM, which at the same time are calculated according to the duty cycle orders generated by the control system. Following the averaging method, if the switching frequency is much higher than the main dynamic of the system (50 Hz in this case), the high frequency part can be neglected and the main dynamic of the system can be represented by the average model. As a consequence, the switching orders, 0 and 1 values generated by the comparison among the duty cycles and the carrier signal, can be directly represented by the duty cycles. At this point, it is important to stress that the duty cycles that will be generated by the controller are signals that are in the range  $[-1, 1]$  while the average model needs signals in the range  $[0, 1]$ . This adjustment of the duty cycle signals is represented by eq. (3.9).

$$\vec{d}^{ts} = \frac{\vec{d}^s + 1}{2} \quad (3.9)$$

Substituting eq. (3.9) in eq. (3.8), the resulting expression in eq. (3.7) and organising the elements, eq. (3.10) can be obtained.

$$\frac{d\vec{i}_{inv}^s}{dt} = \frac{1}{L} \left( \frac{\vec{d}^s + 1}{2} \right) V_{dc} - \frac{R_L}{L} \vec{i}_{inv}^s - \frac{\vec{V}_{N0}^s}{L} \quad (3.10)$$

Equation (3.10) is in *abc* stationary reference system. A transformation to the rotating reference system *dq0* is necessary in order to obtain DC components that represent the three-phase variables. This way, classical control algorithms can be used to regulate the inverter. The transformation from stationary reference system to the rotating reference system is explained in Appendix B. Applying the mentioned transformation and separating the state space system in the *d* and *q* components, the equations shown in eq. (3.11) are obtained. As the system is considered balanced, the zero-sequence component is neglected.

$$\begin{aligned} \frac{di_{inv}^d}{dt} &= -\frac{R_L}{L} i_{inv}^d + \omega i_{inv}^q + \frac{1}{L} d^d \frac{V_{dc}}{2} \\ \frac{di_{inv}^q}{dt} &= -\frac{R_L}{L} i_{inv}^q - \omega i_{inv}^d + \frac{1}{L} d^q \frac{V_{dc}}{2} \end{aligned} \quad (3.11)$$

As it is shown in eq. (3.11), the *i<sub>d</sub>* and *i<sub>q</sub>* components are coupled with each other. The control system is calculated neglecting the coupling parts. Then, the decoupling is carried out adding/subtracting the neglected elements to the control signal of the controller, as it is shown in Figure 3.12.

The *i<sub>ACdq</sub>* current controllers are designed from a control model obtained applying the Laplace's transform to eq. (3.11), once the coupling parts have been eliminated. The voltage of the DC bus is assumed to be constant and consequently the only input of the system is the duty cycle. The transfer function used to design the PI controllers is the same for the *d* and *q* components, and it is shown in eq. (3.12).

$$\frac{I_{inv}^{dq}}{D^{dq}} = \frac{\frac{V_{dc}}{2}}{Ls + R_L} \quad (3.12)$$

The variable of the resistive load *R<sub>L</sub>* is included in eq. (3.12). The controller has been designed to ensure certain time domain characteristics when the load is *R<sub>L</sub>*. Of course, the load will be variable, but the response of the inverter will be close to the dynamics obtained when the load is *R<sub>L</sub>* whenever the load value is around the used one.



### 3.2. Comparison among topologies

Once the control model of the inner loop has been obtained, the PI controller of the current  $dq$  components can be designed following the desired process. In this thesis the *rltool* controller design tool of Matlab has been used to define the different PI controllers. The controllers have been designed to have a time response with no overshoot and a settling time of 3 *ms*.

After designing the PI controllers of the current, it is necessary to design the outer voltage loop controller. Substituting the expression of the inner PI controller in eq. (3.11), applying the Laplace's transform and neglecting the coupling, as it was previously done with the inner current loop, the transfer function of the inner control loop can be obtained. The outputs of this loop are the  $dq$  components of the current of the inverter. Knowing that the load is a resistor, multiplying the inner transfer function by the value of the load  $R_L$ , the voltage  $dq$  components can be obtained. This transfer function is used to design the outer voltage loop and it is shown in eq. (3.13).

$$\frac{V_{inv}^{dq}}{I_{inv}^{dqref}} = \frac{K_{p_i} T_{i_i} V_{dc} R_L s + V_{dc} R_L}{2T_{i_i} L_f s^2 + (2R_L + K_{p_i} V_{dc}) T_{i_i} s + V_{dc}} \quad (3.13)$$

The voltage controller has been designed using the *rltool* function in order to obtain a response with no overshoot and a settling time of 15 *ms*.

**Grid-connected operation mode** Figure 3.11 shows the structure of the grid-connected mode. The inverter works in this case connected to an external voltage source. The static switch is used to connect or disconnect the HESS from the external voltage source depending on the operation characteristics.

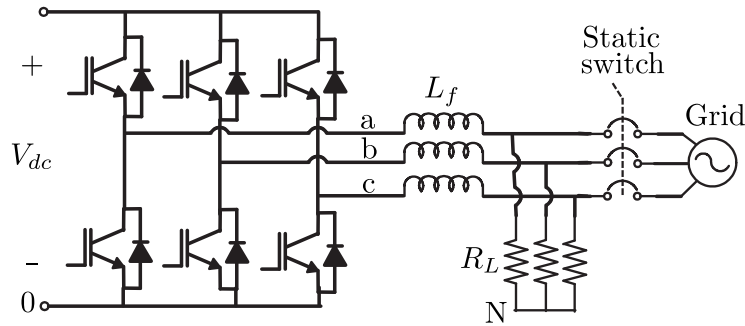


Figure 3.11: Structure of the two-level inverter in the grid-connected case.

### Chapter 3. Power electronics topologies and control for HESS

The equations of this operation mode differ from the ones of the isolated case. The expression of the output voltage of the inverter is shown in eq. (3.14).

$$\vec{V}_{inv}^s = L \frac{d\vec{i}_{inv}^s}{dt} + \vec{V}_{grid}^s + \vec{V}_{N0}^s \quad (3.14)$$

The current of the output of the inverter  $\vec{i}_{inv}^s$ , the current supplied by the grid to the load  $\vec{i}_{grid}^s$  and the AC side voltage  $\vec{V}_{grid}^s$  are related as shown in eq. (3.15).

$$\vec{V}_{grid}^s = R_L(\vec{i}_{inv}^s + \vec{i}_{grid}^s) \quad (3.15)$$

Substituting eq. (3.15) in eq. (3.14) and organising the elements, eq. (3.16) can be obtained.

$$\frac{d\vec{i}_{inv}^s}{dt} = \frac{1}{L} \left( \frac{d^s + 1}{2} \right) V_{dc} - \frac{R_L}{L} (\vec{i}_{inv}^s + \vec{i}_{grid}^s) - \frac{\vec{V}_{N0}^s}{L} \quad (3.16)$$

Converting eq. (3.16) equation from  $abc$  reference system to  $dq0$  rotating reference system as explained in Appendix B, and separating the equation in  $d$  and  $q$  components, eq. (3.17) can be obtained.

$$\begin{aligned} \frac{di_{inv}^d}{dt} &= \frac{1}{L} d^d \frac{V_{dc}}{2} - \frac{R_L}{L} i_{inv}^d + \omega i_{inv}^q - \frac{R_L}{L} i_{grid}^d \\ \frac{di_{inv}^q}{dt} &= \frac{1}{L} d^q \frac{V_{dc}}{2} - \frac{R_L}{L} i_{inv}^q - \omega i_{inv}^d - \frac{R_L}{L} i_{grid}^q \end{aligned} \quad (3.17)$$

In the grid-connected mode there is only one control loop, the one of the current. This current loop is calculated as in the isolated case. The only difference comparing to the isolated case is that in the grid-connected mode apart from the coupling, the effect of the grid current must be also added to the control signal. This effect is injected using the expression eq. (3.18), which has been obtained from eq. (3.15). The injection of the decoupling and the effect of the grid current are shown in the complete control structure of the two-level inverter, in Figure 3.12.

$$i_{grid}^{dq} = \frac{v_{grid}^{dq}}{R_L} - i_{inv}^{dq} \quad (3.18)$$

### 3.2. Comparison among topologies

The current references are generated using the expressions of the active and reactive powers, which are shown in eq. (3.19). A null reference has been selected for the reactive power, while the active power reference is selected to inject different power values to the grid. As the objective of the analysis is to compare the evolution of each topology no droop control nor similar structures have been implemented.

$$\begin{aligned} P &= \frac{3}{2} (v_d i_d + v_q i_q) \\ Q &= \frac{3}{2} (v_d i_q - v_q i_d) \end{aligned} \quad (3.19)$$

The control structure shown in Figure 3.12 includes the regulation of the isolated and grid-connected operation modes, as well as the transition procedure between them. This transition is smoothly carried out initialising the PI and using as the initial condition of the current component the last value of the previous operation mode.

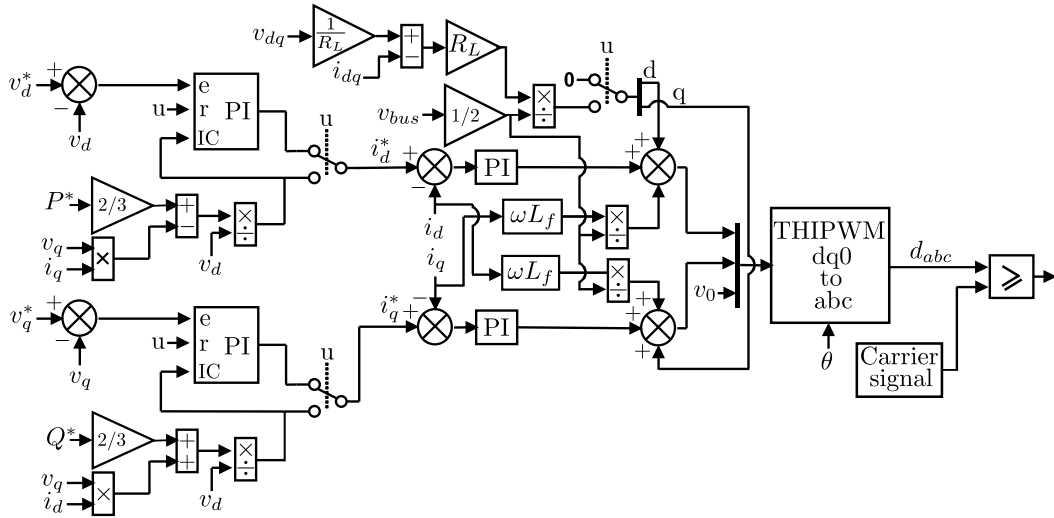


Figure 3.12: Two-level inverter control structure

The Third Harmonic Injection Pulse Width Modulation (THIPWM) is used as the modulation strategy due to the higher DC bus utilisation rate comparing to the Sinusoidal PWM, as it is explained in Chapter 4.

### 3.2.1.3 Grid synchronisation algorithm

The first step to operate in grid-connected operation mode is to synchronise the three-phase voltage system generated by the inverter with the voltage system fixed by the diesel generator. The frequency, phase and amplitudes of both systems must be the same in order to avoid power fluctuations that could put in danger the stability of the microgrid when the static switch shown in Figure 3.11 is closed.

Due to the weaknesses of a microgrid, it is specially sensitive to different disturbances. As a consequence, the frequency as well as the voltage level of a microgrid can suffer variations that do not occur in a stiff grid. Therefore, in this work a synchronisation algorithm capable of ensuring a good synchronisation even at faulty conditions has been implemented. Under ideal voltage conditions, the use of a Phase-Locked Loop (PLL) system is usually enough to ensure a good synchronisation, even if the voltage contains a high rate of harmonics. However, this type of synchronisation method cannot ensure a proper operation when voltage unbalances appear. In this case, algorithms capable of detecting the positive and negative sequences of the voltage must be used. In this work, the different tests have been carried out under balanced conditions. However, a system that is able to operate under unbalanced conditions has been employed due to the simplicity of the method and the improved behaviour that it has demonstrated when the system suffers from high frequency disturbances.

The method that has been implemented is called Dual Second Order Generalized Integrator-Frequency-Locked Loop (DSOGI-FLL) [35–37], which is a frequency adaptive positive sequence detection technique. This method carries out a transformation from the stationary  $abc$  reference system to the  $\alpha\beta$  reference system as a first step (refer to Appendix B). Then, a SOGI-based quadrature signal generator, shown in Figure 3.14, is used to filter and to obtain the  $90^\circ$  shifted versions of the  $\alpha\beta$  voltages. These signals are used to detect the positive and negative sequences of the voltage, following the equations eqs. (3.20) and (3.21) respectively. Finally, a FLL structure, which is shown in Figure 3.13, is used to obtain a frequency adaptive algorithm.

### 3.2. Comparison among topologies

$$\begin{aligned} V_{\alpha}^{+'} &= V_{\alpha}' - qV_{\beta}' \\ V_{\beta}^{+'} &= V_{\beta}' + qV_{\alpha}' \end{aligned} \quad (3.20)$$

$$\begin{aligned} V_{\alpha}^{-'} &= V_{\alpha}' + qV_{\beta}' \\ V_{\beta}^{-'} &= V_{\beta}' - qV_{\alpha}' \end{aligned} \quad (3.21)$$

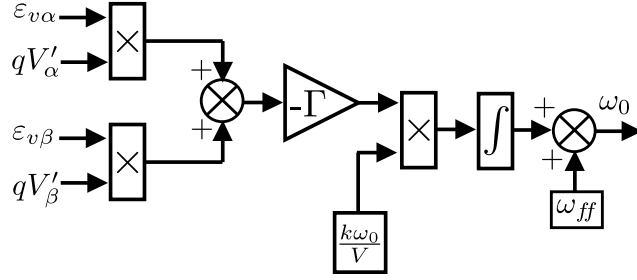


Figure 3.13: Structure of the FLL.

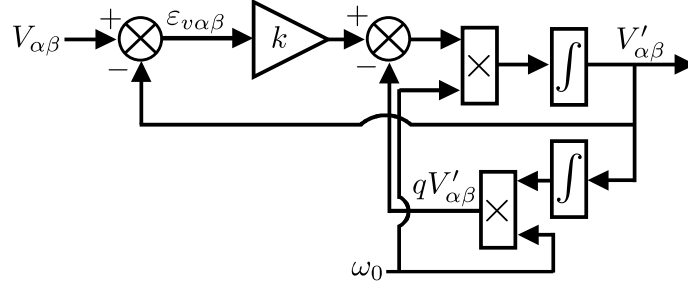


Figure 3.14: Structure of the DSOGI-QSG.

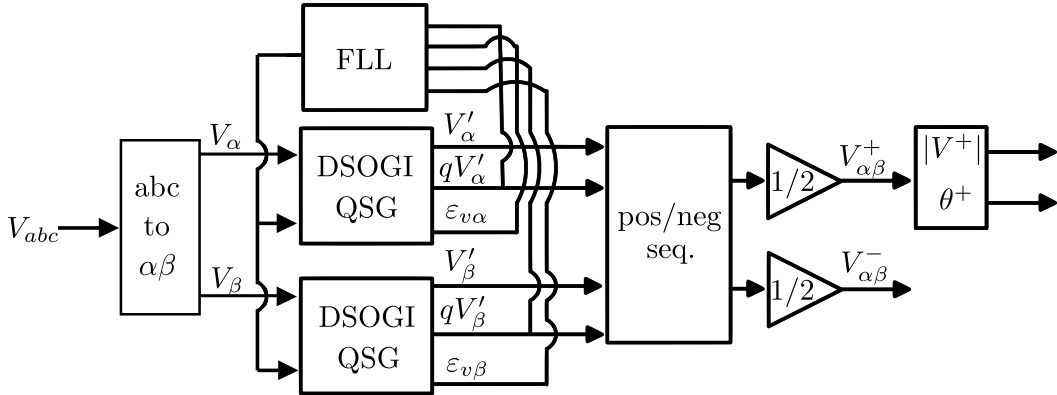


Figure 3.15: General schematic of the DSOGI-FLL algorithm.

The phase and amplitude of the positive and/or negative voltage sequences can be obtained using eq. (3.22).

$$\begin{aligned} |V^\pm| &= \sqrt{(V_\alpha^\pm)^2 + (V_\beta^\pm)^2} \\ \theta^\pm &= \tan^{-1} \frac{V_\beta^\pm}{V_\alpha^\pm} \end{aligned} \quad (3.22)$$

The value of the parameter  $k$  and the parameter  $\Gamma$  have been selected according to their relation with the settling time of the DSOGI algorithm and the frequency loop respectively. Those relations are shown in eqs. (3.23) and (3.24) [37].

$$t_{sDSOGI} = \frac{8}{k\omega_0} \quad (3.23)$$

$$t_{sFLL} = \frac{5}{\Gamma} \quad (3.24)$$

### 3.2.2 Floating topology

In this topology the DC-DC converter of the VRB battery that is used in the parallel topology is eliminated and the battery is directly connected to the DC bus, as it is shown in Figure 3.16. For this reason, and in order to maintain the same DC bus voltage, the voltage rating of the VRB is double as much as in the other two topologies. A DC-DC converter is used to control the SC and a two-level inverter is used to interface the HESS with the rest of the microgrid, as in the parallel topology.

#### 3.2.2.1 Control algorithm

The block diagram of the control algorithm of the DC-DC converter of the SC used in this topology is shown in Figure 3.17. The SC is used to absorb/supply the fast power variations of the DC bus, to prevent the battery from peak currents. At the same time, the average power of the SC is controlled in order to maintain it at 0A; this is achieved using a low pass filter applied to the power of the SC (cut-off frequency of 2 rad/s) and then a PI controller, which has been designed by trial and error.

### 3.2. Comparison among topologies

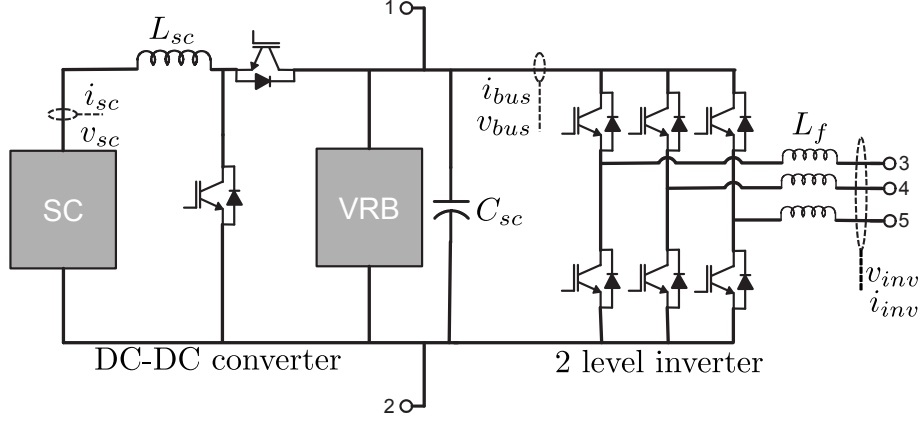


Figure 3.16: Floating topology.

The design of the inner current loop of the DC-DC as well as the control of the two-level inverter is the same of the parallel topology.

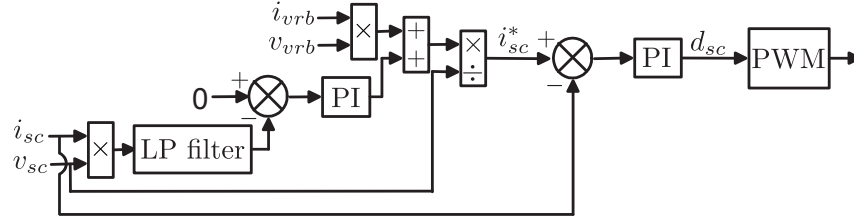


Figure 3.17: Control algorithm of the floating topology.

#### 3.2.3 3LNPC topology

The 3LNPC converters are typically used in high and medium power applications due to their ability to reduce the voltage ratings of the semiconductors (compared to the ratings that are necessary with conventional two-level inverters) and their improved output power quality [38, 39].

In this section, it is shown that this kind of converter can be also useful from the point of view of the association of two ESSs in a microgrid context. The storage devices can be used as the voltage sources of the 3LNPC converter, whereas the capacitors are maintained in order to filter the effect of the switches (Figure 3.18).

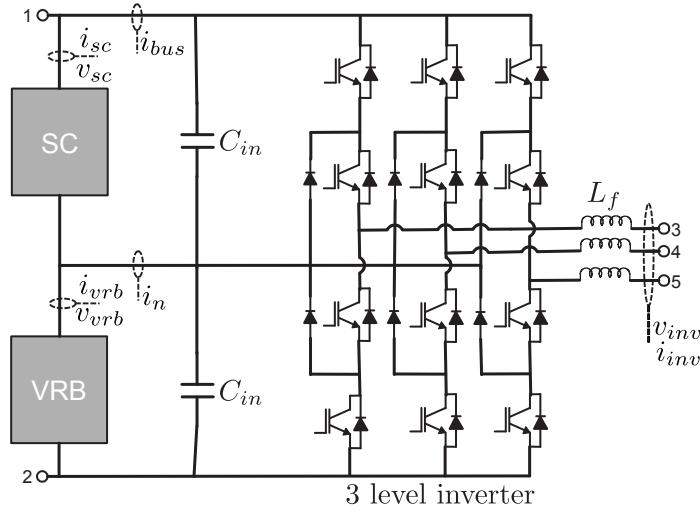


Figure 3.18: 3LNPC converter topology.

### 3.2.3.1 3LNPC switching control

One of the most important problems of the 3LNPC converter is the neutral point voltage balance, i.e. to maintain an equal distribution of the DC bus voltage between the two capacitors. Several methods for maintaining this equality can be found in the literature, like the use of redundant vectors in the Space Vector Modulation (SVM) [40] and the zero-sequence component injection in the carrier based PWM modulations [41–43]. These methods can be used with a different objective and be employed to control the currents of the storage devices.

The possibility of using the small redundant vectors depends directly on the modulation rate. A trade-off between the DC bus voltage value and the use of the small redundant vectors has been carried out to determine the reference DC bus voltage value. Based on this analysis, a value of 900 V has been selected instead of the typical 700 V one. More details about this analysis and other issues related with the 3LNPC converter are addressed in Chapter 4.

The multicarrier THIPWM is used as the modulation strategy, because it allows a modulation index increase of 15% in the linear modulation range, compared to the Sinusoidal PWM, when an one-sixth third harmonic is injected



### 3.2. Comparison among topologies

---

[44]. This way, the same modulation index increase of the SVM is obtained and the possibility of using the small redundant vectors is augmented. The addition of the third harmonic does not affect the output waveform in the case of the three phase-three wire systems [45].

On the other hand, the zero-sequence component injection has been used to control the use of the higher or lower small redundant vectors, which determines the current taken from the input voltage sources. A controlled offset is added to the modulating signal in order to control the current of the VRB, as it is shown in Figure 3.19.

As the use of the storage devices will be different, voltage differences may appear which would create undesirable distortions at the output of the inverter [30, 38]. In order to avoid that and to tend to equalise the voltages of the storage devices, the amplitudes of the carrier signals are modified following the expressions defined in eqs. (3.25) and (3.26) [30]. The modification of the amplitudes of the carrier signals allows to obtain a balanced three-phase voltage system even if the input voltage are not equal.

$$A_{sc} = \frac{2V_{sc}}{V_{sc} + V_{vrb}} \quad (3.25)$$

$$A_{vrb} = \frac{2V_{vrb}}{V_{sc} + V_{vrb}} \quad (3.26)$$

#### 3.2.3.2 Control algorithm

The control algorithm of the 3LNPC converter is similar to the control applied to the two-level inverter. eq. (3.27) shows the relation between the DC bus voltages and the averaged switching signals, assuming that the two voltage sources have the same voltage value, i.e.  $\frac{V_{dc}}{2}$ .

$$\vec{V}_{inv}^s = \vec{d}_1^s \frac{V_{dc}}{2} + \vec{d}_2^s \frac{V_{dc}}{2} \quad (3.27)$$

As in the two-level inverter case, the duty cycles must be in the range  $[0, 1]$  and consequently the duty signals generated by the controller need to be adapted as shown in eqs. (3.28) and (3.29).

$$\vec{d}_1^s = \frac{\vec{d}^s + |\vec{d}^s|}{2} \quad (3.28)$$

$$\vec{d}_2^s = 1 + \frac{\vec{d}^s - |\vec{d}^s|}{2} \quad (3.29)$$

Substituting the adapted duty cycles in eq. (3.27), eq. (3.30) can be obtained.

$$\vec{V}_{inv}^s = \left( \frac{\vec{d}^s + 1}{2} \right) V_{dc} \quad (3.30)$$

As eq. (3.30) is the same as the one obtained in the two-level inverter, the rest of the controller design process is exactly the same.

In the case of the three-level converter, a zero-sequence component is added to the modulating signal in order to control the use of the redundant vectors. This additional part is shown in Figure 3.19. The state-space averaging method has been used to obtain the equations of the inverter and then the  $dq0$  transformation is carried out to control the inverter in this reference system [46].

The current reference of the VRB is generated adding the measured input inverter power in the DC bus level with the measured power of the SC and subtracting the power signal of the neutral point power. Then, the resulting value of the addition is filtered and used as the reference of the VRB current. The final modulating signal is then compared with the carrier signals to generate the switching orders.

### 3.3 Simulation Results

The operation of the three topologies has been compared in the simulation context shown in Figure 3.6. The power generated by different RES is simulated as a variable DC current that is injected directly in the DC bus. The HESS is used to smooth the variability of the incoming power, dividing the power between the SC and the VRB according to the frequency. Low frequency

### 3.3. Simulation Results

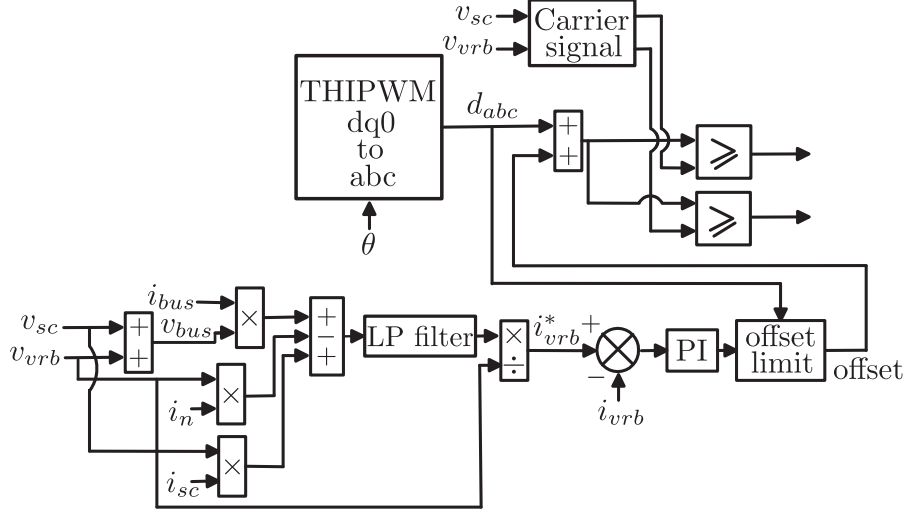


Figure 3.19: Control algorithm of the 3LNPC converter.

variations will be faced by the VRB and the high frequency variations by the SC. The microgrid can operate connected or disconnected to/from a weak grid, which is based on a diesel generator. Two resistive loads are used: the first load is directly connected to the output of the inverter of the HESS and a second load is connected to the diesel generator. Mainly resistive grid-lines have been used to simulate the distance between the elements, as this is the case of a microgrid [47].

Two case studies have been simulated. In the first one, the microgrid operates connected to the main weak grid, while a variable current generated by RES is injected in the DC bus. In the second case study the disconnection of the microgrid from the main weak grid has been analysed. In both cases the ability of each topology to divide the power between the SC and the VRB, as well as the power losses and the THD are analysed and the results have been used to compare the presented three topologies.

The parameters of the SC bank and the VRB battery used in the simulations have been extrapolated from the results of the modelling process of Chapter 2. In the case of the SC, the parameters that have been used are equivalent to a SC bank that has 250 cells connected in series. The total capacity of the used SC is  $6F$ , the serial resistance is  $143.1m\Omega$ , the rated voltage is  $450V$  and

### Chapter 3. Power electronics topologies and control for HESS

the maximum continuous charge/discharge current is  $61A$ . The VRB used in this comparison has a rated stack voltage of  $450V$  (at 50% of SOC and open circuit), a maximum charge/discharge current of  $50A$  and an autonomy of  $0.75\text{ hours}$ . The number of cells used in the simulations has been of 320, which has increased the charge and discharge serial resistors to  $24\Omega$  and  $24.96\Omega$  respectively. Finally, the parallel resistor has been increased proportionally to the increase of the number of cells, obtaining a value of  $456\Omega$ .

Notice that as in the floating topology the VRB is directly connected to the common DC bus and the voltage in this point is  $900V$ , the parameters of the VRB in this topology will be different from the ones used in the other two topologies. These parameters can be easily obtained using a rated voltage of  $900V$ .

The values of the grid-lines, different elements of the power converters, the Diesel Generator and other parameters that are used in the simulations are shown in Table 3.1.

Grid-line		Power converters		Diesel Generator		Others	
Param.	Value	Param.	Value	Param.	Value	Param.	Value
$R_{line}$	$7.6\text{ m}\Omega$	$L_{filter}$	$3\text{ mH}$	$P_{rated}$	$33\text{ kW}$	$C_{bus}$	$4700\text{ }\mu F$
$L_{line}$	$66.53\text{ }\mu H$	$L_{sc}$	$3\text{ mH}$	$R_{dg}$	$5.81\text{ }\Omega$	$R_{load}$	$15\text{ }\Omega$
		$L_{vrb}$	$4.9\text{ mH}$	$J$	$3\text{ kg}\cdot\text{m}^2$		
		$C_{in}$	$10\text{ mF}$	$K_d$	$0.6\frac{T(pu)}{\omega(pu)}$		
		$f_s$	$15\text{ kHz}$	$p$	$2$		

Table 3.1: Simulation parameters

The current ( $i_c$ ) of each semiconductor element has been measured in order to calculate the power losses. The details about the power losses calculations are analysed in Appendix A.

During the first  $0.7$  seconds of all the simulations that have been run, the start-up process of the diesel generator and the synchronisation process between the three-phase voltage of the HESS and the one fixed by the diesel generator are carried out. The DG needs a period of time to stabilise the AC voltages. Once the output is stabilised and the grid frequency is inside the range  $50\pm 0.5\text{ Hz}$ , the inverter output is synchronised with the DG signal using

### 3.3. Simulation Results

the synchronisation method described in Section 3.2.1.3 and at the instant 0.7 s the static switch is closed. These steps are repeated both in the first and second case studies.

#### 3.3.1 First case study

A current profile generated by different RES has been introduced in the DC bus in order to analyse the behaviour of each topology. The resistive loads  $R_{load}$  and  $R_{dg}$  are maintained constant.

The power losses of each topology that are obtained in the first case study are shown in Table 3.2.

Topology	Power converter	Conduction [W]	Switching [W]	Total [W]
Parallel	DC-DC SC	11.64	129.70	679.25
	DC-DC VRB	23.03	136.51	
	2L inverter	27.11	413.04	
Floating	DC-DC SC	10.88	130.84	539.32
	2L inverter	25.64	408.48	
3LNPC	3LNPC inverter	37.06	308.08	308.08

Table 3.2: Power losses of the first case study

The average THDs that are obtained in this first case study are 3.19 %/3.23 % with the parallel topology, 3.16 %/3.22 % with the floating one and 1.53 %/2.16 % with the 3LNPC converter topology for voltage/current respectively.

##### 3.3.1.1 Parallel DC-DC topology

Figure 3.20 shows the evolution of the power of the storage systems as well as the power injected by the RES. As it can be seen, the desired power division between the SC and VRB is achieved.

Figure 3.21 shows that the DC bus voltage is well maintained at its reference value. The inverter is supplying a constant active power and no reactive power. During the first 0.7s the inverter works in grid-disconnected mode and it fixes the frequency and the voltage of the microgrid. During this period, the

power required by the load is saved, and this value is used as the active power reference value when the inverter commutes to work in grid-connected mode.

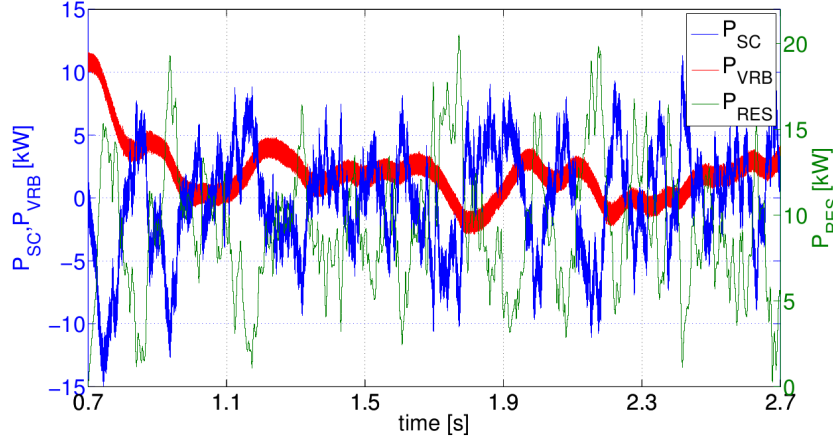


Figure 3.20: Power injected by RES and the power of the HESS in the parallel topology.

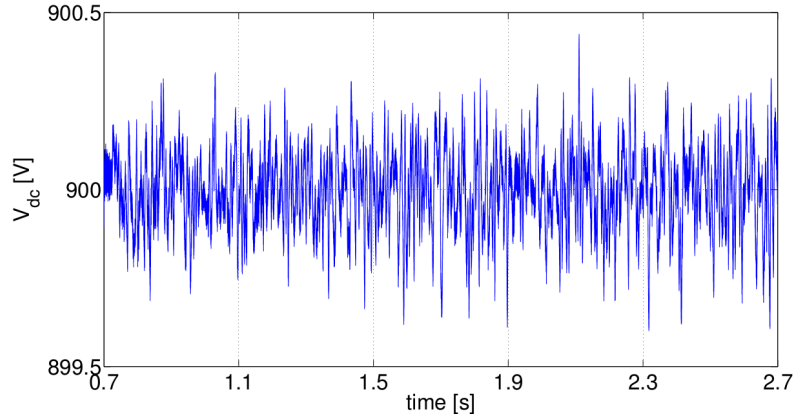


Figure 3.21: DC bus voltage in the parallel topology.

### 3.3.1.2 Floating topology

The results obtained using the floating topology are shown in Figures 3.22 and 3.23. As it is shown in Figure 3.22, the floating topology is also able to divide the power between the SC and VRB. The current of the VRB cannot be maintained completely constant as only the fast variations of the DC bus are absorbed/supplied by the SC. The VRB supplies the current difference

### 3.3. Simulation Results

between the average power coming from the RES and the power required by the load. As the VRB is directly connected to the DC bus and its voltage is dependent on its SOC, the voltage amplitude varies and is slightly different from 900 V (Figure 3.23).

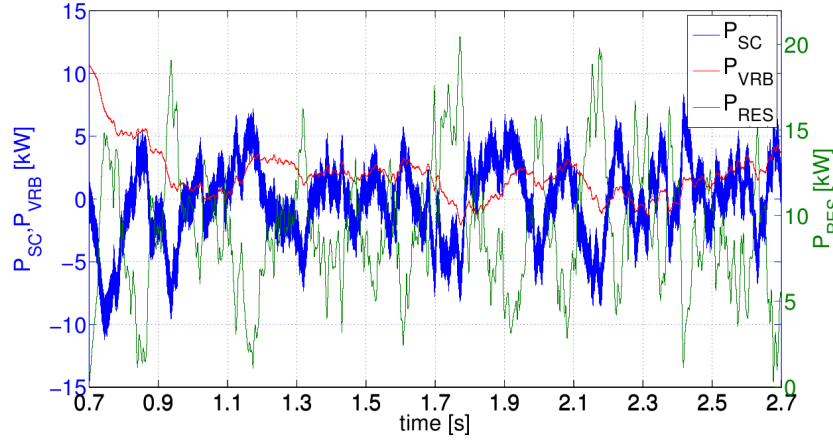


Figure 3.22: Power injected by RES and the power of the HESS in the floating topology.

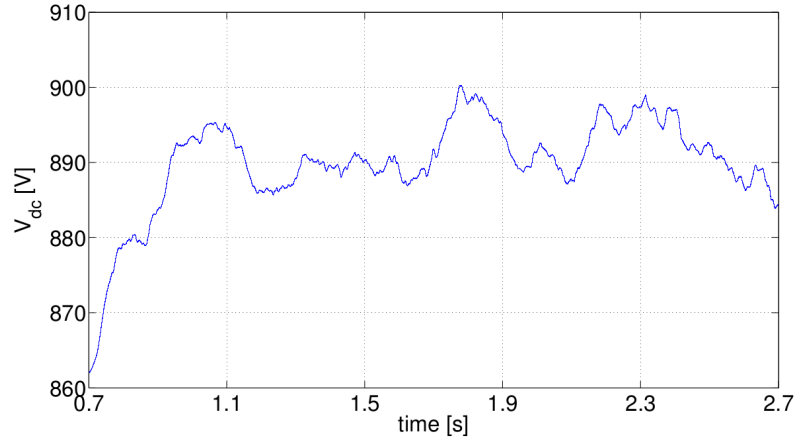


Figure 3.23: DC bus voltage in the floating topology.

#### 3.3.1.3 3LNPC topology

Figures 3.24 and 3.25 shows the results obtained by the 3LNPC topology. From Figure 3.24 it can be seen that the fast power variations are mostly absorbed/supplied by the SC. Taking into account that the state-of-charge of

the VRB is 50%, once the connection to the DG is done the current reference of the VRB is selected to be 0A. This way, the average power generated by the RES will be transferred to the AC side. If the SC gets discharged, the reference of the VRB could be increased to charge it.

Figure 3.25 shows the evolution of the DC bus voltage. As the DC bus voltage in this case is formed by the voltages of the SC and the VRB, it depends on the state-of-charges of both storage devices. However, the variations are not higher than the ones obtained in the floating topology.

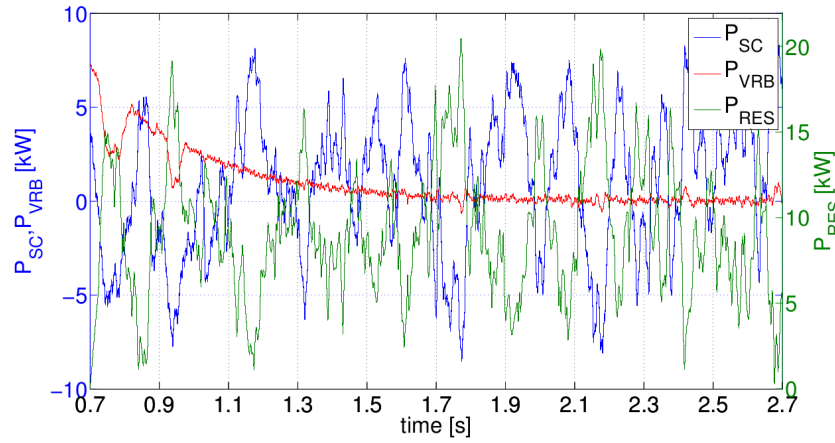


Figure 3.24: Power injected by RES and the power of the HESS in the 3LNPC topology.

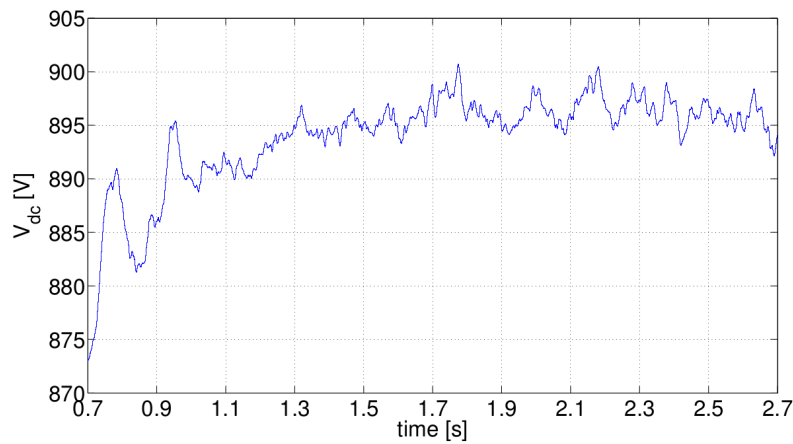


Figure 3.25: DC bus voltage in the 3LNPC topology.



### 3.3. Simulation Results

#### 3.3.2 Second case study

In the second case study the disconnection of the microgrid from the main grid has been analysed. As in the first case study, during the first 0.7 s the connection process of the microgrid to the weak grid is carried out and the power required by  $R_{load}$  is saved in a variable. Then, the grid-connection is done and the power reference of the inverter is reduced slowly until reaching the half of the initial value at the instant 1.2 s, as it is shown for example in Figure 3.29. This is done in order to create a power difference that the inverter must face when the disconnection occurs.

The power losses of this case study are shown in Table 3.3.

Topology	Power converter	Conduction [W]	Switching [W]	Total [W]
Parallel	DC-DC SC	4.25	131.01	703.18
	DC-DC VRB	56.59	167.32	
	2L inverter	24.51	404.85	
Floating	DC-DC SC	8.63	135.24	539.98
	2L inverter	24.46	404.74	
3LNPC	3LNPC inverter	33.77	323.28	323.28

Table 3.3: Power losses of the second case study

The average THD of the second case study are 3.74 %/4.40 % for the parallel topology, 3.63 %/4.31 % for the floating topology and 2.22 %/2.95 % for the 3LNPC topology.

##### 3.3.2.1 Parallel DC-DC topology

Figure 3.26 shows the evolution of the currents of the ESSs during the disconnection of the microgrid from the weak grid. When the disconnection occurs, the current through the inverter increases and thus a decrease of the DC bus voltage occurs. However, the controller of the DC-DC converter of the SC reacts and minimises the DC bus voltage disturbance by injecting a high peak current in the DC bus, as it is shown in Figure 3.27. Therefore, the fast variation is supplied completely by the SC. Once the disturbance is

eliminated and the output of the low pass filter of the SC power increases, the VRB increases its current in order to supply entirely the new load power.

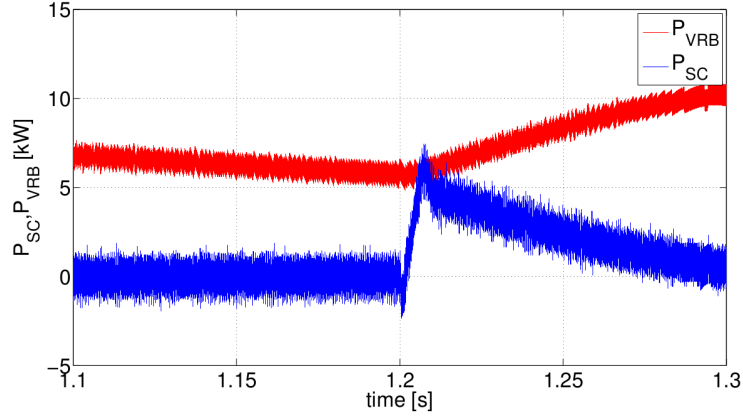


Figure 3.26: Power of the HESS in the parallel topology.

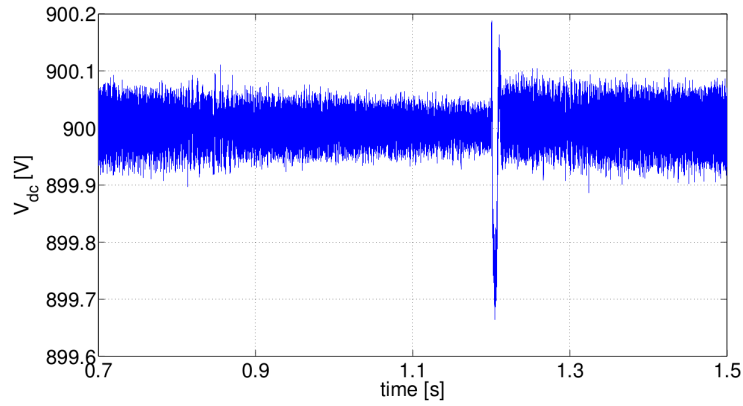


Figure 3.27: DC bus voltage in the parallel topology.

As it can be seen in Figure 3.28, the effect of the disconnection in the AC side voltages is negligible.

The evolution of the power supplied by the inverter to the load is shown in Figure 3.29. It can be seen that the control of the active power of the inverter when it works in grid connected mode is satisfactory.

### 3.3.2.2 Floating topology

Figures 3.30 to 3.33 show the behaviour of the floating topology when the disconnection of the microgrid occurs. As it is shown in Figure 3.30, the fast

### 3.3. Simulation Results

---

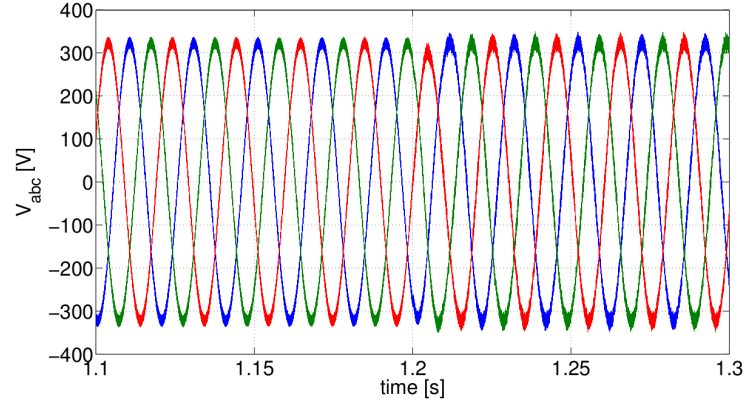


Figure 3.28: Load voltage in the parallel topology.

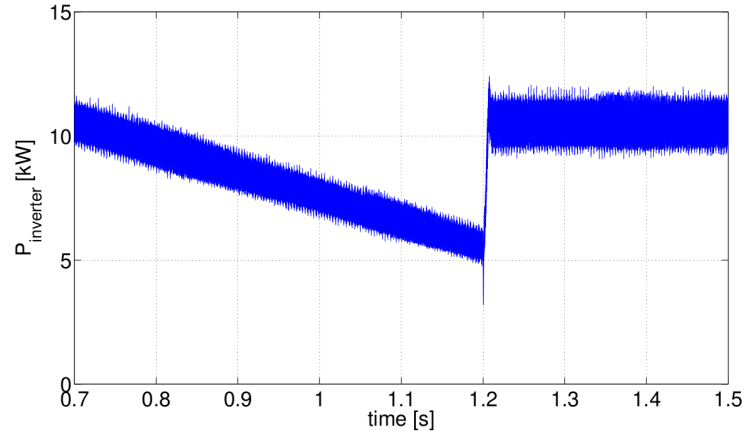


Figure 3.29: Power of the inverter in the parallel topology.

power variation is supplied by the SC, but a small fast current variation can be noticed in the VRB current. As the battery is directly connected to the DC bus, when the disconnection occurs the current taken by the inverter increases rapidly and the DC-DC converter of the SC needs a certain time to increase its output current. Although the fast current variation of the VRB is perceptible its value is small in amplitude, as well as its ratio in relation to the power step of the SC. The effect of the disconnection on the AC side is negligible, as it is shown in Figure 3.31.

The DC bus voltage is directly dependant on the SOC as well as on the current of the VRB. Consequently, it has variations during the simulation as it is shown in Figure 3.32. However, the voltage is maintained around the

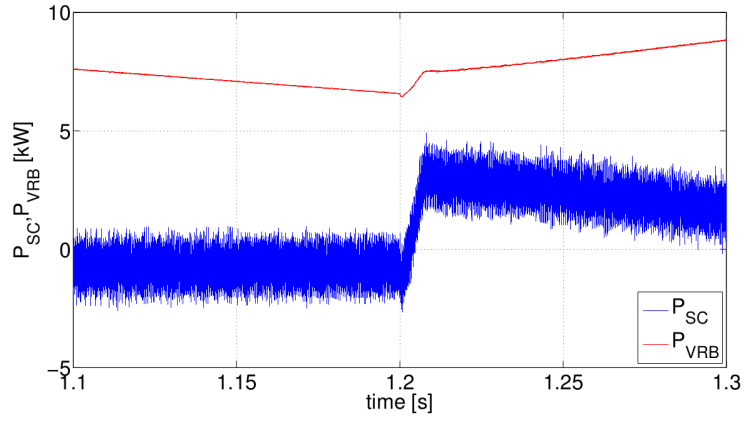


Figure 3.30: Power of the HESS in the floating topology.

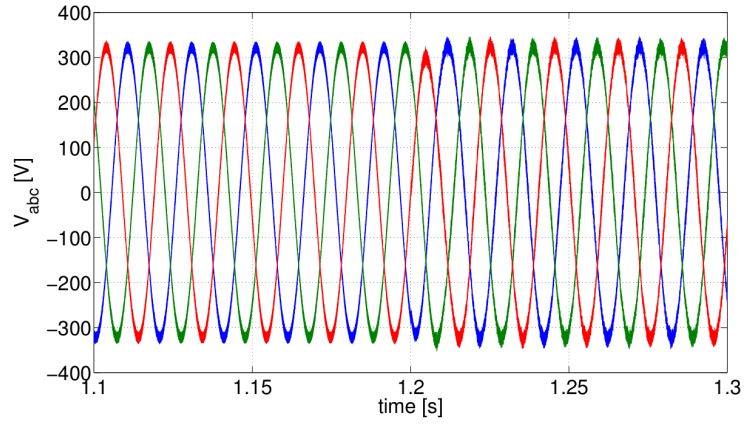


Figure 3.31: Load voltage in the floating topology.

reference 900 V.

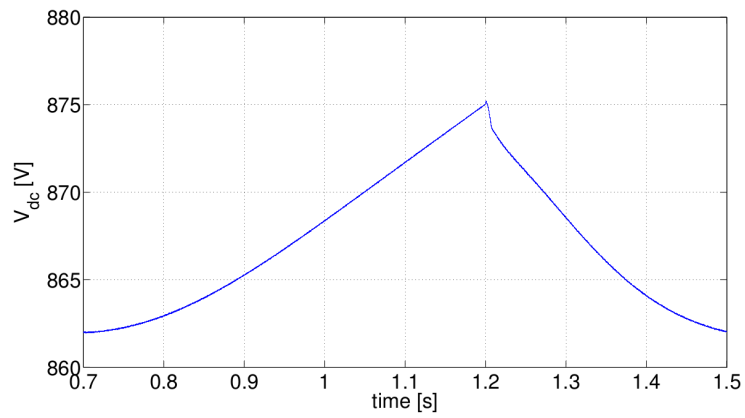


Figure 3.32: DC bus voltage in the floating topology.

### 3.3. Simulation Results

---

As the inverter control is the same in the parallel and floating topologies, the evolution of the power supplied by the inverter is almost the same (Figure 3.33).

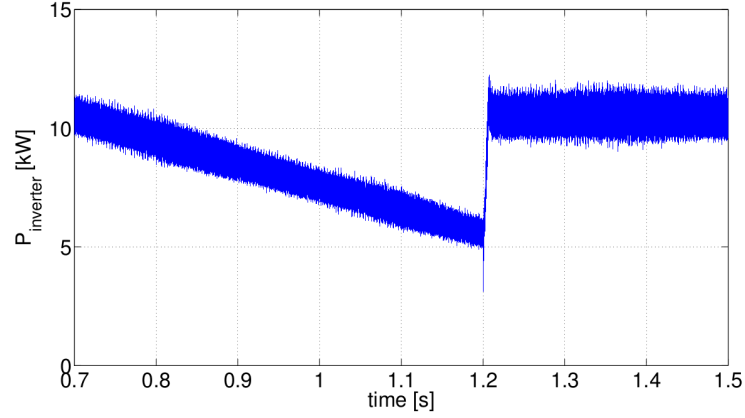


Figure 3.33: Power of the inverter in the floating topology.

#### 3.3.2.3 3LNPC topology

Figures 3.34 to 3.37 show the results obtained with the 3LNPC topology. Figure 3.34 shows the current division between the two ESSs. The sudden disconnection of the microgrid obliges the inverter to supply the total power of the load ( $R_{load}$ ). This fast power variation is supplied completely by the SC, as it is shown in Figure 3.34.

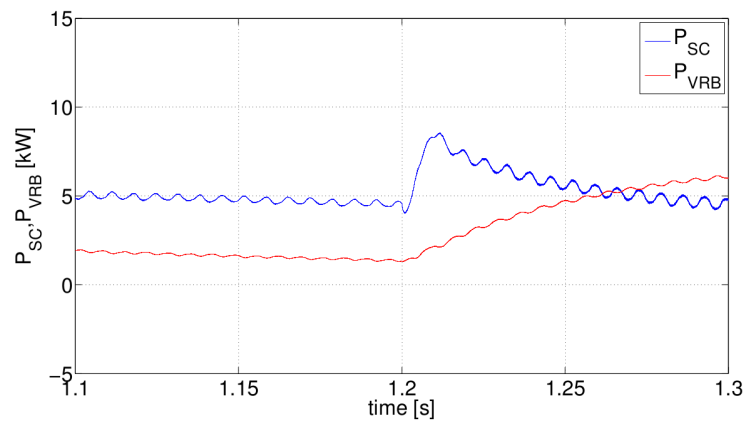


Figure 3.34: Power of the HESS in the 3LNPC topology.

From Figure 3.35 it can be seen that the AC side voltage is properly

maintained at the reference values. Only a small transitory voltage decrease can be noticed when the disconnection occurs.

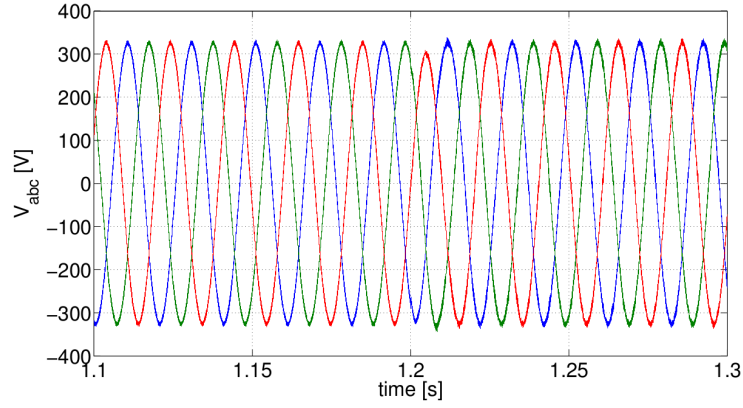


Figure 3.35: Load voltage in the 3LNPC topology.

In the case of the 3LNPC topology, the DC bus voltage depends not only in the SOC and the current of the VRB, but also in the SC. Its evolution is shown in Figure 3.36.

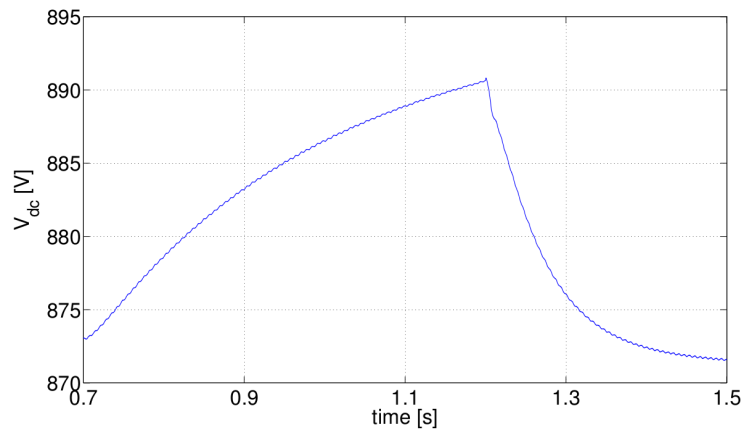


Figure 3.36: DC bus voltage in the 3LNPC topology.

The evolution of the power of the inverter is very similar to the one obtained in the other two topologies, as the employed control algorithm is the same in the three cases. The evolution of the mentioned power in the 3LNPC is shown in Figure 3.37.

### 3.4. Results discussion

---

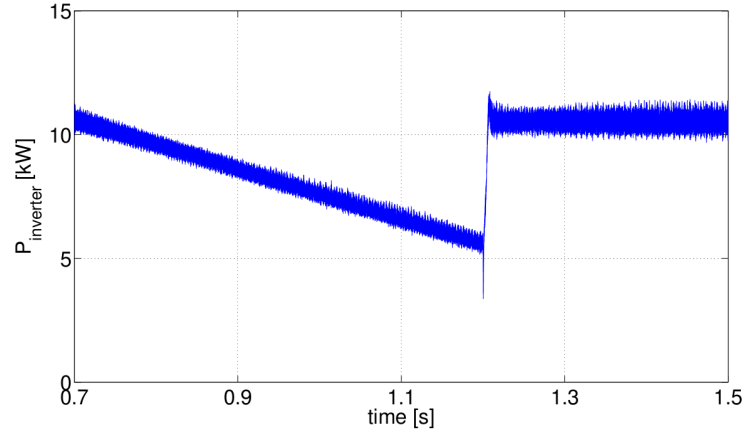


Figure 3.37: Power of the inverter in the 3LNPC topology

## 3.4 Results discussion

The comparison that has been carried out in this chapter proves the feasibility of the parallel topology, the floating topology and the 3LNPC converter topology to control a HESS in a microgrid context.

The results of the first case study show that the three topologies are able to smooth the power coming from RES dividing it between the SC and the VRB. The DC bus voltage is only tightly controllable in the case of the parallel topology. However, in the case of the other two topologies, the selected DC bus voltage gives enough flexibility to reduce the voltage (according to the state-of-charge of the storage devices) while a proper operation of the inverters is assured. The results, concerning the power division, are similar in the three cases, but the 3LNPC topology obtains these results with a reduction of 53.42% and 40.06% of the power losses comparing to the results of the parallel and floating topologies respectively.

On the other hand, the results of the second case study show that the three analysed topologies are able to face the disconnection of the DG and to continue supplying power to the loads with a correct AC side voltage. The sudden power increase is well divided between the SC and the VRB in the case of the parallel and 3LNPC topologies. In the case of the floating topology there is a small fast variation in the current of the VRB due to the

reaction time needed by the DC-DC converter of the SC. The effect of the disconnection on the AC side voltages generates a small transitory voltage decrease in all topologies. However, this transitory part complies with the power quality standards. Concerning the power losses, the 3LNPC obtains a reduction of 54.72% and 37.69% comparing to the losses of the parallel and floating topologies respectively. These power losses reduction could be reduced even more using a modulation strategy designed for that objective, as for example in [48, 49].

In both case studies the 3LNPC converter topology obtains the best THDs.

Although the 3LNPC improves the power losses and the THD, it has some disadvantages: namely the loss of flexibility of the controller, the necessity of maintaining equal the voltages of both ESSs and having a variable DC bus voltage. Comparing to the flexibility of the parallel and floating topologies, the flexibility is more limited as the control of the DC and AC side variables is interdependent. The controller tries to manage the current supplied/absorbed by the ESSs while this current is used to generate the AC side signals. Consequently, a complex control algorithm is necessary to manage properly the 3LNPC topology.

Analysing the advantages and disadvantages of the 3LNPC converter topology, it has been concluded that even if this topology has some flexibility limitations, the 3LNPC topology can be the most interesting choice to manage a HESS and to improve the power quality in a microgrid. The fact of controlling the HESS using just one power converter with reduced power losses and improved THD is highly interesting from the distributed generation application point of view, where the storage system would be installed in many different locations.

## 3.5 Chapter conclusions

In this chapter three topologies that can be employed to control the power flow of a HESS in a microgrid context have been compared by means of simulation.



## Chapter References

---

Two case studies has been selected to carry out the mentioned comparison. In the first one, the microgrid operates connected to the main weak grid, while a variable current generated by a RES is injected in the DC bus. In the second case study the disconnection of the microgrid from the main weak grid has been analysed. The results have shown that the 3LNPC topology is able to obtain a similar behaviour of the power of the HESS to the other two topologies, but with reduced power losses and improved THD.

As a consequence, this topology will be deeply analysed in Chapter 4.

## Chapter References

- [1] T.A. Smith, J.P. Mars, and G.A. Turner. Using supercapacitors to improve battery performance. In *Proc. 33rd Annu. IEEE PESC*, volume 1, pages 124–128, 2002.
- [2] R. A. Dougal, S. Liu, and R. E White. Power and life extension of battery-ultracapacitor hybrids. *IEEE Trans. Components and Packaging Technologies*, 25(1):120–131, 2002.
- [3] S. Colton. A simple series Battery/Ultracapacitor drive system for light vehicles and educational demonstration. In *Proc. EVER*, 2009.
- [4] W. Li and G. Joós. A power electronic interface for a battery supercapacitor hybrid energy storage system for wind applications. In *Proc. 39th Annu. IEEE PESC*, pages 1762–1768, 2008.
- [5] S. Pay and Y. Baghzouz. Effectiveness of battery-supercapacitor combination in electric vehicles. In *Proc. IEEE Power Tech Conf.*, volume 3, 2003.
- [6] L. Gao, R.A. Dougal, and S. Liu. Power enhancement of an actively controlled Battery/Ultracapacitor hybrid. *IEEE Trans. Power Electron.*, 20(1):236–243, 2005.

- [7] L. Palma, P. Enjeti, and J.W. Howze. An approach to improve battery run-time in mobile applications with supercapacitors. In *Proc. 34th Annu. IEEE PESC*, volume 2, pages 918–923, 2003.
- [8] T. Ise, M. Kita, and A. Taguchi. A hybrid energy storage with a SMES and secondary battery. *IEEE Trans. Applied Superconductivity*, 15(2): 1915–1918, 2005.
- [9] E. Ozatay, B. Zile, J. Anstrom, and S. Brennan. Power distribution control coordinating ultracapacitors and batteries for electric vehicles. In *Proc. American Control Conf.*, volume 5, pages 4716–4721, 2004.
- [10] M. Ortuzar, J. Moreno, and J. Dixon. Ultracapacitor-Based auxiliary energy system for an electric vehicle: Implementation and evaluation. *IEEE Trans. Ind. Electron.*, 54(4):2147–2156, 2007.
- [11] M. B. Camara, H. Gualous, F. Gustin, and A. Berthon. Control strategy of hybrid sources for transport applications using supercapacitors and batteries. In *Proc. CES/IEEE 5th Int. Conf. Power Electronics and Motion Control*, volume 1, 2006.
- [12] M. B. Camara, H. Gualous, F. Gustin, A. Berthon, and B. Dakyo. DC/DC converter design for supercapacitor and battery power management in hybrid vehicle Applications-Polynomial control strategy. *IEEE Trans. Ind. Electron.*, 57(2):587–597, February 2010.
- [13] Z. Guoju, T. Xisheng, and Q. Zhiping. Research on battery supercapacitor hybrid storage and its application in MicroGrid. In *Proc. APPEEC*, pages 1–4. March 2010.
- [14] H. Babazadeh, W. Gao, and X. Wang. Controller design for a hybrid energy storage system enabling longer battery life in wind turbine generators. In *Proc. NAPS*, pages 1 –7, August 2011.

## Chapter References

---

- [15] B.A. Niemoeller and P.T. Krein. Battery-ultracapacitor active parallel interface with indirect control of battery current. In *Proc. PECTI*, pages 12–19, February 2010.
- [16] J. D Maclay, J. Brouwer, and G. S Samuelsen. Dynamic modeling of hybrid energy storage systems coupled to photovoltaic generation in residential applications. *J. Power Sources*, 163(2):916–925, 2007.
- [17] C. Abbey, K. Strunz, and G. Joos. A Knowledge-Based approach for control of Two-Level energy storage for wind energy systems. *IEEE Trans. Energy Conversion*, 24(2):539–547, 2009.
- [18] W. Li, G. Joós, and J. Belanger. Real-Time simulation of a wind turbine generator coupled with a battery supercapacitor energy storage system. *IEEE Trans. Ind. Electron.*, 57(4):1137–1145, April 2010.
- [19] H. Yoo, S.-K. Sul, Y. Park, and J. Jeong. System integration and Power-Flow management for a series hybrid electric vehicle using supercapacitors and batteries. *IEEE Trans. Ind. Appl.*, 44(1):108–114, 2008.
- [20] P. Thounthong, S. Raël, and B. Davat. Energy management of fuel cell/battery/supercapacitor hybrid power source for vehicle applications. *J. Power Sources*, 193(1):376–385, 2009.
- [21] H. Zhou, T. Bhattacharya, D. Tran, T. Siew, and A. Khambadkone. Composite energy storage system involving battery and ultracapacitor with dynamic energy management in microgrid applications. *IEEE Trans. Power Electron.*, 26(3):923–930, March 2011.
- [22] M.-E. Choi, S.-W. Kim, and S.-W. Seo. Energy management optimization in a Battery/Supercapacitor hybrid energy storage system. *IEEE Trans. Smart Grid*, 3(1):463–472, March 2012.
- [23] F. Liu, J. Liu, and L. Zhou. A novel control strategy for hybrid energy storage system to relieve battery stress. In *Proc. 2nd IEEE Int. Symposium PEDG*, pages 929–934, June 2010.

- [24] M.E. Glavin, P.K.W. Chan, S. Armstrong, and W.G. Hurley. A stand-alone photovoltaic supercapacitor battery hybrid energy storage system. In *Proc. 13th EPE-PEMCC Conf.*, pages 1688–1695, September 2008.
- [25] M. Georgescu, L. Barote, C. Marinescu, and L. Clotea. Smart electrical energy storage system for small power wind turbines. In *Proc. 12th Int. Conf. OPTIM*, pages 1192–1197, 2010.
- [26] Y. Zhang, Z. Jiang, and X. Yu. Control strategies for Battery/Supercapacitor hybrid energy storage systems. In *Proc. IEEE Energy 2030 Conference*, pages 1–6, November 2008.
- [27] A.L. Allègre, R. Trigui, and A. Bouscayrol. Different energy management strategies of hybrid energy storage system (HESS) using batteries and supercapacitors for vehicular applications. In *Proc. IEEE VPPC*, pages 1–6, 2010.
- [28] S. D. G. Jayasinghe, D. M. Vilathgamuwa, and U. K. Madawala. A new method of interfacing Battery/Supercapacitor energy storage systems for distributed energy sources. In *Proc. IPEC*, pages 1211–1216, 2010.
- [29] S. D. G. Jayasinghe, D. M. Vilathgamuwa, and U. K. Madawala. A direct integration scheme for battery-supercapacitor hybrid energy storage systems with the use of grid side inverter. In *Proc. 26th Annu. IEEE APEC*, pages 1388–1393. March 2011.
- [30] S. D. G. Jayasinghe, D. M. Vilathgamuwa, and U. K. Madawala. Diode-Clamped Three-Level Inverter-Based Battery/Supercapacitor direct integration scheme for renewable energy systems. *IEEE Trans. Power Electron.*, 26(12):3720–3729, December 2011.
- [31] L. Clotea, A. Forcos, C. Marinescu, and M. Georgescu. Power losses analysis of two-level and three-level neutral clamped inverters for a wind pump storage system. In *Proc. 12th Int. Conf. Optimization of Electrical and Electronic Equipment*, pages 1174–1179, 2010.

## Chapter References

---

- [32] E. Pouresmaeil, O. Gomis-Bellmunt, D. Montesinos-Miracle, and J. Bergas-Jané. Multilevel converters control for renewable energy integration to the power grid. *Energy*, 36(2):950–963, February 2011.
- [33] T. Zhou, H. Fakham, and B. Francois. Design of a power management system for an active PV station including various storage technologies. In *Proc. 13th EPE-PEMC*, pages 2142–2149, 2008.
- [34] J. Sun and H. Grotstollen. Averaged modelling of switching power converters: reformulation and theoretical basis. In *Proc. 23rd Annu. IEEE PESC*, pages 1165–1172 vol.2. July 1992.
- [35] P. Rodriguez, A. Luna, M. Ciobotaru, R. Teodorescu, and F. Blaabjerg. Advanced grid synchronization system for power converters under unbalanced and distorted operating conditions. In *Proc. 32nd Annu. IECON*, pages 5173–5178, November 2006.
- [36] F.J. Rodriguez, E. Bueno, M. Aredes, L.G.B. Rolim, F.A.S. Neves, and M.C. Cavalcanti. Discrete-time implementation of second order generalized integrators for grid converters. In *Proc. 34th Annu. IEEE IECON*, pages 176–181, November 2008.
- [37] G.M.S. Azevedo, F.A.S. Neves, M.C. Cavalcanti, L.R. Limongi, and F. Bradaschia. Fault detection system for distributed generation converters. In *Proc. COBEP*, pages 320–327, September 2011.
- [38] L.G. Franquelo, J. Rodriguez, J.I. Leon, S. Kouro, R. Portillo, and M.A.M. Prats. The age of multilevel converters arrives. *IEEE Ind. Electron. Magazine*, 2(2):28–39, June 2008.
- [39] I. Colak, E. Kabalci, and R. Bayindir. Review of multilevel voltage source inverter topologies and control schemes. *Energy Conversion and Management*, 52(2):1114–1128, February 2011.

- [40] K. H. Bhalodi and P. Agarwal. Space vector modulation with DC-Link voltage balancing control for Three-Level inverters. *Int. J. Recent Trends in Engineering*, 1(3):229–233, May 2009.
- [41] N. Celanovic and D. Boroyevich. A comprehensive study of neutral-point voltage balancing problem in three-level neutral-point-clamped voltage source PWM inverters. *IEEE Trans. Power Electron.*, 15(2):242–249, March 2000.
- [42] I. Pereira and A. Martins. Experimental comparison of carrier and space vector PWM control methods for Three-Phase NPC converters. In *Proc. Int. Conf. on Renewable Energies and Power Quality*, 2009.
- [43] J. Pou, J. Zaragoza, S. Ceballos, M. Saeedifard, and D. Boroyevich. A Carrier-Based PWM strategy with Zero-Sequence voltage injection for a Three-Level Neutral-Point-Clamped converter. *IEEE Trans. Power Electron.*, 27(2):642–651, February 2012.
- [44] D. Grahame Holmes and T. A. Lipo. *Pulse width modulation for power converters: principles and practice*. Wiley-IEEE, 2003.
- [45] A.M. Massoud, S.J. Finney, and B.W. Williams. Control techniques for multilevel voltage source inverters. In *Proc. 34th Annu. IEEE PESC*, volume 1, pages 171–176, 2003.
- [46] M. Malinowski and S. Bernet. Simple control scheme of Three-Level PWM converter connecting wind turbine with grid. In *ICREPO*, March 2004.
- [47] T. L Vandoorn, B. Renders, L. Degroote, B. Meersman, and L. Vandevelde. Active load control in islanded microgrids based on the grid voltage. *IEEE Trans. Smart Grid*, 2(1):139–151, March 2011.
- [48] A.K. Gupta and A.M. Khambadkone. A general space vector PWM algorithm for multilevel inverters, including operation in overmodulation range. *IEEE Trans. Power Electron.*, 22(2):517–526, 2007.

## Chapter References

---

- [49] D. Zhao, P.K. Hari, G. Narayanan, and R. Ayyanar. Space-Vector-Based hybrid pulsewidth modulation techniques for reduced harmonic distortion and switching loss. *IEEE Trans. Power Electron.*, 25(3):760–774, 2010.





# CHAPTER 4

## 3LNPC converter for HESS control

---

### Contents

---

<b>4.1</b>	<b>Main characteristics of a 3LNPC converter . . . . .</b>	<b>124</b>
<b>4.2</b>	<b>Switching level analysis . . . . .</b>	<b>126</b>
4.2.1	Neutral point voltage unbalance effect . . . . .	132
4.2.2	Switching model . . . . .	136
<b>4.3</b>	<b>Modulation strategies . . . . .</b>	<b>137</b>
4.3.1	Space Vector Modulation . . . . .	138
4.3.2	Carrier-based PWM . . . . .	138
4.3.3	Relationship between SVM and carrier-based PWM . .	141
<b>4.4</b>	<b>Operational limits of 3LNPC . . . . .</b>	<b>152</b>
4.4.1	Balanced DC side voltages . . . . .	154
4.4.2	Unbalanced DC side voltages . . . . .	159
<b>4.5</b>	<b>DC bus voltage selection . . . . .</b>	<b>165</b>
<b>4.6</b>	<b>Chapter conclusions . . . . .</b>	<b>166</b>
	<b>Chapter References . . . . .</b>	<b>167</b>

---

This chapter analyses in detail the use of a 3LNPC converter in an HESS power flow control application. A comparison among different modulation strategies is carried out from the point of view of the power division between a SC bank and a redox battery. The THIPWM modulation strategy is selected from this analysis. At the same time, the effect of the different variables that affect the DC side currents of the three-level converter are analysed separately. From this analysis the operational limits of the 3LNPC converter from the DC power division point of view are fixed for the entire operation range of the converter.

## 4.1 Main characteristics of a 3LNPC converter

The 3LNPC converter is a type of DC-AC power conversion system that uses two DC bus voltage levels. A 3LNPC converter is considered especially interesting for medium-voltage high power applications due to its ability to reduce the voltage ratings of the semiconductor devices to the half in comparison to a typical two-level converter. The structure of the 3LNPC converter is schematically shown in Figure 4.1.

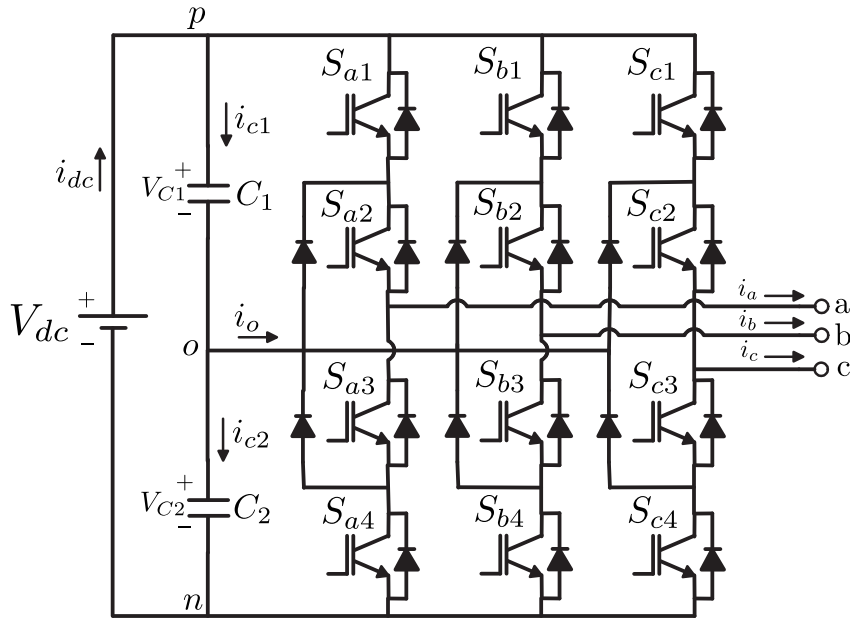


Figure 4.1: Structure of a 3LNPC converter.

The 3LNPC converter was first presented by *A. Nabae, I. Takahashi, and H. Akagi* in [1]. Their objective was to increase the power of the converter increasing the voltage rather than the current. Using this new topology, each power device has to stand, at the most, half voltage compared with the two-level case with the same dc-link voltage. Therefore, if these power semiconductors have the same characteristics as the two-level case, the voltage can be doubled [2].

A 3LNPC converter has many advantages in comparison to the common two-level converter, which are fundamentally focused on improvements in the output signal quality and on the increase of the nominal power of the converter

#### 4.1. Main characteristics of a 3LNPC converter

---

[2].

The most important advantages of a 3LNPC in comparison to a two-level converter are summarised in the following list:

- Less distorted AC voltage generation. As a direct consequence, the output filters do not need to be so restrictive and therefore their size can be reduced [3].
- Higher nominal power for the same switching devices. If the power losses of a three-level converter and a two-level converter are compared in the same conditions, it can be seen that the power losses of the 3LNPC are smaller due to the reduced voltage rating of the switches, while the current is the same in both cases [4].
- Reduced  $dv/dt$  of the output voltage due to the higher amount of DC levels [3, 5].
- Smaller DC side current distortion [3].
- Lower electromagnetic interference problems [6].

However, the high amount of switches as well as the use of more than one DC bus voltage level creates some problems that are not present in a two-level converter. The most important disadvantages of a 3LNPC converter are summarised below:

- Neutral point voltage balancing. This is a well-known issue that has been extensively analysed and which can be solved using different methods.
- The increased number of switches makes the control of this converter more complicated [7, 8].

The developments in the semiconductor elements and the computational capacity of digital processors have facilitated the increase of the use of 3LNPC converters. 3LNPC converters have been used in large motor drives like

conveyors, pumps, fans, and mills, among others, which offer solutions for industries including oil and gas, metals, power, mining, water, marine, and chemistry. Another application has been the back-to-back configuration for regenerative applications like for example in grid interfacing of RES [2, 6, 9].

However, in this work the 3LNPC power converter has been used to control the power flow of a HESS due to the possibilities offered by the high amount of switching devices of the mentioned converter.

## 4.2 Switching level analysis

This section introduces the switching model of the 3LNPC, model that is used afterwards to obtain the average model necessary to determine the operational limits of the controller.

The 3LNPC converter has 12 switches, 4 per phase. If all the switching combinations are taken into account, there are  $2^4 = 16$  different combinations in each phase (2 states, 0 and 1, and 4 switches that can have those states). However, only 2 switches per phase are independent, the others are commutated in a complementary way. In this work, the first two vertical switches are supposed to be the independent ones, i.e.  $S_{p1}$  and  $S_{p2}$  according to Figure 4.1.  $S_{p3}$  and  $S_{p4}$  are commutated using the complementary signals of  $S_{p1}$  and  $S_{p2}$  respectively ( $p$  refers to the phase,  $a$ ,  $b$  or  $c$ ). The complementary commutation of the switches limits the number of existing combinations to  $2^2 = 4$  per phase. However, this number is reduced even more due to the fact of having an inductance (which acts as a filter to eliminate the high frequency component added by the commutations) in the AC side of the converter. When a current flows through an inductance, it stores energy in its magnetic field. If the circuit is opened and the inductance has no electric way to give the stored energy back, this energy will generate a very high voltage in the inductance, an event that can destroy the switching circuitry. Consequently, in order to avoid the mentioned problem, each AC phase is always connected to the  $p$ ,  $o$  or  $n$  point of the DC side. If the inner two switches,  $S_{p2}$  and  $S_{p3}$ , are opened,

## 4.2. Switching level analysis

the phase is floating and the inductance has no way to discharge its energy. Therefore, this configuration must be avoided, which limits the number of switching possibilities to 3 per phase. Thus, the final number of combinations or switching vectors that can be obtained using a 3LNPC converter is  $3^3 = 27$ .

These 27 switching vectors are shown in Table 4.1. This table shows as well the point to which each phase is connected in each switching configuration.

Vector	$S_{a1}$	$S_{a2}$	$S_{b1}$	$S_{b2}$	$S_{c1}$	$S_{c2}$	a	b	c
1	0	0	0	0	0	0	n	n	n
2	0	0	0	0	0	1	n	n	o
3	0	0	0	0	1	1	n	n	p
4	0	0	0	1	0	0	n	o	n
5	0	0	0	1	0	1	n	o	o
6	0	0	0	1	1	1	n	o	p
7	0	0	1	1	0	0	n	p	n
8	0	0	1	1	0	1	n	p	o
9	0	0	1	1	1	1	n	p	p
10	0	1	0	0	0	0	o	n	n
11	0	1	0	0	0	1	o	n	o
12	0	1	0	0	1	1	o	n	p
13	0	1	0	1	0	0	o	o	n
14	0	1	0	1	0	1	o	o	o
15	0	1	0	1	1	1	o	o	p
16	0	1	1	1	0	0	o	p	n
17	0	1	1	1	0	1	o	p	o
18	0	1	1	1	1	1	o	p	p
19	1	1	0	0	0	0	p	n	n
20	1	1	0	0	0	1	p	n	o
21	1	1	0	0	1	1	p	n	p
22	1	1	0	1	0	0	p	o	n
23	1	1	0	1	0	1	p	o	o
24	1	1	0	1	1	1	p	o	p
25	1	1	1	1	0	0	p	p	n
26	1	1	1	1	0	1	p	p	o
27	1	1	1	1	1	1	p	p	p

Table 4.1: The 27 different switching vectors that can be generated by a 3LNPC converter.

If it is assumed that the AC load connected to the 3LNPC converter is balanced and the two input voltages have the same voltage, equal to  $\frac{V_{dc}}{2}$ , the voltages that will be generated in each phase in  $abc$  and  $\alpha\beta$  reference systems are the ones shown in Table 4.2.

Using the results shown in Table 4.2 the space vector diagram shown in Figure 4.2 can be constructed. This diagram shows all the 27 different vectors that is able to create a 3LNPC converter. Depending on the state of the switches, the voltage of the upper or lower voltage source will be used, as it was shown in Table 4.2.

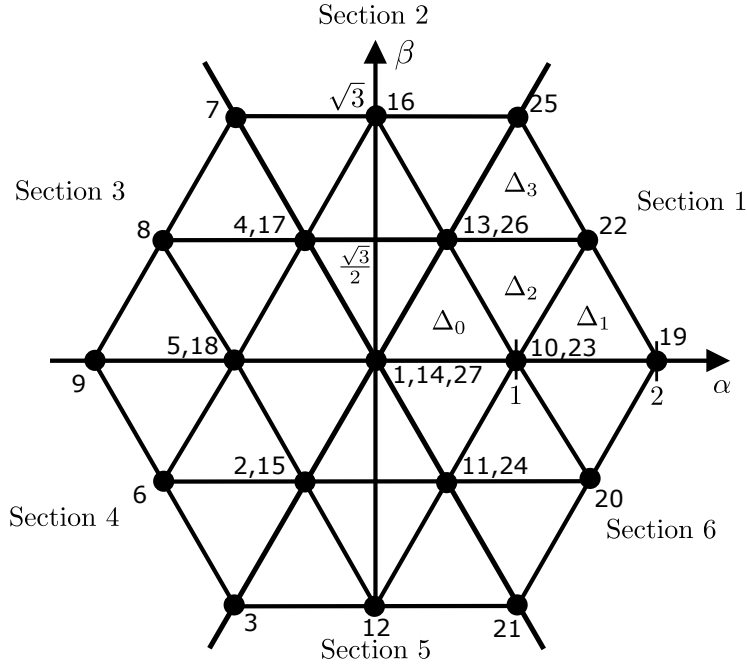


Figure 4.2: Space vector diagram of a 3LNPC in the balanced neutral point voltage case.

From the switching diagram Figure 4.2, it can be seen that the existing switching vectors can be classified in five main groups:

- Null redundant vectors (only  $p$ ,  $n$  or  $o$  connections): 1, 14, 27
- Small upper redundant vectors (no  $p$  connection): 2, 4, 5, 10, 11, 13
- Small lower redundant vectors (no  $n$  connection): 15, 17, 18, 23, 24, 26

## 4.2. Switching level analysis

Vector	$V_{an}$	$V_{bn}$	$V_{cn}$	$V_\alpha$	$V_\beta$
1	0	0	0	0	0
2	$\frac{-V_2}{3}$	$\frac{-V_2}{3}$	$\frac{2V_2}{3}$	$\frac{-V_2}{2}$	$\frac{-\sqrt{3}V_2}{2}$
3	$\frac{-(V_1+V_2)}{3}$	$\frac{-(V_1+V_2)}{3}$	$\frac{2(V_1+V_2)}{3}$	$\frac{-(V_1+V_2)}{2}$	$\frac{-\sqrt{3}(V_1+V_2)}{2}$
4	$\frac{-V_2}{3}$	$\frac{2V_2}{3}$	$\frac{-V_2}{3}$	$\frac{-V_2}{2}$	$\frac{\sqrt{3}V_2}{2}$
5	$\frac{-2V_2}{3}$	$\frac{V_2}{3}$	$\frac{V_2}{3}$	$-V_2$	0
6	$\frac{-2(V_1+V_2)}{3}$	$\frac{V_2-V_1}{3}$	$\frac{2V_1+V_2}{3}$	$-V_2 - \frac{V_1}{2}$	$\frac{-\sqrt{3}V_1}{2}$
7	$\frac{-(V_1+V_2)}{3}$	$\frac{2(V_1+V_2)}{3}$	$\frac{-(V_1+V_2)}{3}$	$\frac{-(V_1+V_2)}{2}$	$\frac{\sqrt{3}(V_1+V_2)}{2}$
8	$\frac{-(2V_2+V_1)}{3}$	$\frac{2V_1+V_2}{3}$	$\frac{V_2-V_1}{3}$	$\frac{-V_1}{2} - V_2$	$\frac{\sqrt{3}V_1}{2}$
9	$\frac{-2(V_1+V_2)}{3}$	$\frac{V_1+V_2}{3}$	$\frac{V_1+V_2}{3}$	$-V_1 - V_2$	0
10	$\frac{2V_2}{3}$	$\frac{-V_2}{3}$	$\frac{-V_2}{3}$	$V_2$	0
11	$\frac{V_2}{3}$	$\frac{-2V_2}{3}$	$\frac{V_2}{3}$	$\frac{V_2}{2}$	$\frac{-\sqrt{3}V_2}{2}$
12	$\frac{V_2-V_1}{3}$	$\frac{-(2V_2+V_1)}{3}$	$\frac{2V_1+V_2}{3}$	$\frac{-V_1}{2} + \frac{V_2}{2}$	$\frac{-\sqrt{3}(V_1+V_2)}{2}$
13	$\frac{V_2}{3}$	$\frac{V_2}{3}$	$\frac{-2V_2}{3}$	$\frac{V_2}{2}$	$\frac{\sqrt{3}V_2}{2}$
14	0	0	0	0	0
15	$\frac{-V_1}{3}$	$\frac{-V_1}{3}$	$\frac{2V_1}{3}$	$\frac{-V_1}{2}$	$\frac{-\sqrt{3}V_1}{2}$
16	$\frac{V_2-V_1}{3}$	$\frac{2V_1+V_2}{3}$	$\frac{-(2V_2+V_1)}{3}$	$\frac{V_2-V_1}{2}$	$\frac{\sqrt{3}(V_1+V_2)}{2}$
17	$\frac{-V_1}{3}$	$\frac{2V_1}{3}$	$\frac{-V_1}{3}$	$\frac{-V_1}{2}$	$\frac{\sqrt{3}V_1}{2}$
18	$\frac{-2V_1}{3}$	$\frac{V_1}{3}$	$\frac{V_1}{3}$	$-V_1$	0
19	$\frac{2(V_1+V_2)}{3}$	$\frac{-(V_1+V_2)}{3}$	$\frac{-(V_1+V_2)}{3}$	$V_1 + V_2$	0
20	$\frac{2V_1+V_2}{3}$	$\frac{-(V_1+V_2)}{3}$	$\frac{V_2-V_1}{3}$	$V_1 + \frac{V_2}{2}$	$\frac{-\sqrt{3}V_2}{2}$
21	$\frac{V_1+V_2}{3}$	$\frac{-2(V_1+V_2)}{3}$	$\frac{V_1+V_2}{3}$	$\frac{V_1+V_2}{2}$	$\frac{-\sqrt{3}(V_1+V_2)}{2}$
22	$\frac{2V_1+V_2}{3}$	$\frac{V_2-V_1}{3}$	$\frac{-(V_1+2V_2)}{3}$	$V_1 + \frac{V_2}{2}$	$\frac{\sqrt{3}V_2}{2}$
23	$\frac{2V_1}{3}$	$\frac{-V_1}{3}$	$\frac{-V_1}{3}$	$V_1$	0
24	$\frac{V_1}{3}$	$\frac{-2V_1}{3}$	$\frac{V_1}{3}$	$\frac{V_1}{2}$	$\frac{-\sqrt{3}V_1}{2}$
25	$\frac{V_1+V_2}{3}$	$\frac{V_1+V_2}{3}$	$\frac{-2(V_1+V_2)}{3}$	$\frac{V_1+V_2}{2}$	$\frac{-\sqrt{3}(V_1+V_2)}{2}$
26	$\frac{V_1}{3}$	$\frac{V_1}{3}$	$\frac{-2V_1}{3}$	$\frac{V_1}{2}$	$\frac{\sqrt{3}V_1}{2}$
27	0	0	0	0	0

Table 4.2: Phase-neutral voltages and their  $\alpha\beta$  transforms.

- Medium vectors (all connections,  $p, n$  and  $o$ ): 6, 8, 12, 16, 20, 22
- Large vectors (no  $o$  connection): 3, 7, 9, 19, 21, 25

Figure 4.3 shows the configuration of the three-level converter in each one of the mentioned switching vector types. The AC loads have been simulated by a balanced current source system. This allows to relate the DC bus current with the AC side currents according to the switching orders. At the same time, using ideal current sources it is easy to simulate different load power factors and analyse their effect on the DC side. Null vectors are neglected as they do not allow any current flow. Figure 4.3a corresponds to a small upper redundant vector, Figure 4.3b to a small lower redundant vector, Figure 4.3c to a medium vector and Figure 4.3d to a large vector.

A neutral point unbalance will appear if the neutral point current  $i_o$  is different from zero. It can be seen from Figure 4.3 that the configurations that can affect the neutral point unbalance are the small redundant and medium vectors. Large vectors will not affect the neutral point unbalance, as the same current will flow through both capacitors, charging or discharging them at the same rate.

Using the values of the load current  $i_{abc}$  of each configuration, the DC side currents  $i_o$ ,  $i_{c1}$  and  $i_{c2}$  can be readily obtained. Table 4.3 shows the values of the DC side and AC side currents in function of the  $i_{abc}$  currents.

Several conclusions can be obtained from Table 4.3. As it was stated previously, the large vectors cannot alter the neutral point voltage, only small and medium vectors have that possibility. However, in the case of the small redundant vectors they can be used in such a way that the average neutral point unbalance is null. This affirmation can be better explained with an example: in the case of the  $nno$  (small upper redundant vector, number 2) and  $oop$  (small lower redundant vector, number 15) vectors, it can be seen from Figure 4.2 that both create the same AC side voltage, as they are located in the same location in the space vector diagram. However, even if from the AC side point of view there is no difference between both vectors, the configuration



## 4.2. Switching level analysis

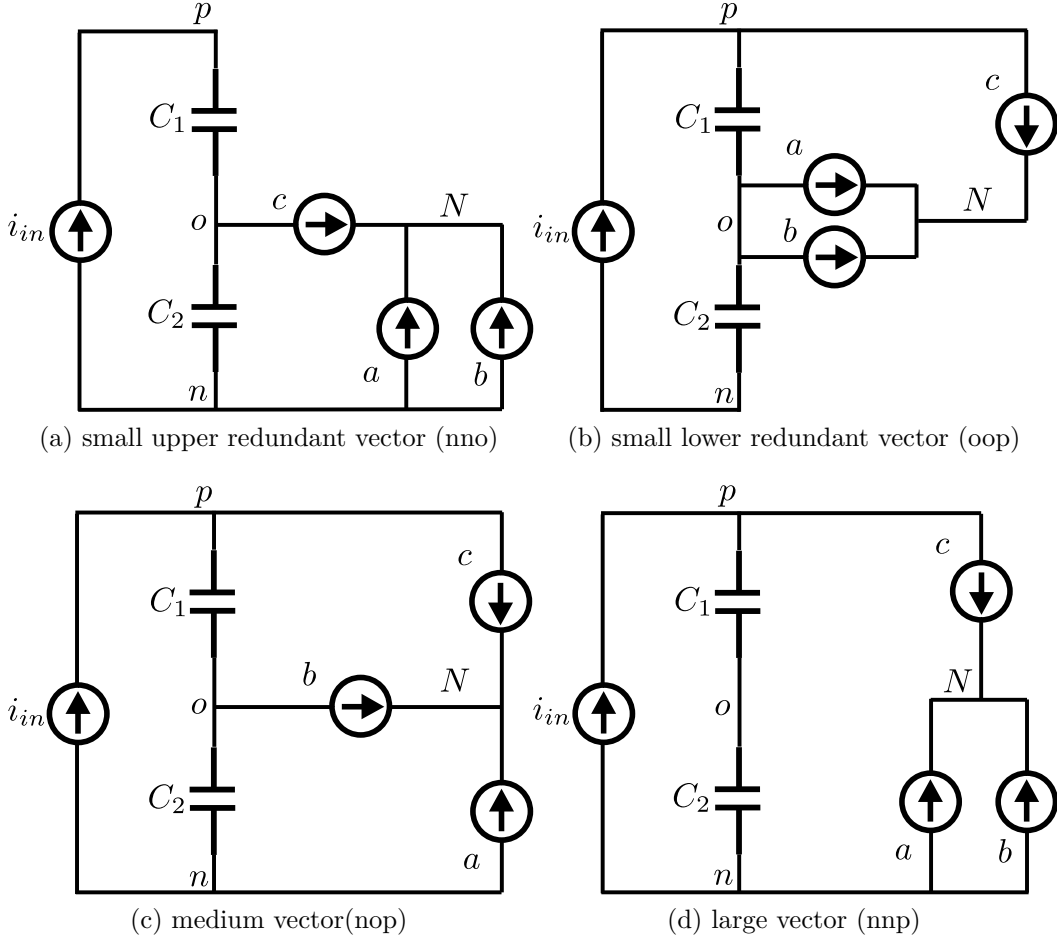


Figure 4.3: Configurations of the different vector types.

of the DC side is different in each case, as it is shown in Figure 4.3a and Figure 4.3b. From Table 4.3 it can be seen that the vector *nno* and *oop* create opposite  $i_o$  currents. Consequently, instead of using only one of them, if both are successively used during the same time, the average effect on the neutral point voltage will be null. In the case of the medium vectors there is not any possibility of controlling their effect on the neutral point voltage; therefore small redundant vectors must be used to compensate their effect.

Redundant vectors are typically used to avoid the neutral point unbalance. In this thesis the redundant vectors will be used to control the power flow of the input storage devices. It can be seen from Table 4.3 that using the

Vector	Conf.	$i_o$	$i_{c1}$	$i_{c2}$
Upper	nno	$i_c$		$i_{in} - i_c$
	non	$i_b$		$i_{in} - i_b$
	noo	$-i_a$	$i_{in}$	$i_{in} + i_a$
	onn	$i_a$		$i_{in} - i_a$
	ono	$-i_b$		$i_{in} + i_b$
	oon	$-i_c$		$i_{in} + i_c$
Lower	oop	$-i_c$	$i_{in} - i_c$	
	opo	$-i_b$	$i_{in} - i_b$	
	opp	$i_a$	$i_{in} + i_a$	$i_{in}$
	poo	$-i_a$	$i_{in} - i_a$	
	pop	$i_b$	$i_{in} + i_b$	
	ppo	$i_c$	$i_{in} + i_c$	
Medium	nop	$i_b$	$i_{in} - i_c$	$i_{in} + i_a$
	npo	$i_c$	$i_{in} - i_b$	$i_{in} + i_a$
	onp	$i_a$	$i_{in} - i_c$	$i_{in} + i_b$
	opn	$i_a$	$i_{in} - i_b$	$i_{in} + i_c$
	pno	$i_c$	$i_{in} - i_a$	$i_{in} + i_b$
	pon	$i_b$	$i_{in} - i_a$	$i_{in} + i_c$
Large	nnp		$i_{in} - i_c$	
	npn		$i_{in} - i_b$	
	npp	0	$i_{in} + i_a$	
	pnn		$i_{in} - i_a$	
	pnp		$i_{in} + i_b$	
	ppn		$i_{in} + i_c$	

Table 4.3: Relation between AC and DC currents in each switching vector.

redundant vectors it is possible to control the  $i_o$  current. As the currents of both input capacitors are related by this current, the control of  $i_o$  has as a consequence the control of the currents of the capacitors as well. However, the system has some limitations that must be taken into account and that will be analysed in Section 4.4.

### 4.2.1 Neutral point voltage unbalance effect

Figure 4.2 shows the vectors of the space vector diagram for the case where the neutral point voltage is balanced, i.e. the two input voltage sources have the

## 4.2. Switching level analysis

same value. However, using the results shown in Table 4.2, a voltage difference in the two voltage sources creates differences in the location of the switching vectors. Consequently, the neutral point unbalance changes the space vector diagram from Figure 4.2 to Figure 4.4. A difference in the voltage of the input sources creates differences in the redundant vectors, which at the same time will generate differences in the current supplied or absorbed by each source.

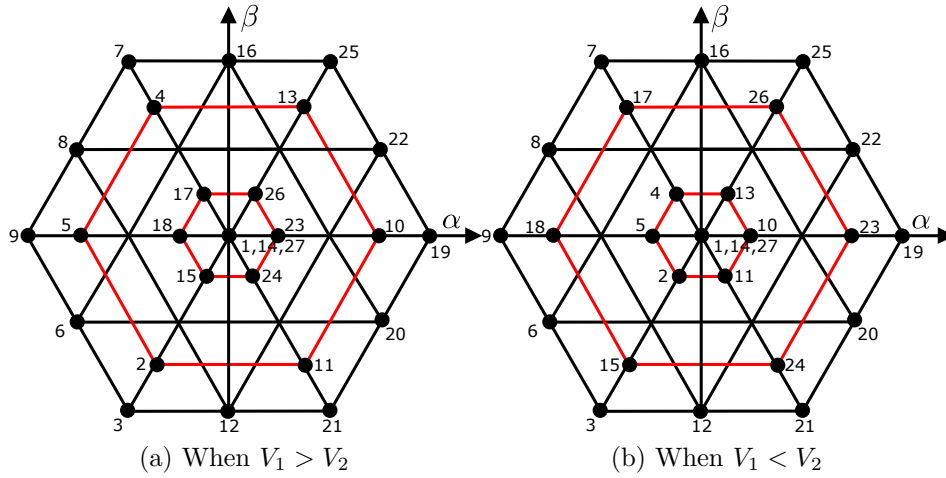


Figure 4.4: Effect of neutral point unbalances on the space vector diagram.

Due to the voltage difference in the two input sources, if a typical modulation strategy is employed, the AC side voltages generated by the inverter will not have a zero average value. Figure 4.5 shows the effect on the AC side voltage when the DC side voltages are varied in the range  $[250, 450]$  V and the 3LNPC converter operates in open loop with a SPWM strategy, a modulation index of 1 and a resistive and balanced load.

Due to the voltage difference between the two voltage inputs, the AC side voltages will have an average value different from zero, as it is shown in Figure 4.5.

A solution to this problem was presented in [5]. This solution can be applied in multicarrier PWM modulation strategies, and it is based on the variation of the amplitudes of the carrier signals. It is proved in [5] that in the case of a three-level converter, where two carrier signals are used, a variation

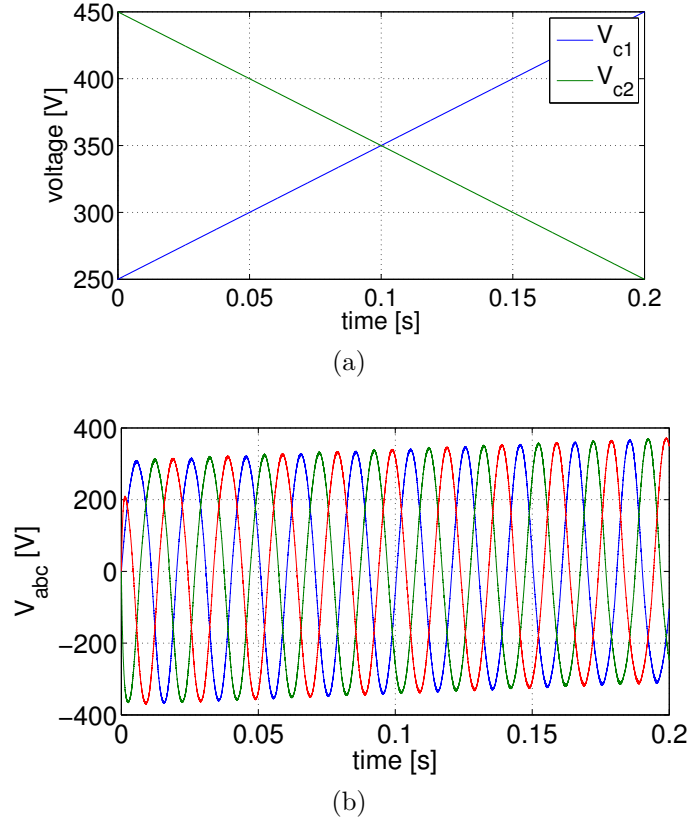


Figure 4.5: (a) Variations in the DC voltage sources, (b)  $V_{abc}$  voltages.

of the amplitudes ( $A_{c1}, A_{c2}$ ) of those carrier signals explained in eq. (4.1) is able to generate a correct zero average value AC side voltages even if the DC side voltages have a different value.

$$\begin{aligned} A_{c1} &= \frac{2V_{c1}}{V_{c1} + V_{c2}} \\ A_{c2} &= \frac{2V_{c2}}{V_{c1} + V_{c2}} \end{aligned} \quad (4.1)$$

In this thesis the same method has been used to solve the mentioned problem, but instead of changing the amplitudes of the carrier signals, the same effect has been achieved changing the modulating signals. The practical implementation of the adapted solution was easier than the use of variable carrier amplitudes. The modified amplitudes of the carrier signals obtained from eq. (4.1) are used to vary the input modulating signal  $d_i$ . Following the

## 4.2. Switching level analysis

modification of the modulating signals represented by eq. (4.2) the carrier signals can be maintained as in a balanced multicarrier PWM, as the applied modification will eliminate the negative effect of the unbalanced voltages of the DC side. In eq. (4.2)  $d_{i_1}$  and  $d_{i_2}$  represent the duty cycles of the switches  $S_{i_1}$  and  $S_{i_2}$  respectively, and  $i$  represents each one of the  $abc$  phases.

$$\begin{aligned} d_{i_1} &= \frac{A_{c1} - 1 + d_i}{A_{c1}} \\ d_{i_2} &= \frac{A_{c1} - 1 + d_i}{A_{c2}} \end{aligned} \quad (4.2)$$

Using eq. (4.2) the modulating signal is varied in its amplitude and offset, emulating exactly the same effect as the amplitude variation of the carrier signals shown by eq. (4.1). Figure 4.6 shows the comparison between the two methods presented to compensate the voltage unbalance of the DC side. The comparison has been carried out in open loop, with a modulation index of 1 and a resistive and balanced load.

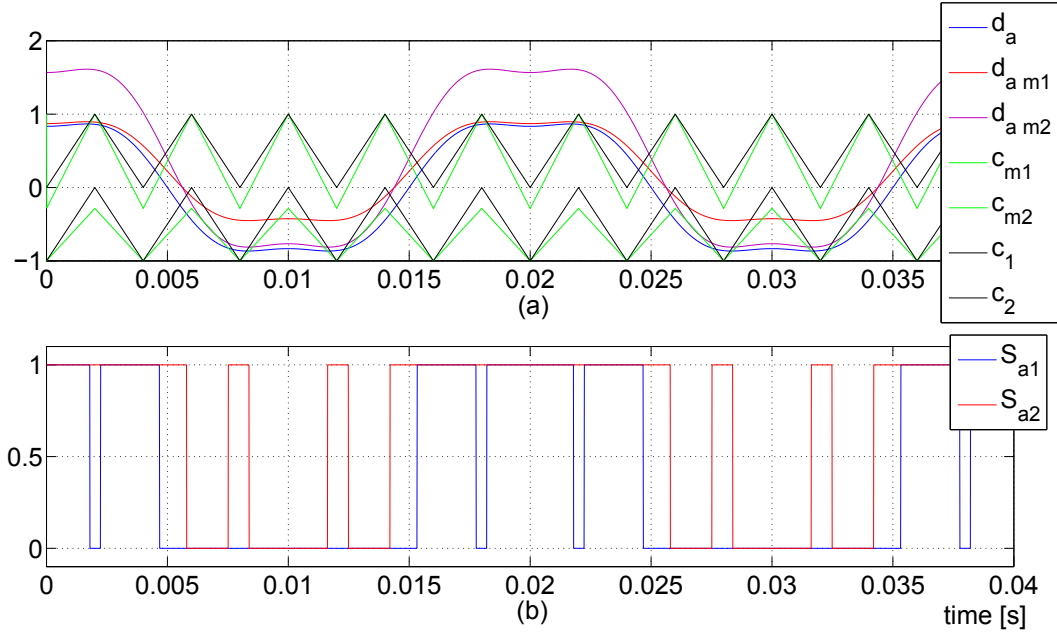


Figure 4.6: Comparison between the modification of the carrier signals and of the modulating signal.

Figure 4.6(a) shows the modulating signals and the carrier signals for

the two analysed cases:  $d_a$  and  $c_{m1}, c_{m2}$  represent the modification of the amplitudes of the carrier signals and  $d_{am1}, d_{am2}$  and  $c_1, c_2$  the modification of the modulating signals. Figure 4.6(b) shows the resulting switching signals. It can be seen from this figure that using both methods the resulting switching signals are exactly the same, as the signals are superposed.

### 4.2.2 Switching model

The switching model of the 3LNPC is formed by a group of equations that relate the AC side variables with the DC side variables. These relations are given in function of currents, voltages and the switching orders of the switches. The switching model assumes that the switches are ideal, i.e. there are no voltage drops in on state, in off state the switches are open circuits and the commutation times are 0. From Figure 4.1 and using the 27 different switching vectors that can be used in the 3LNPC converter, which are shown in Table 4.1, the relation among the AC phase-to-0 voltage and the DC side voltages can be readily obtained. These equations are shown in eq. (4.3).

$$\begin{aligned} V_{a0} &= S_{a1}S_{a2}V_{c1} - S_{a3}S_{a4}V_{c2} \\ V_{b0} &= S_{b1}S_{b2}V_{c1} - S_{b3}S_{b4}V_{c2} \\ V_{c0} &= S_{c1}S_{c2}V_{c1} - S_{c3}S_{c4}V_{c2} \end{aligned} \quad (4.3)$$

The relation among the phase, DC currents and switches can be obtained in a similar manner, analysing the conducting elements according to the sign of the phase current, as it is shown in eqs. (4.4) and (4.5).

$$\begin{aligned} i_a &= S_{a1}S_{a2}i_1 + (1 - S_{a1})S_{a2}i_0 + S_{a3}S_{a4}i_n \\ i_b &= S_{b1}S_{b2}i_1 + (1 - S_{b1})S_{b2}i_0 + S_{b3}S_{b4}i_n \\ i_c &= S_{c1}S_{c2}i_1 + (1 - S_{c1})S_{c2}i_0 + S_{c3}S_{c4}i_n \end{aligned} \quad (4.4)$$

$$\begin{aligned} i_1 &= S_{a1}S_{a2}i_a + S_{b1}S_{b2}i_b + S_{c1}S_{c2}i_c \\ i_0 &= (1 - S_{a1})S_{a2}i_a + (1 - S_{b1})S_{b2}i_b + (1 - S_{c1})S_{c2}i_c \\ i_n &= S_{a3}S_{a4}i_a + S_{b3}S_{b4}i_b + S_{c3}S_{c4}i_c \end{aligned} \quad (4.5)$$

### 4.3. Modulation strategies

---

The equations of the currents of DC side capacitors can be easily obtained from eq. (4.5) and are shown in eq. (4.6).

$$\begin{aligned} i_{c1} &= i_{dc} - S_{a1}S_{a2}i_a - S_{b1}S_{b2}i_b - S_{c1}S_{c2}i_c \\ i_{c2} &= i_{dc} - (S_{a1}S_{a2} + S_{a2}S_{a3})i_a - (S_{b1}S_{b2} + S_{b2}S_{b3})i_b - (S_{c1}S_{c2} + S_{c2}S_{c3})i_c \end{aligned} \quad (4.6)$$

Knowing that  $S_{i1}S_{i2} = S_{i1}$  and  $(S_{a1}S_{a2} + S_{a2}S_{a3}) = S_{a2}$ , eq. (4.6) are simplified to eq. (4.7).

$$\begin{aligned} i_{c1} &= i_{dc} - S_{a1}i_a - S_{b1}i_b - S_{c1}i_c \\ i_{c2} &= i_{dc} - S_{a2}i_a - S_{b2}i_b - S_{c2}i_c \end{aligned} \quad (4.7)$$

Once the switching model has been defined the average equations of the 3LNPC converter can be obtained applying the well known averaging method. This way, eq. (4.7) has been averaged, obtaining eq. (4.8).

$$\begin{aligned} i_{c1} &= i_{dc} - d_{a1}i_a - d_{b1}i_b - d_{c1}i_c \\ i_{c2} &= i_{dc} - d_{a2}i_a - d_{b2}i_b - d_{c2}i_c \end{aligned} \quad (4.8)$$

eq. (4.8) will be used in Section 4.4 to determine the operational limits of the 3LNPC in its entire operation range. Those limits are used afterwards to design a rule-based control algorithm for the zero-sequence injection regulation in Chapter 5.

### 4.3 Modulation strategies

A modulation strategy is a method that is used to generate the switching signals for the power converter in order to generate the desired output voltage or current signal. The modulation strategies of 3LNPC converters, when they work at high switching frequency, can be roughly divided in two main groups: sine-triangle PWM and SVM [10, 11]. Typical two-level modulation methods have been extended to three-level converters with consistent results [12]. The following two subsections shortly introduce the most important details of the mentioned modulation strategies.

### 4.3.1 Space Vector Modulation

The SVM is a method of synthesising the voltage of a DC-AC converter. It is based on the use of the different switching vectors that the analysed converter is able to use. The vectors that can be used in a 3LNPC are 27, as it was explained in Section 4.2, and they were summarised in Tables 4.1 and 4.2. These 27 vectors can be represented in a 3D diagram if the *abc* reference system is used. However, if the Clarke transform is applied (Appendix B), this diagram is simplified to a 2D one as the zero-sequence has no effect. This holds only if the system is a three-phase three-wire one and the neutral is not connected to the neutral point of the DC side. The mentioned 2D diagram is shown in Figure 4.2 for the case where the DC side voltages are balanced. The unbalanced case has been analysed in Section 4.2.1.

The voltage reference vector that must be generated by the converter in each moment can be represented in that 2D diagram, and it is possible to synthesise it using several combinations of different switching vectors. Due to the elevated number of switching vectors that can be used, there are several SVM methods that make a different use of those vectors in order to satisfy different requirements. According to the on-time of each switching vector the generated voltage will be different and therefore those times must be carefully defined. A survey of the different SVM algorithms that define several methods to determine the vectors that are used and to calculate their on-time can be found in [13].

### 4.3.2 Carrier-based PWM

The base of the carrier-based PWM methods is the comparison between a modulating signal (typically generated by a control algorithm to satisfy the regulation requirements) and a carrier signal (a triangular signal of fixed amplitude and frequency) in order to generate the switching orders. The frequency of the carrier signal is generally several orders of magnitude higher than the frequency of the modulating signal. The factor that defines the relation between these two frequencies is called frequency modulation ratio ( $m_f$ ) and



### 4.3. Modulation strategies

---

it is defined by eq. (4.9). At the same time, the amplitude modulation ratio or modulation index ( $m_a$  or  $m$ ) defines the relation between the amplitudes of the carrier signal ( $A_c$ ) and the modulating signal ( $A_m$ ), as specified by eq. (4.10) [14].

$$m_f = \frac{f_c}{f_m} \quad (4.9)$$

$$m_a = \frac{A_m}{A_c} \quad (4.10)$$

The simplest carrier-based PWM is the one formed by a sinusoidal modulating signal ( $m_p$ ) and a carrier signal ( $c_p$ ). This structure is used in the two-level converters to generate the switching signals of a phase following eq. (4.11). The complementary signal of  $S_p$  must be generated applying a dead-time in order to avoid short-circuits.

$$\begin{aligned} S_p &= 1 \text{ if } m_p \geq c_p \\ S_p &= 0 \text{ if } m_p < c_p \end{aligned} \quad (4.11)$$

In the case of a three-level converter, there are four switches per phase, which are switched in pairs:  $S_{p1} - S_{p3}$  and  $S_{p2} - S_{p4}$ , according to the nomenclature shown in Figure 4.1. Consequently, there are only two independent switching signals ( $S_{p1}$  and  $S_{p2}$ ) in each phase, as the other two signals are the complementary of the mentioned ones. Therefore, it is necessary to change the PWM method of the typical two-level converter in order to generate the necessary number of switching signals. This task is carried out increasing the number of carrier signals according to the number of levels of the converter. The number of carrier signals must be adapted to the number of levels  $n$  of the multilevel converter according to the expression  $n - 1$  [2]. The peak-to-peak value of those carriers is selected using the expression eq. (4.12) [15].

$$A_{pp} = \frac{2}{n - 1} \quad (4.12)$$

Once the number of carrier signals and their amplitudes have been selected, the last parameter to be defined is the phase difference among them. There

are three main possibilities for carrier disposition [15]:

- Phase disposition: all carriers are in phase.
- Phase opposition disposition: carriers above the sinusoidal reference zero point are  $\pi$  rad out of phase with those below the zero point.
- Alternate phase opposition disposition: each carrier is phase shifted by  $\pi$  rad from its adjacent carrier.

In the case of three-phase systems, the most used solution is the one where all carrier signals are in phase, as the switching frequency harmonic is cancelled out when looking into the line-to-line voltages. Additionally, most of the remaining harmonics have lower amplitudes than with the other methods [8]. Thus, in this work the phase disposition method is used for the carrier disposition.

The modulating signal is generated typically by a controller that is designed in the  $dq0$  reference system. Consequently, once the duty cycles have been fixed by the control algorithm, they must be converted back to the  $abc$  reference system in order to compare them with the carrier signals and generate the switching orders. If no change is introduced, and following the transformation of Park (Appendix B), the modulating signals will be sinusoids.

### 4.3.2.1 Third Harmonic Injection PWM

Theoretically, the maximum AC side voltage value that can be generated using a SPWM method is  $\frac{V_{dc}}{2}$ . This case is obtained when the modulation index is 1. However, the SVM method obtains a higher maximum value, namely  $\frac{V_{dc}}{2} \frac{2}{\sqrt{3}}$ . The same effect can be generated in the carrier-based PWM methods if a third harmonic is introduced to the sinusoidal modulating signals  $m_{abc}$ , following eq. (4.13).

### 4.3. Modulation strategies

---

$$\begin{aligned}
m'_a &= m \sin(\omega t) + \frac{m}{6} \sin(3\omega t) \\
m'_b &= m \sin(\omega t + \frac{4\pi}{3}) + \frac{m}{6} \sin(3\omega t) \\
m'_c &= m \sin(\omega t + \frac{2\pi}{3}) + \frac{m}{6} \sin(3\omega t)
\end{aligned} \tag{4.13}$$

The maximum point of the modulating signal of the THIPWM shown in eq. (4.13) must be obtained in order to define the limit for the offset. It can be easily checked that this limit is defined by the expression eq. (4.14). Consequently, an increase of 15.47% is obtained comparing to the SPWM using the THIPWM or the SVM.

$$m'_{max} = m \sin(\frac{\pi}{3}) \tag{4.14}$$

However, eq. (4.13) cannot be implemented in the control system of the 3LNPC. The output signals of the transformation of Park are sinusoidal waves. A method to inject a one-sixth third harmonic is necessary to use the THIPWM strategy. Each sinusoidal modulating signal  $m_{abc}$  must be varied following eq. (4.15), as it is explained in [16], in order to obtain the THIPWM modulating signals  $m'_{abc}$ .

$$m'_{abc} = \frac{3}{2}m_{abc} - \frac{2}{3} \frac{m_{abc}^3}{m_{\alpha}^+ m_{\beta}^2} \tag{4.15}$$

#### 4.3.3 Relationship between SVM and carrier-based PWM

The modulation strategies SVM, SPWM and THIPWM were presented in Section 4.3. At a first sight the SVM and carrier-based modulation strategies might seem different, but this section will prove that from the point of view of a 3LNPC converter application both are equivalent and one modulation strategy can be turned to the other with a proper zero-sequence component injection.

The objective of this subsection has been to compare the effect of the SVM, SPWM and THIPWM by means of simulations in order to determine

their differences from the point of view of the DC side currents. The three modulation strategies are applied to a 3LNPC converter that operates in open-loop with a resistive load of  $15\ \Omega$ . The structure of the employed converter is shown in Figure 4.1. A first order filtering system based on inductances is used to filter the AC output waveforms. The value of those inductances is  $3\text{ mH}$ . Ideal DC side voltage sources that have the same voltage have been used, each one with a voltage of  $350\text{ V}$ .

The modulation index value has been selected to be 1 for the SVM, and consequently  $\frac{2}{3}$  for the SPWM and THIPWM. The objective of this modulation level has been to obtain the same AC side voltages and currents with the three modulation strategies. The effect of the compared modulation strategies on the DC side currents will be analysed in order to determine the feasibility of each one for the control of the power flow of the presented HESS.

The SVM method that has been selected for this comparison is the one explained in [17]. This SVM algorithm divides the 2D diagram in different sections and triangles. Then, each triangle is assumed to be a section of a space diagram of a typical two-level converter, and the same on-time calculation is carried out as in a two-level converter.

Two different cases will be analysed (Sections 4.3.3.1 and 4.3.3.2). In the first case no zero-sequence is injected to the carrier-based modulation signals, while in the second case the injected zero-sequence component is defined as the positive maximum value that can be used with the selected modulation index, in order to avoid the overmodulation. It will be shown that the first case is equivalent of using all redundant vectors and that the second case is equivalent of using only upper redundant vectors.

### 4.3.3.1 Symmetric SVM/Null zero-sequence injection

In the first case study there is no zero-sequence injection in the carrier-based strategies and all redundant vectors are used in SVM.

Figure 4.7 shows the modulating signals of the phase  $a$  of each modulation strategy.

### 4.3. Modulation strategies

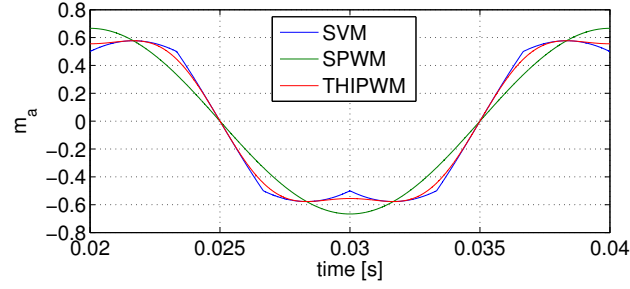


Figure 4.7:  $a$  phase duty cycles.

The difference between SVM and SPWM presented in Figure 4.8 shows that this difference has a component which has a frequency of  $150\text{ Hz}$ , three times the fundamental frequency. Consequently, if a third harmonic is injected to the SPWM, forming the THIPWM, the relation between SVM and the resulting modulating signal is improved. Figure 4.8 proves that the only difference between SVM and the carrier-based PWM strategies is an offset. If this offset is added to the carrier-based modulation strategies the same performance of the SVM can be obtained.

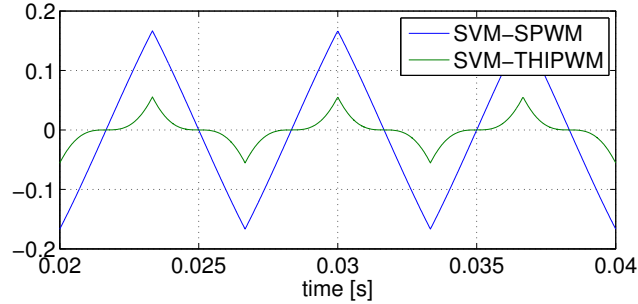


Figure 4.8: Differences among the three types of duty cycles.

Figure 4.9a shows the evolution of  $i_{abc}$  currents, which is almost the same in the three modulations. Figure 4.9b shows the section and triangle (see Figure 4.2) detection in the SVM. As the modulation index is 1, the reference vector is always in triangle 2. Therefore, the used vectors will be 2 redundants and one medium vector.

The first two sections are limited in Figure 4.9a using two vertical black lines and the middle point of each one using a vertical red line, as they will be

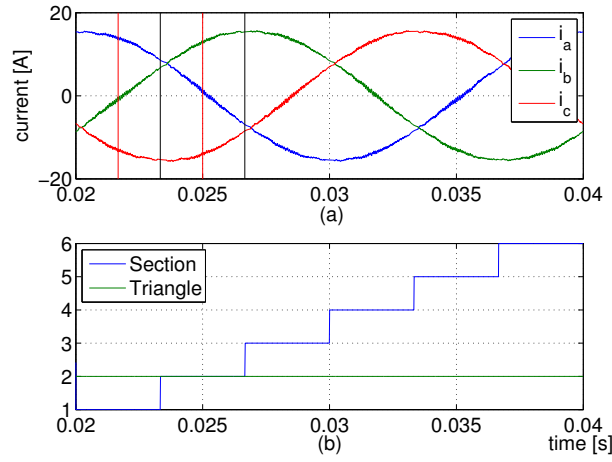


Figure 4.9: (a) Load current evolution and (b) section and triangle evolution.

used to analyse the behaviour of the 3LNPC afterwards.

The DC side currents obtained in the first case study are shown in Figure 4.10.

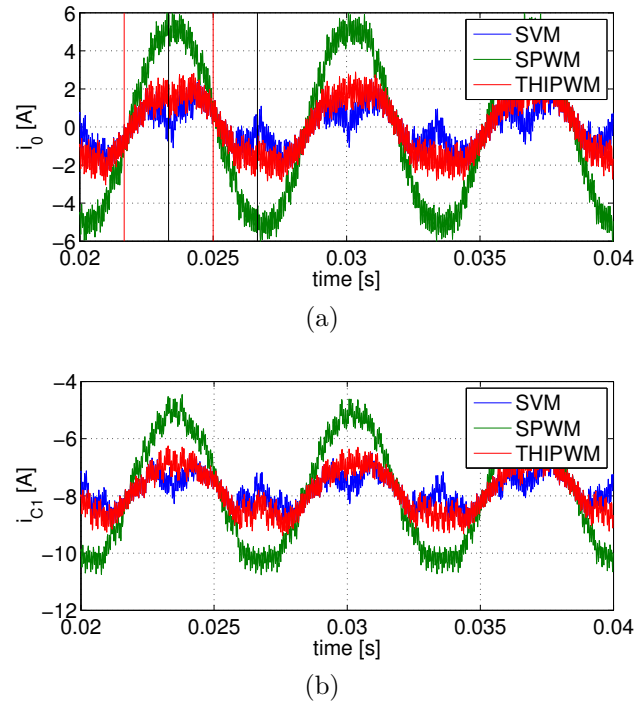


Figure 4.10: Evolution of (a)  $i_0$  and (b)  $i_{c1}$  during the first case study.

### 4.3. Modulation strategies

From the switching signals generated by each modulation method and using the relations defined in Table 4.1 it is possible to identify the switching vector applied in each moment by any modulation strategy. This method has been used to analyse the use of vectors of the compared modulations. The use of vectors of the first case study are shown in Figure 4.11. Only the first section is presented and the switching frequency has been reduced to 2 kHz in order to show the differences among the three modulation strategies in a visible way.

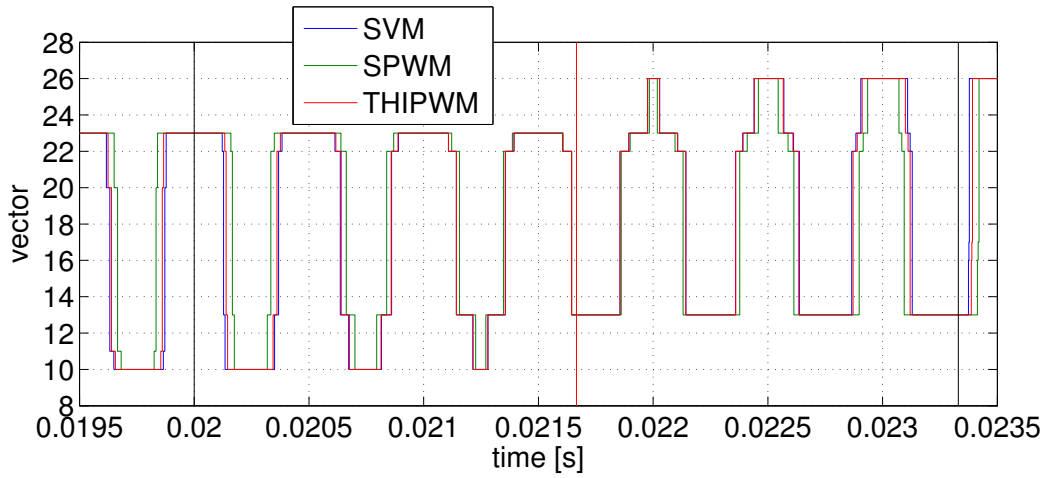


Figure 4.11: Use of vectors in section 1.

During the first section the three modulation strategies use the same vectors: 10 and 13 (upper redundant), 23 and 26 (lower redundant) and 22 (medium). The upper and lower redundant vectors that are located in the same point in the space vector diagram shown in Figure 4.2 generate the opposite effect on the neutral point current  $i_0$ , as it is shown in Table 4.3. The effect of each vector on the DC side current has been summarised in Table 4.4, which shows only the vectors that are used in sections 1 and 2.

Section 1 is divided in two equal parts: first between 0.02 s and 0.0216 s (limited by the red vertical line), and the second one between 0.0216 s and 0.023 s (limited by the black vertical line). During the first half the vectors 10, 13, 22 and 23 are used and during the second half the vectors 13, 22, 23 and 26. Each part will be separately analysed. The positive sense of the different

Section	Vector	Conf.	$i_0$	$i_{c1}$	$i_{c2}$
1	10	<i>onn</i>	$i_a$	0	$-i_a$
	13	<i>oon</i>	$-i_c$	0	$i_c$
	22	<i>pon</i>	$i_b$	$-i_a$	$i_c$
	23	<i>poo</i>	$-i_a$	$-i_a$	0
	26	<i>ppo</i>	$i_c$	$i_c$	0
2	4	<i>non</i>	$i_b$	0	$-i_b$
	13	<i>oon</i>	$-i_c$	0	$i_c$
	16	<i>opn</i>	$i_a$	$-i_b$	$i_c$
	17	<i>opo</i>	$-i_b$	$-i_b$	0
	26	<i>ppo</i>	$i_c$	$i_c$	0

Table 4.4: Effect of switching vectors in the DC side currents.

currents is specified in Figure 4.1.

At 0.2 s the smallest value of  $i_0$  is obtained by SPWM because it has the highest utilisation rate of 23 ( $i_0 = -i_a$ , being  $i_a$  positive and the highest load current in absolute value) and the lowest usage of 10 ( $i_0 = i_a$ ). Then, the use of 10 and 23 decreases, the use of 13 ( $i_0 = -i_c$ , being  $i_c$  negative) increases and  $i_a$  starts to decrease. Therefore, the current  $i_0$  will continuously increase during the first half of section one. The use of vectors becomes equal in all modulation strategies at 0.21666 s. Consequently, at this instant the current  $i_0$  is the same in all cases too.

During the second half the use of vectors starts to be different again, obtaining the maximum differences at 0.023 s. At this point SPWM has a higher utilisation of vector 13 ( $i_0 = -i_c$ , being  $i_c$  negative) and a lower utilisation of 26 ( $i_0 = i_c$ ) than the other two modulations. This will have as a consequence a higher increase of  $i_0$  than in the other two topologies. The use of the vectors 22 and 23 is similar in all modulations during the entire second half. As in the end of section 1  $i_c$  obtains its minimum value and 13 its highest usage ratio,  $i_0$  obtains its maximum value at this point.

During the second section, the used vectors are 4, 13, 16, 17 and 26. Their use is shown in Figure 4.12.



### 4.3. Modulation strategies

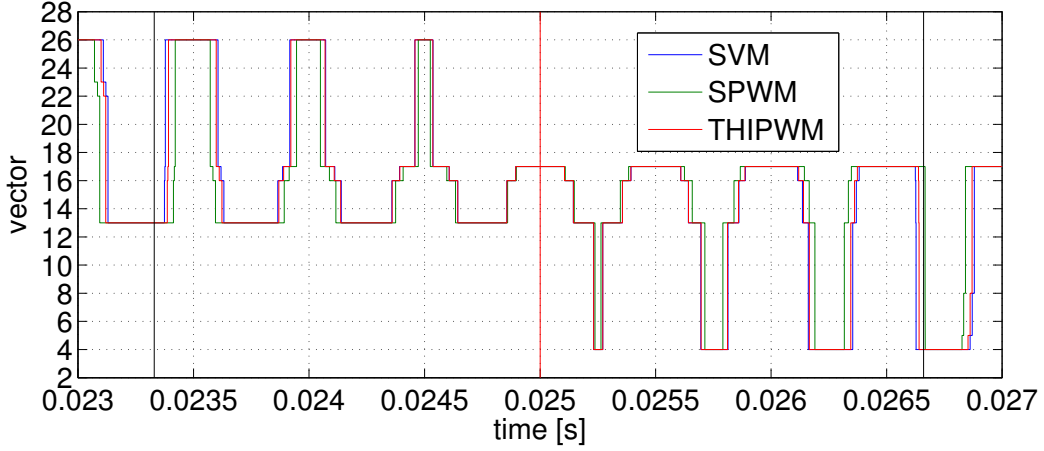


Figure 4.12: Use of vectors in section 2.

The second section is divided in two parts, as section 1: first half in the range  $[0.023, 0.025]$  s and second in the range  $[0.025, 0.026]$  s. Notice that in section 2  $i_a$  passes from being positive to be negative,  $i_b$  is positive and it is increasing and  $i_c$  is negative and it is decreasing.

During the first half of section 2 the use of the vectors 13 and 26 starts to decrease while the use of 16 and 17 starts to increase. Although vectors 13 and 26 have the opposite effect, the use of 13 is higher and consequently its effect is dominant. Taking into account 13 injects a  $i_0 = -i_c$ , being  $i_c$  negative and decreasing, the value of  $i_0$  will be decreasing too. At the end of the first half (0.025 s), the use of vectors is the same in all modulations and consequently  $i_0$  is the same in all cases.

In the second half of section two, the use of vectors starts to change, using less 4 and more 17. The differences on the use of these vectors continue to increase until a maximum difference is obtained in the end of the second half (0.026 s). The use of the vectors 13 and 16 can be considered to be equal in all modulations. The combination of vectors 4 ( $i_0 = i_b$ ) and 17 ( $i_0 = -i_b$ ) with a higher usage rate of the latter one has as a consequence a negative slope in the evolution of  $i_0$  ( $i_b$  is positive and it is increasing towards its maximum value). This way, in the end of section two, where the current  $i_b$  is close to its maximum value,  $i_0$  is also close to its maximum negative value. As the use of

4/17 is lower/higher in SPWM, the obtained minimum value of  $i_0$  is smaller than in the other two modulation strategies.

In sections 3/4 and 5/6 the same behaviour of sections 1/2 is repeated.

During this first case study upper/lower redundant vectors are used in the same rate and therefore the only vectors capable of generating a non-zero  $i_0$  current are the medium vectors (22 in section 1 and 16 in section 2). However, these vectors are barely used in both sections and furthermore their effect is opposite in the first and second parts of each section. Thus,  $i_0$  only has some oscillations around its average 0 value. It is necessary to use the redundant vectors at a different rate or inject a non-null zero-sequence component to be able to divide the power between the two input voltage sources.

#### 4.3.3.2 Upper redundant vectors/maximum positive zero-sequence injection

In the second analysis only upper redundant vectors will be used in the SVM strategy, while a maximum positive zero-sequence component will be injected in the carrier-based modulations. It will be proven that both strategies are equivalent and that they have the effect of maximising/minimising the power supplied by the lower/upper voltage sources respectively. The case where only lower redundant vectors are used and a maximum negative offset is injected will not be analysed as the results will be exactly the opposite.

The duty cycles of phase  $a$  in the second case study are shown in Figure 4.13 and the  $i_0$  and  $i_{c1}$  currents in Figure 4.14.

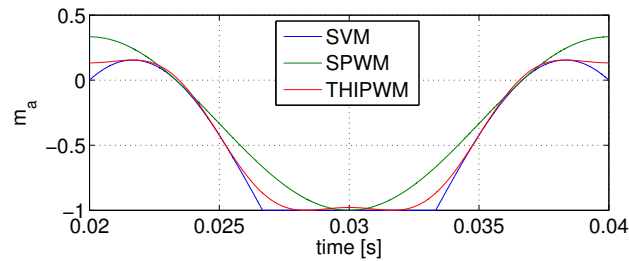


Figure 4.13:  $a$  phase duty cycles when only upper vectors are used.

As it can be seen in Figure 4.14 the currents obtained by each modulation

### 4.3. Modulation strategies

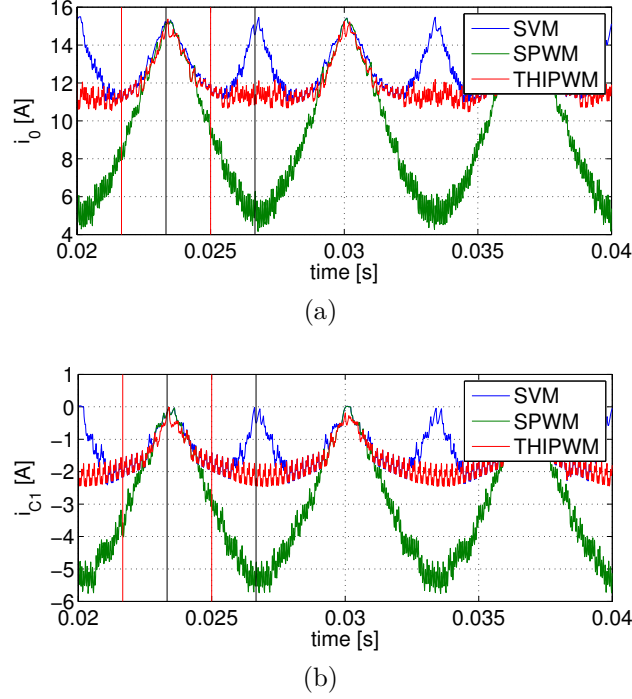


Figure 4.14: Evolution of (a)  $i_0$  and (b)  $i_{c1}$  during the second case study.

have oscillations that are repeated every two sections. It can be visually concluded that the average  $i_{c1}$  value closest to zero is created by SVM strategy. Thus, it can be said that the highest power division ratio is obtained by SVM. If the average value of  $i_{c1}$  current is calculated during the first section, the normalised value of  $i_{c1}/i_{rms}$  for SVM is 12.1%, for SPWM is 27.62% and for THIPWM is 15.05%.

The use of vectors in the first section of the second case study are shown in Figure 4.15. In the second case study the evolution of  $i_{c1}$  will be analysed.

In the second case study the vectors that are used by each modulation strategy are different. SVM uses the vectors 10, 13 and 22, i.e. the three upper vectors of section 1. On the other hand, the carrier-based modulations employ not only the mentioned vectors, but also the vector 23, a lower vector that has the opposite effect of vector 10.

At 0.02 s, SVM only uses vector 10, but the carrier-based methods also use vector 23 (SPWM at a higher utilisation ratio than THIPWM). As SVM

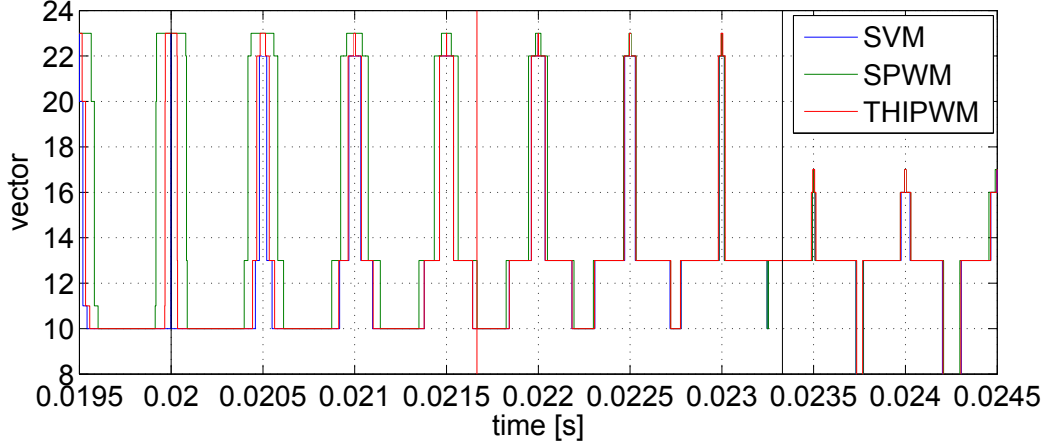


Figure 4.15: Use of vectors in section 1.

is only using vector 10 ( $i_{c1} = 0$ ), the 3LNPC converter tends to supply all the current from  $i_{c2}$  at the maximum possible rate and  $i_{c1}$  is zero. On the other hand, the carrier-based strategies use in parallel to 10 and the vector 23 ( $i_{c2} = 0$ ), creating the opposite effect. Thus, the current  $i_{c1}$  has a negative value.

Then, the use of vector 10 ( $i_{c1} = 0$ ) starts to decrease while the usage of vectors 13 ( $i_{c1} = 0$ ) and 22 ( $i_{c1} = -i_a$ ) starts to increase in all modulations. As the time approaches the end of the first half of section 1 (0.0216 s) the use of 22 reaches its maximum value. However,  $i_a$  has its maximum value in the beginning of section 1 and then it starts to decrease. Consequently, at a certain point in the first half the relation between the use of 22 and the current  $i_a$  becomes maximum and  $i_0$  obtains its minimum value.

In the case of THIPWM, the maximum use of 23 is located at 0.02 s, which in parallel to the maximum value of  $i_a$  fixes the minimum value of  $i_{c1}$  at that point. As  $i_a$  starts to decrease after that point and the use of 13 ( $i_{c1} = 0$ ) starts to increase, even if 22 ( $i_{c1} = -i_a$ ) starts to be used, the current  $i_{c1}$  experiences a small increase. While the end of the first half of section one is approaching, the use of vectors in THIPWM is similar to the one in SVM, becoming both equal in the end. As a consequence, at this point the current  $i_{c1}$  has the same value in both cases.

### 4.3. Modulation strategies

In SPWM the evolution of vectors is the same as in THIPWM. The difference is that the use of 23 is much higher at 0.02 s, obtaining a smaller  $i_{c1}$  current. Then, the reduction rate of 23 and the increasing rate of 13 are also higher, which have the effect of increasing  $i_{c1}$ .

In the second half of section 1 the use of the vectors 10, 22 and 23 is reduced till 0, value that is reached at 0.023 s. At this point the only vector that is used is 13, in all modulations. The continuously increasing use of 13 ( $i_{c1} = 0$ ) increases the value of  $i_{c1}$  in all modulations. As a consequence, the current  $i_{c1}$  has the same value in all modulations, 0 A.

The vectors that are used during section 2 are 4, 13 and 16 in SVM, and those ones and also 17 in SPWM and THIPWM. This section is divided in two parts, first half in the range [0.023,0.025] s, and the second half in the range [0.025,0.026] s. The use of vectors in section 2 is shown in Figure 4.16.

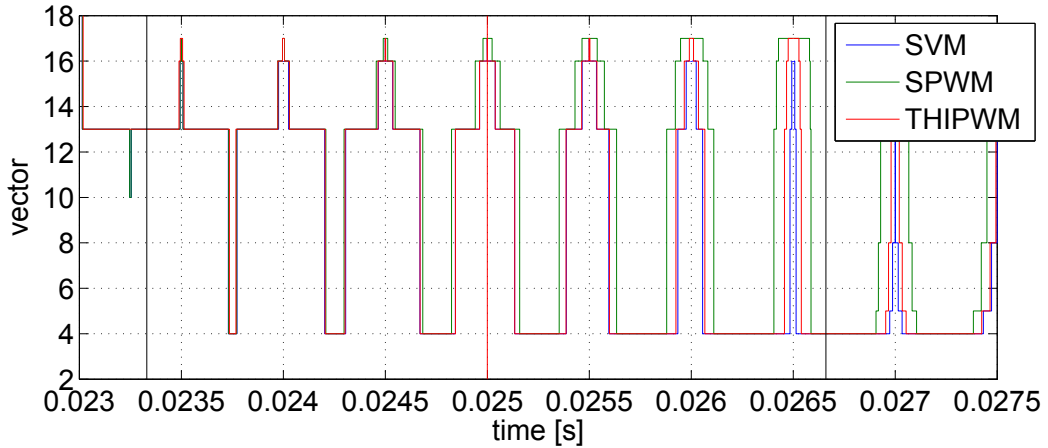


Figure 4.16: Use of vectors in section 2.

During the first half, the use of 13 ( $i_{c1}=0$ ) reduces, while the use of 4 ( $i_{c1}=0$ ), 16 ( $i_{c1} = -i_b$ ) and 17 ( $i_{c1} = -i_b$ ) increases. Taking into account that  $i_b$  is positive, the increasing use of 16 and 17 will reduce  $i_{c1}$ , even if vector 4 will have the opposite effect. As the use of vectors in SVM and THIPWM is similar, so it is the reduction of  $i_{c1}$ . The minimum point of  $i_{c1}$  is obtained when the effect of 16 and 17 on the one hand and 4 and 13 on the other hand are equalised. SPWM has a smaller use of 4 as well as a higher one of 17, while

the usage of 13 is similar, in comparison to SVM. Consequently, the reduction of  $i_{c1}$  is higher with this modulation.

In the range  $[0.025, 0.026]$  s in the case of SVM the use of 13 and 16 is reduced to zero, and the only vector used in the end is 4. Therefore,  $i_{c1}$  is increased till 0 A.

In the case of THIPWM and in comparison to SVM, the use of 4 is smaller due to the utilisation of vector 17. As  $i_b$  obtains its maximum value at 0.026 s, the vector 17 is able to overcompensate the effect of 4. This way,  $i_{c1}$  suffers a slight reduction during this period.

In the case of SPWM the usage of vector 17 is much higher, and consequently the use of 4 much lower, than in the other two modulations. As a consequence  $i_{c1}$  continues to decrease till the end of the section. At this point the current  $i_{c1}$  reaches its minimum.

The second case study has proven that the use of upper redundant vectors and the injection of a maximum positive offset have similar consequences in the operation of a 3LNPC converter. The results have shown that among the compared modulation strategies SVM is the one able to obtain the highest power division ratio between the two input voltage sources. However, THIPWM is able to obtain similar results. A control system that varies the use of redundant vectors according to the operating conditions would be much more complicated to be designed than the use of a THIPWM with a zero-sequence component injection. For this reason and taking into account that the DC bus usage ratio is the same in SVM and THIPWM, the latter modulation strategy will be used in this thesis.

### 4.4 Operational limits of 3LNPC

The operation of the 3LNPC converter will be analysed using the average equations shown in eq. (4.8). These equations represent the relation between the AC side currents and the DC side currents in function of the duty cycles generated by the control system of the converter. During this analysis the

#### 4.4. Operational limits of 3LNPC

---

voltage of each source of the DC side will be assumed to be constant and consequently the only analysed variable will be the current, but the conclusions will be the same for the power.

It is assumed that the load is a three-phase balanced ideal current sources system. In the two operation modes in which the 3LNPC converter can work, i.e. isolated and grid-connected, this representation of the power converter is representative as in both cases a certain AC side current system and switching orders will determine a different DC side currents values.

The duty cycles are generated by the control system, following a THIPWM modulation strategy. The amplitude of the duty cycle is the modulation index, and it determines the relation between the DC bus voltage and the AC side voltages. Furthermore, these duty cycles also include the zero-sequence component injected to the modulating signals in order to control the power flow between the two input ESS. Finally, in the case where the DC side voltages are not equal, the duty cycles are modified as it is explained in Section 4.2.1, which is also represented by the duty cycles.

Consequently, the average equations (eq. (4.8)) represent the entire operation of the 3LNPC converter, and they will be used to analyse its operation under different operating conditions. Following the mentioned equations and the explanations given previously, it can be said that the DC side currents  $i_{c1}, i_{c2}$  of a 3LNPC converter are defined by the following four variables:

- Modulation index
- Phase difference between AC side currents and voltages
- Zero-sequence component injected to the modulating signals
- Unbalance level on the DC side voltages

The objective of this section is to analyse the behaviour of the 3LNPC in the entire operation range of the mentioned four variables. As it is not possible to represent those results in a unique figure, the analysis will be divided in several parts that are shown in the next subsections.

First of all the case where the DC side voltage is supposed to be balanced will be analysed. This way, the effect of the offset, the modulation index and the phase difference will be studied.

Then, the offset will be assumed maximum and minimum, and the effect of the modulation index, voltage unbalances and the phase difference will be analysed. The results of this latter analysis will be used to design the control of the zero-sequence injection.

#### **4.4.1 Balanced DC side voltages**

If the DC side voltages are assumed to be balanced, a variable is eliminated and consequently the effect of the other three must be taken into account. However, one of them will be initially selected to be constant, in order to simplify the analysis to two variables and to represent the results using 3D figures.

##### **4.4.1.1 Constant zero-sequence injection**

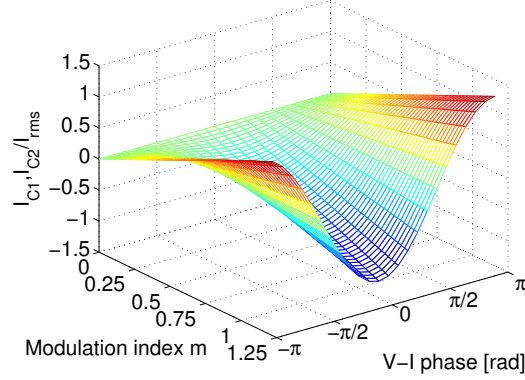
First of all, the effect of the variation of the phase difference between the AC side voltages and currents has been analysed at different modulation index values. The offset has been assumed constant. The analysed variable ranges are  $[0, \frac{1}{\sin(\pi/3)}]$  in the case of the modulation index, in order to avoid overmodulation, and  $[-\pi, \pi]$  *rad* in the case of the phase difference. The current injected in the DC side,  $i_{dc}$ , is supposed to be null.

Figure 4.17a shows this relation when a null offset is added to the modulating signals. In this case the use of the redundant vectors is done in such a way that the neutral point unbalance is avoided. Consequently, the average value of the currents of the capacitors is the same. It can be seen that the minimum  $i_{c1}, i_{c2}$  currents are obtained when the phase difference is null. The positive or negative increase of the phase difference has the same effect on the DC side currents, the effect of the phase difference is symmetric in  $[-\pi, 0]$  and  $[0, \pi]$  *rad* ranges. At the phase value  $\frac{\pi}{2}$  the average  $i_{c1}, i_{c2}$  currents are zero as no active power is required by the AC loads. A maximum  $i_{c1}, i_{c2}$  current value

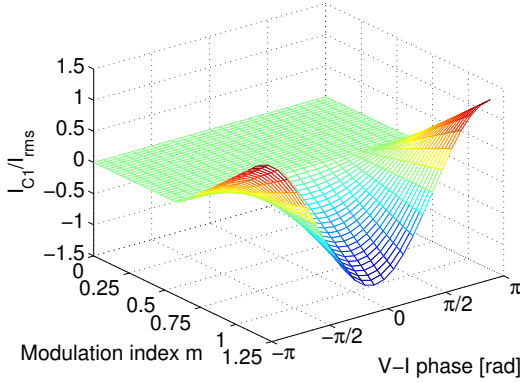


#### 4.4. Operational limits of 3LNPC

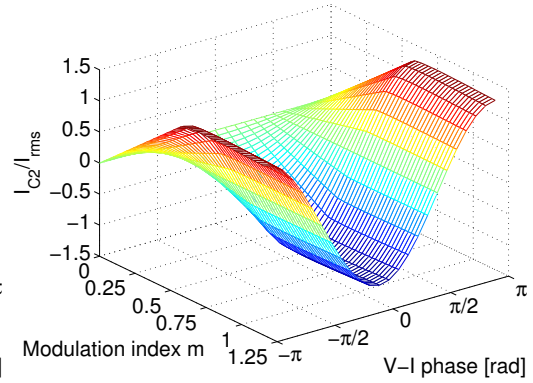
is obtained at  $\pm\pi$  radians, exactly the opposite value to the one obtained at  $0 \text{ rad}$ . In the range  $[0, \frac{\pi}{2}] \text{ rad}$  the power flows from the DC side to the AC side. On the other hand, in the range  $[\frac{\pi}{2}, \pi] \text{ rad}$  the power flow is the opposite. From the point of view of the maximum power obtaining from the DC side ESS, it is preferable to have a phase difference that is close to  $0 \text{ rad}$ .



(a)  $i_{c1}$  and  $i_{c2}$  when offset is 0.



(b)  $i_{c1}$  current.



(c)  $i_{c2}$  current.

Figure 4.17: Relation between capacitor currents, modulation index and  $v-i$  phase difference.

Figures 4.17b and 4.17c show the results of the same analysis, but when a minimum zero-sequence component is added to the modulating signals in each modulation index value. Figure 4.17b shows the result of the  $i_{c1}$  current and Figure 4.17c the results of the  $i_{c2}$  current. Due to the injection of the zero-sequence the current taken from each capacitor is different, in such a way that the converter tends to take the maximum possible current from

one capacitor and the minimum from the other, the maximum from  $C_2$  and the minimum from  $C_1$  in the analysed case. It can be seen that when the modulation index is smaller than  $\frac{0.5}{\sin(\pi/3)}$  it is possible to supply all the required current by only  $C_2$  while the current of  $C_1$  is maintained at 0 A for the entire phase difference range. If the modulation index is higher than the mentioned value both capacitors must provide a current to satisfy the requirements of the load. Notice that in Figure 4.17 the current injected in the DC side is supposed to be 0 A. The injection of a DC side current will move the curves presented in Figures 4.17b and 4.17c vertically with a value of  $\frac{i_{dc}}{i_{rms}}$ .

#### 4.4.1.2 Constant phase difference

Once the effect of the phase difference was analysed, the effect of the offset has been addressed at different modulation index values. As in the previous case, the third variable, in this case the phase difference, has been maintained constant. Two different cases were analysed, in the first one the phase difference is 0 rad and in the second case it is  $\pi$  rad. This way, both limits of the operation of the 3LNPC inverter have been analysed. The current injected in the DC side is 0 A in the two cases. The results of these tests are shown in Figure 4.18. The modulation index ( $m$ ) has been varied between  $[0, \frac{1}{\sin(\pi/3)}]$  and the offset between  $[-1 + m \sin(\pi/3), 1 - m \sin(\pi/3)]$ .

Figures 4.18a and 4.18b show the results when the phase difference is 0 rad, i.e. the power factor of the load is 1. As it was shown in Figure 4.17, when the modulation is smaller than  $\frac{1}{\sin(\pi/3)}$  it is possible to supply all the power required by the load using just one capacitor. The use of the offset allows to supply this power using one capacitor or the other. The effect of the offset when it is negative and positive is symmetric, whenever the absolute value is the same (notice that Figure 4.18a and Figure 4.18b are symmetric about the  $\frac{i_{c1}}{i_{rms}} - m$  plane). A negative offset tends to take the maximum possible current from the lower  $C_2$  capacitor minimising the current supplied by  $C_1$ , while a positive offset has the opposite tendency. The higher the modulation index, the smaller the options to have different currents in the capacitors, i.e. smaller

#### 4.4. Operational limits of 3LNPC

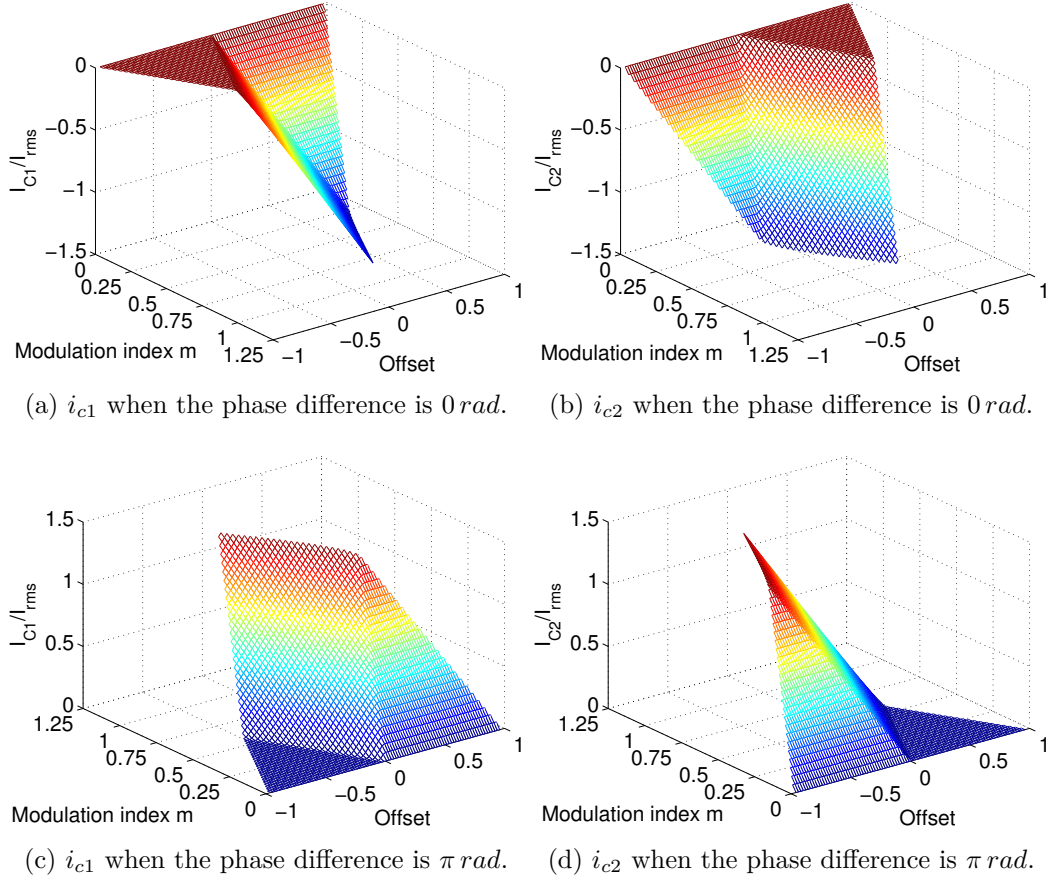


Figure 4.18: Relation between capacitor currents, modulation index and the zero-sequence.

the possibilities of dividing the power between the two input storage devices. Consequently, taking into account that the objective of this thesis is to use the 3LNPC converter to control the power flow of a HESS, it is preferable to have the smallest possible modulation rate. The disadvantage of this is that for the same AC side RMS voltage value the DC bus voltage needs to be higher. This trade-off between the DC bus voltage and the modulation index is carried out in Section 4.5.

Figures 4.18c and 4.18d show the results when a phase difference of  $\pi \text{ rad}$  is used. The obtained average  $i_{c1}, i_{c2}$  currents are exactly the same as in the  $0 \text{ rad}$  case, with the only difference that the sign is the opposite. Consequently,

Figures 4.18c and 4.18d show that the effect of the offset is symmetric in relation to the phase difference and modulation index variations when the DC side voltages are assumed to be the same. All the operation points of the 3LNPC converter will be inside the space limited by Figures 4.18a and 4.18b and Figures 4.18c and 4.18d under the mentioned supposition.

#### 4.4.1.3 Experimental tests at maximum-minimum offset values

The different tests carried out in this subsection have been performed by means of simulations. Consequently, in order to validate experimentally the presented results, a simple laboratory test was carried out. For this test a 3LNPC prototype, which will be described in detail in Chapter 5, has been used. The 3LNPC converter supplies a resistive balanced load and the two constant DC voltage sources have been obtained using two lead-acid batteries. A zero-sequence component was injected in the modulating signal to demonstrate experimentally the feasibility of dividing the power between the input power sources using the offset injection. The converter is operating in open loop with a modulation index of 0.5. Figure 4.19 shows the results of this test.

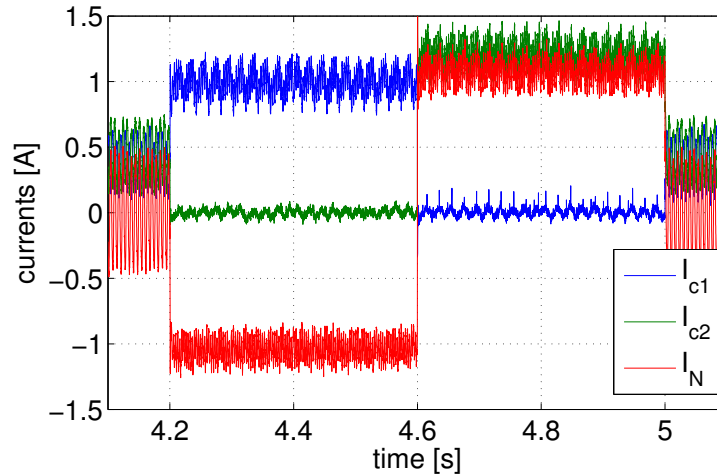


Figure 4.19: Experimental test of the effect of a zero-sequence injection.

The injected zero-sequence component is maintained at 0 until the instant 4.2 s. At 4.2 s the offset is changed to 0.5 until 4.6 s. Then the offset is reduced to -0.5 until 5 s, when the offset is returned to 0. The input currents of the

#### 4.4. Operational limits of 3LNPC

---

two batteries prove that the injection of a zero-sequence allows controlling the power division between two input voltage sources.

##### 4.4.1.4 Maximum current division limits

Two other important characteristics of the operation of a 3LNPC converter that have been analysed are the power division possibilities between the input ESS and the maximum and minimum  $i_{c1}$  current flow. The maximum current division level between  $i_{c1}$  and  $i_{c2}$  will show the possibilities that exist in each operation point to divide the power between one ESS and the other. On the other hand, the maximum  $i_{c1}$  current difference between the case where a maximum offset is injected and the case when a minimum offset is used will show the existing possibilities in each operation point to face fast power variations. Notice that in the HESS the SC is located in the upper position of the DC side of the 3LNPC converter and it is the ESS used to face those variations.

The maximum current division between both ESS can be easily obtained from Figures 4.17b and 4.17c. As the maximum current division is defined as the difference between  $i_{c1}$  and  $i_{c2}$  when a maximum or minimum offset is used (due to the balanced DC voltages the usage of a maximum or minimum zero-sequence will generate the same results, but symmetric about the XY plane), the subtraction of both 3D surfaces will determine the mentioned maximum division. The result of this subtraction is shown in Figure 4.20. As the DC side voltages are assumed to be balanced this curve also represents the difference between the maximum and minimum  $i_{c1}$  current.

The maximum current division is obtained at 0 *rad* phase difference and 0.5  $\sin(\pi/3)$  modulation index value.

#### 4.4.2 Unbalanced DC side voltages

This section analyses the effect of having unbalanced DC side voltages. This way, the analysis carried out in Section 4.4.1 will be extended to the complete operation range of a 3LNPC converter. The effect of those unbalances will

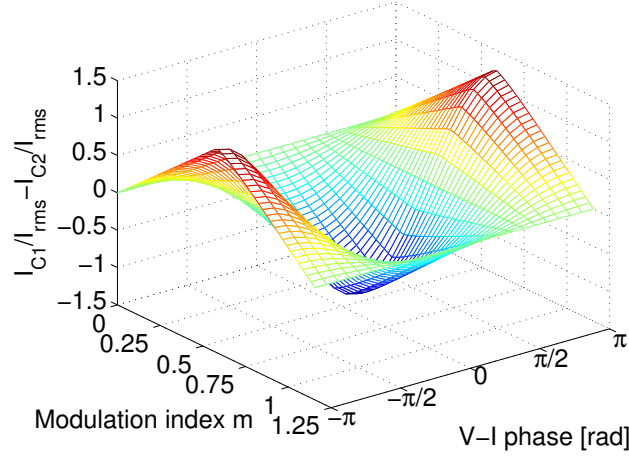


Figure 4.20: Maximum current division in the balanced DC voltages case when a maximum offset is injected.

be represented when the offset is assumed to be maximum and minimum. Furthermore, the phase difference will be assumed constant in order to reduce the number of variables that affect the DC side currents to two, the modulation index and a variable that represents the voltage unbalance.

From the current division point of view, the important variable is the relation between  $V_{c1}$  and  $V_{c2}$  rather than the total  $V_{dc}$  voltage value. Consequently, the unbalance will be represented by eq. (4.2). The variables  $A_{c1}$  and  $A_{c2}$  are not independent, as their addition must be always 2. Consequently, only  $A_{c1}$  will be used to represent the effect of the voltage unbalance. A 0 value of  $A_{c1}$  would mean that the upper voltage source has a voltage of 0 V, while a value of 2 would mean that the lower voltage source has a 0 V voltage. The case where  $A_{c1}$  is 1 corresponds to the balanced DC bus voltages case analysed in Section 4.4.1.

Figures 4.21a and 4.21b show the results of the case when a maximum zero-sequence is injected. As it was previously explained, a positive zero-sequence will have as a consequence the increase of the current supplied or absorbed by the upper voltage source. From Figures 4.21a and 4.21b it can be concluded that when the voltage of the upper source is smaller than the voltage of the lower source, both currents increase comparing to the average currents of the

#### 4.4. Operational limits of 3LNPC

case when the DC voltages are equal. On the other hand, when the upper voltage is higher than the lower voltage, both currents are smaller for the same modulation index.

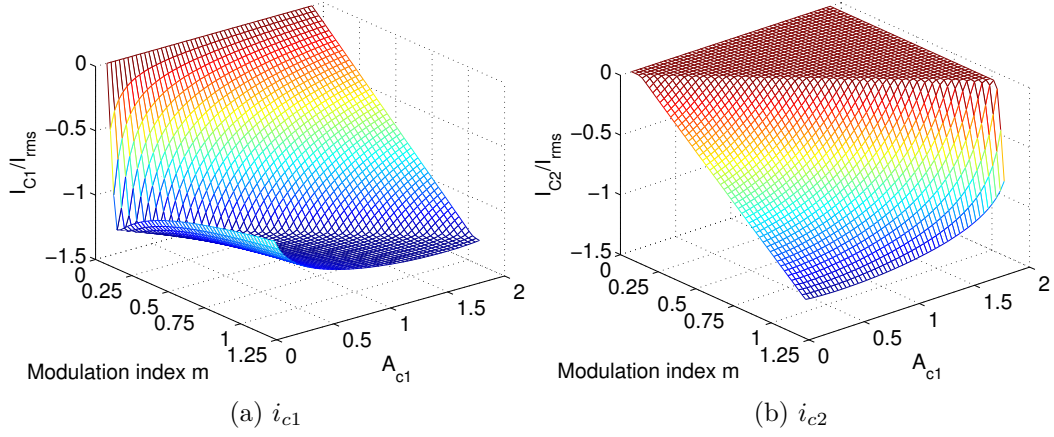


Figure 4.21: DC currents when a maximum zero-sequence is injected.

Figures 4.22a and 4.22b show the results of the case when a minimum zero-sequence is used. The fact of using a negative offset has as the opposite effect of the previous case. As a consequence, the converter tends to use the lower voltage source. It can be seen that the obtained results are symmetric to the ones shown in Figures 4.21a and 4.21b about the plane modulation- $i_c$  currents. Therefore, the effects of the voltage unbalances are the opposite. In this case a lower voltage of the lower source requires a lower  $i_{c1}$  current, while a higher voltage requires a higher current.

In the balanced voltages case studied in Section 4.4.1 the effect of the zero-sequence injection on  $i_{c1}$  and  $i_{c2}$  currents was the same (using a positive offset the obtained  $i_{c1}$  was equal to the current  $i_{c2}$  obtained using the same absolute value offset, but negative). However, when the voltages are unbalanced this relation between  $i_{c1}$  and  $i_{c2}$  currents according with a positive/negative zero-sequence injection is obtained making the voltage unbalance the opposite; i.e., when the offset is positive, the obtained  $i_{c1}$  current is equal to the  $i_{c2}$  current obtained when the offset is negative, but assuming that the voltage



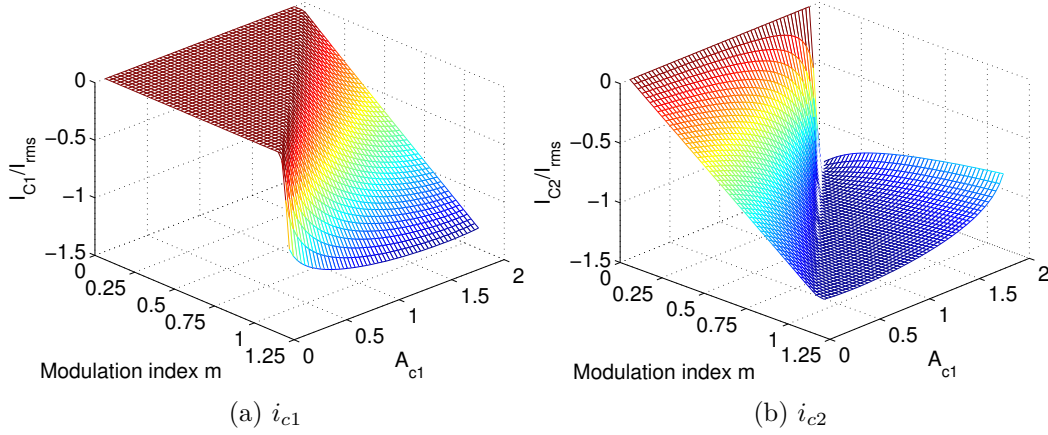


Figure 4.22: DC currents when a minimum zero-sequence is injected.

unbalance is exactly the opposite in both cases.

#### 4.4.2.1 Maximum current division limits

To finish with the analysis of the operation of the 3LNPC and its representation, the effect of unbalanced voltages on the maximum current division has been studied. The results are shown in Figure 4.23a for the case where a maximum offset is added and in Figure 4.23b for the case where a minimum offset is injected.

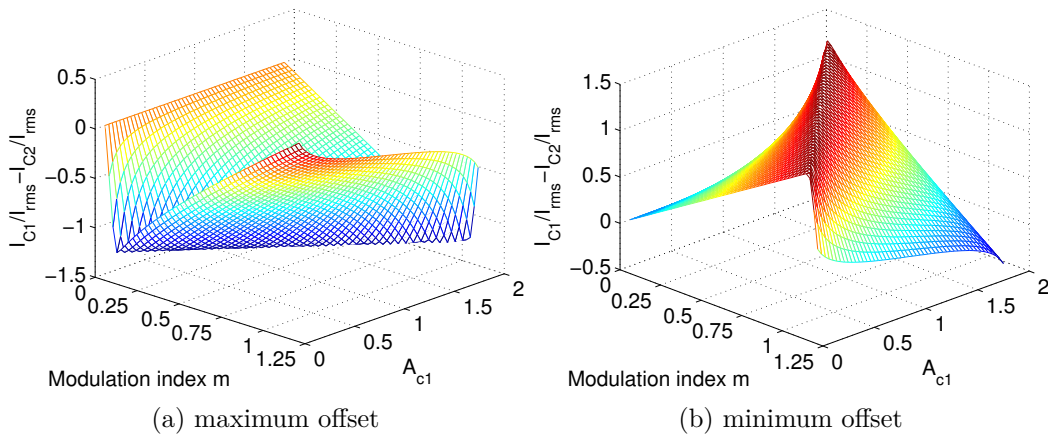


Figure 4.23: Maximum current division in the unbalanced DC voltages case.

It can be seen from Figures 4.23a and 4.23b that the injected zero-sequence



#### 4.4. Operational limits of 3LNPC

---

component has a direct effect on the maximum current division that can be obtained. If the middle operation point is used as a reference, the point where the modulation is 0.5774 and the voltage relation 1, the current division is maximum for both maximum and minimum zero sequences. The main difference between Figures 4.23a and 4.23b is location of the maximum current division. In Figure 4.23a, the maximum current line is defined between the points 0 modulation index/ $0 A_{c1}$  and 1.15 modulation index/ $2 A_{c1}$ , and on the other hand in Figure 4.23b is defined between 0 modulation index/ $2 A_{c1}$  and 1.15 modulation index/ $0 A_{c1}$ .

##### 4.4.2.2 Effect of the phase difference

In order to represent the complete operation range of a 3LNPC when a maximum and minimum zero-sequence is injected it is necessary to take also into account the effect of different phase difference values. The previous analysis, as it was specified, was carried out for the  $0 \text{ rad}$  case. For every phase difference and zero-sequence values 3D figures like for example Figure 4.23 can be obtained. But they represent the operation of the 3LNPC converter at a fixed phase difference.

In order to study the effect of the phase difference the average  $i_{c1}$  and  $i_{c2}$  currents were calculated as a function of the modulation index and the unbalance, as it was done previously, but at different phase difference values. For each value, a pair of 3D figures was obtained. Then, the obtained  $i_{c1}$  and  $i_{c2}$  currents were divided by the results of the  $0 \text{ rad}$  case, which was used as a reference case. The results at several phase difference values revealed that the relation between them and the reference  $0 \text{ rad}$  case can be represented by a constant doing a negligible error.

Figure 4.24 shows the result of the division between the results of  $i_{c1}$  at  $\frac{\pi}{4}$  phase difference and the reference results, when a maximum offset is used.

It can be clearly seen that the difference between the minimum point and the maximum point is very small in comparison to the value itself. Therefore, the value of the middle point is selected in order to minimise the approximation

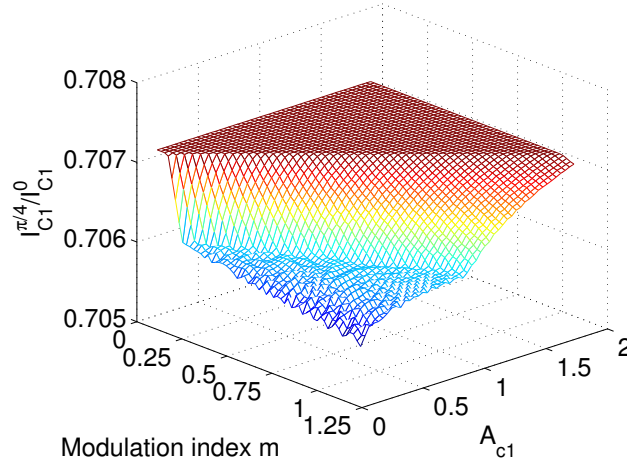


Figure 4.24: Division between  $i_{c1}$  results when the phase shift is  $\frac{\pi}{4}$  and  $0 \text{ rad}$  and a maximum offset is injected.

error. In this specific case the approximation error is of 0.1%.

If this procedure is repeated at several phase difference values, it can be concluded that the values obtained at different phase difference values follows the curve represented in Figure 4.25. The relation between  $[-\pi, 0]$  and  $[0, \pi]$  is symmetric about the vertical axis, and consequently only the positive range is shown in Figure 4.25.

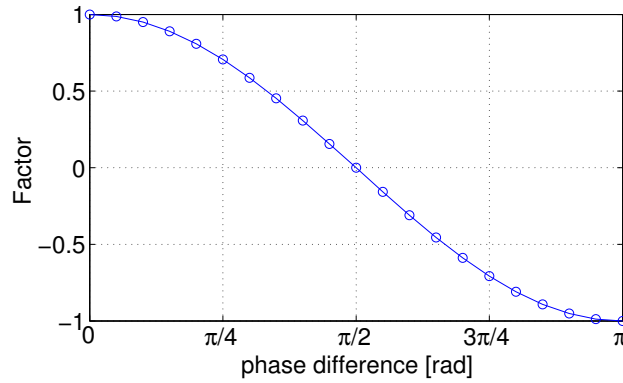


Figure 4.25: Constant value used to represent the effect of the phase shift.

This simplification of the effect of the phase difference allows representing easily the maximum and minimum  $i_{c1}$  and  $i_{c2}$  currents in the entire operation range of the 3LNPC converter. The knowledge of the limits allows the user to know in each operation point which are the existing options to charge or

#### 4.5. DC bus voltage selection

---

discharge the two input storage systems. Consequently, the controller that regulates the injection of the zero-sequence can be designed perfectly knowing which are the limits of the system in each moment and consequently fixing the injected offset based on the known information.

### 4.5 DC bus voltage selection

The DC bus voltage value must be selected following a trade-off between the modulation index that is desired and the maximum voltage ratings of the semiconductor elements. The modulation index, as it was proved in Section 4.4, is directly linked with the maximum accessible power division between the input voltage sources. If the balanced DC bus voltages case is analysed, it can be concluded from Figure 4.20 that the maximum power division is always obtained at  $\frac{1}{2\sin(\pi/3)}$  modulation index level.

However, a modulation index of  $\frac{1}{2\sin(\pi/3)}$ , following the equation that related the modulation index with the DC bus voltage required to generate  $230 V_{rms}$  (eq. (4.16)), needs a DC bus voltage value of  $1126.8 V$ . The DC bus voltage must be limited to reduce the voltage ratings of the semiconductors and passive elements of the 3LNPC converter, which directly affects the price as well as the power losses of the mentioned converter. Consequently, a trade-off between the maximum current division possibility and the DC bus voltage value must be carried out.

$$V_{dc} = 230\sqrt{2}\frac{2}{m} \quad (4.16)$$

Table 4.5 shows the DC bus voltage required by each of the modulation index values shown in Figure 4.20.

In this work a modulation index of 0.72282, which requires  $900 V$ , has been selected for the simulation case, as the resulting pair of values of the trade-off between the current division possibilities and the DC bus voltage. Using this modulation index, the current division is 19.69% lower than in the maximum current division case, when the phase shift is  $0 \text{ rad}$ .

$m$	$V_{dc} [V]$
0.57735	1126.8
0.65838	988.09
0.73941	879.8
0.82045	792.91
0.86096	755.6

Table 4.5: Relation between modulation index and the DC bus voltage.

In the case of the experimental test, due to the characteristics of the selected storage devices, the DC bus voltage value is around  $60 V_{dc}$ . Thus, using the same modulation index as in the case of the simulations, an AC side voltage of  $15.33 V_{rms}$  should be selected. However, due to the voltage drops of the IGBT and diodes of the 3LNPC converter, this voltage has been selected to be  $11 V_{rms}$ .

## 4.6 Chapter conclusions

This chapter is focused on the operation of the 3LNPC converter, which has been deeply analysed. First of all, a comparison among the most used modulation strategies has been carried out to analyse the DC current division that is obtained with each one of them. The results showed that the SVM obtains the highest current division level, but as its implementation for the zero-sequence control is complicated, the THIPWM strategy has been selected for this work. The current division obtained by this method is similar to the one of the SVM.

Then, the operation of the 3LNPC converter was analysed depending on the variables that have an effect on it, i.e. the relation between the DC voltages, the phase difference between the AC currents and the duty cycle signals, the modulation index and the injected zero-sequence component. The operational limits of the 3LNPC converter were determined for the cases where a maximum and minimum zero-sequence is injected.

## Chapter References

- [1] A. Nabae, I. Takahashi, and H. Akagi. A new neutral-point-clamped PWM inverter. *IEEE Trans. Ind. Appl.*, IA-17(5):518–523, September 1981.
- [2] L.G. Franquelo, J. Rodriguez, J.I. Leon, S. Kouro, R. Portillo, and M.A.M. Prats. The age of multilevel converters arrives. *IEEE Ind. Electron. Magazine*, 2(2):28–39, June 2008.
- [3] S. Alepuz Menéndez. *Aportación al Control del Convertidor CC/CA de Tres Niveles*. Ph.D. dissertation, Universitat Politècnica de Catalunya, 2004.
- [4] G. I Orfanoudakis, S. M Sharkh, M. A Yuratich, and M. A Abusara. Loss comparison of two and three-level inverter topologies. In *Proc. 5th IET Int. Conf. PEMD*, pages 1–6. April 2010.
- [5] N. Celanovic. *Space vector modulation and control of multilevel converters*. Ph.D. dissertation, Faculty of the Virginia Polytechnic Institute and State University, September 2000.
- [6] A.K. Gupta. *Space vector pulsewidth modulation for multilevel inverters for modulation dependent problems*. Ph.D. dissertation, National University of Singapore, 2008.
- [7] J. Pou. *Modulation and control of three-phase PWM multilevel converters*. Ph.D. dissertation, Universitat Politècnica de Catalunya, November 2002.
- [8] J. Zaragoza. *Modulation Strategies for the Neutral-Point-Clamped Converter and Control of a Wind Turbine System*. PhD thesis, Universitat Politècnica de Catalunya, November 2011.
- [9] H. Abu-Rub, J. Holtz, J. Rodriguez, and G. Baoming. Medium-Voltage multilevel Converters-State of the art, challenges, and requirements in

- industrial applications. *IEEE Trans. Ind. Electron.*, 57(8):2581–2596, 2010.
- [10] F. Wang. Sine-triangle versus space-vector modulation for three-level PWM voltage-source inverters. *IEEE Trans. Ind. Appl.*, 38(2):500–506, 2002.
- [11] J. Rodriguez, L. Moran, P. Correa, and C. Silva. A vector control technique for medium-voltage multilevel inverters. *IEEE Trans. Ind. Electron.*, 49(4):882–888, 2002.
- [12] A. Pandey, B. N. Singh, A. Chandra, K. Al-Haddad, and D. P. Kothari. A review of multilevel power converters. *J. of the Institution of Engineers (India): Electrical Engineering Division*, 86:220–231, 2006.
- [13] L.G. Franquelo, J.I. Leon, M.M. Prats, and R. Portillo. Space vector modulation techniques for multilevel converters - a survey. *Przeglad Elektrotechniczny*, 82(4):56–61, 2006.
- [14] N. Mohan, T. M. Undeland, and W. P. Robbins. *Power electronics: converters, applications, and design*. John Wiley & Sons, 2003.
- [15] B.P. McGrath and D.G. Holmes. Multicarrier PWM strategies for multilevel inverters. *IEEE Trans. Ind. Electron.*, 49(4):858–867, 2002.
- [16] A. Yazdani and R. Iravani. *Voltage-Sourced Converters in Power Systems*. John Wiley & Sons, 2010.
- [17] A.K. Gupta and A.M. Khambadkone. A space vector PWM scheme for multilevel inverters based on Two-Level space vector PWM. *IEEE Trans. Ind. Electron.*, 53(5):1631–1639, 2006.

# 3LNPC controller design and experimental results

---

## Contents

<b>5.1</b>	<b>Control of a 3LNPC converter</b>	<b>169</b>
5.1.1	AC variables control system design	171
5.1.2	VRB current controller design	174
<b>5.2</b>	<b>Experimental results</b>	<b>179</b>
5.2.1	Description of the platform	179
5.2.2	3LNPC converter	184
5.2.3	Isolated case study	186
5.2.4	Grid-connected case study	193
<b>5.3</b>	<b>Chapter conclusions</b>	<b>197</b>
	<b>Chapter References</b>	<b>198</b>

---

The main objective of this chapter is to show the experimental validation of the proposed topology and its control system. First of all the control algorithm of the 3LNPC converter is explained. Then, the experimental platform is shortly described and the details of the system analysed in this PhD work are given. Finally, the obtained experimental results are shown for two cases, the isolated case and the grid-connected case. These results have validated the simulation results and have proved that the proposed solution satisfies the defined specifications. Finally, the conclusions of the chapter are summarised.

## 5.1 Control of a 3LNPC converter

The 3LNPC converters are mainly used in medium voltage high power applications. In this field the switching frequency is limited to a few 100  $Hz$  [1] in

order to minimise the switching losses and increase the efficiency. However, this reduction on the switching frequency increases the harmonic distortion of the generated AC waveforms. As a consequence, at this power level one of the most important research topics from the control algorithm point of view has been the trade-off between the power losses and the THD. This trade-off is generally represented by a hyperbolic function that can be used to compare the performances at steady-state of different control algorithms [2].

One of the most well known control strategies of 3LNPC consists on the use of linear controllers and modulation strategies of typical two-level converters that have been adapted to multilevel converters. However, this control system does not provide the best performance at low switching frequencies, as the obtained harmonic distortion is higher than the one obtained by other control algorithms. In this context, the predictive control has received much attention in the last years due to the possibility of implementing a cost function that would allow to optimise several control functions, which in the case of 3LNPC converters have been the minimisation of the switching losses and the harmonic distortion of the generated waveforms. Several model predictive algorithms have been presented: some of them substitute the current control of the linear controllers but keep the modulator, and others substitute by the predictive control both the current controller and the modulator [2]. Other control algorithms that have been used include the hysteresis control [3], linear quadratic regulator control [4] and input-output feedback linearisation [5].

However, the present work is focused on an application of lower power ( $kW$ ). At this power level it has been demonstrated that the performance of 3LNPC converters is superior regarding the power losses and harmonic distortion of AC waveforms in comparison to two-level converters, for switching frequencies above  $5 kHz$  [6]. The switching frequency can be increased as the effect of the switching losses is not as important as in high power applications, and a good compromise between the frequency and power losses is found at the mentioned switching frequency level. In this work a switching frequency of  $15 kHz$  has been selected.



## 5.1. Control of a 3LNPC converter

---

The control of the AC side variables and the DC side variables has been carried out by separated algorithms in order to emphasize the possibility of using a 3LNPC converter to control the DC power flow. It has been proved that the DC side control has no effect on the AC side variables regulation. Therefore, and for the sake of simplicity, the AC side variables have been controlled using the well known *PI* algorithm in the  $dq0$  reference frame. Typical linear control algorithms that work in parallel with PWM modulation strategies are able to satisfy the steady state and transitory requirements that have been fixed in this work.

The second part of the control system of the 3LNPC converter is the one related to the zero-sequence injection control. This algorithm focuses on the DC power division between the input ESS, and it is based on a *PI* regulator and a current reference generator. The current reference generator selects the value of the current reference of the VRB according to the state of the HESS and to the operational limits of the 3LNPC converter. The *PI* controller receives the error of the current of the VRB and generates the necessary zero-sequence component to make this error null. The designing process of this control system is explained in Section 5.1.2.

### 5.1.1 AC variables control system design

The control of the DC side variables is carried out by an independent control system that modifies the modulating signal according to several requirements and that does not have any effect on the AC side variables. In the designing process of the control system of the AC variables it will be assumed that the DC side voltages are constant and balanced. Furthermore, the well known averaging method is applied knowing that the switching frequency is several orders higher than the fundamental frequency of the AC signals.

Due to the mentioned assumptions, in Sections 3.2.1.2 and 3.2.3.2 it was proved that from the AC side variables point of view there is no difference between a two-level and a 3LNPC converter. As a consequence, the control system design procedure is the one that was previously explained in Section 3.2.1.2.

However, in the case of the experimental tests, the final calculation of the parameters of the different PI algorithms has been adapted to the conditions of the platform. The DC bus voltage value can be selected as  $60\text{ V}$  and the AC side filter inductance has a value of  $3\text{ mH}$ .

The control of the AC side variables has been designed taking into account that the 3LNPC converter will have two different operation modes: the isolated operation and the grid-connected operation.

In the isolated case, the objective is to fix the frequency and the voltage of the AC side as the inverter is the element that will fix those variables. Consequently, according to the power required by the loads connected to the AC bus, the power given by the inverter will be different. The power supplied by the inverter will be defined by the loads and is not a user-selectable parameter. In this operation mode the control algorithm is formed by two loops. An inner loop for the  $dq$  current components regulation, and an outer loop for the  $dq$  voltage components regulation. The inner current  $PI$  controller has been designed to have a settling time of  $10\text{ ms}$  and no overshoot. On the other hand, the outer voltage  $PI$  controller has been designed to have an overshoot of  $3\%$  and a settling time of  $25\text{ ms}$ . The value of the load  $R_L$  that has been employed to calculate the controllers has been  $9.2\ \Omega$ . The values of the parameters of these regulators are given in Table C.1. Figure 5.1 shows the structure of the control algorithm in the isolated case.

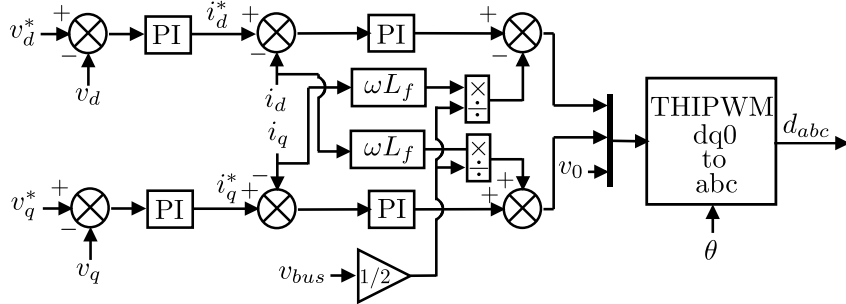


Figure 5.1: Control structure of the isolated case.

In the grid-connected operation, the inverter works connected to an external voltage source that fixes the voltage of the AC side. The first consequence is

### 5.1. Control of a 3LNPC converter

that the inverter will need a synchronisation method to connect to the AC bus in a safe mode (refer to Section 3.2.1.3 for more details). The second consequence is that the inverter is not the responsible of fixing the AC variables any more. In the grid-connected mode the controlled variables are the active power and the reactive power supplied/absorbed by the converter to/from the AC bus. As it was explained in Section 3.2.1.2, the active and reactive powers can be controlled through the  $i_d$  and  $i_q$  components respectively. Therefore, in this operation mode the control algorithm only needs one control loop, the one of the current, and it will be the same of the isolated case. However, in this case the current reference values will be calculated according to the  $P$  and  $Q$  reference values. From the HESS power management point of view, those power variables can be selected to improve the operation of the HESS according to the needs of the system. Figure 5.2 shows the structure of the control algorithm in the grid-connected case.

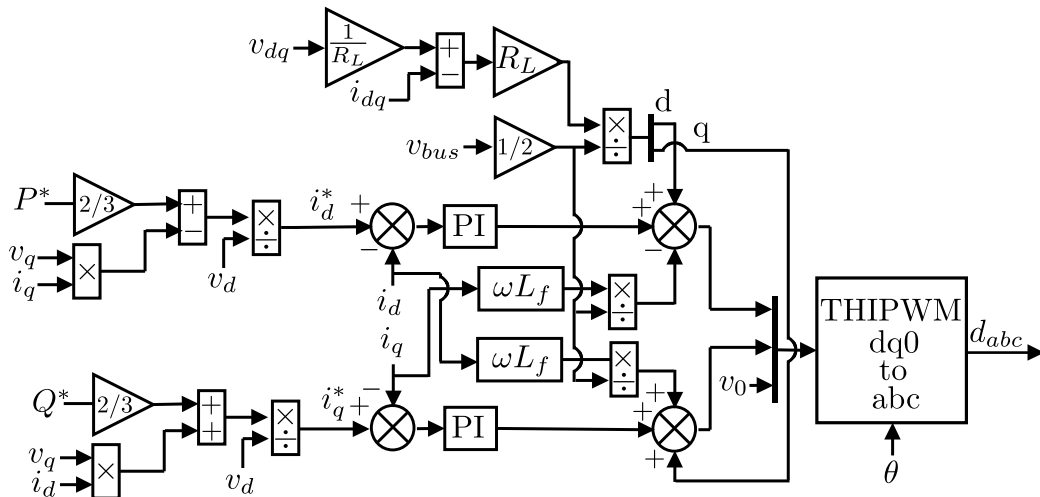


Figure 5.2: Control structure of the grid-connected case.

The transition from one operation mode to the other is carried out smoothly resetting and initialising the PI controllers, as it was explained in Section 3.2.1.2.

### 5.1.2 VRB current controller design

The zero-sequence component is used to control the power flow of the HESS. It has been proved in Section 4.4 that this is feasible, and at the same time the limits of that power division have been fixed. Using the results of the analysis of the 3LNPC converter it is possible to define a controller for the zero-sequence injection that selects the offset applied in each moment in function of the values of the different measured variables and knowing perfectly which the limits of the operation of the converter are.

The power division between the SC and VRB must be carried out according to the frequency: fast power variations must be absorbed or supplied by the SC and the low frequency part by the VRB, as it was explained in Chapter 2. The injection of the zero-sequence can be selected with the objective of controlling the current of the VRB. Therefore, the power of the VRB will be directly controlled, while the remaining power will be absorbed or supplied by the SC. The power control of the SC is carried out indirectly, thus.

From the analysis carried out in Section 4.4, it is known that a positive zero-sequence tends to supply power from the SC while a negative one tends to take the power from the VRB. Consequently, if the current of the VRB is to be controlled, a higher discharge current (assumed to be positive in the control design process) will require a higher negative zero-sequence and inversely a higher charge current (assumed to be negative) will require a higher positive zero-sequence injection. Therefore, it is clear that the regulator of the current of the VRB will need a negative gain. The dynamics of the DC currents of the 3LNPC converter are defined by the  $d_{abc}$  duty cycles and the  $i_{abc}$  currents of the AC side. The duty cycle signals include the zero-sequence. On the other hand, the AC side currents are determined by the  $PI$ -based control system designed in the  $dq0$  reference system. Furthermore, the switching frequency and the DC capacitors have a direct effect on the high frequency component of the DC currents, which limits the proportional parameter of the zero-sequence controller. The  $PI$  control system of the current of the VRB has been designed by trial and error using the *Simulink* simulation model.

### 5.1. Control of a 3LNPC converter

The reference signal of the *PI* controller of the zero-sequence is generated by a rule-based algorithm that is explained in Section 5.1.2.1.

#### 5.1.2.1 Rule-based algorithm

The reference signal of the *PI* controller of the current of the VRB is defined by a rule-based algorithm according to the limits of the 3LNPC converter, which were defined in Section 4.4. Those limits establish the maximum/minimum accessible VRB and SC currents according to three variables: the modulation index, the relation between the voltages of the VRB and the SC as well as the phase difference between the duty cycle signals and the AC currents.

The modulation index and the duty cycle signals are obtained from the *PI* controllers of the  $i_{dq}$  currents, while the different currents are measured by sensors. The phase difference between the duty cycles and the currents is calculated applying the Clarke transform and then using the arctan function and a simple code to avoid to have the phase difference limited to the range  $[0, \pi]$  *rad*. The operational limits are implemented in the control system through lookup tables. Figure 5.3 shows the structure of the control of the current of the VRB.

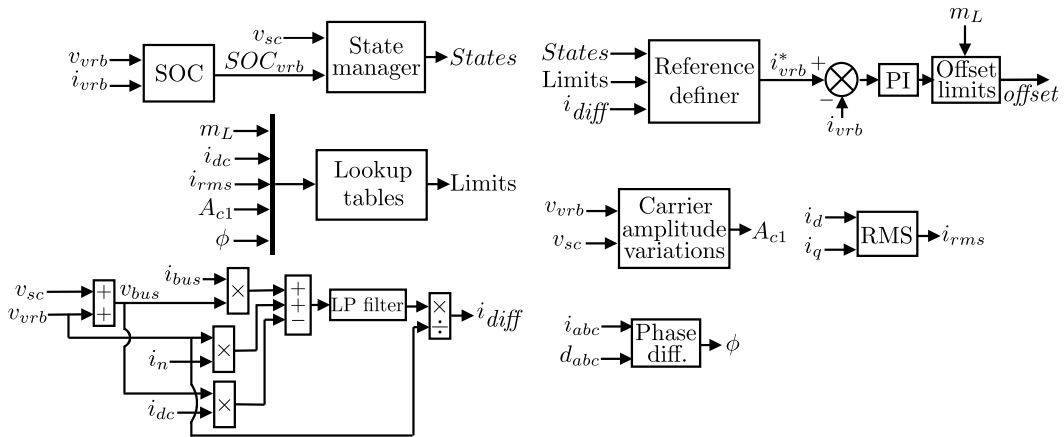


Figure 5.3: Control structure of the current of the VRB.

The  $i_{vr}$  reference generation must be carried out according to the operational limits of the 3LNPC in each operation point, but also according to the SOC of the storage systems. For example, if the SC is at low SOC the system

should try to charge it in order to ensure its proper operation. Therefore, the reference generation is based on two parts:

1. State manager: it is the responsible of defining the state of each storage system according to their SOC.
2. Reference definer: it is the responsible of defining the reference of the current of the VRB according to the operational limits and the state of each ESS.

Three different ranges (upper, middle and lower) have been defined for each ESS in order to determine their charge level (1 for the upper, 2 for middle and 3 for lower). In the case of the SC, as its serial resistance is low, the voltage has been used to determine its charge level. On the other hand, in the case of the VRB the serial resistance is higher and consequently it is necessary to use the SOC in order to select its charge level. Nevertheless, the voltage and currents limits of each ESS have been also taken into account in order to ensure a safe operation and stop the execution if the safety limits are exceeded. Figure 5.4 shows the graphical representation of the division of the three ranges of the state manager. Each range contains an hysteresis in order to avoid fast transitions from one state to the other.

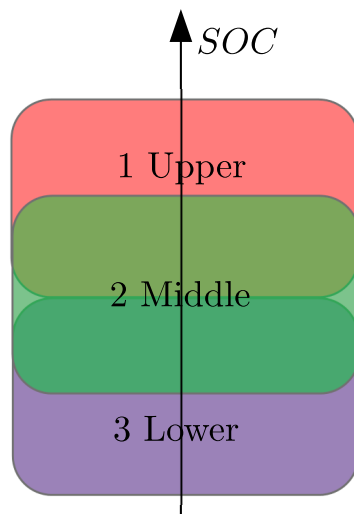


Figure 5.4: Schematical representation of the operation of the state manager.

### 5.1. Control of a 3LNPC converter

---

The reference selector employs the information of the charge level of each ESS to define the current reference for the offset controller. There are nine different possibilities according to the charge levels. In each of those nine cases, the reference selector defines three new possibilities according to the current limits and the relation between the DC power received by the converter and the AC power required by the load. These new possibilities are defined by a variable that is called simply *state*. This variable is selected according to the maximum and minimum limits of the current of the SC and the VRB, as well as to the relation between the input DC power and the power required by the load. This power difference is calculated as defined by eq. (5.1), and then it is converted into the VRB current level ( $i_{diff}$ ) dividing it by the voltage of the VRB and filtered by a second order filter (cut-off frequency of  $2\pi 100 \text{ rad/s}$ ) to facilitate its use by the reference selector.

$$P_{diff} = i_n V_{vrb} + i_{bus} V_{dc} - i_{dc} V_{dc} \quad (5.1)$$

Table 5.1 summarises the selection of the current reference according to the charge level of the SC and VRB, the *state* variable and the power difference variable. The selection of the reference current must take into account several aspects. Firstly, the charge level of the ESS, which represent their SOC. Secondly, the *state* variable, which represents the relation among the power received from RES in the DC side and the power required by the load. Finally, the ability of the 3LNPC to face increasing or decreasing power variations. For example, if in a certain operation point the zero-sequence injection is positive and maximum, the 3LNPC converter will not be able to divide the power between the SC and the VRB if a sudden power increase is required by the AC load. Consequently, the offset level is another factor to be taken into account.

The reference defined by the reference selector is filtered to avoid the possible fast variations introduced by the *state* variable. The cut-off frequency of this filter has been selected to be at  $10 \text{ rad/s}$ , but as it will be explained later, in some experimental tests it has been reduced in order to be able to show the desired results.

Charge level SC/VRB	<i>State</i>		
	1	2	3
1/1	$\min(i_{c2_{max}}, i_{c2_{min}})$	$\frac{i_{c2_{max}} + i_{c2_{min}}}{2}$	$\frac{i_{c2_{max}} + i_{c2_{min}}}{2}$
1/2	$\min(i_{c2_{max}}, i_{c2_{min}})$	$\min(i_{c2_{max}}, i_{c2_{min}})$	$\min(i_{c2_{max}}, i_{c2_{min}})$
1/3	$\min(i_{c2_{max}}, i_{c2_{min}})$	$\min(i_{c2_{max}}, i_{c2_{min}})$	$\min(i_{c2_{max}}, i_{c2_{min}})$
2/1	$\frac{i_{c2_{max}} + i_{c2_{min}}}{2}$	$i_{diff}$	$\frac{3 i_{c2_{max}} - i_{c2_{min}} }{4} + \min(i_{c2_{max}}, i_{c2_{min}})$
2/2	$\frac{i_{c2_{max}} + i_{c2_{min}}}{2}$	$i_{diff}$	$\frac{i_{c2_{max}} + i_{c2_{min}}}{2}$
2/3	$\frac{3 i_{c2_{max}} - i_{c2_{min}} }{4} + \min(i_{c2_{max}}, i_{c2_{min}})$	$\frac{i_{c2_{max}} + i_{c2_{min}}}{2}$	$\frac{i_{c2_{max}} + i_{c2_{min}}}{2}$
3/1	$\max(i_{c2_{max}}, i_{c2_{min}})$	$\max(i_{c2_{max}}, i_{c2_{min}})$	$\max(i_{c2_{max}}, i_{c2_{min}})$
3/2	$\max(i_{c2_{max}}, i_{c2_{min}})$	$\max(i_{c2_{max}}, i_{c2_{min}})$	$\max(i_{c2_{max}}, i_{c2_{min}})$
3/3	$\max(i_{c2_{max}}, i_{c2_{min}})$	$\max(i_{c2_{max}}, i_{c2_{min}})$	$\max(i_{c2_{max}}, i_{c2_{min}})$

Table 5.1: Selection of the current reference of the VRB.



## 5.2. Experimental results

---

Once the reference is generated, the VRB current error is calculated and used by the previously mentioned  $PI$  in order to modify the injected zero-sequence and to keep the current of the VRB at the reference level. However, the 3LNPC converter is not supposed to work in overmodulation in this work. Consequently, it is necessary to limit the zero-sequence generated by the  $PI$  to avoid that. As the modulation index can suffer variations in its value, the offset limits must be variable as well. This variable limits have been implemented by the simple method shown in eq. (5.2). The modulation index is directly obtained from the controller, and it is shown in Figure 5.5 as  $m_L$  variable. This figure, Figure 5.5, schematically shows the final control structure of the 3LNPC that has been used in this work.

$$Offset = \begin{cases} u_{PI}, & \text{if } |u_{PI}| \leq 1 - m_L \\ \text{sign}(u_{PI})(1 - m_L), & \text{else} \end{cases} \quad (5.2)$$

## 5.2 Experimental results

This section shows the experimental results obtained at the isolated and grid-connected case studies.

### 5.2.1 Description of the platform

An experimental platform formed by several elements and that can be used to represent the operation of a microgrid is installed in *Estia-Recherche* laboratory. The installed microgrid is configured in such a way that many different element configurations can be created. This flexibility of connecting several elements in many different configurations is done using manual switches and it allows the user to experimentally validate different microgrid topologies. The schematic representation of the platform is shown in Figure 5.6.

The most important elements of the microgrid are summarised in the following paragraphs.

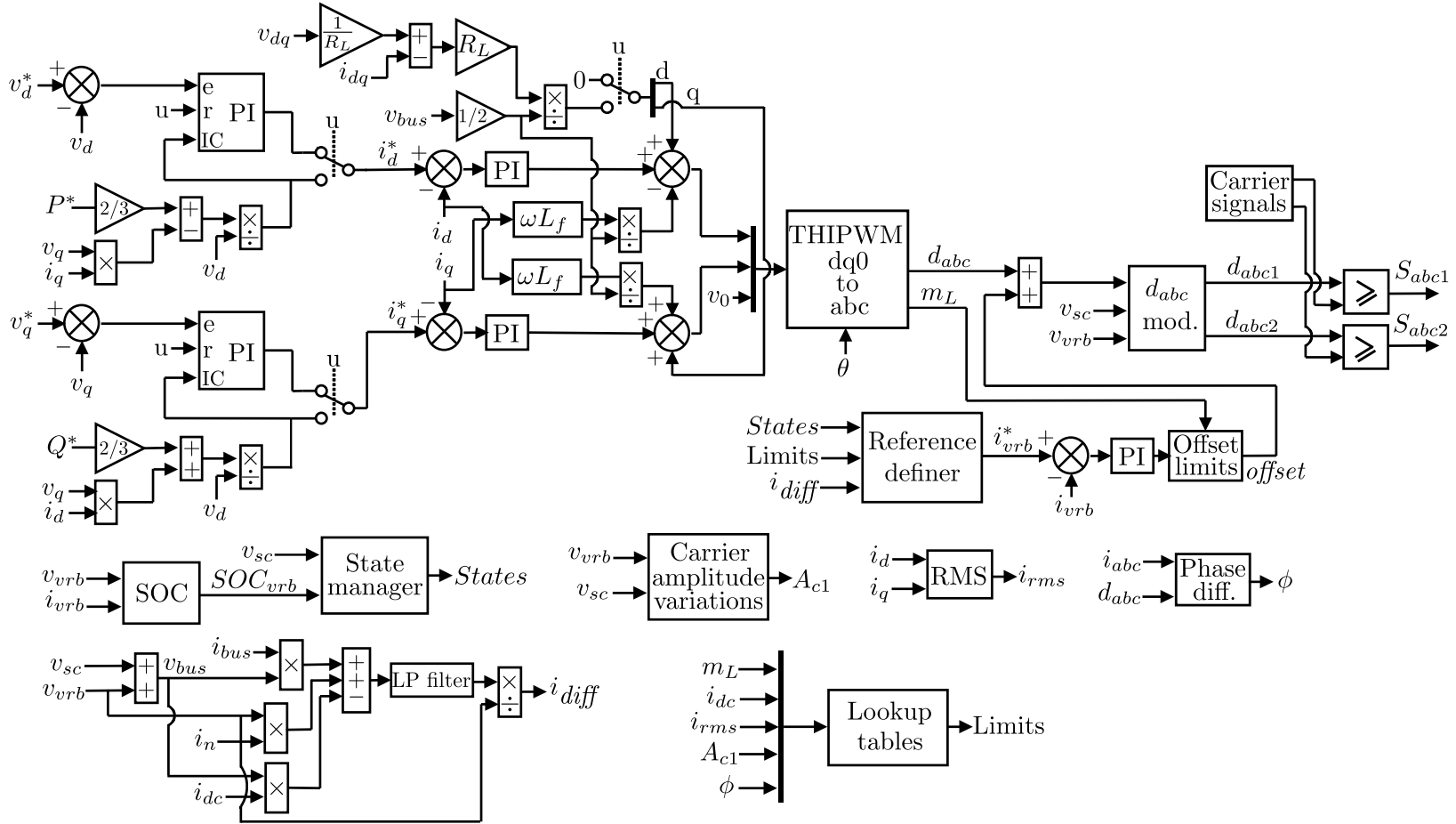


Figure 5.5: Complete control algorithm of the 3LNPC converter.

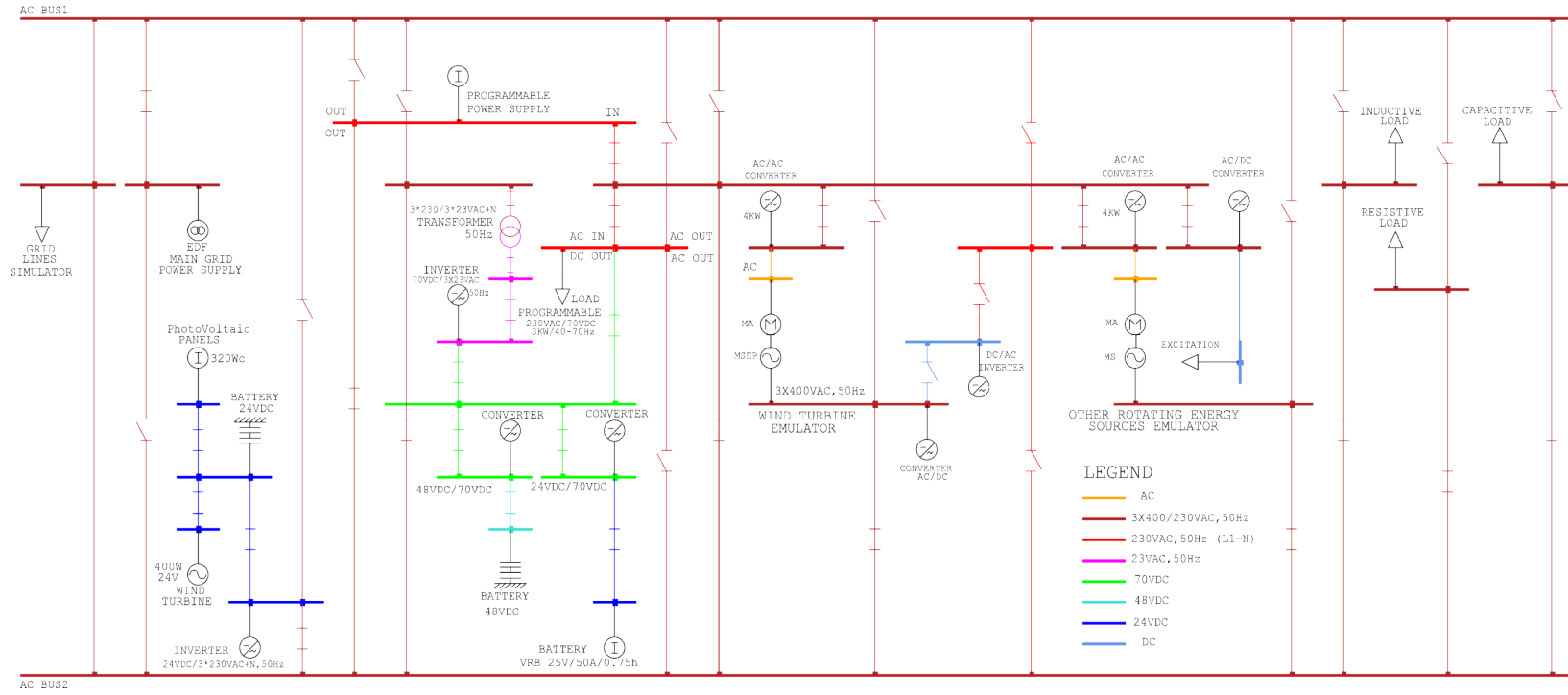


Figure 5.6: Scheme of the experimental microgrid.

## Chapter 5. 3LNPC controller design and experimental results

---

**RES:** There are two low power RES, a WT (400 W) and a group of PV panels (320 Wp).

**Emulators:** Two different emulators are installed in the microgrid. The first one (rated power of 2.2 kW) is formed by an asynchronous machine and a permanent magnet synchronous generator, and it is used to emulate WTs. The second one (rated power of 3 kW) is formed by an asynchronous machine and a DC excited rotor synchronous generator that is used to emulate different renewable or non renewable energy sources based on synchronous generators.

**Programmable voltage source:** A *California Instruments Compact 2253iX* voltage source (2.25 V A, 47 – 63 Hz) is installed in the microgrid. This programmable source can be used for both AC and DC power testing with high precision output regulation and accuracy. It includes the possibility of working in mono or multi phase cases, to generate line distortion and arbitrary waveform generation for power quality tests. It carries out power analyser measurements as well.

**Programmable AC loads:** Three *California Instruments 3091(LD)* (3 kV A, 45 – 440 Hz) AC loads, one master and two slaves, are used to emulate different types of loads and analyse the behaviour of different systems installed in the microgrid. These loads are designed to provide precisely controlled, non-linear loads for testing AC power generation equipment in real operating conditions. The *3091LD* AC Load can simulate high crest factor and variable power factor load conditions. The measurements that this load can perform include voltage/current RMS and peak, crest factor, true power, apparent power, power factor and frequency.

**WindyBoy SB3000:** It is a commercial power converter of *SMA Solar Energy* enterprise for grid-interfacing of WT, that has a rated power of 3 kW.

## 5.2. Experimental results

---

**Xantrex XW42024-230-50:** It is a commercial inverter-charger of *Xantrex* enterprise, that has a rated power of  $4\text{ kW}$ . It is used for both residential and commercial stand-alone, grid-backup and grid-connected applications with battery energy storage. This unit includes an inverter, a battery charger and an integrated AC transfer switch.

**SuperCapacitor:** The unit *BMOD0083* of *Maxwell* manufacturer is installed in the microgrid. It has a rated power of  $3\text{ kW}$ , a maximum continuous current of  $61\text{ A}$  and a maximum voltage of  $48.6\text{ V}$ .

**Vanadium Redox Battery:** A custom-made VRB battery constructed by *GEFC* enterprise is installed in the platform. It has a rated power of  $1.5\text{ kW}$ , a maximum current of  $50\text{ A}$ , a maximum voltage of  $32\text{ V}$  and an energy capacity of  $37.5\text{ Ah}$ .

**Lead-Acid batteries:** These batteries offer a considerably higher autonomy than the other two storage systems, which is rated at  $255\text{ Ah}$ .

**DC-DC converters:** 2 custom-made DC-DC converters constructed by *Arcel* enterprise are used to regulate the power flow of the different types of ESS.

**4-leg two-level converter:** This converter was designed and constructed in *Estia-Recherche*. The main advantage of this converter is its capability to ensure a balanced three-phase voltage supply in isolated conditions even if the three-phase load is unbalanced, thanks to an innovative control algorithm.

**Passive components:** Resistive, capacitive, inductive loads and line emulators for different operating conditions.

**OP5600 HILbox:** Even if it is not shown in the schematic representation of the microgrid, the OP5600 HIL simulator plays a vital role in the system as

it is used to measure the different variables, implement the control system and generate the control signals. Figure 5.7 shows the front panel view of *OP5600*. It can be used to conduct a number of real-time simulation applications, including HIL testing, rapid control prototyping and FPGA development projects. The *OP5600* Chassis can be used either as a desktop system, or rack-mounted as part of a network of *OPAL-RT* simulators communicating through high-speed PCI-E links. It also comes with 6 PCI expansion slots to provide more flexibility to add I/Os and communication devices and two user-programmable FPGA options for I/O management, signal processing and fast models.

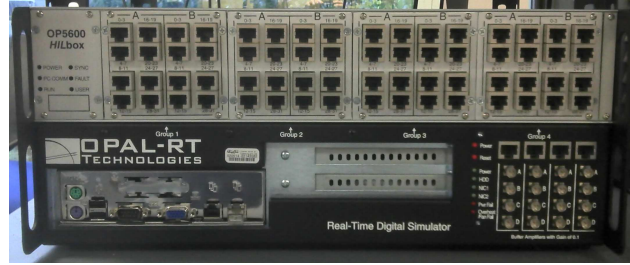


Figure 5.7: Front panel view of the OP5600 HILbox.

As the solution proposed in this work is based on the use of a 3LNPC converter, its details will be analysed in an independent subsection.

### 5.2.2 3LNPC converter

A custom made 3LNPC converter constructed by *Arcel* enterprise has been installed in the platform during this thesis work. Figure 5.8 shows a picture of the converter.

The converter was sized to work at  $1200\text{ V}/50\text{ A}$  maximum values (it uses IGBT switches) in order to allow a big operation range that would enable different types of tests in the flexible microgrid. However, the tests that have been carried out in this thesis were of low voltage values, around  $60\text{ V}_{dc}/11\text{ V}_{rms}$ , due to the limitation of the characteristics of the used storage devices: the maximum voltage levels of the used storage devices are  $48.6\text{ V}$  for the SC and  $32\text{ V}$  for the VRB. Consequently, small-scale tests have been carried out. Even

## 5.2. Experimental results

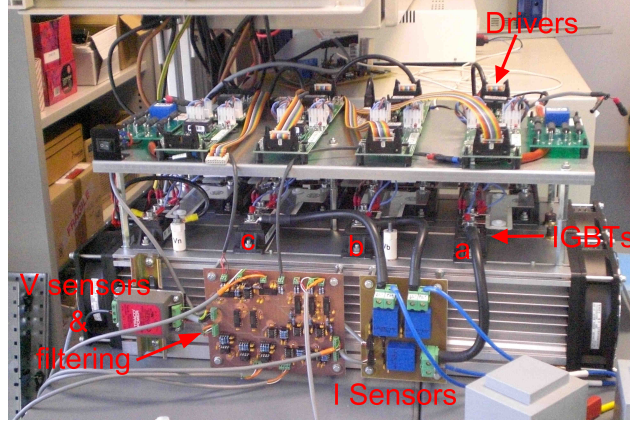


Figure 5.8: Picture of the 3LNPC unit used in the experimental tests.

if the tests were performed in non-conventional voltage levels, the tests are completely representative of what would happen at higher voltage levels.

Two printed circuit boards have been designed and constructed in order to sense, scale and filter the measured signals, i.e. the voltages and currents of the DC and the AC sides. 11 signals have been measured, two DC bus voltages, three DC currents and the voltages and currents of each of the three phases. A second order filter with a cut-off frequency of  $3\text{ kHz}$  has been selected to eliminate the effect of the switching frequency ( $15\text{ kHz}$ ) and to avoid the aliasing effect.

Table 5.2 summarised the most important characteristics of the 3LNPC converter (Figure 5.8).

Parameter	Value
$C_1, C_2$	$3.3\text{ mF}$
$L_{\text{filter}}$	$3\text{ mH}$
$V_{dc}$	$60\text{ V}$
$V_{rms}$	$11\text{ V}$
$f_{fund}$	$50\text{ Hz}$
$f_s$	$15\text{ kHz}$
$f_{c\text{filter}}$	$3\text{ kHz}$

Table 5.2: Parameters of the 3LNPC converter.

Figure 5.9 shows the picture of the different elements that have been used to experimentally validate the solution proposed in this thesis.

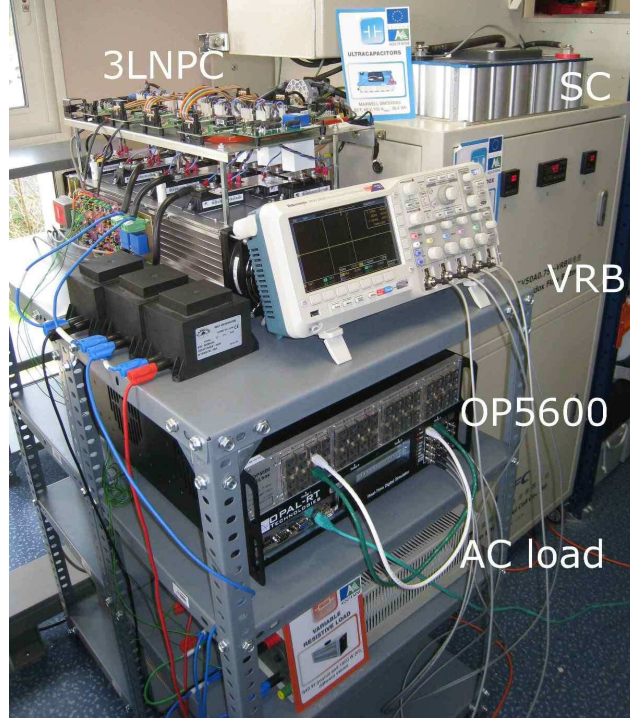


Figure 5.9: Photograph of the experimental platform.

### 5.2.3 Isolated case study

The operation of the proposed control system has been tested when the HESS is supplying power to an AC resistive and balanced load. Two different case studies are analysed. In the first case study the injected DC power is null, while the AC power is suddenly increased. The obtained results are compared with simulation results, which prove the agreement between both results. In the second case study the AC load is kept constant while a variable current is injected in the DC bus. In this case, due to the long execution time, it has not been possible to compare the obtained results with simulation results and consequently only the experimental part is shown.

Figure 5.10 shows the general block diagram of the configuration of the system that has been used to carry out the above mentioned tests.



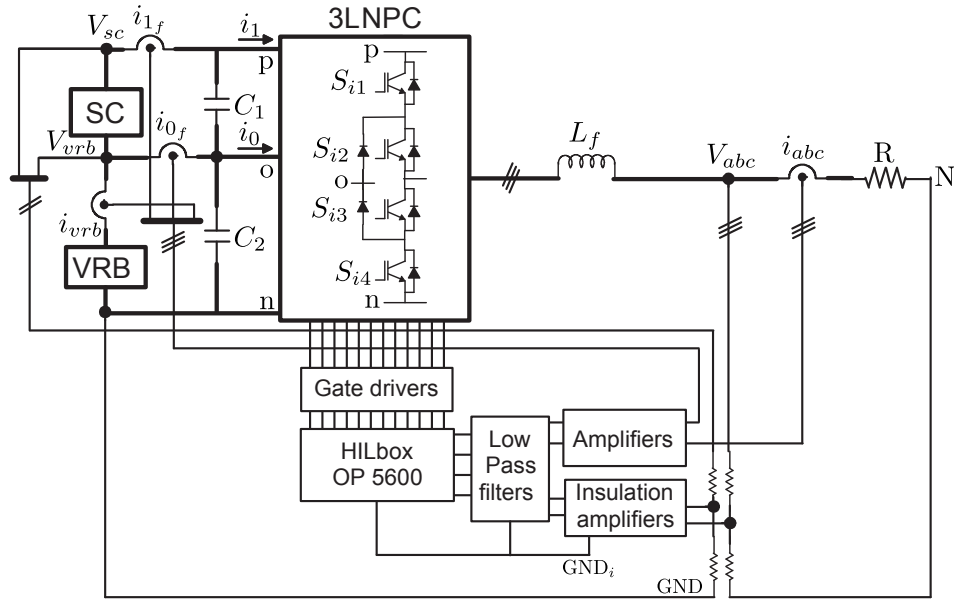


Figure 5.10: Block diagram of the experimental tests in the isolated case study.

### 5.2.3.1 Sudden AC power increase

In this case study the HESS supplies a constant resistor of  $9.2\ \Omega$  and this resistor is suddenly reduced to  $3.25\ \Omega$ , which creates a sudden power requirement increase. According to the power division requirements, this power increase must be supplied by the SC. The AC side voltage was selected to be  $11\ V_{rms}$ , as it was explained in Section 4.5.

The same case study has been analysed by means of simulations using *Matlab/Simulink* and the *SimPowerSystems* toolbox. In the case of the semiconductor elements, only the conduction losses have been simulated, the effect of the switching losses is not included in the simulation results. From the data-sheet of the IGBT and diodes of the 3LNPC unit it can be concluded that the voltage drop of those elements at the current level that has been used can be represented by 1 V value.

Figure 5.11a and Figure 5.11b show the evolution of the  $d$  component of the AC voltage and current respectively. In both cases the experimental and simulation results show a good agreement. Figure 5.11c shows the evolution of

the active power, while Figure 5.11d shows the reactive power. In the latter case, it can be seen that in the experimental results a reactive power different from  $0\text{ VAr}$  is absorbed by the load. This is explained taking into account two different factors. On the one hand, the anti-aliasing filtering applied to every measured signal in order to eliminate the high frequency components generated by the switching of the IGBT, introduce a delay in the signals. The employed filters have a cut-off frequency of  $3\text{ kHz}$  and they introduce a phase shift of  $-1.42^\circ$  at  $50\text{ Hz}$ . On the other hand, the sampling of the signals can have also an effect. In the worst case, the maximum error that can be done in the phase difference measurement through the digitalisation would be of  $0.2\text{ ms}$ , which if it is converted into degrees results in a value of  $3.6^\circ$ . The phase difference between the voltage and current of the load has been measured and a value of  $1.4^\circ$  has been obtained. The mixture of the problems that may arise from the filtering and the digitalisation end in the detection of a reactive power that does not exist in reality, as the load is completely resistive. Nevertheless, the measured reactive power is negligible in comparison to the active power value.

Figure 5.12a shows the power of the VRB, Figure 5.12b the power of the SC and Figure 5.12c the total DC power for the experimental and simulation results.

In the case of the DC powers, some differences can be noticed. These differences are created by several factors. The first factor that should be taken into account is the accuracy of the used current sensors. As it has been previously explained, the 3LNPC unit was sized to work at higher voltage and current levels than the ones used in this test. Therefore, the installed sensors have a measurement range of  $50\text{ A}$  and consequently their accuracy, which is  $1\%$ , has a direct effect on the range that is being analysed. The other factors that cause these differences will be explained analysing Figure 5.13a, Figure 5.13b and Figure 5.13c, which represent the evolution of the injected zero-sequence, the modulation index and the phase difference between the duty cycles and the AC currents respectively.

The switching losses have not been simulated and the conduction losses

## 5.2. Experimental results

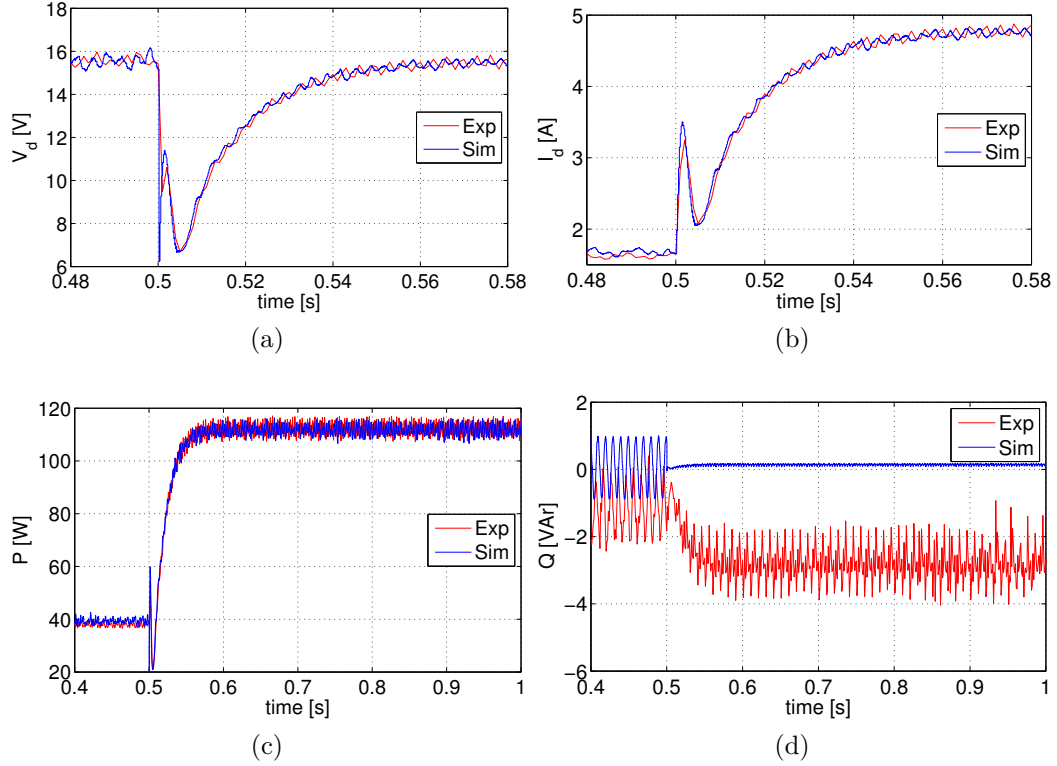


Figure 5.11: Evolution of (a)  $V_d$ , (b)  $I_d$ , (c)  $P$  and (d)  $Q$  variables during the sudden power increase test.

have been calculated approximately. Consequently, it has not been possible to accurately obtain a similar phase difference and modulation index at simulation level. Therefore, following the average equations of the 3LNPC converter eq. (4.8), these differences on the phase difference and the modulation index have logically their effect on the obtained DC currents. As a consequence of all this, the offset injected in simulations and the one of the experimental tests are not exactly the same.

Nevertheless, as the differences among the different signals are not big, it can be said that all the experimental results are in agreement with the simulation results. It has been proved as well that the simulation context is able to represent the behaviour of the physical system in an acceptable manner and consequently it can be used to analyse other case studies.

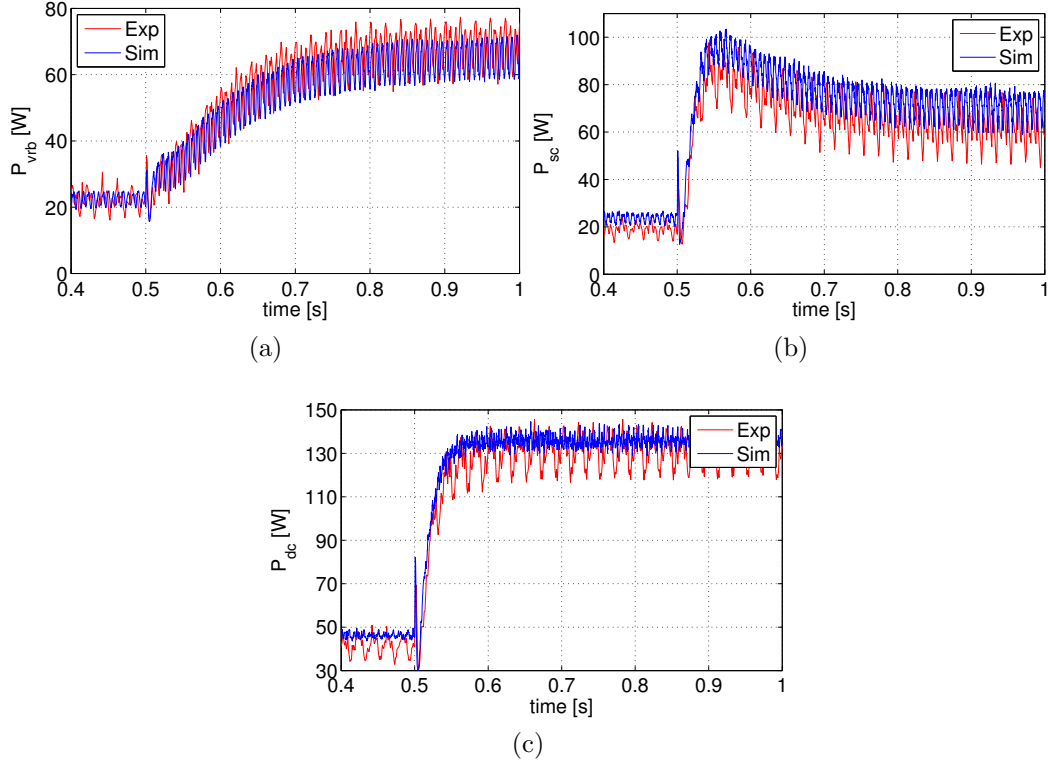


Figure 5.12: Evolution of (a)  $P_{vrb}$ , (b)  $P_{sc}$  and (c)  $P_{dc}$  variables during the sudden power increase test.

### 5.2.3.2 Variable DC power injection

In this case study a variable  $i_{dc}$  current has been injected in the DC bus while the AC load has been kept constant at  $9.2\Omega$ . The objective of this case study has been to show the ability of the proposed control structure to divide the power between the SC and the VRB according to the frequency, when the variation comes from the DC side. This DC side current represents the power variations generated by different RES.

The  $i_{dc}$  variations have been manually generated by a voltage source. Therefore, the variations of the current profile were limited in frequency and it has been necessary to reduce the cut-off frequency of the filter of the current reference of the VRB from  $10\text{ rad/s}$  to  $1.25\text{ rad/s}$ . Due to the long execution time, it has not been possible to simulate the experimental tests

## 5.2. Experimental results

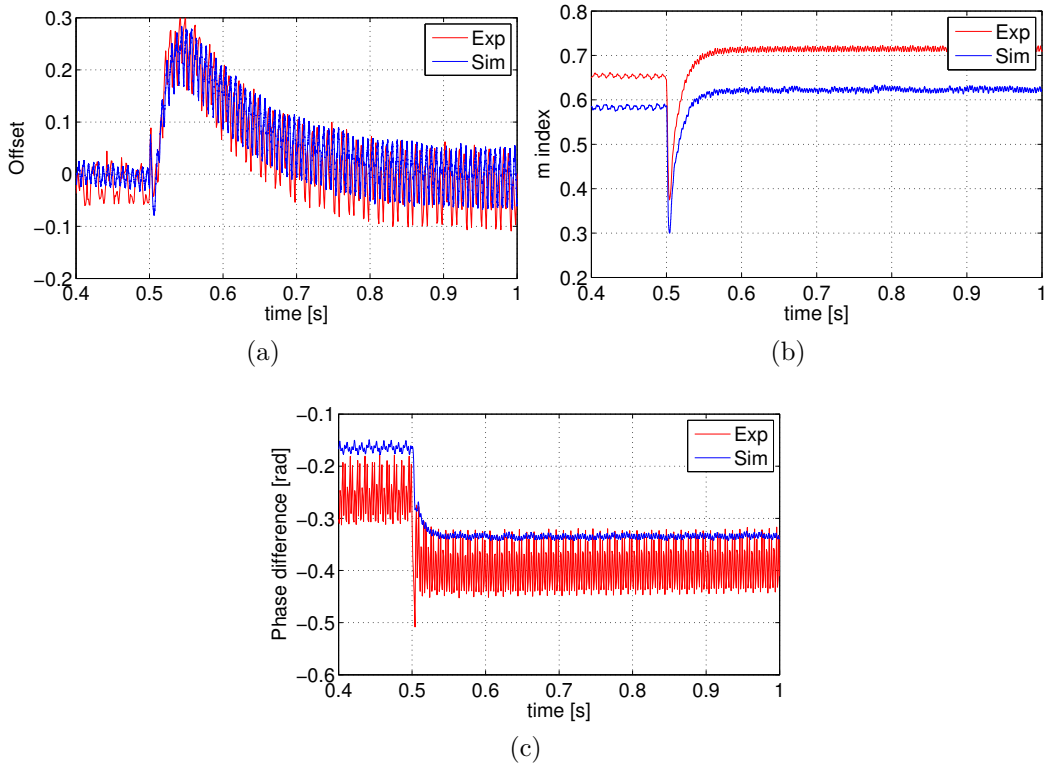


Figure 5.13: Evolution of (a) offset, (b)  $m$  and (c) phase difference variables during the sudden power increase test.

in *Matlab/Simulink*. Consequently, only experimental results are shown. It has been taken into account also that both ESS are in the state 2 during the entire test.

Figure 5.14a shows the power that is injected in the DC bus using the voltage source, while Figure 5.14b shows the evolution of the power of the VRB, its reference and the power of the SC. In the range  $[0, 4]$  s the injected power is higher than the power required by the load (around 40 W). Consequently, the rule-based algorithm starts to decrease the power reference of the VRB. While the power supplied by the VRB is being reduced, the power difference between the input DC power and the power required by the load is absorbed by the SC. The power division is carried out following the fixed requirements, as the SC faces the fast power variations. On the other hand, from the instant 4 s till the end of the test the power received from the voltage source is not

enough to satisfy the power requirement of the load. Thus, the power supplied by the VRB is increased. As both the SC and the VRB are located in the state 2, the algorithm tends to supply the same power in order to keep the offset around 0 level and increase the capacity of the HESS to face increasing or decreasing power variations.

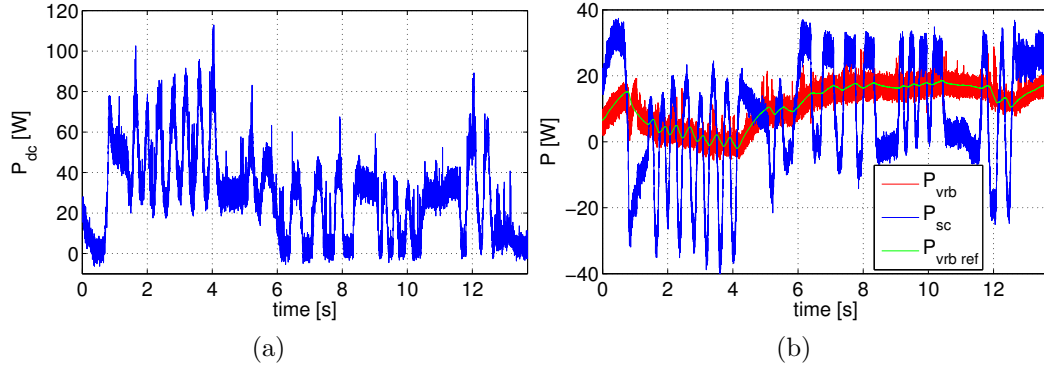


Figure 5.14: Evolution of (a)  $P_{dc}$  and (b)  $P_{vrb\_ref}$ ,  $P_{vrb}$ ,  $P_{sc}$  variables during the variable DC power injection test.

Figure 5.15 shows the evolution of the zero-sequence injected to the modulating signals in order to control the power flow of the HESS. It can be seen that the rule-based algorithm is able to keep the offset around 0 value, and also to divide the power according to its frequency between the SC and the VRB.

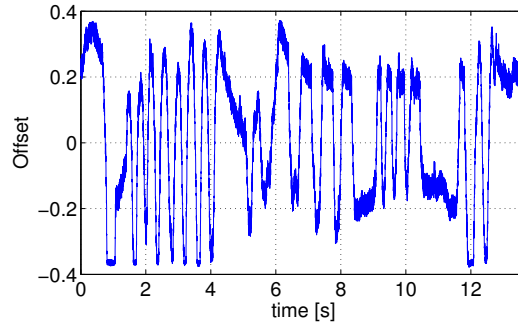


Figure 5.15: Evolution of the offset during the variable DC power injection test.

Figure 5.16 shows the main variables of the AC side of the 3LNPC converter.

## 5.2. Experimental results

---

This figure shows that the zero-sequence injection has no effect on the AC side and therefore the variables remain constant during the entire test as the AC load does not have any variation.

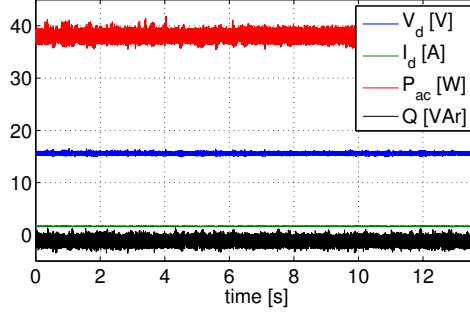


Figure 5.16: Evolution of the AC side variables during the variable DC power injection test.

### 5.2.4 Grid-connected case study

This case study analyses the behaviour of the 3LNPC converter when the disconnection from the main grid occurs. The results obtained from this case study show that the presented multilevel inverter can divide the power between the SC and the VRB according to its frequency when the islanding transition occurs.

Figure 5.17 schematically shows the configuration of the system that has been used during these tests.

The 3LNPC converter is connected to the main grid through a step-down transformer ( $230 V_{rms}/12 V_{rms}$ ). The converter feeds a three-phase resistive balanced load ( $R_1$ ) of  $1.8 \Omega$ , while the grid feeds another resistive load ( $R_2$ ) of  $4.7 \Omega$  in the secondary of the step-down transformer. A contactor is used to connect or disconnect the converter from the main grid.

The active power required by the resistive load of the converter is  $240 W$ . Once the grid-connection is done, the active power supplied by the converter is reduced to  $100 W$  in order to create a power difference that the converter will have to face once the disconnection occurs. This way, the converter needs

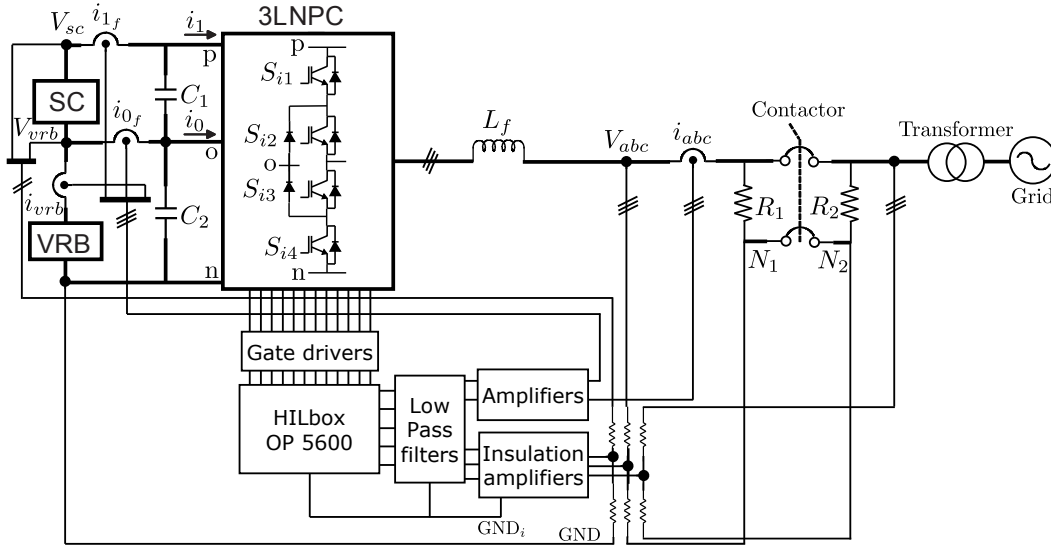


Figure 5.17: Block diagram of the experimental tests in the grid-connected case study.

to face a power step of  $140\text{ W}$ , which must be supplied by the SC. The grid-disconnection is done to show that the 3LNPC converter is able to face this event, while the power division between the SC and the VRB is carried out according to the defined requirements. Therefore, no fault detection algorithm has been implemented, the disconnection has been done directly by the user.

The same case study has been analysed experimentally and by means of simulations using *Matlab/Simulink* and the *SimPowerSystems* toolbox. The simulation and experimental results are compared in Figures 5.18 to 5.20.

Figure 5.18 shows the variables of the AC side of the 3LNPC converter. Figure 5.18a and Figure 5.18b represent the evolution of the  $d$  component of the AC voltage and current respectively. In both cases the simulation and experimental results show a similar evolution.

When the converter operates connected to the grid, the voltage is smaller than  $12 V_{rms}$  due to the effect of the lines used to connect the different elements. When the disconnection occurs at  $1\text{ s}$  instant, the control mode switches from grid-connected to the isolated mode. Thus, after the disconnection the voltage is kept at the reference  $12 V_{rms}$ . Figure 5.18c shows the evolution of the active power, where the mentioned variation from  $100\text{ W}$  to  $240\text{ W}$  is shown. On



## 5.2. Experimental results

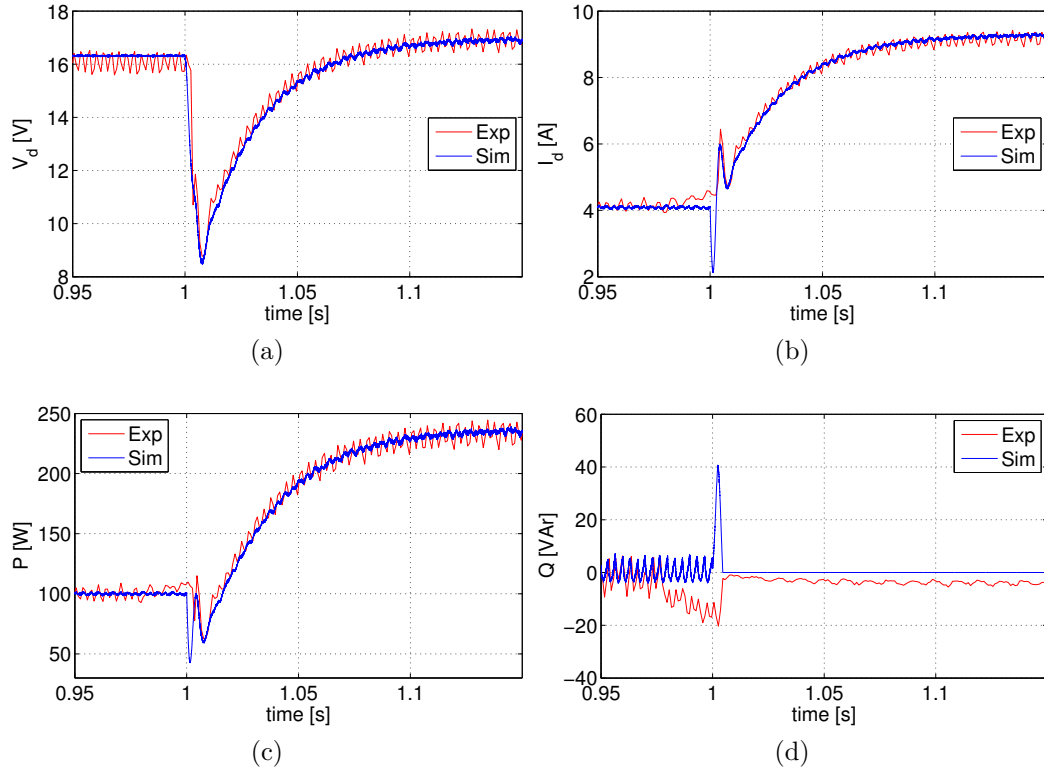


Figure 5.18: Evolution of (a)  $V_d$ , (b)  $I_d$ , (c)  $P$  and (d)  $Q$  variables during the disconnection from the main grid.

the other hand, the evolution of the reactive power of the converter is shown in Figure 5.18d. As in the isolated case, a non-zero value is detected in the experimental results due to the effect of the filtering and the digitalisation.

Figure 5.19a, Figure 5.19b and Figure 5.19c show the evolution of the power of the VRB, SC and the addition of both respectively. A difference between experimental and simulation results can be noticed due to the reasons explained in the results of the isolated case study. However, the dynamics of the power of the SC and the VRB show a good agreement between simulations and experimental results. These dynamics show how the power step is completely supplied by the SC and then how the control algorithm varies the current of the VRB in order to adapt it to the new operation point according to the rules defined in Section 5.1.2.1.

Figure 5.20a shows the evolution of the zero-sequence injected to the

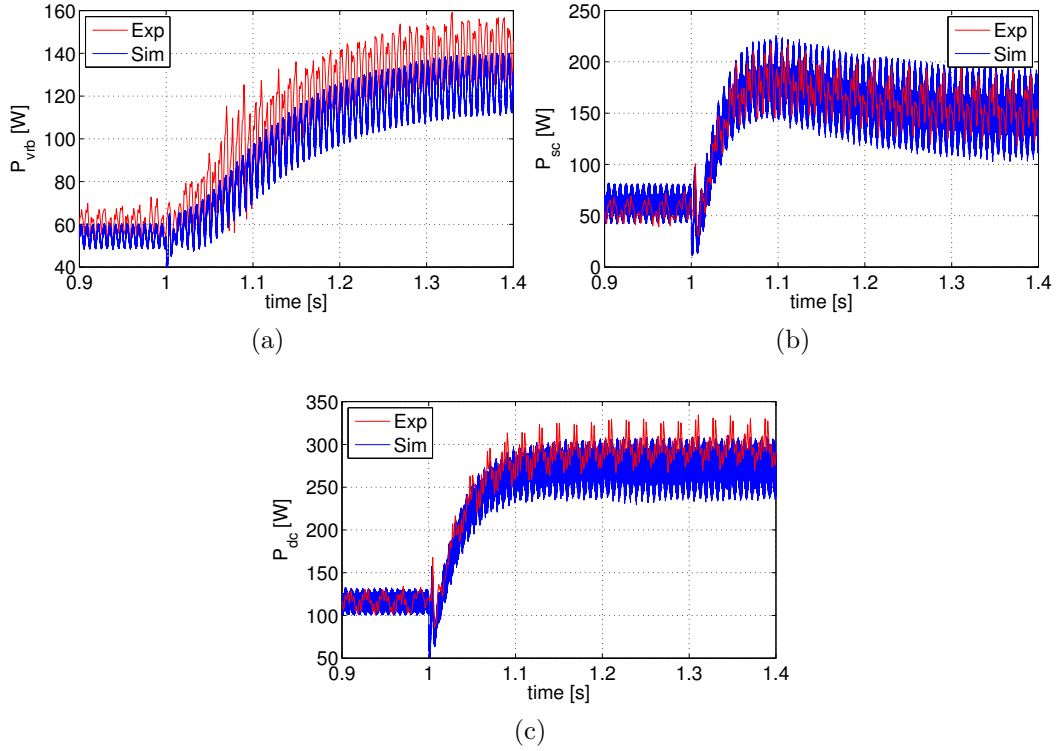


Figure 5.19: Evolution of (a)  $P_{vrb}$ , (b)  $P_{sc}$  and (c)  $P_{dc}$  variables during the disconnection from the main grid.

modulating signal in order to control the current of the VRB. The simulation and experimental results show a good agreement in the case of the offset, but not in the case of the modulation index and the phase difference between the duty cycle signals and the AC currents, shown in Figure 5.20b and Figure 5.20c respectively. As in the case of the isolated case study, the approximative conduction losses calculation and the fact of not simulating the switching losses result in noticeable differences among the experimental and simulation results of the modulation index and the phase difference.

The shown results prove that the converter and the presented control algorithm are able to divide the power between the SC and the VRB when the disconnection occurs. The results also show that the transition from the grid-connected operation mode to the isolated operation mode is carried out smoothly, resetting and initialising the controllers and the phase detection

### 5.3. Chapter conclusions

---

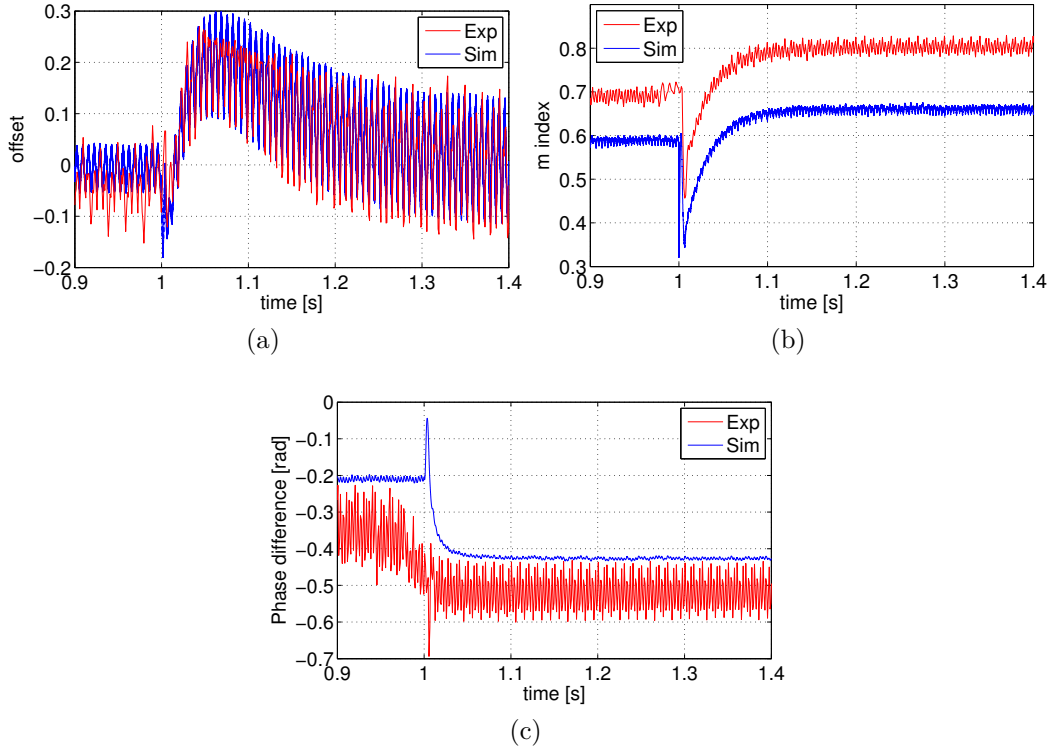


Figure 5.20: Evolution of (a) offset, (b)  $m$  and (c) phase difference variables during the disconnection from the main grid.

according to the previous values.

### 5.3 Chapter conclusions

This chapter has explained the control method of the 3LNPC converter. Special emphasis has been put on the design of the DC power flow control. The presented new control method is based on the average model of the 3LNPC converter and it uses the information measured in real time to calculate which are the limits of the converter and decide in consequence the best power division in each instant.

On the other hand, the experimental tests have proved that the proposed solution is feasible and the defined requirements are satisfied by the proposed topology and control algorithm. The good agreement between simulation and experimental results have also validated the simulation scenario, proving that

it can be used to analyse other scenarios to investigate the behaviour of the system in different conditions.

## Chapter References

- [1] T. Geyer. Model predictive direct current control for multi-level converters. In *Proc. IEEE ECCE*, pages 4305–4312, September 2010.
- [2] T. Geyer. A comparison of control and modulation schemes for medium-voltage drives: Emerging predictive control concepts versus PWM-Based schemes. *IEEE Trans. Ind. Appl.*, 47(3):1380–1389, June 2011.
- [3] T. Ghennam, E. M. Berkouk, B. Francois, K. Aliouane, and K. Merouani. New space-vector hysteresis current control with neutral point voltage balancing applied on three-level VSI for wind power conversion. In *Proc. ICREPQ*, 2007.
- [4] S. Alepuz, J. Salaet, A. Gilabert, J. Bordonau, and J. Peracaula. Control of three-level VSIs with a LQR-based gain-scheduling technique applied to DC-link neutral voltage and power regulation. In *Proc. 28th Ann. IECON*, volume 2, pages 914–919, November 2002.
- [5] M. Mehraza and M. Ahmadigorji. Input/output feedback linearization control for three level/phase NPC voltage-source rectifier using its dual lagrangian model. In *Proc. 11th Int. Conf. (EEEIC)*, pages 712–718, May 2012.
- [6] N. Pluschke and T. Grasshoff. Power supply design-more efficiency for 3-level inverters. *Power Electronics Europe*, 2, March 2010.

# Conclusions and Future Lines

---

## Contents

---

<b>6.1</b>	<b>Conclusions</b>	<b>199</b>
<b>6.2</b>	<b>Future lines</b>	<b>201</b>
<b>6.3</b>	<b>Publications</b>	<b>202</b>

---

This chapter shows the main conclusions of the thesis, to stress its main contributions and to suggest future lines that could be followed in the future to continue working in the presented subject. The publications that have been done during the three years of the PhD are also listed in this chapter.

## 6.1 Conclusions

The main objective of this thesis has been to propose a storage system and its associated power electronics interface and control in order to keep the energy balance, the power balance and also to improve the power quality of a MG.

A state-of-the-art analysis of the currently available storage technologies was carried out in Chapter 2. The characteristics of several storage systems have been carried out, focusing on their advantages and drawbacks from the point of view of the microgrid application. The different characteristics have been presented in tables in order to facilitate the comparison. The results of this analysis showed that none of the currently available storage technologies is capable of satisfying the power and energy requirements fixed in Chapter 1, which has stressed the necessity of using a HESS. According to the comparison analysis, a HESS formed by a SC bank and a VRB is one of the best associations for the microgrid application. The VRB has been

selected due to the possibility of easily increasing the storage capacity using higher tanks and more electrolyte, which makes them highly interesting for the microgrid application. Furthermore, its self-discharge is negligible and the efficiency is similar to the one of other types of batteries, a key feature for long-term storage applications. In addition, they can be fully discharged with no life expectancy reduction. The VRB is considered to be a promising storage technology for RES integration. On the other hand, SC has been selected to be used to face fast power variations, due to a smaller self-discharge, easier installation, no security issues and no maintenance costs in comparison to other types of storage devices that can be used for the same purpose. The modelling of the selected storage systems was also carried out in Chapter 2, models that have been experimentally validated.

Once the HESS was defined, in Chapter 3 a comparison among the most interesting power conversion topologies was carried out in order to determine which is the topology best adapted to the defined application. Two case studies were selected to carry out the mentioned comparison. In the first one, the microgrid operates connected to a main weak grid fixed by a diesel generator, while a variable current generated by a RES is injected in the DC bus. In the second case study the disconnection of the microgrid from the main weak grid has been analysed. The comparison was carried out to investigate the possibilities offered by each topology to obtain the desired power division between the VRB and the SC, the power losses and the harmonic distortion of the generated AC waveforms. The results showed that the 3LNPC topology is able to obtain a similar behaviour of the power of the HESS comparing to the other two topologies, but with reduced power losses and improved THD. Therefore, the 3LNPC topology has been selected to be used as the power interface to control the HESS.

Chapter 4 analyses in detail the operation of the 3LNPC converter. First of all a comparison between different modulation strategies was carried out from the point of view of the DC current division among the HESS. The results showed that the SVM modulation obtains the highest current division,

## 6.2. Future lines

---

but the implementation of the control of the current division is much more complex due to the necessity of selecting the redundant vectors according to the operation point than in the carrier-based modulation strategies, where this control is done adding an offset to the modulating signals. Therefore, THIPWM strategy was used, even if the maximum current division is smaller than in SVM. Then, the operational limits of the 3LNPC converter were determined, limits that are fixed by the use of a maximum and minimum zero-sequence. These operational limits are able to determine in function of the modulation index, phase difference between the duty cycle signals and the AC currents signals, and the relation between the voltages of the SC and the VRB the maximum/minimum current of the SC and the VRB that can be obtained in each instant.

Knowing those limits, in Chapter 5 a rule-based energy management method was designed to select the current reference of the VRB, which is afterwards controlled by a *PI* varying the zero-sequence that is injected in the modulating signals. This control system refers only to the DC side of the 3LNPC converter and has no effect on the AC side variables, which are controlled through a typical two-loop *PI*-based control system. The experimental tests that were carried out have proved that the proposed topology and the designed control method are feasible and the defined requirements are satisfied. The good agreement between simulation and experimental results has also validated the simulation scenario, proving that it can be used to analyse other scenarios to investigate the behaviour of the system in different conditions.

## 6.2 Future lines

Some of the future lines that have been identified and will be followed in order to improve the presented solution are listed below:

- Analyse the behaviour of the 3LNPC topology in a specific microgrid scenario, with a determined renewable generation and load profiles. This would allow analysing the sizing of the storage systems according to the

characteristics of the selected application and the 3LNPC topology. At the same time, this analysis will prove the feasibility of the proposed solution in an entire context, and not only in certain case scenarios, as it has been done during this thesis.

- The operational limits of the 3LNPC converter that were fixed in Chapter 4 allow to design any energy management strategy to manage the power flow of the HESS. Therefore, advanced management systems can be designed and applied to obtain an operation of the HESS that satisfies the desired criteria.
- The operation of the 3LNPC converter has only been analysed in the linear modulation range. The operation in the overmodulation range will allow a higher conversion gain and consequently the possibility of reducing the DC bus voltage and/or increasing the power division possibilities, generating at the same time higher harmonic distortions. The analysis of those advantages and drawbacks could be analysed in a future work.
- It was proved that the SVM modulation strategy is able to obtain a higher current division between the HESS than the employed THIPWM. Thus, another future line would be to investigate how the designed offset control can be done through a proper selection of redundant vectors.
- Methods like the soft-switching could be applied to the 3LNPC converter in order to reduce even more the power losses of the selected topology in comparison to other solutions.

### 6.3 Publications

- A. Etxeberria, I. Vechiu, A. Arnedo, L. Romero, H. Camblong, *Simplified Model of a Fuel Cell for Microgrids Applications*, EVER Conference, Monaco, 2010



### 6.3. Publications

---

- A. Etxeberria, I. Vechiu, H. Camblong, J.M. Vinassa, *Hybrid Energy Storage Systems for Renewable Energy Sources Integration in Microgrids: a Review*, 9th International Power and Energy Conference (IPEC), Singapore, 2010.
- A. Etxeberria, I. Vechiu, H. Camblong, J.M. Vinassa, *Comparison of Sliding Mode and PI Control of a Hybrid Energy Storage System in a Microgrid Application*, International Conference on Smart Grid and Clean Energy Technologies (ICSGCE), Chengdu, China, 2011.
- I. Vechiu, A. Etxeberria, H. Camblong, J.M. Vinassa, *Three-level Neutral Point Clamped Inverter Interface for Flow Battery/Supercapacitor Energy Storage System used for Microgrids*, IEEE-PES Innovative Smart Grid Technologies Europe (ISGT), Manchester, UK, 2011.
- I. Vechiu, A. Etxeberria, H. Camblong, J.M. Vinassa, *Advanced Power Electronic Interface for Hybrid Energy Storage System*, International Renewable Energy Congress (IREC), Hammamet, Tunisia (2011).
- A. Etxeberria, I. Vechiu, H. Camblong, J.M. Vinassa, *Comparison of Three Topologies and Controls of a Hybrid Energy Storage System for Microgrids*, Energy Conversion and Management 54, pp 113-121, 2012. Impact factor (2012) of 2.216.
- A. Etxeberria, I. Vechiu, S. Baudoin, H. Camblong, J.M. Vinassa, *Control of a Hybrid Energy Storage System Using a Three Level Neutral Point Clamped Converter*, IECON, Montréal, Canada (2012).



## APPENDIX A

# Power losses

---

The power losses of a semiconductor component are usually divided in three groups:

- Conduction losses
- Blocking losses
- Switching losses

The conduction losses are also named as on-state losses and they refer to the power losses generated by the voltage drop of the semiconductor device and the current flowing through it. The blocking losses, on the other hand, refer to the off-state or leakage losses. As the leakage current is small these losses are typically neglected. Finally, the switching losses refer to the energy that is lost during the turn-on and turn-off transitions.

The most important losses of a semiconductor device are represented by the conduction and switching losses and in this work only those are taken into account.

### A.1 Conduction losses

The conduction losses represent the on-state losses of a semiconductor device. These losses are obtained linearising the static characteristics of the power elements and representing them by a voltage source ( $V_{ce}$ ) and a series resistor ( $R_{ce}$ ) in the on state. This way, the mean value of the conduction losses can be represented by the equation eq. (A.1).

$$P_{conduction} = (V_{ce} + R_{ce}i_c)i_c \quad (\text{A.1})$$

where  $V_{ce}$  is the threshold voltage,  $R_{ce}$  the dynamic resistance and  $i_c$  the current through the semiconductor element. These parameters can be obtained from the data-sheets of the used elements.

In this thesis the conduction losses have been simulated measuring the currents of each semiconductor device and then calculating the power losses applying eq. (A.1).

## A.2 Switching losses

The switching losses are generated during turn-on and turn-off transients. During these transients, both voltage and current can take significant values and consequently an energy is lost as heat. Logically, the switching losses are directly dependant on the switching frequency. At a higher switching rate there are more commutations and consequently the switching losses are also higher.

The manufacturers of the semiconductor devices usually provide the energy lost in the turn-on and turn-off transients versus the forward current. A relation between the turn-on ( $E_{on}$ )/turn-off ( $E_{off}$ ) dissipated energies and the forward current ( $i_c$ ) can be obtained approximating the curves provided by the manufacturer using a second order equation. Then, the eq. (A.2) can be used to calculate the switching losses.

$$P_{switching} = \frac{1}{t_{sim}} \sum_{j=1}^n \left( E_{on_j}(i_c, V_{off}) + E_{off_j}(i_c, V_{off}) \right) \quad (A.2)$$

where  $i_c$  is the on-state current,  $V_{off}$  is the off-state voltage,  $n$  is the amount of commutations during the simulation and  $t_{sim}$  is the simulation time. The curves of the data-sheets usually show the relation between the dissipated energies and the on-state current for a specific voltage value. The dependence of the dissipated energy (both on and off) and this voltage  $V_{off}$  is assumed to be proportional.

## A.3 Power losses calculation

In this work a method that is directly applied *in Simulink* has been implemented in order to calculate the switching and conduction losses. The power losses calculation is based on the voltage and current measurement of each semiconductor device as well as on the characteristics specified in their data-sheets. The on-state voltage drop, the series resistance, the on-state and off-state transition energy losses are employed to estimate the conduction and switching losses online, while the simulation is being executed.

The conduction losses of all semiconductor devices are calculated using the measured current of each semiconductor device and applying eq. (A.1). Once the simulation is finished the average value is calculated and used for analysis.

The switching losses calculation is based on the on and off transitions detection of the diodes and switches. In the case of the diodes the turn-off energy is considered to be negligible and therefore only the turn-on energy is taken into account. As the diode has a positive voltage drop when it is conducting current, measuring its voltage the on transition can be detected. The current of the diode is also measured and when the on transition is detected it is used to calculate the  $E_{on}$  energy based on the relation between the current and the lost energy given in the data-sheet. The energy lost in each transition is accumulated during the entire simulation and then the average power loss in each diode is calculated. The calculation of the switching losses is schematically shown in fig. A.1.

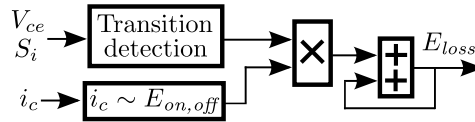


Figure A.1: Block diagram of the switching losses calculation.

In the case of the switches both the on and off transitions must be taken into account. Consequently, the implemented code detects both types of transitions. Once the event has been detected the lost energy is calculated and accumulated, as in the case of the diodes.



# Clarke and Park transforms

---

Any three-phase system can be represented in different reference frames. The natural representation is made on a three-dimensional stationary  $abc$  reference system. However, in many cases for the sake of simplicity other reference systems are used. The most used reference systems are the stationary  $\alpha\beta 0$  and rotational  $dq0$  reference frames. If the three phase system is balanced then the zero-sequence in both cases is 0 and consequently it can be neglected, obtaining a two-dimensional reference system.

In this thesis the three mentioned reference systems have been used and this appendix explains the mathematical process to pass from one reference system to another.

The transformation from the natural  $abc$  coordinate system to  $\alpha\beta 0$  is named *Clarke* transform and the one from  $\alpha\beta 0$  to  $dq0$  *Park* transform. These three reference systems are graphically shown in Figure B.1.

## B.1 Clarke transform

The transform from  $abc$  to  $\alpha\beta 0$  can be done applying the transformation defined by eqs. (B.1) and (B.2).

$$\begin{bmatrix} X_\alpha \\ X_\beta \\ 0 \end{bmatrix} = T_{\alpha\beta 0} \begin{bmatrix} X_a \\ X_b \\ X_c \end{bmatrix} \quad (\text{B.1})$$

$$T_{\alpha\beta 0} = \frac{2}{3} \begin{bmatrix} 1 & -\frac{1}{2} & -\frac{1}{2} \\ 0 & \frac{\sqrt{3}}{2} & -\frac{\sqrt{3}}{2} \\ \frac{1}{2} & \frac{1}{2} & \frac{1}{2} \end{bmatrix} \quad (\text{B.2})$$

The advantage of this representation is that the number of axes is reduced from three to two in comparison to the natural reference system. If the three-

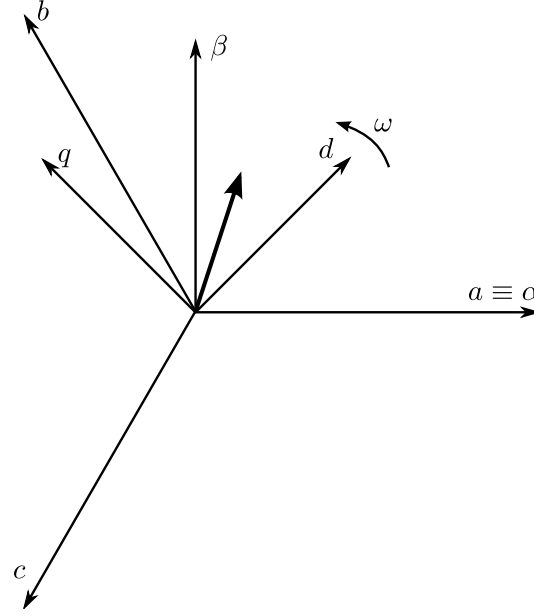


Figure B.1:  $abc$ ,  $\alpha\beta 0$  and  $dq0$  reference systems.

phase system is balanced, the zero-component is null and the vector turns with an angular velocity of  $\omega$  on the plane  $\alpha\beta$ . This reference system is stationary and consequently its components show a variable value in function of the time.

## B.2 Park transform

The Park transform is able to pass from the stationary coordinate system  $\alpha\beta 0$  to the rotational coordinate system  $dq0$ . In the rotational reference system, the angular velocity  $\omega$  of the coordinate system is selected to be the same angular velocity of the vectors. Consequently, the  $d$ ,  $q$  and  $0$  components are constant, while in the other two coordinate systems they are variable. This rotational reference system is specially useful in the control of AC-DC converters, as it permits to represent the vectors using constant components and consequently allowing to use classical control algorithms.

The Park transform can be done carried out applying eqs. (B.3) and (B.4).

$$\begin{bmatrix} X_d \\ X_q \\ 0 \end{bmatrix} = T_{dq0} \begin{bmatrix} X_\alpha \\ X_\beta \\ X_0 \end{bmatrix} \quad (\text{B.3})$$



### B.3. Application to the converter case

---

$$T_{dq0} = \begin{bmatrix} \cos(\omega t) & \sin(\omega t) & 0 \\ -\sin(\omega t) & \cos(\omega t) & 0 \\ 0 & 0 & 1 \end{bmatrix} \quad (\text{B.4})$$

The transformation from  $abc$  to  $dq0$  can be directly done combining the Clarke and Park transforms following eqs. (B.5) and (B.6).

$$\begin{bmatrix} X_d \\ X_q \\ 0 \end{bmatrix} = T \begin{bmatrix} X_a \\ X_b \\ X_c \end{bmatrix} \quad (\text{B.5})$$

$$T = \frac{2}{3} \begin{bmatrix} \cos(\omega t) & \cos(\omega t - \frac{2\pi}{3}) & \cos(\omega t - \frac{4\pi}{3}) \\ -\sin(\omega t) & -\sin(\omega t - \frac{2\pi}{3}) & -\sin(\omega t - \frac{4\pi}{3}) \\ \frac{1}{2} & \frac{1}{2} & \frac{1}{2} \end{bmatrix} \quad (\text{B.6})$$

where  $\omega$  is the reference angular velocity of the Park transformation.

## B.3 Application to the converter case

The defined conversion from  $abc$  to  $dq0$  has been used to obtain the rotational frame equations of the two-level and three-level converters. This section explains the steps that were omitted in Section 3.2.1.2. The mentioned conversion will be analysed in the isolated and grid-connected operation modes.

### B.3.1 Isolated operation mode

In the case of the isolated operation, the starting point is the equation of the AC side of the converter in the  $abc$  reference frame, shown in eq. (B.7).

$$\frac{d\vec{i}_{inv}^s}{dt} = \frac{1}{L} \left( \frac{\vec{d}^s + 1}{2} \right) V_{dc} - \frac{R_L}{L} \vec{i}_{inv}^s - \frac{\vec{V}_{N0}^s}{L} \quad (\text{B.7})$$

Applying eq. (B.5) to eq. (B.7), eq. (B.8) can be obtained.

$$\frac{d \left( T^{-1} \vec{i}_{inv}^r \right)}{dt} = \frac{1}{L} \left( \frac{\vec{d}^s + 1}{2} \right) V_{dc} - \frac{R_L}{L} \vec{i}_{inv}^s - \frac{\vec{V}_{N0}^s}{L} \quad (\text{B.8})$$

Developing the derivative part of eq. (B.8) the expression eq. (B.9) is obtained.

$$\frac{d}{dt} \left( T^{-1} \vec{i}_{inv}^r \right) = T^{-1} \frac{d\vec{i}_{inv}^r}{dt} + \frac{dT^{-1}}{dt} \vec{i}_{inv}^r \quad (\text{B.9})$$

Substituting eq. (B.9) in eq. (B.8) and multiplying the entire expression with the transformation matrix  $T$  eq. (B.10) can be calculated.

$$\frac{d\vec{i}_{inv}^r}{dt} = -T \frac{dT^{-1}}{dt} \vec{i}_{inv}^r + \frac{1}{L} \left( \frac{\vec{d}^r + \vec{A}^r}{2} \right) V_{dc} - \frac{R_L}{L} \vec{i}_{inv}^r - \frac{\vec{V}_{N0}^r}{L} \quad (\text{B.10})$$

Knowing that the expressions of eq. (B.11) hold, the final  $d$  and  $q$  components of the current of the converter can be easily deducted, which are shown in eq. (B.12).

$$\begin{aligned} T T^{-1} &= I \\ \vec{A}^s &= \begin{bmatrix} 1 \\ 1 \\ 1 \end{bmatrix} \rightarrow \vec{A}^r = \begin{bmatrix} 0 \\ 0 \\ 1 \end{bmatrix} \\ V_{NO}^s &= \begin{bmatrix} V_{NO} \\ V_{NO} \\ V_{NO} \end{bmatrix} \rightarrow V_{NO}^r = \begin{bmatrix} 0 \\ 0 \\ V_{NO} \end{bmatrix} \\ T \frac{dT^{-1}}{dt} &= \begin{bmatrix} 0 & -\omega & 0 \\ \omega & 0 & 0 \\ 0 & 0 & 0 \end{bmatrix} \end{aligned} \quad (\text{B.11})$$

$$\begin{aligned} \frac{di_{inv}^d}{dt} &= -\frac{R_L}{L} i_{inv}^d + \omega i_{inv}^q + \frac{1}{L} d^d \frac{V_{dc}}{2} \\ \frac{di_{inv}^q}{dt} &= -\frac{R_L}{L} i_{inv}^q - \omega i_{inv}^d + \frac{1}{L} d^q \frac{V_{dc}}{2} \end{aligned} \quad (\text{B.12})$$

### B.3.2 Grid-connected operation mode

In the grid-connected operation mode, the initial equations are different but the process is exactly the same. The equation that defines the AC side of the converters is shown in eq. (B.13).

$$\frac{d\vec{i}_{inv}^s}{dt} = \frac{1}{L} \left( \frac{\vec{d}^s + 1}{2} \right) V_{dc} - \frac{R_L}{L} (\vec{i}_{inv}^s + \vec{i}_{grid}^s) - \frac{\vec{V}_{N0}^s}{L} \quad (\text{B.13})$$

### B.3. Application to the converter case

---

Substituting eq. (B.9) in eq. (B.13) and multiplying the entire expression with the transformation matrix  $T$  as in the case of the isolated operation mode, eq. (B.14) can be calculated.

$$\frac{d\vec{i}_{inv}^r}{dt} = -T \frac{dT^{-1}}{dt} \vec{i}_{inv}^r + \frac{1}{L} \left( \frac{\vec{d}^r + \vec{A}^r}{2} \right) V_{dc} - \frac{R_L}{L} (\vec{i}_{inv}^r + \vec{i}_{grid}^r) - \frac{\vec{V}_{N0}^r}{L} \quad (\text{B.14})$$

Finally, from eq. (B.14) and using eq. (B.11) the  $d$  and  $q$  components of the current of the grid-connected operation mode can be obtained, which are shown in eq. (B.15).

$$\begin{aligned} \frac{di_{inv}^d}{dt} &= \frac{1}{L} d^d \frac{V_{dc}}{2} - \frac{R_L}{L} i_{inv}^d + \omega i_{inv}^q - \frac{R_L}{L} i_{grid}^d \\ \frac{di_{inv}^q}{dt} &= \frac{1}{L} d^q \frac{V_{dc}}{2} - \frac{R_L}{L} i_{inv}^q - \omega i_{inv}^d - \frac{R_L}{L} i_{grid}^q \end{aligned} \quad (\text{B.15})$$



# Digitalisation of continuous algorithms

---

As the control system has been implemented in a digital processor, it has been necessary to digitalise all the continuous algorithms. This digitalisation process has been carried out applying the well-known bilinear transform or *Tustin* method. The approximation of *Tustin* uses eq. (C.1) to facilitate the digitalisation process of the continuous algorithms.

$$s = \frac{2}{T_s} \frac{z - 1}{z + 1} \quad (\text{C.1})$$

The sampling period that has been employed to carry out this digitalisation process has been of  $T_s = 0.2 \text{ ms}$ . This value has been necessary as the zero-sequence injection depends on the phase difference between the duty cycle and the current of the AC side of the 3LNPC converter. Therefore, a small sampling period has been used to reduce the phase difference measurement error. Even if different sampling periods could be used to optimise the computational load of the implemented algorithm, in this work the same  $T_s$  has been used for all the discrete algorithms for the sake of simplicity and because the used processor was powerful enough to execute the entire code.

## C.1 PI controllers and low-pass filters

The *PI* controllers used to control the  $d$  and  $q$  components of the voltage and current, and also to control the injected zero-sequence component have been digitalised from eq. (C.2) to eq. (C.3) applying eq. (C.1).

$$PI(s) = K_p + \frac{1}{T_i s} \quad (\text{C.2})$$

## Appendix C. Digitalisation of continuous algorithms

---

$$PI(z) = \frac{(2K_p T_i + T_s)z - 2K_p T_i + T_s}{2T_i(z - 1)} \quad (\text{C.3})$$

The same conversion can be applied to the different low-pass filters that have been used in the control algorithm. The continuous transfer functions of these first order and second order low-pass filters are shown in eqs. (C.4) and (C.5) respectively. Applying eq. (C.1) the discretised expressions of those filters, shown in eq. (C.6) for the first order filter and in eq. (C.7) for the second order one, can be obtained.

$$G_1(s) = \frac{1}{\tau s + 1} \quad (\text{C.4})$$

$$G_2(s) = \frac{\omega_0^2}{s^2 + 2\xi\omega_0 s + \omega_0^2} \quad (\text{C.5})$$

$$G_1(z) = \frac{T_s(z + 1)}{(2\tau + T_s)z - 2\tau + T_s} \quad (\text{C.6})$$

$$G_2(z) = \frac{a^2(z^2 + 2z + 1)}{(4 + a^2 + 4\xi a)z^2 + (-8 + 2a^2)z - 4\xi a + 4 + a^2} \quad (\text{C.7})$$

$$a = \omega_0 T_s$$

The parameters of the controllers that have been used in the experimental tests are shown in Table C.1. In the case of the filters, a value of  $\tau = 0.1$  for the first order low-pass filter, and a natural frequency of  $\omega_0 = 2\pi 100 \text{ rad/s}$  and a damping factor of  $\xi = 1$  for the second order filter have been used.

Controller	$PI$	
	$K_p$	$T_i$
$V_{dq}$	0.01	0.05
$I_{dq}$	0.05	0.01
Offset	-0.2	-0.0125

Table C.1: Parameters of the controllers used in the experimental tests.

## C.2 Synchronisation algorithm

The discretisation of the synchronisation algorithm has been divided in two parts. On the one hand, the discretisation of the quadrature signal generator has been carried out. As it is formed by two independent and decoupled SOGI (shown in Figure C.1), each SOGI can be individually discretised. The second part is the discretisation of the frequency detector, the FLL algorithm.

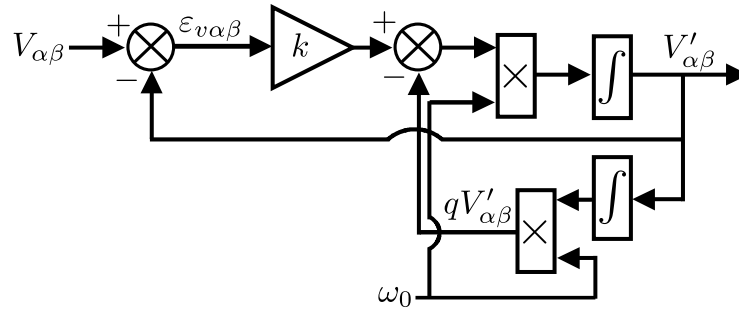


Figure C.1: Structure of the DSOGI-QSG.

From Figure C.1 the transfer functions eqs. (C.8) and (C.9) can be obtained.

$$\frac{V'_{\alpha\beta}(s)}{V_{\alpha\beta}(s)} = \frac{k\omega_0 s}{s^2 + k\omega_0 s + \omega_0^2} \quad (\text{C.8})$$

$$\frac{qV'_{\alpha\beta}(s)}{V_{\alpha\beta}(s)} = \frac{k\omega_0^2}{s^2 + k\omega_0 s + \omega_0^2} \quad (\text{C.9})$$

The discretisation of the SOGI must be carried out ensuring that the employed discretisation method obtains a phase difference of  $90^\circ$  in order to generate the two outputs of the orthogonal system ( $V'_{\alpha\beta}$  and  $qV'_{\alpha\beta}$ ) exactly in quadrature. This must be satisfied in order to avoid the ripples that appear both in the amplitude and the frequency detection if the mentioned signals are not shifted  $90^\circ$ .

In this work the Tustin or trapezoidal approximation (shown in eq. (C.1)) has been employed to discretise the SOGI-QSG algorithm. This approximation cannot be directly applied in Figure C.1 though, as algebraic loops would appear [1]. Therefore, the trapezoidal method is applied only to the transfer function eq. (C.8), obtaining eq. (C.10).

$$\begin{aligned}
 \frac{V'_{\alpha\beta}(z)}{V_{\alpha\beta}(z)} &= \frac{b_0 (1 - z^{-2})}{1 - a_1 z^{-1} - a_2 z^{-2}} \\
 b_0 &= \frac{2k\omega_0 T_s}{2k\omega_0 T_s + \omega_0^2 T_s^2 + 4} \\
 a_1 &= \frac{2(4 - \omega_0^2 T_s^2)}{2k\omega_0 T_s + \omega_0^2 T_s^2 + 4} \\
 a_2 &= \frac{2k\omega_0 T_s - \omega_0^2 T_s^2 - 4}{2k\omega_0 T_s + \omega_0^2 T_s^2 + 4}
 \end{aligned} \tag{C.10}$$

This way, the final implementation of the discretised SOGI-QSG can be obtained from eq. (C.10) and it is shown in Figure C.2.

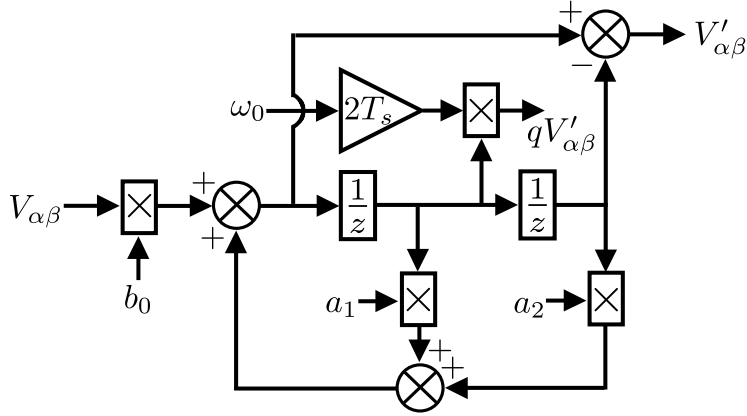


Figure C.2: Discrete implementation of SOGI-QSG algorithm.

The value  $\omega_0$  is calculated each computational cycle by the FLL algorithm, which has been discretised using the Tustin approximation.

The numerical values of the parameters of the DSOGI-FLL synchronisation algorithm are shown in Table C.2.

Parameter	Value
$k$	1.41
$\Gamma$	125

Table C.2: Parameters of the DSOGI-FLL algorithm.



## References

- [1] M. Ciobotaru, R. Teodorescu, and F. Blaabjerg. A new single-phase PLL structure based on second order generalized integrator. In *Proc. 37th Annu. IEEE PESC*, pages 1 – 6, June 2006.

